Brain Energy Supply and Usage

Clare Howarth

A thesis submitted to the University of London

for the degree of

Doctor of Philosophy

Department of Physiology, University College London

January 2008

ProQuest LLC
789 East Eisenhower Parkway
P.O. Box 1346
Ann Arbor, MI 48106-1346

For my parents

ABSTRACT

Although a coupling between cerebral energy consumption and neuronal activity was initially suggested over a hundred years ago, the exact relationship remains unclear. This thesis addresses four aspects of the energy supply to the brain. First, blood flow is increased to areas where neurons are more active, and it is this blood flow increase which forms the basis of functional imaging techniques. In contrast to the common assumption that blood flow regulation occurs solely at the arteriole level, I have demonstrated experimentally that blood flow control, mediated by pericytes, also occurs in capillaries. Second, it has been proposed that glutamate transporters coordinate CNS glucose and oxygen usage: glutamate released from neurons is taken up into astrocytes, evoking glycolysis which is suggested to export lactate to power neuronal oxidative phosphorylation. I tested this hypothesis by measuring oxygen use when glial glutamate uptake was blocked, and found that this had little effect on the oxygen use evoked by neural activity, arguing against the idea that glutamate uptake and astrocyte lactate export regulate neuronal oxidative phosphorylation. Third, although it is known that most of the brain's energy is used on reversing the ion fluxes which generate action potentials and synaptic currents, in general it is unknown how the energetic resources to the brain are allotted to carry out different aspects of neuronal information processing. I constructed an energy budget for the cerebellum using the measured properties of cells in this area. This provides insight into how evolution has allocated energy at the cellular and subcellular levels to different parts of a neural computation. Finally, I estimated the amount of brain energy use expended on conscious perception of stimuli, as opposed to being used on unconscious information processing. Surprisingly, only a small percentage of brain energy is used on conscious perception.

Statement of the candidate's contribution to this thesis

The work in the thesis is described in 4 results chapters, to which Clare Howarth's contribution was as described below. All of the data analysis, figure production and writing was done by Clare Howarth.

(1) The mechanisms of switching of blood flow to active neurons
Because of the complexity of these experiments, they were partly undertaken in collaboration with Claire Peppiatt-Wildman. I performed 60% of the total experiments described in this section (they took 3 person years to carry out) and 90% of the figures are from experiments I did personally.

(2) An energy budget for the cerebellum
I performed 95% of the work for this chapter the other 5% being supervisorial input.

(3) O_2 use on various processes in the cerebellum
I was responsible for 90% of this work, with the other 10% being performed in collaboration with Marieke Scholvinck.

(4) Energy used on perceptual decisions
I performed this work in collaboration with Marieke Scholvinck; I was responsible for 50% of the work.

Signed (candidate) Date

Clare Howarth

Signed (supervisor) Date

David Attwell 21.12.7

Acknowledgements

I would like to thank my supervisor Prof. David Attwell, for his guidance, support and encouragement throughout my PhD. I would like to thank all my fellow lab members who have kindly offered their help and encouragement over the past few years. For making my time in the lab so enjoyable thanks go to: Nicola Allen, Yamina Bakiri, Valeria Burzomato, Pauline Cavelier, Anna De Simoni, Guillaume Frugier, Camilla Haglerod, Catherine Hall, Niki Hamilton, Ines Hans, Ragnhildur Karadottir, Josef Kittler, Karolina Kolodziejczyk, Nanna Luneborg, Paikan Marcaggi, Peter Mobbs, Simen Owe, Rachael Pearson, Claire Peppiatt-Wildman, Johanne Rinholm, Marieke Scholvinck, Anna Wade and Louise Whiteley.

I would like to extend special thanks to Claire Peppiatt-Wildman who performed the NG2 labelling shown in Fig. 3.2. Thanks for both a productive and enjoyable collaboration, the results of which are presented in Chapter 3. Furthermore, I would like to thank Marieke Scholvinck with whom I collaborated on the theoretical project presented in Chapter 6 and who also performed some of the experiments looking at the oxygen use on various processes in the cerebellum, presented in Chapter 5.

Finally I would like to thank my parents who have supported and encouraged me throughout my education and have always made me believe I can achieve whatever I set out to do. Without them none of this would have been possible.

The work presented in this thesis was supported by the Wellcome Trust.

Table of Contents

List of Figures

List of Tables

List of Movies

Chapter 1: Introduction

1.1 Overview

This thesis is concerned with the energy supplied to the brain, in the form of glucose and oxygen provided in the blood. I will look experimentally at how this energy supply is regulated, and assess theoretically the cellular and subcellular signalling tasks it is used for. In this Introduction I will provide the general background needed to understand the experiments and theoretical work described in the Results chapters. More specific background relevant to each set of experiments is presented in the Introduction to each Results chapter.

1.2 The relationship between the brain's energy supply and its computational power

Although Roy and Sherrington (1890) first suggested a coupling between cerebral energy consumption and neuronal activity over a hundred years ago, the exact relationship between these variables remains unclear. The brain continuously consumes metabolic energy at a high rate: although the human brain accounts for only 2% of the body's weight it uses 20% of the body's resting energy use (Clarke and Sokoloff, 1999). During evolution, changes in diet and the efficiency of the gut may have allowed humans to devote more energy to the brain than would be expected for its size compared to that of lower primates (Aiello and Wheeler, 1995). We will see below that the high energy demand of the brain occurs largely because the neural processing of information is metabolically expensive.

The processing power of any computational device is limited by its energy supply (Sarpeshkar, 1998). The majority of the energy used in the brain is expended on signalling, and most of that energy is expended on reversing the ionic fluxes caused by synaptic potentials and action potential propagation (Clarke and Sokoloff, 1999; Attwell and Laughlin, 2001). In the whole brain (i.e. grey matter plus white matter) if the Na^+/K^+ pump is blocked, or if coma is induced with anaesthetics, the energy usage is reduced to less than 50% (Kety,

1957; Sokoloff, 1960; Siesjo, 1978; Winkler, 1981; Astrup et al., 1981; Ames, III and Li, 1992; Ames, III et al., 1992; Rolfe and Brown, 1997). The residual energy consumption (~ 10 μmol ATP/g/min in rodent) presumably sustains basic cellular non-signalling processes. These 'housekeeping' tasks include protein synthesis, phospholipid metabolism, axoplasmic transport and mitochondrial proton leak. It should be noted that the white matter accounts for around half the brain but, as the energy use in white matter is less than in grey matter, the percentage of total energy which is 'housekeeping' is greater there than in grey matter. Although it is established that most brain energy use is on signalling, it is unknown how the energetic resources available to the brain are allotted to carry out different parts of a neural computation.

Attwell and Laughlin (2001) took a bottom up modelling approach to produce an energy budget for the grey matter of rodent cortex, which suggested that most signalling energy consumption is associated with synaptic currents and action potential propagation (34% and 47% of the total signalling energy use, respectively). Synaptic energy cost was defined by three parameters: the probability that an action potential releases transmitter at a bouton and the number and conductance of postsynaptic channels activated by the transmitter. The remaining signalling-related ATP consumption was predicted to be split as follows: maintaining the neuronal and glial resting potentials 13%, presynaptic Ca^{2+} entry 3%, glutamate recycling 3% and Ca^{2+} transients in spines and vesicle recycling <1% (Attwell and Laughlin, 2001). The large differences in energy usage for each process stem from the different numbers of ions (or molecules) involved which have to be pumped across the membrane (or phosphorylated).

The total predicted energy use for rodent grey matter was 40 μmol ATP/g/min, of which 30 μmol ATP/g/min was signalling-related energy, and perhaps 10 μmol ATP/g/min was housekeeping energy (Attwell and Laughlin, 2001). This agrees with the measured total energy consumption of 33-50 μmol ATP/g/min (Sokoloff et al., 1977), and suggests that 75% of the energy expenditure in the grey matter is devoted to signalling, with the remaining 25%

spent on housekeeping tasks. This figure of 25% is lower than the 50% quoted above for the whole brain which includes the white matter as well. This is probably explained by the fact that the brain grey matter has a higher energy usage per gram than the whole brain, due to the high signalling-related energy demand which exists in grey matter (Sokoloff et al., 1977; Siesjo, 1978; Kennedy et al., 1978; Rolfe and Brown, 1997; Clarke and Sokoloff, 1999), which largely reflects the fact that grey matter has a high density of synapses while white matter does not (but see Kukley et al., 2007; Ziskin et al., 2007).

As most of the brain's energy is used on reversing ion fluxes which generate action potentials and synaptic currents, there will be evolutionary pressure for metabolically efficient wiring patterns and neural codes, and an ability to reconfigure the information processing of neural networks over a wide range of time scales in response to computational needs (Laughlin and Sejnowski, 2003). Brain areas are topographically arranged (for example, within the primary visual cortex neighbouring regions of the visual field are represented by neighbouring neurons) resulting in a much greater connectivity existing between neurons close together (<1 mm apart) than between those that are further apart (Laughlin and Sejnowski, 2003). This arrangement minimises the length of connections between neurons, minimising the energetic costs of 'wiring'. In addition, reducing signal delay by shortening axonal connections will also reduce the energy expended on action potentials. The layout of cortical areas minimises the total lengths of axons which are needed to join them (Klyachko and Stevens, 2003). To minimise conduction delays in axons, while maximising the synaptic density, axons and dendrites are predicted to occupy 60% of the volume in optimally wired gray matter (Chklovskii et al., 2002). This idea has been extended to show that, with an acceptable delay on the order of a millisecond, the maximum length of local connections is of the order of a cortical column (Wen and Chklovskii, 2005). The segregation of the brain into grey and white matter may be a consequence of minimising conduction delay in a highly interconnected neuronal network (Wen and Chklovskii, 2005).

1.3 Energy supply limits brain information processing to the millisecond timescale

The brain's energy supply limits the average signalling rate to around 4 Hz (in rodent, (Attwell and Laughlin, 2001); Lennie (2003) suggests less than 1 Hz in humans). This rate seems low for a system which can respond as quickly as the brain, suggesting that metabolic constraints must influence the way in which the brain processes information (Laughlin and Sejnowski, 2003). Energy efficiency is improved by using sparse coding (Field, 1994; Levy and Baxter, 1996), with which only a small proportion of cells signal at any one time, thus using little energy, but by using a combinatorial code to represent information the firing neurons can still have a high representational capacity. For maximum efficiency it has been estimated that only 1-16% of neurons should be active at once (Levy and Baxter, 1996; Attwell and Laughlin, 2001).

Synaptic failures lower the grey matter energy consumption (Attwell and Laughlin, 2001). The brain increases its efficiency by altering the probability of transmission depending on the pattern of activity (as occurs in short and long term plasticity). Plasticity allows the cortex to rapidly reconfigure connectivity to meet changes in computational needs (Laughlin and Sejnowski, 2003).

The energy available to the brain for signalling, and its cellular distribution, limits the time scale of information processing, in both axons and dendrites, to the millisecond range (see below). In turn, this timescale constrains the AMPA receptor kinetics and the rate of glutamate removal from the synaptic cleft to also be on a millisecond time scale (Attwell and Gibb, 2005).

The time scale of processing of subthreshold signals in dendrites is partly limited by the membrane time constant, τ_m, which is the product of cell resistance and capacitance and is usually within the range of 1-20 ms. In order to process higher frequency synaptic signals τ_m must decrease, in which case the resistance or capacitance must be lowered. However, decreasing the cell resistance by inserting more ion channels into the membrane will result in

a higher conductance and larger ion fluxes, which would lead to a higher energy expenditure on maintaining the resting potential (Attwell and Laughlin, 2001). Consequently it is not possible to increase the upper frequency limit for information processing with synaptic potentials, because that would decrease the energy available for expenditure on action potentials (Attwell and Gibb, 2005). This would decrease the highest frequency at which action potentials can occur, and lower the temporal resolution with which signals can be encoded in axons. Thus, a balance between energy usage on the resting potential and action potentials must be maintained. Similarly, increasing energy use by raising the frequency of action potentials would decrease the energy available to maintain the resting potential, thus requiring a higher membrane resistance and membrane time constant, which would slow the possible processing speed of synaptic signals (Attwell and Gibb, 2005).

The AMPA receptors used for rapid information transfer between neurons have kinetics which are matched to the millisecond time scale imposed by the brain's energy supply – activation by glutamate and deactivation once the glutamate is removed both occur in milliseconds. The fast unbinding rate for glutamate implies that there is a low glutamate affinity for AMPA receptors (Attwell and Gibb, 2005). In order to make use of these fast kinetics, glutamate must be cleared from the synaptic cleft rapidly, requiring synapse diameters of less than 1 μm for fast glutamate diffusion out of the cleft, a rapid initial glutamate removal step by transporters and a high transporter density surrounding synapses (Attwell and Gibb, 2005). In contrast, the kinetic properties of NMDA receptors are not set by energetic factors. NMDA receptors are responsible for coincidence detection and so need to remain activated for longer than the AMPA receptors, thus they have a slow unbinding rate for glutamate and are high affinity receptors (Attwell and Gibb, 2005).

Even with all these adaptations it is important for the brain to carefully allot energy to active neurons. Exactly which processes consume energy is a major topic of this thesis, and a detailed analysis of this is presented for the cerebellum in Chapter 4.

1.4 Regulation of the brain's energy supply

1.4.1 Coupling of neural activity to energy supply

The total brain energy supply is essentially constant, so energy resources must be allocated flexibly among regions according to neuronal demand, which requires a local control of cerebral blood flow (CBF). A tight spatial and temporal coupling exists between local blood flow regulation and neuronal metabolic need. Blood flow is increased to areas where neurons are more active, and it is this blood flow increase which forms the basis of functional imaging techniques (Attwell and Iadecola, 2002; Shulman et al., 2004; Logothetis and Wandell, 2004; Raichle and Mintun, 2006) including the BOLD (blood oxygen level-dependent) signal used in fMRI (functional magnetic resonance imaging), as will be discussed in section 1.7, below.

The usual substrates for cellular energy metabolism within the brain are oxygen and glucose, forming products of ATP, CO_2 and H_2O (Sokoloff, 1960; Siesjo, 1978; Clarke and Sokoloff, 1999). Approximately 31 ATP are produced per glucose molecule consumed (allowing for proton leakage in the mitochondria (Rolfe and Brown, 1997)). At rest, the cerebral metabolic ratio (ratio of oxygen/glucose consumed) is close to 6, implying that the majority of energy is supplied by oxidation of glucose. During neuronal activation, there is a greater increase in CMR_{glc} (glucose utilisation) than in CMR_{O2} (oxygen utilisation) (Fox et al., 1988), resulting in a decrease in the cerebral metabolic ratio, perhaps because glycolysis is initially increased more than oxidative phosphorylation, although this is debated (Chih et al., 2001).

During hard exercise, arterial lactate levels increase as lactate is produced by skeletal muscle. The brain takes up this lactate in amounts comparable to glucose, contributing to the decrease in cerebral metabolic ratio following exhaustive exercise (Ide et al., 2000; Dalsgaard et al., 2002). The lactate is assumed to be metabolised as there is apparently no lactate accumulation within, or release from, the brain (Dalsgaard et al., 2002; Dalsgaard et al., 2004; and see review by Dalsgaard, 2006).

When a neuron is active its metabolic demands increase, and more oxygen and glucose must be supplied. A signal is passed to the vasculature to increase the blood flow and so increase the supply of oxygen and glucose (Fig. 1.1). Although the idea of neural activity being coupled to CBF was first suggested over 100 years ago (Roy and Sherrington, 1890), the exact mechanisms underlying this phenomenon remain to be determined.

1.4.2 Energy supply is not controlled by an energy lack signal

CBF is proportional to oxygen usage (Hoge et al., 1999) and it used to be assumed that the signal responsible for the increase in blood flow following increased neural activity was a lack of oxygen or glucose, or the accumulation of CO_2. Thus, blood flow increases were thought to be driven directly by energy use, particularly in presynaptic terminals or glia (Magistretti et al., 1999; Shin, 2000), although most energy is used on postsynaptic currents and action potentials (Attwell and Laughlin, 2001). However, Powers et al. (1996) found that there was no significant difference in the local increase of blood flow following neuronal activation when the initial glucose concentration was lowered by ~50% with insulin, compared to at physiological glucose levels. If CBF was regulated to provide a fixed amount of glucose to power a neural task, one would predict that the CBF increase should double in these circumstances. Thus, these data argue against a lack of glucose driving the haemodynamic response to neuronal activity. Similar experiments, investigating neuronal activity-induced increases in CBF when the blood oxygen level was lowered, were performed by Mintun et al. (2001). The data showed no significant difference in the local increase in blood flow compared to control conditions, indicating that CBF increases are also not regulated by local oxygen requirements. Other studies (Astrup et al., 1978; Pinard et al., 1984) have shown that the blood flow increase associated with neural activity is not driven by an accumulation of CO_2 evoking an acid pH change. Although an acid pH does increase CBF, the extracellular pH during neural activity was actually found to become alkaline due to the CBF increase removing CO_2. These results suggest that blood flow is controlled by factors

other than those discussed so far. In fact, as described below, the blood flow increase is generated by neurotransmitter release rather than being driven directly by energy use (Attwell and Iadecola, 2002).

1.4.3 Amine control of energy supply

Blood flow is thought to be controlled, in part, globally by amine-mediated neural systems (reviewed by Attwell and Iadecola, 2002). The smooth muscle in cerebral arterioles is innervated by noradrenergic fibres from the sympathetic system (vessels on the surface of the brain: Harper et al., 1972) and locus coeruleus (intraparenchymal vessels: Raichle et al., 1975). When noradrenaline binds to α_1-receptors (which are G-protein coupled receptors) it activates the receptors, leading to IP_3 signalling which results in the release of Ca^{2+} from stores within the sarcoplasmic reticulum. The Ca^{2+} binds to calmodulin, forming a complex which activates myosin light chain kinase (MLCK). The MLCK phosphorylates the myosin head groups enabling them to bind actin and the smooth muscle cell contracts (see Fig. 1.2). Cerebral arterioles also receive serotonergic innervation from the raphe nucleus (Cohen et al., 1996). Intraparenchymal microvessels are also innervated by dopaminergic axons (Krimer et al., 1998) from the mesencephalic ventral tegmental area (Phillipson et al., 1987). All of these amines have been shown to cause vasoconstriction. Opposing these amine influences, cholinergic axons from the basal forebrain have close associations with both arterioles and capillaries, and can produce vasodilatation (Sato and Sato, 1992; Chedotal et al., 1994). Such diffuse projections could mediate control of blood flow over a wide area of the brain.

1.4.4 Local control of energy supply by glutamate

Local blood flow control, on the other hand, is achieved by fast neurotransmitter-mediated signalling (Attwell and Iadecola, 2002). Glutamate and NMDA have been shown to elicit vasodilatory responses in neocortical and hippocampal microvessels, and in pial arteries (Busija and Leffler, 1989; Faraci and Breese, 1993; Meng et al., 1995; Fergus and Lee,

1997b). In the cerebellum, pharmacological evidence suggests that glutamate receptor activation mediates the increase of blood flow following neural stimulation (Li and Iadecola, 1994; Iadecola et al., 1996).

During neuronal activity, glutamate is released and can act via NMDA/AMPA receptors to raise postsynaptic $[Ca^{2+}]_i$, activating neuronal nitric oxide (NO) synthase (Southam et al., 1991; Fergus and Lee, 1997b). The glutamate-evoked release of NO activates guanylate cyclase in arteriolar smooth muscle, producing cGMP (Katsuki et al., 1977; East and Garthwaite, 1991). This, in turn, activates K^+ channels in the smooth muscle, producing a hyperpolarization that reduces Ca^{2+} entry and results in vasodilation (Fig. 1.2 and 1.3 and Robertson et al., 1993). In addition to these neuronal effects on the vasculature, several recent studies have shown that astrocytes also play a key role in the control of the brain vasculature at the arteriole level (Zonta et al., 2003; Mulligan and MacVicar, 2004; Filosa et al., 2004; Takano et al., 2006). There is controversy in the literature (reviewed by Peppiatt and Attwell, 2004) over whether glutamate results in astrocyte-mediated vasoconstriction (Mulligan and MacVicar, 2004) or vasodilation (Zonta et al., 2003), but both responses involve neuronally released glutamate acting on astrocyte metabotropic glutamate receptors (mGluRs), which raise astrocyte $[Ca^{2+}]_i$ (Pasti et al., 1997). Interestingly, astrocytes show spontaneous $[Ca^{2+}]_i$ elevations (Hirase et al., 2004b) which are probably generated by neural activity releasing glutamate. As a result of the astrocytic $[Ca^{2+}]$ rise phospholipase A_2 (PLA_2) is activated, producing arachidonic acid (AA). This can be processed locally to produce cyclooxygenase (COX) generated derivatives, such as prostaglandin E_2 (PGE_2). These are released from astrocyte endfeet, apposed to the smooth muscle layer surrounding arterioles, resulting in activation of K^+ channels in the smooth muscle, and hence vasodilation (Fig. 1.2 and 1.3). Based on results using COX inhibitors (Zonta et al., 2003; Takano et al., 2006), PGE_2 is thought to mediate a significant component of the dilatory response to raised astrocytic calcium. AA can also be metabolized by cytochrome P450 (CYP) epoxygenase to epoxyeicosatrienoic acids (EETs), which are vasodilators that activate K^+ channels and hyperpolarise smooth muscle cells (Gebremedhin et al., 1992; Alkayed et al., 1996; Alkayed

et al., 1997; Harder et al., 1998). Alternatively, the AA itself can diffuse to the smooth muscle layer surrounding the arterioles, producing 20-HETE via ω-hydroxylases (enzymes of the CYP4A family: for review see Roman, 2002). The 20-HETE inhibits K^+ channels, thus evoking more depolarisation activated Ca^{2+} entry and arteriole constriction (Fig. 1.2 and 1.3).

Metea and Newman (2006) have proposed that, in the retina, in addition to NO dilating via cGMP, low levels of NO may mediate vasodilation by inhibiting ω-hydroxylases, which synthesize the vasoconstrictor 20-HETE, while high levels of NO mediate vasoconstriction by inhibiting cytochrome P450 epoxygenase, which synthesizes EETs. They found that inhibiting prostaglandin synthesis had no effect on light-evoked vasodilation. However, in contrast to these findings, Takano et al. (2006) found that glial stimulation in the somatosensory cortex resulted in vasodilation via COX-1 metabolites.

1.4.5 Other factors regulating energy supply

Adenosine, a product of neuronal metabolism which is produced when ATP is broken down during neuronal activation, has also been shown to be vasodilatory in both the cerebral cortex and the cerebellum, and is thought to be involved in the coupling of CBF to neuronal activity (Dirnagl et al., 1994; Akgoren et al., 1997). ATP itself acts as an extracellular messenger to propagate astrocytic calcium waves in response to stimulation (Guthrie et al., 1999) and is also itself a potent vasomodulator as I will demonstrate in Chapter 3.

The inhibitory neurotransmitter, GABA, has also been implicated in neurovascular signalling in the hippocampus (Fergus and Lee, 1997a). GABA released from hippocampal interneurons causes $GABA_B$ receptor-mediated elevations of $[Ca^{2+}]_i$ in astrocytes (Kang et al., 1998), in a mechanism analogous to that proposed for glutamate (Zonta et al., 2003), and dilates arterioles (Fergus and Lee, 1997a).

Following on from the work in brain slices by Zonta et al. (2003) and Mulligan and MacVicar (2004), Takano et al. (2006) suggested that the products of metabolism of COX-1 play a key role in astrocyte-mediated vasodilation in response to increased neural activity in

vivo. However, they found no evidence for a role of NO, adenosine/purinergic signalling or P450 metabolites (e.g. EETs). Their results, suggesting that neuronally released glutamate raises astrocytic $[Ca^{2+}]_i$ via an mGluR5 pathway, are in agreement with previous studies (Parri et al., 2001; Zonta et al., 2003). However, this work cannot explain the vasoconstriction seen in response to Ca^{2+}-uncaging in astrocytes (Mulligan and MacVicar, 2004), nor the inhibitory effect on vasodilation of blocking NO synthase seen by Wang et al. (1992) and Iadecola (1992).

Increases in extracellular potassium concentration are also known to cause vasodilation in cerebral arterioles (Kuschinsky and Wahl, 1978), and the high potassium conductance of astrocyte endfeet (Newman, 1986) has led to the hypothesis that astrocytic 'siphoning' of potassium in response to neuronal activity plays a role in local blood flow regulation (Paulson and Newman, 1987). An increase in $[K^+]_o$ following neuronal activity results in K^+ influx into glial cells. This influx locally depolarises glial cells causing a K^+ efflux from other regions of the cell. As the highest density of K^+ channels is at the glial endfeet (Newman, 1986; Brew et al., 1986), most K^+ is "siphoned" onto blood vessels (where the endfeet terminate). Recently, an alternative mechanism by which potassium may mediate a calcium-dependent vasodilatory response was suggested (Filosa et al., 2006). Neuronal activity-evoked increases in astrocytic $[Ca^{2+}]_i$ (via mGluRs, as described above) can activate BK channels in the astrocyte endfoot, releasing K^+ ions. This causes a local elevation in $[K^+]_o$ which activates an outward current through smooth muscle cell K_{ir} channels, hyperpolarising the cell and leading to vasodilation. However, the role of potassium in the local regulation of blood flow remains controversial, since a study by Metea et al. (2007) demonstrated that glial K^+ siphoning does not contribute significantly to neurovascular coupling in the retina.

Local interneurons may also have a role to play in neurovascular coupling. In cortical brain slices, stimulation of interneurons resulted in vasodilation through the release of VIP (vasoactive intestinal polypeptide) and through NOS (Akgoren et al., 1994; Cauli et al., 2004) and caused vasoconstriction through the release of neuropeptide Y (Cauli et al., 2004). In addition to their direct projections to, and vasoactive effects on, cortical microvessels,

subcortical acetylcholine and serotonin pathways target cortical GABA interneurons. The interneurons may act as local relays in regulating CBF (Cauli et al., 2004).

All of the studies discussed above have focussed on CBF regulation at the arteriole level. In Chapter 3, I will show that regulation also occurs at the capillary level.

1.5 The division of brain energy use between neurons and glia

Nearly all cerebral energy consumption is derived from glucose oxidation (Siesjo, 1978). In rodent cortex, when brain activity was altered with differing levels of anaesthesia, it was found that ~80% of glucose oxidation was used for action potential driven processes (Sibson et al., 1998). Under deep anaesthesia (resulting in an isoelectric EEG recording) there was an 84% reduction in glucose oxidation compared to under mild anaesthesia (where EEG activity was similar to that recorded in an awake animal). These results suggest that 16% of glucose oxidation is used for 'housekeeping' tasks (including the resting potential), which is a smaller fraction than previously estimated (Creutzfeldt, 1975; Gjedde, 1993).

1.5.1 The astrocyte-neuron lactate shuttle hypothesis

Astrocyte glutamate transporters have been proposed to coordinate CNS glucose and oxygen usage (Fig. 1.4), linking energy production to synaptic glutamate release (Pellerin and Magistretti, 1994; Magistretti and Pellerin, 1999a; Magistretti and Pellerin, 1999b; Voutsinos-Porche et al., 2003). It has been hypothesized that synaptically released glutamate is taken up by Na^+-dependent transporters into astrocytes and converted to glutamine, thus consuming ATP and stimulating astrocytic glycolysis (essentially all the increase in astrocyte ATP use during neural activity is hypothesized to be used on these processes). Lactate produced in astrocytes from glycolysis is then proposed to be exported to neurons and used to fuel mitochondrial oxidative phosphorylation (neurons are assumed to have little glycolysis; astrocytes are assumed to have little oxidative phosphorylation) (Pellerin and Magistretti, 1994; Magistretti et al., 1999; Magistretti and Pellerin, 1999a; Magistretti and Pellerin,

1999b). This mechanism is referred to as the astrocyte-neuron lactate shuttle (ANLS) (Magistretti et al., 1999).

Poitry-Yamate et al. (1995) were the first to present direct evidence for the transfer of glucose-derived lactate from glia (retinal Muller cells) to neurons (photoreceptors), where it was oxidatively metabolised. It is known that lactate can act as an adequate substrate for neurons (Schurr et al., 1988) and more recently it was suggested that lactate may be the preferred energy substrate for neurons (Poitry-Yamate et al., 1995; Bouzier-Sore et al., 2003; Itoh et al., 2003). Indeed, glutamate was found to inhibit neuronal glucose transport while stimulating it in astrocytes (Porras et al., 2004), and in hippocampal slices lactate produced by glial glycolysis following exposure to glutamate was used as an energy substrate by neurons (Schurr et al., 1999). Neurons express the monocarboxylate transporter MCT2 which transports lactate into the neuron (Pierre et al., 2002) and astrocytes express MCT1 & 4 which release lactate into the extracellular space (Bergersen et al., 2002; Pellerin et al., 2005). Further evidence supporting the idea of a regulated lactate flux between glia and neurons is the differential expression of lactate dehydrogenase (LDH) subunits in human brain (Bittar et al., 1996). LDH-5, which favours the production of lactate and is expressed in glycolytic tissue, is present in astrocytes, while LDH-1, which favours the metabolism of lactate, is expressed in neurons. Interestingly, Kadekaro et al. (1985) have previously shown that during neuronal activation glucose utilisation increases in the neuropil (where neuronal dendrites and astrocytes are located) rather than in the cell body. These observations raised the possibility that astrocytes contribute to glucose uptake and phosphorylation during neuronal activation.

As an update to this hypothesis it was recently proposed that under resting conditions glucose is used as an energy substrate by both neurons and glia, while during neural activity glia become primarily glycolytic and the lactate they release is used by neurons to maintain their oxidative metabolism (for review see Pellerin et al., 2007). Evidence in favour of a compartmentalisation of glycolytic and oxidative components between astrocytes and neurons includes the fact that capillaries (the source of glucose) are largely enveloped by astrocyte endprocesses, glycogen is mainly confined to astrocytes, and astrocytes in culture

metabolise glucose to lactate and release it into the medium (Walz and Mukerji, 1988; McKenna et al., 1993). Additionally, glutamate has been shown to stimulate glycolysis in cultured astrocytes (Pellerin and Magistretti, 1994) and recent evidence (discussed below) suggests that there is both spatial and temporal segregation of glycolytic and oxidative components (Kasischke et al., 2004). However, the only in vivo studies supporting this idea are those of Sibson et al. (1998) and Shen et al. (1999).

In agreement with the ANLS hypothesis, Sibson et al. (1998) used ^{13}C NMR spectroscopy to show a 1:1 stoichiometry between the rates of oxidative glucose metabolism and of glutamatergic neuronal activity. Over a range of anaesthetic concentrations, rodent cortical glucose consumption was approximately equal to the rate of glutamine formation from glutamate taken up by astrocytes. However, neither the site of glucose uptake nor the mode of glial glucose metabolism (pure glycolysis to lactate, or glycolysis followed by oxidative phosphorylation in astrocytes) were determined in this study (Chih et al., 2001). In agreement with Sibson's finding, Shen et al. (1999) found that the rate of glutamate/glutamine cycling in the human brain is equal to approximately 80% of the rate of glucose oxidation.

1.5.2 Criticisms of the ANLS hypothesis

Kasischke et al. (2004) present direct evidence, for the first time, that during neural activity the activation of mitochondrial oxidative metabolism and cytoplasmic glycolysis are segregated both spatially and temporally. However, the sequence of the observed metabolic events disagrees with the ANLS hypothesis. By combining NADH imaging and confocal microscopy, Kasischke et al. (2004) showed that there is an early activation of neuronal oxidative metabolism (detected by a fall of NAD(P)H concentration) followed by a later activation of astrocytic glycolysis (detected as an overshooting rise of NAD(P)H concentration) in response to neuronal stimulation. This temporal sequence of events had also been suggested by an earlier study (Hu and Wilson, 1997), where a biphasic change in

extracellular lactate was observed. In contrast the ANLS theory would predict early astrocyte glycolysis followed by later neuronal oxidative phosphorylation (Fig. 1.4).

However, the work by Kasischke et al. (2004) was contradicted by Brennan et al. (2006), who found that the late overshooting rise of the NAD(P)H response to electrical stimulation in hippocampal slices (attributed to astrocyte glycolysis by Kasischke et al. (2004)) was unaffected by inhibition of glycolysis (in the presence of pyruvate as an alternative substrate for oxidative phosphorylation), suggesting that mitochondrial metabolism, rather than astrocytic glycolysis, is responsible for this signal. Furthermore, Galeffi et al. (2007) have proposed that neuronal lactate uptake via monocarboxylate transporters contributes significantly to the generation of the late overshooting rise of the NAD(P)H response to neuronal stimulation in hippocampal slices.

The ANLS hypothesis has also been disputed on other grounds (Chih et al., 2001; Dienel and Hertz, 2001; Gjedde and Marrett, 2001; Marcaggi and Attwell, 2004). First, neurons as well as astrocytes consume glucose. Neurons express glucose transporters (Nagamatsu et al., 1992; Maher et al., 1994) and in fact, neuronal GLUT-3 transports glucose 7-fold faster than the glial GLUT-1 (Maher et al., 1996). Second, although Pellerin and Magistretti (1994) and Sokoloff et al. (1996) observed glutamate-induced glial glycolysis in cultured astrocytes, in other studies (Swanson, 1992; McKenna et al., 1996; Hertz et al., 1998; Peng et al., 2001) glial glutamate uptake was accompanied by little or no lactate production. It is possible that the differing results obtained may be due to differences in the oxidative metabolic capacity in the culture preparations. Pellerin and Magistretti (1994) and Sokoloff et al. (1996) used unphysiologically high glucose concentration (25 mM) which may have influenced their results (Hertz et al., 1998). In addition, glutamate has been shown to decrease the glucose utilisation in astrocytes, possibly because glutamate's carbon can act as an energy substrate, after oxidative deamination of glutamate to α-ketoglutarate, in cultured astrocytes (Yu et al., 1982; Swanson et al., 1990; Sonnewald et al., 1996; Peng et al., 2001) and isolated Muller cells (Poitry et al., 2000). Third, there is also evidence that oxidative metabolism of lactate can occur in glia as well as neurons (Tildon et al., 1993). Lactate

strongly inhibited glycolysis in cultured neurons and astrocytes (Tabernero et al., 1996) which could explain the observation that lactate is the preferred energy substrate for neurons (Bouzier-Sore et al., 2003). Finally, the ANLS hypothesis predicts a lag between the increase in neural activity and the increase in extracellular lactate concentration. As the increase in energy needed during activation is mainly neuronal, it would be quicker to supply the extra energy required if glycolysis and oxidative phosphorylation occurred in the same cell, i.e in the neurons (Chih et al., 2001).

Recently, Cerdan et al. (2006) proposed an alternative to the ANLS hypothesis, involving a reversible exchange of lactate and pyruvate between neurons and astrocytes rather than a unidirectional transfer of lactate molecules. In agreement with this theory, monocarboxylate transporters (MCT1 and MCT2) and lactate dehydrogenase isozymes (LDH1 and LDH5) are known to be reversible (Halestrap and Price, 1999; Halestrap and Meredith, 2004; Hertz and Dienel, 2005). Oxidative metabolism in neurons and astrocytes can switch between using glucose or lactate as substrate, depending on their relative availability in extracellular fluid (Garcia-Espinosa et al., 2004). This switch is made possible by the fact that pyruvate is split into two kinetically different intracellular pools. The relative extracellular concentrations of lactate, pyruvate and glucose determine, by operation of a 'redox switch', the final oxidation of the two pools (Cruz et al., 2001). This hypothesis predicts that, following synaptic glutamate release, both glial glycolysis and the glial TCA cycle are activated. The energy demands may exceed the capacity of the TCA cycle, resulting in a net production of lactate and pyruvate which are then released into the extracellular medium and taken up by neurons. In the neuronal cytosol, lactate is converted to pyruvate by LDH5, which is in competition with glycolysis for cytosolic NAD^+. As the cytosolic NAD^+/NADH ratio falls, glycolysis may be reduced or stopped completely (Cerdan et al., 2006).

If the ANLS hypothesis is true, one would expect that if neuronal stimulation occurred in the presence of glutamate uptake block there would be no increase in astrocytic Na^+/K^+ ATPase activity or conversion of glutamate to glutamine (Fig. 1.4), and consequently

no increase in astrocytic glycolysis. Glutamate uptake block would thus result in an inhibition of lactate release by astrocytes. As increased lactate would no longer be available to the neurons, there should be a block of the increase in level of neuronal oxidative metabolism induced by neural activity. This prediction will be tested in Chapter 5.

1.6 The higher level distribution of brain energy use

Spontaneous ongoing electrical activity in the brain is visible in EEG (electroencephalogram) recordings and local field potentials (LFPs). It has been suggested that incoming sensory information produces only small changes to the ongoing activity in cortical neurons (Arieli et al., 1996; Kenet et al., 2003; Fiser et al., 2004), implying that sensory input may alter cortical energy use only slightly. An interesting question, then, is how does energy use change during transient changes in activity, i.e during the neuronal 'activations' seen in fMRI associated with cognitive tasks (Raichle and Gusnard, 2002)?

Although the blood flow increase associated with increased neuronal energy use is the basis of functional imaging techniques such as positron emission tomography (PET) and BOLD fMRI (Attwell and Iadecola, 2002; Shulman et al., 2004; Logothetis and Wandell, 2004; Raichle and Mintun, 2006 and see section 1.7, below), blood flow measurements cannot be used to calculate the energy usage supporting a cognitive task, because the blood flow increase is generated by a variety of neurotransmitter-mediated mechanisms (see section 1.4 above), rather than being driven directly by energy use (Attwell and Iadecola, 2002). The relative size of the changes in neural firing rate and energy use devoted to unconscious processing of incoming information, and representing conscious percepts, is unknown. Because of the importance of conscious perception for determining behaviour, one might expect that the perception of a stimulus attribute would be associated with a set of neurons increasing their firing and energy use robustly, however this has not been thoroughly investigated. In Chapter 6 I will present an analysis of this.

1.7 Relevance to functional brain imaging

Energy resources must be allocated flexibly among brain regions according to neuronal demand. Blood flow is increased to areas where neurons are more active (Roy and Sherrington, 1890). This blood flow increase is exploited by functional imaging techniques which detect the mismatch between energy use and supply in small brain areas. A local increase in signal (which is produced by blood flow increasing more than oxygen consumption in that area) is assumed to reflect an increase in neural activity.

Using appropriate tracer molecules, positron emission tomography (PET) can be used to measure glucose metabolism, blood volume, blood flow and cerebral oxygen utilisation (Raichle, Mintun, and Herscovitch, 1985). A radioactive tracer isotope incorporated into a metabolically active molecule is injected into, or breathed in by, the subject of the PET scan. The labelled molecule accumulates in the tissue of interest and the radioactive isotope decays by emitting a positron. The positron travels a short distance before encountering an electron, creating a pair of photons as the positron and electron annhiliate each other. The photons move in opposite directions and are detected by a coincidence detector. PET-based neuroimaging is based on the assumption that areas of high radioactivity are associated with brain activity (due to the higher metabolism of these areas).

An alternative technique commonly used for both anatomical and functional brain imaging is magnetic resonance imaging (MRI) of protons. When an object is exposed to a magnetic field all the protons within the object align themselves with (parallel to) or against (antiparallel to) the direction of the imposed magnetic field, B_0 (Fig. 1.5a-c). Protons aligned parallel to B_0 have a lower energy than those aligned antiparallel and at any given time there is a tendency for a greater number of protons to be aligned parallel to the field. However, the magnetic dipole moments of the nuclei are not perfectly aligned with the field, but precess around its direction. Pulses of electromagnetic energy (radiofrequency (RF) pulses, B_1) which are perpendicular to the main field, are then applied to 'flip' the protons out of alignment with B_0 (Fig. 1.5d). The net magnetization is now aligned more perpendicular to B_0 and continues

to precess around the direction of B_0 (Fig. 1.5d,e). The small, oscillating, magnetic field induces a current in the receiver coil and hence produces the MRI signal. When B_1 is no longer applied two relaxation processes occur, which result in loss of signal:

(i) Longitudinal relaxation (described by the time constant T1): the protons relax back to their original orientation aligned with B_0 as energy is dispersed from the protons to neighbouring nuclei, (Fig. 1.5f,g).

(ii) Transverse relaxation (also known as 'spin-spin relaxation', described by time constant T2): the protons go out of phase with neighbouring protons due to tiny differences in the local magnetic field, caused by other magnetic nuclei and atoms moving nearby. T2 characterises the temporal decay of the signal (Fig. 1.5h).

BOLD contrast depends on the ratio of oxy/deoxyhaemoglobin in the blood. The iron in deoxyhaemoglobin is paramagnetic and so creates local inhomogeneities in the magnetic field which result in the precessing nuclei no longer moving in phase. During an increase in neuronal activity, the oxygen use increases. This is followed within a few seconds by a larger fractional increase in blood flow and blood volume, resulting in a net decrease in the concentration of deoxyhaemoglobin (Fox and Raichle, 1986; Malonek et al., 1997). It is this decrease in deoxyhaemoglobin which is detected as a BOLD signal. When deoxyhaemoglobin levels decrease there are fewer magnetic field inhomogeneities and so transverse relaxation occurs slower and the BOLD signal increases (Ogawa et al., 1990a; Ogawa et al., 1990b).

Several aspects of the work in my thesis are relevant to understanding functional imaging signals such as BOLD fMRI and PET. First, knowing exactly where energy is used in the brain at the cellular and subcellular level is an essential basis for understanding why the CBF is increased to certain brain areas. This cellular and subcellular distribution of energy use is addressed in Chapter 4. Second, understanding the increase in blood flow which occurs following an increase in neural activity is necessary to explain where positive BOLD signals will be produced. How the blood flow is increased is addressed in Chapter 3. Third, understanding the fraction of neural activity and energy use associated with conscious

perception gives valuable insight into the results of certain BOLD fMRI experiments, and is addressed in Chapter 6.

Rather than being energy driven, blood flow regulation is transmitter (and possibly K^+ (Filosa et al., 2006)) driven (Attwell and Iadecola, 2002; for review see Drake and Iadecola, 2007), as discussed in section 1.4 above. Although functional imaging signals have generally been assumed to reflect the energy use on principal neuron firing, Logothetis et al. (2001) showed that there is a slightly better correlation of the BOLD signal with local field potentials reflecting synaptic activity, rather than with multi-unit action potential activity. This suggests that BOLD fMRI data reflect more the input and processing within a brain area rather than spiking output. This is in agreement with earlier work by Mathiesen et al. (1998) who showed that an increase in Purkinje cell spike rate is not required for regional cerebral blood flow (CBF) to increase. These results suggest that an increase in CBF does not necessarily indicate increased firing in the principal neurons of a cortical area (although, in general, more input to an area tends to generate more firing). In addition, a recent study by Viswanathan and Freeman (2007) found that, at some sites in the visual cortex, stimulus-induced changes in tissue oxygen concentration occurred even in the absence of a neuronal spiking response. Sites showing this behaviour also had strong synaptic field potential responses. Together, these findings suggest that changes in tissue oxygen concentration (and by extension, the fMRI BOLD signals) are more closely coupled to synaptic, rather than to spiking, activity.

Functional imaging experiments often subtract brain "activation" images for two situations designed to differ only in the perception of some stimulus attribute. As the BOLD signal is thought to change only where there is a change in neural activity (causing a local change in blood flow), performing such a subtraction highlights the brain region responsible for the perception. However, the following possibilities could lead to misinterpretation of BOLD data. It is possible in some brain areas for CBF to increase (as a result of glutamate release, see above) without a change in metabolism (Reis and Golanov, 1997), so a change in the BOLD signal may occur with no accompanying change in energy use. Additionally, a

change in spiking output may occur without a change in the signalling processes which control blood flow, and in this case it is possible that no BOLD signal would be generated (Attwell and Iadecola, 2002). In order to fully understand the data produced in functional imaging experiments, it is necessary to understand how CBF increases relate to information processing.

Neuronal spiking is associated with a rapid decrease in local oxygen concentration. However, whereas oxygen consumption by active neurons is localized to the active area, the blood flow increase to provide extra oxygen appears to occur over a larger area (Malonek and Grinvald, 1996). Thus it should be possible to use high resolution fMRI, based on the initial dip seen in the oxygen concentration, to localize neural activity at a columnar level with better spatial resolution than is provided by conventional fMRI which detects a decrease in deoxygenated haemoglobin concentration (Thompson et al., 2003). The Attwell and Laughlin (2001) model would suggest that if blood flow changes are correlated with energy usage, then fMRI signals are likely to reflect mainly energy consumption associated with excitatory postsynaptic currents and action potential propagation. An interesting question is the relative contributions of excitatory and inhibitory synapses. Traditionally, inhibitory processes were thought to require either very little, or no, energy (Waldvogel et al., 2000). However, Patel et al. (2005) have shown that energy consumption increases with activity in both excitatory and inhibitory cells, and suggested that GABAergic neurons contribute 13-15% of the total oxidative metabolism of neurons and glia.

Attwell and Laughlin (2001) predicted that in primates the dominant energy consumption is by postsynaptic responses, so if the BOLD signal did reflect energy consumption in humans it would be dominated by postsynaptic currents. In fact, although BOLD signals are coupled to postsynaptic events, it is via the action of neurotransmitters rather than through energy use (see section 1.4 above).

1.8 What is not known about brain energy use?

Although a strong coupling between neuronal activity and energy metabolism was first suggested over 100 years ago (Roy and Sherrington, 1890), there are still many questions which remain to be answered concerning brain energy supply and use.

In terms of energy supply, it is assumed that blood flow regulation occurs at the arteriole level, but how do signals pass from active neurons to the relatively distant pre-capillary arterioles? Capillaries are closer than arterioles to the active neurons for example in the lacunosum moleculare, in hippocampal slices, the mean distance to the nearest arteriole was 70 μm but only 8 μm to the nearest capillary (Lovick et al., 1999). Malonek et al. (1997) have suggested that regulation at the capillary level is essential in order to explain the spatial resolution they achieved using optical imaging techniques. However it is not known if CBF regulation occurs at the capillary level. This will be addressed in Chapter 3.

In terms of energy use, it is not known how energy is allotted between cells and subcellular mechanisms to carry out a computational task nor how it is allotted to unconscious versus conscious information processing. I will investigate these issues in Chapters 4 and 6, respectively. Additionally, there is growing evidence for a split in energy production mode between neurons and glia, with the astrocyte neuron lactate shuttle hypothesis proposing glutamate uptake as the message which triggers an increase in substrate provision to feed neuronal metabolic need (Pellerin and Magistretti, 1994). Despite growing support for this hypothesis, it remains controversial. I will present experiments which test the ANLS hypothesis in Chapter 5.

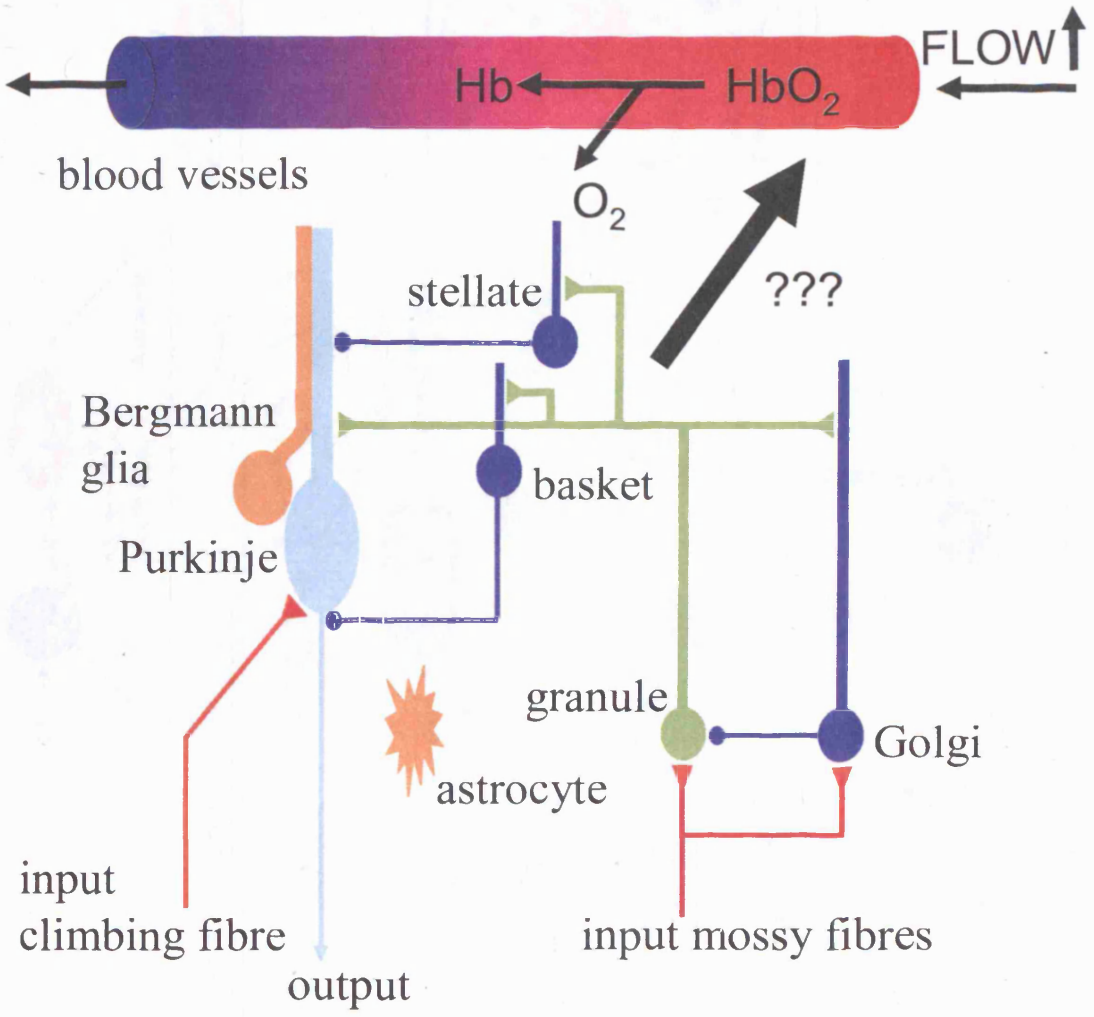

Figure 1.1 Blood flow increases to areas where neurons are active. When a neuron in a brain region (e.g. the cerebellum) is active, a signal passes to the vasculature to increase the blood flow and so increase the supply of oxygen and glucose. The nature of this signal has been debated since Roy and Sherrington first proposed the idea of a coupling between cerebral energy consumption and neuronal activity in 1890.

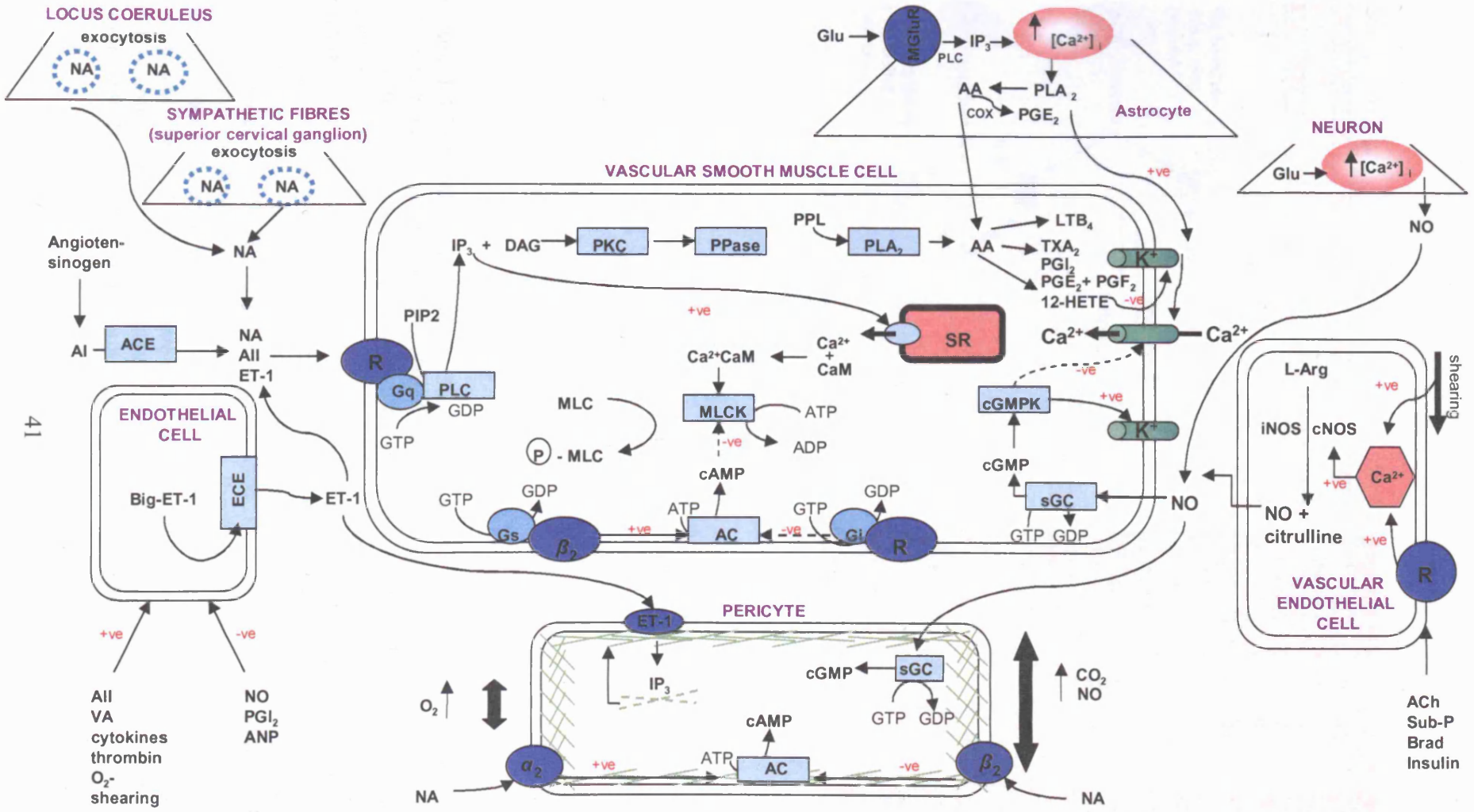

Figure 1.2 Signalling pathways underlying vasodilation and vasoconstriction.

Figure 1.3 Controlling blood flow in the brain. During neuronal activity, glutamate is released which acts on neuronal NMDA receptors, raising the intracellular calcium. This, in turn, activates nitric oxide synthase (NOS) and it is this glutamate-evoked release of NO which causes vasodilation. Glutamate can also act via glial metabotropic glutamate receptors (mGluRs), raising the intracellular calcium in glial cells and generating arachidonic acid (AA) via phospholipase A_2 (PLA_2). This can be processed locally to produce cycloxygenase generated derivatives, such as prostaglandin E_2 (PGE_2). These are released from astrocyte endfeet, causing vasodilation. Alternatively, AA can diffuse to the smooth muscle layer surrounding the arterioles, producing 20-HETE via the CYP4A enzyme. 20-HETE evokes arteriole constriction. Astrocyte calcium levels can also be raised by noradrenaline – released from neurons that control the circulation – which works through α_1 receptors to evoke vasoconstriction (bottom left). Figure from Peppiatt and Attwell (2004).

Figure 1.4 Regulating neuronal energy supply. Synaptically released glutamate (bottom right) is taken up by Na^+-dependent transporters into astrocytes (bottom left) and converted to glutamine, thus consuming ATP and stimulating astrocytic glycolysis. Lactate produced by this glycolysis is proposed to be exported to neurons and used to fuel mitochondrial oxidative phosphorylation. Diagram adapted from Pellerin and Magistretti (1994).

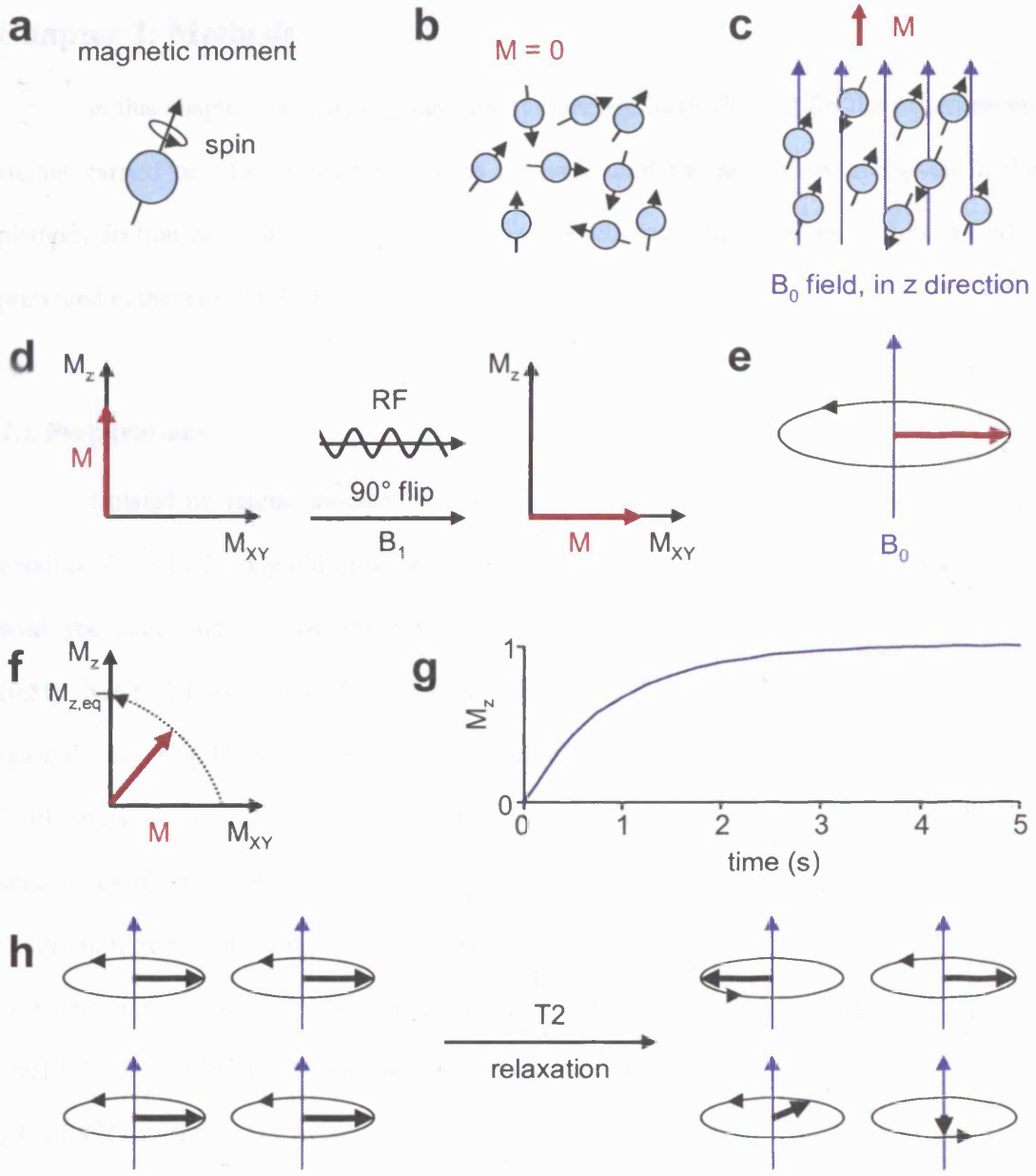

Figure 1.5 Basics of MRI. **a:** Each proton (mainly present in water) has a "spin" or magnetic moment. **b:** In the absence of an externally applied magnetic field, the spins of the protons are randomly oriented. **c:** In the presence of a magnetic field, B_0, protons are aligned roughly parallel or antiparallel to B_0, producing a net magnetization, M. Each nucleus precesses around the direction of B_0. **d:** Following a radiofrequency pulse at 90° to B_0, the spins are flipped out of alignment with B_0. **e:** M continues to precess around the direction of B_0, producing the MR signal, and initially all spins precess in phase with each other. **f**: Gradually the spins re-align with B_0 – this is called longitudinal relaxation and occurs with a time constant called T1. **g:** Recovery of magnetization over time following an RF pulse, grey matter, T1 = 920ms. **h:** In addition the phase alignment of the precessing displaced nuclei is lost. This transverse relaxation is produced by local inhomogeneities in magnetic field produced, e.g., by paramagnetic deoxyhaemoglobin molecules, and occurs with a time constant called T2.

Chapter 2: Methods

In this chapter I will mainly describe the general methods used for the experimental studies carried out. Details of the specific methods used for each study are given in the methods section of each Results chapter. The methods used for theoretical work are also presented in the relevant Results chapter.

2.1 Preparations

Isolated rat retinae mounted vitreal side up, or 200 μm slices of cerebellum, were obtained from 14-21 day old Sprague-Dawley rats or 17-21 day old GLAST knockout and wild-type mice, and (in most experiments) superfused with solution at 33-35°C containing (mM): NaCl 124, $NaHCO_3$ 26, NaH_2PO_4 1, KCl 2.5, $CaCl_2$ 1.8, $MgCl_2$ 2, D-glucose 10 (gassed with 95% O_2/5% CO_2), pH 7.4 (bicarbonate Ringer's). Kynurenic acid (1 mM, to block glutamate receptors, to reduce potential excitotoxic damage) was included in the solution used for dissection and incubation before tissue use (referred to below as slicing solution). In some experiments, brain slices from GLAST mice were superfused with solution at room temperature (~25 °C) containing (mM): NaCl 140, KCl 2.5, $MgCl_2$ 1, $CaCl_2$ 2, NaH_2PO_4 1, HEPES 10, D-glucose 10 (gassed with air prior to the experiment), pH 7.4 (HEPES Ringer's).

2.1.1 Cerebellar slice protocol

All animals were killed humanely by cervical dislocation in accordance with the Animals (Scientific Procedures) Act (1986). Animals were decapitated, following cervical dislocation, and the head was immersed in ice-cold oxygenated slicing solution (described above). The scalp was removed and the skull opened by cutting between the eyes and around the side of the head. The scalp was lifted back with forceps and the brain removed and placed in ice-cold oxygenated slicing solution. The cerebellum was separated from the rest of the brain and the cerebellar hemispheres removed. The cerebellar vermis was mounted on the

stage of a vibrating tissue slicer (Campden Instruments or Leica) using superglue and stabilised using an agar block glued to the stage. The cerebellum was covered by ice-cold, oxygenated slicing solution throughout the slicing procedure. 200 μm thick sagittal or transverse slices of cerebellar vermis were obtained and stored in oxygenated slicing solution at room temperature until used. All slices were allowed to recover from slicing for at least one hour prior to use.

2.1.2 Flat mount retina preparation

Animals were decapitated following cervical dislocation as described above. A cut was made down the centre of the scalp and the eyeballs were removed and placed in oxygenated slicing solution. Excess tissue and muscle was removed from the eyeballs before cutting around the iris. The lens and vitreous were removed and the retina (in the eyecup) was covered with oxygenated slicing solution. The eyecup was carefully removed with forceps and the retina stored in oxygenated slicing solution at room temperature until used. One retina was used immediately after the dissection was completed. The retina was placed on the perfusion bath and gently straightened out with a paintbrush. The flat retina was then held in place by a harp, as described below.

2.2 Solutions

Neurotransmitters and other drugs were added to the superfusion solution. Solutions were made up either from stock solutions or from powder. Stock solutions were made in distilled water and diluted to the final concentration in bicarbonate Ringer's or HEPES Ringer's solution as specified in the Results chapters to follow. To prevent oxidation when using noradrenaline, 100 μM ascorbic acid was added to the solution. Solutions were applied at a perfusion rate of ~2.2 ml/min to the preparation in the bath. In the case of GABAzine and TPMPA, solution was puffed locally onto the retina from a pipette. Ischaemia was simulated by replacing 10 mM glucose with 7 mM sucrose, bubbling with 95% N_2/5% CO_2

and, to get a reproducible fast onset to the ischemic response, adding 2 mM sodium iodoacetate and 25 μM antimycin to block glycolysis and oxidative phosphorylation (Reiner et al., 1990; Allen et al., 2005).

2.3 Mechanical and optical set-up

Experiments were carried out using an Olympus BX51 WI upright microscope, with a moving stage. Tissue was held in place in the perfusion bath by a harp, which consists of a platinum frame strung with nylon threads, and perfused with external solution in the perfusion bath, via a peristaltic pump (flow rate ~ 2.2 ml/min). Tissue was viewed using either a 40x or 60x water immersion objective with differential interference contrast (DIC) optics.

2.4 Imaging of capillaries

Capillaries, lacking the continuous smooth muscle seen around arterioles (see Fig. 3.1 in Chapter 3) and <11 μm diameter, were imaged with a cooled Hamamatsu C4880-80 CCD camera every 2-10 sec. Images were recorded with Kinetic software and capillary diameter was measured off-line manually. Vessels were selected if both walls were visible and in focus. Data were discarded if preparation movement led to the vessel no longer being in focus. Pericytes were identified by their position on the outer walls of capillaries and characteristic 'bump on a log' shape (Sakagami et al., 1999; Wu et al., 2003), as shown in Chapter 3.

2.5 Ca^{2+} imaging

For imaging of Ca^{2+} waves in the layer of retinal glia underlying the ganglion cell axons on the vitreal surface of the retina, retinae were incubated with Fluo-4-AM (10 μM, with 1 μl/ml Cremaphore to solubilize the dye) for 70 minutes at room temperature, before exciting fluorescence at 475 nm and monitoring emitted light at 535 nm. Surface glia were

stimulated electrically. The propagation velocity of the Ca^{2+} wave was calculated by measuring the time to half maximum of the fluorescence at three points located at different distances from the stimulating electrode.

2.6 Labelling with NG2 antibody and isolectin B4

The proteoglycan NG2 is a marker for pericytes (Ozerdem et al., 2001). Isolectin B4 can be used to label blood vessel walls including those of capillaries (Lyer et al., 1976). Blood vessels in 200 μm cerebellar slices were labelled with isolectin B4 conjugated to Alexa 488 (Invitrogen) or FITC (Sigma), by incubation with 50 μg/ml of the lectin for 45 minutes at room temperature. Slices were washed in bicarbonate solution for 30 minutes and then fixed in 4% paraformaldehyde (PFA) in phosphate buffered solution (PBS) for 40 minutes at room temperature. For NG2 labelling, slices were washed in PBS and blocked with 10% goat serum / 0.05% Triton (in PBS with NaN_3) for 4 hours before being incubated with 1 mg/ml antibody to NG2 (rabbit, Chemicon) at a concentration of 1:200 (diluted in PBS with NaN_3 and 1% goat serum) for 16 hours at room temperature. Slices were then incubated with an Alexa 555 conjugated goat anti-rabbit secondary antibody (Molecular Probes) at a concentration of 1:200 for 4 hours at room temperature. Slices were mounted on a slide (BDH) with Citifluor (glycerol/PBS, Citifluor) and imaged using a Zeiss Pascal confocal microscope. Fluorescence of the isolectin B4 labelled blood vessels in cerebellar slices was excited at 488 nm and emission was collected at 535 nm. Fluorescence of the Alexa 555 labelled pericytes was excited at 553 nm and emission was collected at 569 nm.

2.7 Confocal imaging

Fixed slices were imaged in a Zeiss Pascal confocal laser scanning upright microscope. Images were obtained using a 10x or 20x DIC objective. High resolution images were acquired with a 63x oil DIC objective. Imaging with multiple wavelengths was performed as sequential scans at each wavelength. The argon laser 488 nm line was used to

excite FITC and Alexa 488 fluorophores and the HeNe laser 543 nm line was used for the Alexa 555 fluorophore.

2.8 Analysis of blood vessel density

Confocal stack images, 119 ± 4 μm deep, were taken of the molecular and granular layers, with image planes separated by 5.5-6.67 μm (at 10x magnification) and by 2.76-3.03 μm (at 20x magnification).

Isolectin-B4 labels the endothelial cells on the outside surface of the blood vessel, and so delineates the blood vessel surface area available for O_2 and glucose exchange, which we assume is a measure of the potential O_2 and glucose supply to the tissue. To obtain an approximate quantification of the relative blood vessel surface area in the molecular and granular layers, we therefore summed all the pixels containing isolectin-B4 labelling in each layer. To do this, a minimum threshold was applied to each image. The threshold was chosen by eye in order to minimise background fluorescence while maintaining the maximum number of vessels visible. The image was then binarised, ensuring that each fluorescent pixel only contributed a value of one to the total pixel count. Blood vessel surface area was summed over 12-53 image planes for one cerebellar lobe, and data were then averaged over 26 different lobes. The diameter of the capillaries thus measured was in the range 5-9.4 μm. Microglia are also labelled by isolectin-B4 but contributed less than 2% of the fluorescent signal observed, and so were ignored. Images were analysed using MetaMorph software (Molecular Devices, Downingtown, PA).

2.9 Patch-clamping and stimulation

Pericytes were whole-cell clamped with ~8 MΩ electrodes containing Alexa 488 (1 mg/ml), to reveal the cell morphology, and (mM): K-gluconate 130, NaCl 10, $MgCl_2$ 1, $CaCl_2$ 0.1, HEPES 10, K_2EGTA 1.1, Na_2ATP 1, pH adjusted to 7.0 with KOH. Patch-clamping was carried out after pre-treating the retina with collagenase (1 mg/ml for 30 minutes at 37°C) to

remove connective tissue. Similar electrodes filled with extracellular solution were used to stimulate pericytes and surface glia, by pressing the electrode tip against the cell and applying voltage pulses (40-90 V, 0.02-0.2 ms, 9 Hz; 3 pulses were sufficient to evoke constriction). Similarly, neurons in the inner retina were stimulated by placing the electrode tip 22 μm below the retinal surface (calculated from the angle of the electrode to the horizontal and the distance inserted) and applying voltage pulses (60-90 V, 0.02-0.06 ms, 9 or 20 Hz for 20-30 sec). Electrodes were held in a pipette holder, attached to and moved by an electric micro-manipulator (SMI, Luigs and Neumann).

2.10 Cerebellar energy use calculations

The calculation of cerebellar energy use followed the approach of Attwell and Laughlin (2001), and was based on the measured electrical properties of all the cell types in the cerebellar cortex. Full details of the calculations will be presented in Chapter 4.

2.11 O_2 electrode measurements

A Clark-type oxygen electrode with tip diameter 5 - 10 μm (Unisense) was used to measure the O_2 consumption of 200 μm cerebellar slices from 18 - 21 day old rats and 17 – 21 day old GLAST knockout mice. The tip of the electrode was placed approximately 50 μm deep in the slice within the molecular layer. The stimulating electrode (described in section 2.9, but with a resistance of ~2 - 3 MΩ) was placed approximately 100 μm along the parallel fibre from the O_2 electrode. A 10 second 20 Hz train of pulses (75 - 100 V, 0.06 – 0.3 ms) was used to stimulate the parallel fibres. The O_2 electrode was connected to a picoammeter and its output was acquired digitally using Axoscope (Axon Instruments) and analysed offline using Clampfit 9 (Axon Instruments). Solutions were bath perfused onto the slice and the changes in oxygen level occurring in response to stimulation were measured. Oxygen electrodes were calibrated daily by obtaining 21% and 0% O_2 readings in solution bubbled with air and 100% N_2, respectively, at room temperature.

2.12 Statistics

Data are presented as mean ± s.e.m. P values are from 2 tailed Student's t-tests or chi-squared tests, as appropriate.

2.13 Chemicals

Table 2.1 Source and concentration of compounds used

Chemical	Final concentration used	Supplier
Antimycin-A	25 μM	Sigma
ATP	0.5 – 1 mM	Sigma
Cadmium	250 μM	Sigma
DHK	200 μM	Sigma / Ascent Scientific
GABAzine (SR95531)	100 μM	Sigma
Glutamate	100 – 500 μM	Tocris / Fluka
Iodoacetic acid	2 mM	Sigma
Muscimol	20 μM	Ascent Scientific
Noradrenaline	0.3 – 10 μM	Sigma
NBQX	25 μM	Tocris
PPADS	100 μM	Sigma
Suramin	100 μM	Sigma
TBOA	200 μM	Tocris
TPMPA	100 μM	Tocris
TTX	1 μM	Tocris
UTP	50 – 100 μM	Sigma

Chapter 3: Bidirectional control of CNS capillary diameter by pericytes

3.1 Introduction

Within the brain it is essential to match the supply of glucose and oxygen to the metabolic demands of neurons. An increase in neural activity leads to a rise in glucose and oxygen use and, in order to supply these substrates, local blood flow in the CNS increases, which is the basis of BOLD fMRI and PET functional imaging techniques (Roy and Sherrington, 1890; Ogawa et al., 1990a; Raichle, 1998; Attwell and Iadecola, 2002). Changes in blood flow are generated by alterations in the diameter of local blood vessels (see Chapter 1).

Recent work has suggested that glutamate release by active neurons, rather than energy use, increases blood flow, since glutamate receptor blockers prevent the blood flow increase (Iadecola et al., 1996; Mathiesen et al., 1998; Zonta et al., 2003; Mulligan and MacVicar, 2004; Takano et al., 2006). As described in Chapter 1, section 1.4.4, two mechanisms have been proposed to explain how glutamate regulates blood flow. The first involves a neuronal-NO-cGMP pathway resulting in vasodilation (Faraci and Breese, 1993; Fergus and Lee, 1997b). Second, in addition to glutamate and NO released from neurons, Zonta et al. (2003) suggested that glutamate can act on mGluRs to increase $[Ca^{2+}]_i$ in astrocytes, which then release cyclooxygenase products of arachidonic acid from their endfeet to relax smooth muscle, and this has also been demonstrated in vivo (Takano et al., 2006).

Blood flow is normally assumed to be regulated locally by the smooth muscle surrounding pre-capillary arterioles, while more global control is achieved by smooth muscle around larger vessels near the surface of the brain and around arterioles deeper within the brain (see Chapter 1, section 1.4).

The morphology and constriction characteristics of arterioles are shown in Fig. 3.1. Arterioles in the cerebellum (Fig. 3.1a) and retina (Fig. 3.1b) are covered by a continuous

layer of smooth muscle formed of annuli around the vessel. The constriction generated by this layer of smooth muscle when noradrenaline is applied is spatially uniform, as shown in Fig. 3.1c,d.

By contrast, capillaries adjacent to active neurons lack a continuous layer of smooth muscle and so might not be expected to constrict (Fig. 3.2). However, pericytes, which are also contractile cells, are located along the capillary wall. Pericytes contain muscle and non-muscle actin, and non-muscle myosin (Herman and D'Amore, 1985; Bandopadhyay et al., 2001). Interestingly, most (65%) of the noradrenergic innervation of the CNS vasculature is of capillaries rather than arterioles (Cohen et al., 1997), and in both muscle and brain a vasodilatory signal propagates from blood vessels near metabolically active cells back to larger arterioles (Berg et al., 1997; Iadecola et al., 1997), suggesting that blood flow control may be initiated at the capillary level. Pericytes are potential initiators of such signalling. Neurotransmitters make pericytes contract in culture (Rucker et al., 2000), and angiotensin, ATP and ACh raise $[Ca^{2+}]_i$ and constrict pericytes on microvessels isolated from the retina (Wu et al., 2003; Kawamura et al., 2003; Kawamura et al., 2004). Since neocortical pericytes *in situ* show neuronally-evoked $[Ca^{2+}]_i$ elevations (Hirase et al., 2004a), pericytes might control blood flow downstream of precapillary arterioles (Fig. 3.2a). However, data are lacking to show whether pericytes regulate capillary diameter *in situ*, either in retina or brain, and it is unknown whether signals initiated in capillary pericytes can propagate along vessels towards precapillary arterioles.

The low density of blood vessels within the retina ensures minimal interference with incoming light but requires the ability to efficiently match the local blood supply to local neuronal nutrition needs (Funk, 1997). This makes it an ideal system in which to test blood flow regulation in response to local signals. In addition I studied vessels in cerebellar slices to see whether results obtained in the retina extend also to more central areas. I show below that pericytes can control capillary diameter *in situ* in whole retina and cerebellar slices.

3.2 Methods

3.2.1 Preparations

Experiments were performed on isolated rat retina mounted vitreal side up, or 200 μm sagittal slices of cerebellum, from 14-21 day old rats. Tissue preparation and solutions used are described in Chapter 2, sections 2.1-2.

3.2.2 Imaging

Capillaries, lacking the continuous smooth muscle seen around arterioles (Fig. 3.1 and 3.2) and <11 μm diameter, were imaged with a CCD camera. As will be shown below, capillaries, unlike arterioles (Fig. 3.1), showed pericyte-mediated spatially restricted constrictions in response to transmitter application, and this difference provides one check on the fact that I was imaging capillaries and not arterioles.

3.2.3 Ca^{2+} imaging

Retinae were incubated with Fluo-4-AM in order to image Ca^{2+} waves in the retinal glia. Surface glia were stimulated electrically and the propagation velocity of the Ca^{2+} wave was calculated. See Chapter 2, section 2.5 for further details.

3.2.4 NG2 labelling of pericytes

Pericytes were labelled with NG2 antibody using an Alexa 555 conjugated goat anti-rabbit secondary antibody. Blood vessels were labelled with isolectin B4 conjugated to Alexa 488 or FITC. See Chapter 2, section 2.6 for further details.

3.2.5 Patch-clamping and stimulation

Pericytes were whole-cell clamped with ~8 MΩ electrodes containing Alexa 488 (1 mg/ml), to reveal the cell morphology, as described in Chapter 2, section 2.9. Pericytes were stimulated with electrodes (described in Chapter 2, section 2.9), by pressing the electrode tip

against the cell and applying voltage pulses (40-90 V, 0.02-0.2 ms, 9 Hz; 3 pulses were sufficient to evoke constriction). Similarly, neurons in the inner retina were stimulated by placing the electrode tip 22 μm below the retinal surface and applying voltage pulses (60-90 V, 0.02-0.06 ms, 9 or 20 Hz for 20-30 sec).

3.2.6 Statistics

Data are presented as mean ± s.e.m. P values are from 2 tailed Student's t-tests or chi-squared tests, as appropriate.

3.3 Results

3.3.1 Anatomical features of pericytes conferring potential control of blood flow

To characterise the distribution of pericytes in the retina and cerebellar molecular layer, in collaboration with Claire Peppiatt-Wildman, I used an antibody to the NG2 proteoglycan, which from postnatal day 21 (P21) labels mainly the pericyte somata (Hughes and Chan-Ling, 2004). Two types of pericyte were observed: those with a "bump on a log" morphology on straight parts of a capillary, separated by 34.2 ± 3.6 μm (n = 24) in retina, which might regulate flow through that single capillary and downstream vessels, and pericytes at capillary junctions, which could conceivably switch flow between capillaries (Fig. 3.2a-c). In both retina and cerebellum, pericyte processes radiating from the soma along and around the capillary were labelled (Fig. 3.2d). Using whole-cell clamping to load dye into retinal pericytes revealed processes extending like claws around the capillary (Fig. 3.2e), and ranging up to 11.3 ± 0.7 μm (n = 3) on either side of the soma. These processes form a likely anatomical substrate for generating the capillary constriction described below.

3.3.2 Electrical stimulation constricts retinal pericytes *in situ*

To establish the potential for retinal pericytes to regulate capillary diameter, I stimulated them electrically with a pipette pressed against their soma, with the aim of raising

$[Ca^{2+}]_i$, since in isolated vessels pericyte constriction is associated with a $[Ca^{2+}]_i$ rise (Wu et al., 2003). Stimulation generated a slowly developing but strong constriction of most (90%) of the 30 pericytes studied (Fig. 3.3a-d). The constriction started 3.6 ± 1.6 sec after the start of the stimulation, and reached 50% of its maximum after 12.6 ± 3.6 sec. On stopping stimulation, the constriction decayed to half of its maximum in 60.3 ± 12.4 sec. For 17 pericytes on the straight part of capillaries, the mean vessel constriction was 73 ± 5%, from an initial diameter of 8.6 ± 0.5 μm (Fig. 3.3e). Pericytes at branch points also constricted in response to stimulation by 76 ± 8% (n=11) from an initial diameter of 5.8 ± 0.6 μm. For branch point pericytes constriction was sometimes of just one vessel and sometimes of both vessels at the branch point. Stimulating the capillary wall between pericytes did not elicit a constriction either at that point or at adjacent pericytes (Fig. 3.3e, n=7, significantly different to stimulating pericytes, $p=1.3x10^{-5}$). This shows first, that endothelial cells and astrocyte endfeet do not constrict, and second that the stimulating current does not spread through the extracellular space sufficiently to make nearby pericytes constrict.

The greatest constriction was not always at the centre of the soma of the pericyte, but could be up to 12 μm along the vessel (mean displacement was 1.24 ± 0.83 μm in 14 stimulated pericytes). Thus, for some pericytes, either the force generated by the pericyte contractile proteins is largest in the cells' processes, or the capillary compliance is greater away from the soma.

3.3.3 Electrically-evoked pericyte constriction is Ca^{2+}-dependent

Removing calcium from the extracellular solution evoked a dilation of capillaries near pericytes (by 28% in 4 vessels, p=0.023), that slowly decayed during prolonged absence of Ca^{2+}. By contrast, no dilation was seen at non-pericyte sites (p=0.22, Fig. 3.4a,b). Removing calcium also abolished the stimulation evoked constriction (Fig. 3.4a,c), consistent with the constriction being triggered by a raised $[Ca^{2+}]_i$. It is likely that the stimulation

depolarises the pericyte, activating voltage-gated calcium channels, allowing a calcium influx which results in constriction (Sakagami et al., 1999; Kamouchi et al., 2004).

3.3.4 Pericyte constriction can spread along the retinal capillary wall

When pericytes were stimulated to constrict, sometimes more distant pericytes also constricted at a later time, as though a signal had passed along the capillary wall (Fig. 3.5a and see Movie 1 on the disk inside the rear cover of this thesis). However, at sites on the capillary between the pericytes there was no constriction (Fig. 3.5b), confirming that the endothelial cells of the capillary wall do not exhibit contractile properties. The constriction of distant pericytes cannot be due to extracellular spread of the stimulus because placing the electrode between pericytes did not evoke a constriction (Fig. 3.3e). In 4 capillaries the mean speed of the spread of constriction was 2.0 ± 1.3 μm/sec.

3.3.5 Neurotransmitter-evoked constriction of retinal pericytes

In the brain, elevations of $[Ca^{2+}]_i$ in astrocytes have been proposed to regulate precapillary arteriole diameter (Zonta et al., 2003; Mulligan and MacVicar, 2004; Takano et al., 2006). ATP is known to be released when waves of $[Ca^{2+}]_i$ elevation spread between retinal astrocytes and Muller cells (Newman, 2001). In addition, ATP constricts pericytes on isolated blood vessels, by raising $[Ca^{2+}]_i$ via $P2X_7$ and P2Y receptors (Kawamura et al., 2003). I therefore tested the effect of ATP, and the P2Y receptor agonist UTP, on the diameter of capillaries in the intact retina. Both agents constricted capillaries at locations near pericytes, while leaving non-pericyte regions of the capillary unconstricted (Fig. 3.6a-c and see Movie 2 on the disk inside the rear cover of this thesis). This occurred both in pericytes on the straight part of capillaries and at branch points (for which constriction was sometimes of just one vessel and sometimes of both vessels at the branch point). However constriction was not seen in all pericytes: 50-100 μM UTP constricted vessels at 30% (12 out of 40) of pericytes tested, while 0.5-1 mM ATP constricted vessels at 25% (5 out of 20 pericytes: not

significantly different, p=0.92 by χ^2 test). In the responding vessels, the peak constrictions evoked by 100 μM UTP (56 ± 9%, n=10, from an initial diameter of 7.1 ± 0.9 μm) and 1 mM ATP (35 ± 6%, n=4, from 7.9 ± 2.3 μm) were not significantly different (p=0.19).

The lack of response of some pericytes to neurotransmitter agonists is similar to earlier findings on isolated vessels. For example, on isolated vessels, the $P2X_7$ agonist BzATP evoked a contraction in only 37% of pericytes and capillary constriction was visible in only 1/3 of these cases or 12% of the total (Kawamura et al., 2003), while the muscarinic agonist oxotremorine induced contractions in only 10% of pericytes (Wu et al., 2003).

As shown in Fig. 3.6b, the UTP-evoked constriction was larger initially and then decreased (to 34 ± 3% of the initial constriction). Similarly for 1 mM ATP the sustained constriction was 32 ± 17% of the initial constriction. Glutamate (500 μM) did not affect retinal capillary diameter (39 vessels), and noradrenaline (0.3-10 μM) constricted pericytes on only 3 out of 61 retinal capillaries although it always constricted arterioles.

In contrast to the spatially restricted pericyte-mediated constriction evoked by ATP and UTP in capillaries, retinal arterioles were found to constrict uniformly in response to noradrenaline (Fig. 3.1c,d). The mean constriction evoked by 1μM noradrenaline was 20.5 ± 4.1% (in 8 of 8 vessels) from an initial diameter of 32.1 ± 3.3 μm.

I considered the possibility that ATP release from underlying glia might explain the constriction of pericytes evoked by electrical stimulation in Fig. 3.3, or the propagation of the constriction between pericytes seen in Fig. 3.5. To test this I applied together the P2 receptor blockers suramin (100 μM) and PPADS (100 μM), which greatly reduce the spread of ATP-releasing Ca^{2+} waves through retinal glia (Newman, 2001) and will also reduce the actions of any released ATP on the $P2Y_2$, $P2Y_4$ and $P2X_7$ receptors that raise $[Ca^{2+}]_i$ and trigger pericyte contraction (Kawamura et al., 2003). These blockers affected neither the fraction of pericytes responding to electrical stimulation nor the constriction seen (p=0.96 and 0.63 respectively in 10 vessels), ruling out the possibility that stimulation releases ATP from underlying glia (Newman, 2001) which constricts pericytes (Kawamura et al., 2003). Furthermore, although

stimulation of pericytes sometimes evoked a Ca^{2+} wave in underlying glia (Fig. 3.7), as did direct glial stimulation, the propagation speed of the wave (10.5 ± 1.2 μm/sec, n=8; 3 waves evoked by stimulating pericytes and 5 by stimulating glia, no significant difference between pericytes and glia: Fig. 3.7c) was 5-fold faster (p=0.0014) than the propagation of the constriction described above. This tentatively suggests that a glial Ca^{2+} wave (with subsequent ATP release) does not mediate the spread of constriction. However, it is not possible to rule out the possibility that the latency of pericyte constriction is shorter at the directly stimulated pericyte than at the distant pericytes which are hypothesised to constrict in response to ATP released by the Ca^{2+} wave.

3.3.6 Neurotransmitter-evoked constriction and dilation of cerebellar pericytes

In cerebellar slices, noradrenaline (1-2.5 μM) constricted 50% (10 out of 20) of capillaries at spatially restricted locations near pericytes (Fig. 3.8a). In the constricting vessels noradrenaline reduced the capillary diameter at the pericyte by 63 ± 8% from an initial diameter of 7.2 ± 0.8 μm, but did not significantly affect the diameter at other sites lacking pericytes (Fig. 3.8b,c). Constriction by noradrenaline cannot be due to fluid movement caused by constriction of upstream arterioles, because this would make the capillary dilate. In all 7 constricting vessels tested, superimposing glutamate (100-500 μM) on the noradrenaline decreased the constriction produced by noradrenaline, i.e. dilated the vessel, by 40 ± 8% of the preconstricted diameter at the pericyte, but had no effect at other (non-pericyte) sites (Fig. 3.8a,b,d and see Movie 3 on the disk inside the rear cover of this thesis; 100 μM and 500 μM glutamate produced a 55 ± 10%, and a 34 ± 9% dilation in 2 and 5 vessels respectively, not significantly different, p=0.2). In one capillary glutamate dilated the vessel beyond the initial diameter it had in the absence of noradrenaline (by 14%), and in 4 (of 20) vessels tested 500 μM glutamate alone (in the absence of noradrenaline) dilated capillaries (by 22 ± 9%), showing that glutamate can produce a net dilation.

These data show that control of capillary diameter by pericyte constriction occurs in the brain as well as the retina.

3.3.7 Assessing the quantitative contribution of capillary pericytes to regulation of cerebral blood flow and the generation of BOLD and PET signals

As noted above, the majority of the noradrenergic innervation of the brain terminates near capillaries not arterioles (Cohen et al., 1997), and capillaries are closer than arterioles to metabolically active neurons, suggesting that neurons may control blood flow by signalling to capillaries as well as to the more distant arterioles. The neurotransmitter-evoked pericyte-mediated constrictions and dilations of capillaries reported above suggest that this is possible. Consistent with this, modelling studies employ a brain capillary bed resistance that is 45% of the resistance in the precapillary arterioles and arteries (Lu et al., 2004), and experimental reduction of capillary resistance increases cerebral blood flow (Vogel et al., 2000), suggesting that a quantitatively significant component of blood flow regulation could occur at the capillary level. The potential importance of this regulation can be estimated quantitatively as follows, based on the cerebellar data described in the preceding section.

With basal pericyte constriction produced *in vivo* by noradrenaline released from locus coeruleus neurons, I assume for simplicity that essentially all of the cerebellar capillary resistance occurs at pericytes. In the presence of noradrenaline, glutamate increases capillary diameter at pericytes by a factor of 2.11 (calculated from the average data in Fig. 3.8c: in noradrenaline the diameter is 100%-64% = 36% of its control value without drugs present, and this increases to 36%+40% of the control value = 76% when glutamate is superimposed). This would reduce the capillary resistance 20-fold (by Poiseuille's law, which states that resistance is proportional to the fourth power of the diameter), and thus decrease the total flow resistance by 30% (assuming a resistance ratio for capillaries to arterioles/arteries of 45:100 as in Lu et al. 2004). Consequently the flow will increase by 43% (since 100%/(100%-30%) = 1.43). Thus, pericyte-evoked capillary dilation could control blood flow

significantly, and would then be expected to contribute to BOLD and PET signals. Consistent with this, regulation of blood flow at the capillary level has been suggested as essential to explain the ability to image 200 μm functional columns in visual cortex using spectroscopy of haemoglobin (Malonek et al., 1997).

3.3.8 Neuronal activity can regulate capillary diameter via pericytes

The experiments described above on retina and cerebellum establish that superfused neurotransmitters can constrict and dilate pericytes. To assess whether changes of neuronal activity (and associated neurotransmitter release) can regulate capillary diameter via pericytes, I locally altered the firing of retinal ganglion cells in two different ways. I either stimulated electrically, or puffed solution containing the $GABA_A$ and $GABA_C$ blockers GABAzine (100 μM) and TPMPA (100 μM), ~22 μm below the surface of the retina near the inner plexiform layer.

Electrical stimulation (Fig. 3.9a-c) evoked a pericyte constriction of 39 ± 6% (from an initial diameter of 4.6 ± 0.4 μm) in 13 of 43 capillaries tested. This constriction was blocked by TTX ($p=0.034$ by χ^2 test: a second stimulus evoked no constriction in 6 of 6 cells tested in 1 μM TTX, but did constrict 4 of 5 cells without TTX, Fig. 3.9d), showing that neuronal action potentials were involved in generating the response. Pericyte constriction evoked by inner retinal stimulation cannot be due to extracellular current spread directly activating pericytes because no such response was seen when stimulation was applied to the capillary wall between pericytes (see section 3.3.2), and the distance from the electrode tip to the pericyte is less in the latter stimulation (and current flow is not hindered by the presence of intervening cells) than when stimulating in the inner retina.

Puffing GABA blockers evoked a constriction of 69 ± 12% (from 4.8 ± 0.4 μm, latency 34 ± 3 sec, in 4 out of 41 vessels tested, Fig. 3.9e,f), showing that endogenous GABA release controls capillary diameter via pericytes.

3.3.9 The pericyte response to ischaemia

After ischaemia, cerebral blood flow is initially increased, but is later reduced due to a defect in vasodilatory pathways (Leffler et al., 1989; Nelson et al., 1992; Hauck et al., 2004). To test the contribution of pericytes to these changes, I simulated retinal ischaemia (see Methods, Chapter 2, section 2.2). Metabolic inhibition leads to a regenerative depolarization of nervous tissue, the anoxic depolarization (Hansen, 1985), which in the retina is associated with increased opacity similar to that seen in spreading depression. Ischaemic solution led to this opacity developing after ~7 minutes (435 $\pm$ 24 sec). Before the anoxic depolarization some pericytes (4/38) constricted capillaries, by 53 $\pm$ 9%, from an initial diameter of 6.8 $\pm$ 0.4 μm (Fig. 3.10a,b).

3.4 Discussion

3.4.1 Pericytes can regulate capillary diameter in rat retina and cerebellum

Five novel aspects of these data establish pericytes as likely regulators of blood flow at the capillary level. First, I demonstrate that neurotransmitters can evoke pericyte-mediated capillary constriction *in situ*. Previous work has shown this only in isolated retinal capillaries, and indeed it has been suggested that vasoactive agents do not affect capillary diameter *in situ* (Butryn et al., 1995). Although one study claimed pericyte mediated alterations of retinal capillary diameter *in situ* (Schonfelder et al., 1998), these were small and the study showed neither stability of the diameter before, nor reversibility of the diameter change after, application of the vasoactive agent. Second, I demonstrate that the capillary diameter changes are generated by pericytes rather than endothelial cells, because they do not occur in pericyte-free regions of the vessels. Third, although retinal vessels have a higher density of pericytes than brain capillaries (Shepro and Morel, 1993), the constriction of cerebellar capillary pericytes by noradrenaline indicates that pericyte regulation of blood flow can occur throughout the brain. Fourth, I show that a decrease of pericyte contractile tone dilates capillaries: removal of extracellular Ca^{2+} dilates retinal capillaries and glutamate dilates

cerebellar capillaries by acting via pericytes. The dilatory effect of glutamate may reflect release of nitric oxide, which inhibits Ca^{2+} influx in retinal pericytes and decreases contraction of cultured pericytes (Haefliger et al., 1994; Sakagami et al., 2001), and could contribute to the increase of local blood flow evoked by neural activity (Chapter 1, section 1.4) as discussed above in sections 3.1 and 3.3.7. Finally, I show that pericytes may contribute to the vascular response to ischaemia.

The constriction that ATP and noradrenaline produce (35% in retina, and 63% in cerebellum, respectively) would increase flow resistance 5.6-fold and 53-fold by Poiseuille's law (for laminar flow), and might completely prevent red blood cells passing through the capillary. Thus, pericytes have the potential to significantly redirect blood flow at the capillary level. Further work is needed to test whether ATP and noradrenaline act directly on pericytes, or indirectly, e.g. via astrocytes which express ATP and noradrenaline receptors (Duffy and MacVicar, 1995; Simard et al., 2003); however pericytes on isolated vessels contract (Kawamura et al., 2003) in response to ATP, suggesting a direct action for this transmitter.

Electrical stimulation of pericytes presumably evokes constriction by mimicking the $[Ca^{2+}]_i$-elevating effects of neurotransmitters (Wu et al., 2003), since the constriction was abolished by removing extracellular Ca^{2+}. Electrical stimulation sometimes produced a propagating constriction which was only manifested at pericytes. The speed of this propagation was 5-fold slower than the speed of $[Ca^{2+}]$ waves in retinal astrocytes, suggesting that it is generated by a different mechanism, possibly an electrical signal propagating through endothelial cells or an effect of the pressure or flow change generated by constriction of the stimulated pericyte. Although further work is needed to establish the propagation mechanism, the existence of a pericyte-pericyte communication system could provide a basis for vascular detection of neural activity near capillaries being propagated back to precapillary arterioles to amplify blood flow changes (Iadecola et al., 1997), as occurs in muscle (Berg et al., 1997).

The low fraction of pericytes responding to superfused neurotransmitters (25% and 30%, respectively, for ATP and UTP in retina, and 50% for noradrenaline in cerebellum), contrasts with the reliability with which electrical stimulation evoked constriction (90%). This may reflect variable expression of transmitter receptors on pericytes at different sites along the vascular bed, or a loss of factors released by blood flow or pressure in the capillary network. The lack of blood flow and pressure in my unperfused brain slices may also slow the onset of the capillary constrictions and dilations reported here: dilations of arterioles produced by $[Ca^{2+}]_i$ rises in astrocytes are also faster *in vivo* than in slices (Zonta et al., 2003; Takano et al., 2006). In addition, although some pericytes do not visibly constrict, the stiffness of their processes around the capillary may be increased by ATP or noradrenaline, leading them to oppose dilation by other agents or by the deformation that is necessary for red blood cells to pass along small capillaries.

The early constriction of pericytes during ischaemia presumably results from $[Ca^{2+}]_i$ rising when the cells' ATP production is inhibited. This might accelerate the reduction of energy supply from the capillaries to the neurons, and an altered pericyte responsivity to transmitters after a period of ischaemia might contribute (along with altered arteriolar function) to the decreased capillary diameter and impaired reperfusion which occurs after cerebral ischemia (Hauck et al., 2004).

These data suggest that pericytes may contribute to the regulation of cerebral blood flow in health and disease. Spatially restricted constrictions of brain microvessels previously attributed to arteriole smooth muscle (Cauli et al., 2004; Takano et al., 2006; Metea and Newman, 2006; Rancillac et al., 2006) may, in fact, have been mediated by pericytes. These results prompt a re-examination of the idea that precapillary arterioles are solely responsible for the increase of blood flow evoked by neural activity which underlies functional imaging techniques (see Chapter 1 sections 1.4 and 1.7).

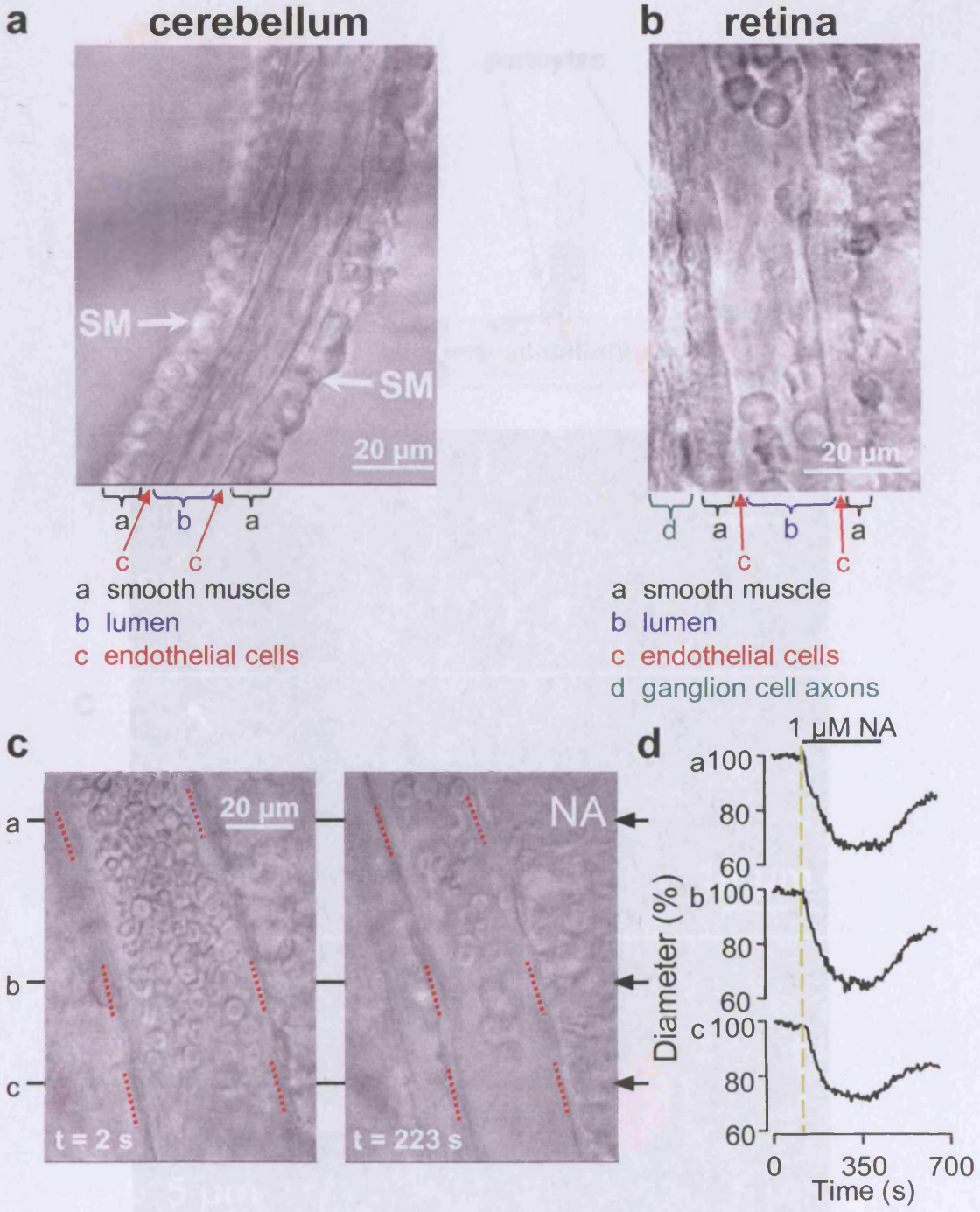

Figure 3.1 Morphology and constriction characteristics of arterioles. **a,b** Arterioles in the cerebellum (**a**) and retina (**b**) are covered by a continuous layer of smooth muscle (arrows, SM) formed of annuli around the vessel; on focussing through the muscle when doing the experiment, striations are visible in the smooth muscle. **c,d** Retinal arterioles constrict spatially uniformly in response to noradrenaline. **c** Images of a retinal arteriole responding to 1 µM superfused noradrenaline (NA). Red blood cells are seen within the vessel; red dotted lines delineate the edge of the lumen. **d** Plots of constriction against time for 3 locations separated by 90 µm along the vessel show an essentially uniform constriction. Mean constriction in 8 vessels (all of which responded) to which 1 µM noradrenaline was applied was 20.5 ± 4.1% from an initial diameter of 32.1 ± 3.3 µm.

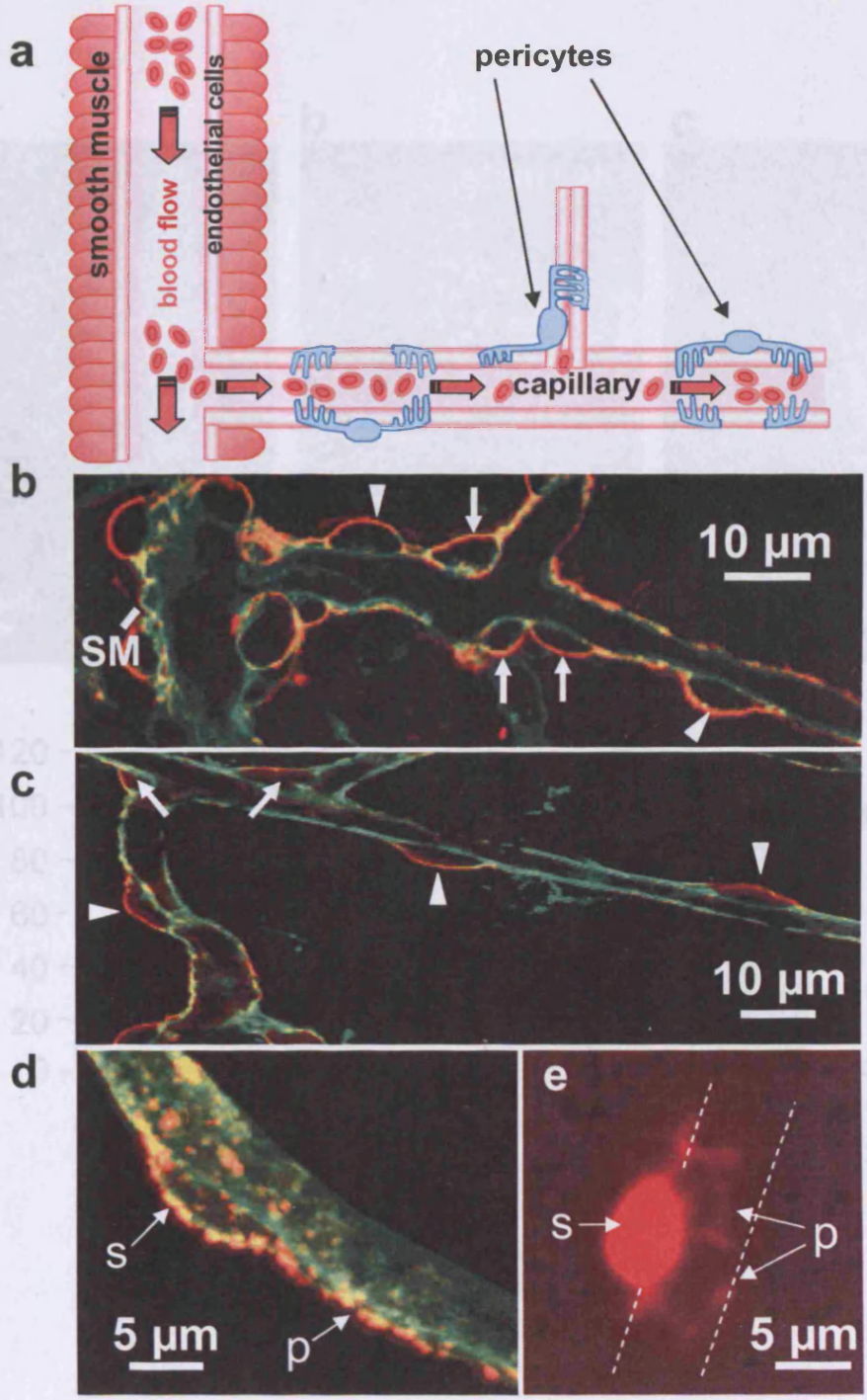

Figure 3.2 Pericyte anatomy confers flow regulating capability downstream of arterioles. **a** A schematic diagram of the CNS vasculature, showing two potential sites of blood flow control: smooth muscle around arterioles, and pericytes on capillaries or at capillary junctions. **b** Cerebellar molecular layer arteriole (left), surrounded by smooth muscle (SM), giving off a capillary to the right. Capillary labelled with isolectin B4 (green); pericytes labelled for NG2 (red) are on the straight part of capillaries (arrow heads) and at junctions (arrows). **c** Retinal capillaries labelled as in b. **d** Soma (s) of cerebellar pericyte gives off processes (p) running along and around capillary. **e** Dye fill of retinal pericyte reveals processes running around capillary (dashed lines). Shown by kind permission of Claire Peppiatt-Wildman.

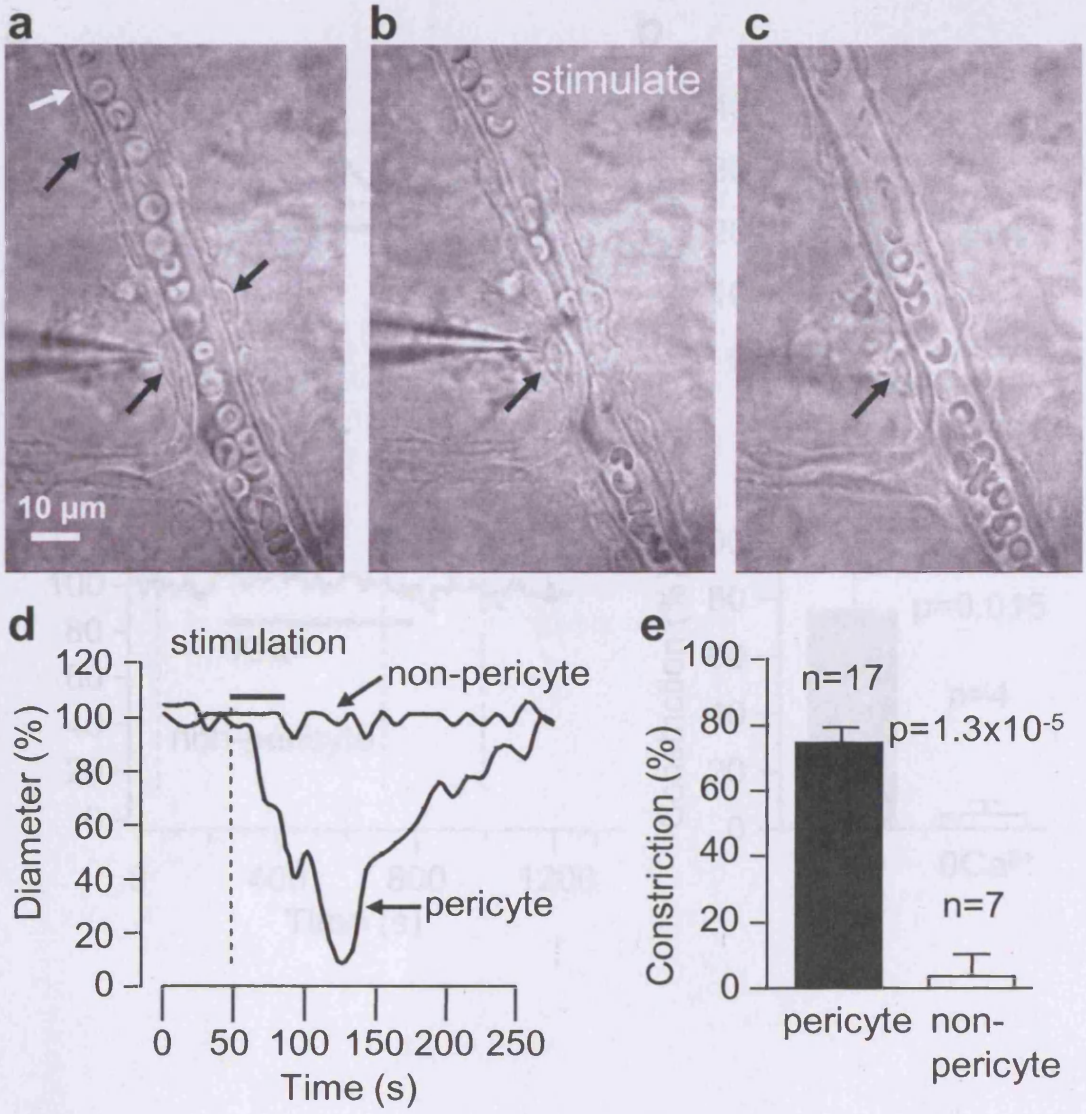

Figure 3.3 Electrical stimulation evokes a localized constriction of retinal pericytes. **a-c** Capillary with pericytes (black arrows) before (**a**), during (**b**) and after (**c**) stimulation. Red blood cells are within capillary; thin structures on outside of capillary are astrocyte endfeet. **d** Diameter of capillary in a-c at stimulated pericyte and at a non-pericyte site (shown as the white arrow in a). **e** Mean constriction when stimulating at pericyte or non-pericyte sites.

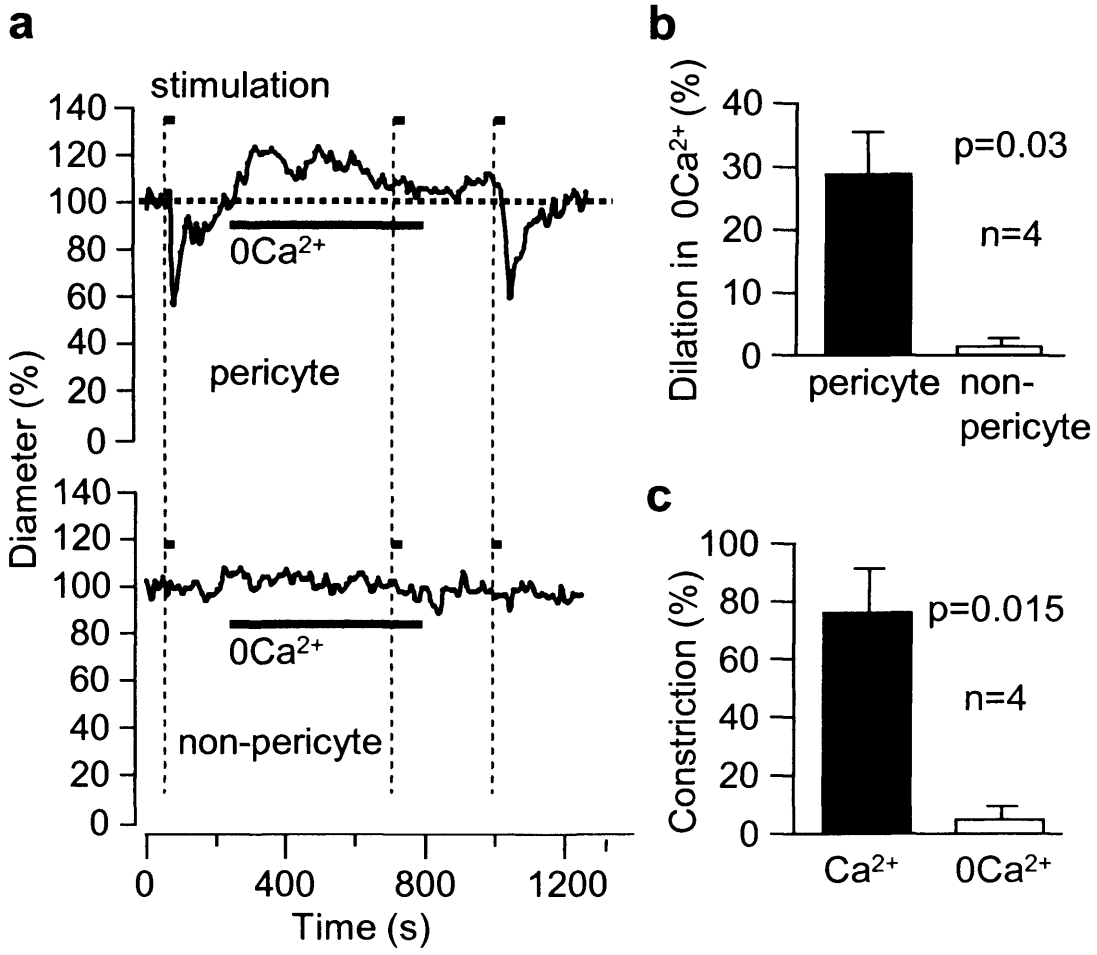

Figure 3.4 Electrical stimulation evokes a Ca^{2+}-dependent localized constriction of retinal pericytes. **a** Effect of removing extracellular Ca^{2+} on the resting diameter of a retinal capillary and on the response to pericyte stimulation, at pericyte and nearby non-pericyte sites. **b** Mean dilation produced by removing Ca^{2+}. **c** Mean effect of Ca^{2+}-removal on constriction of pericyte, as in a.

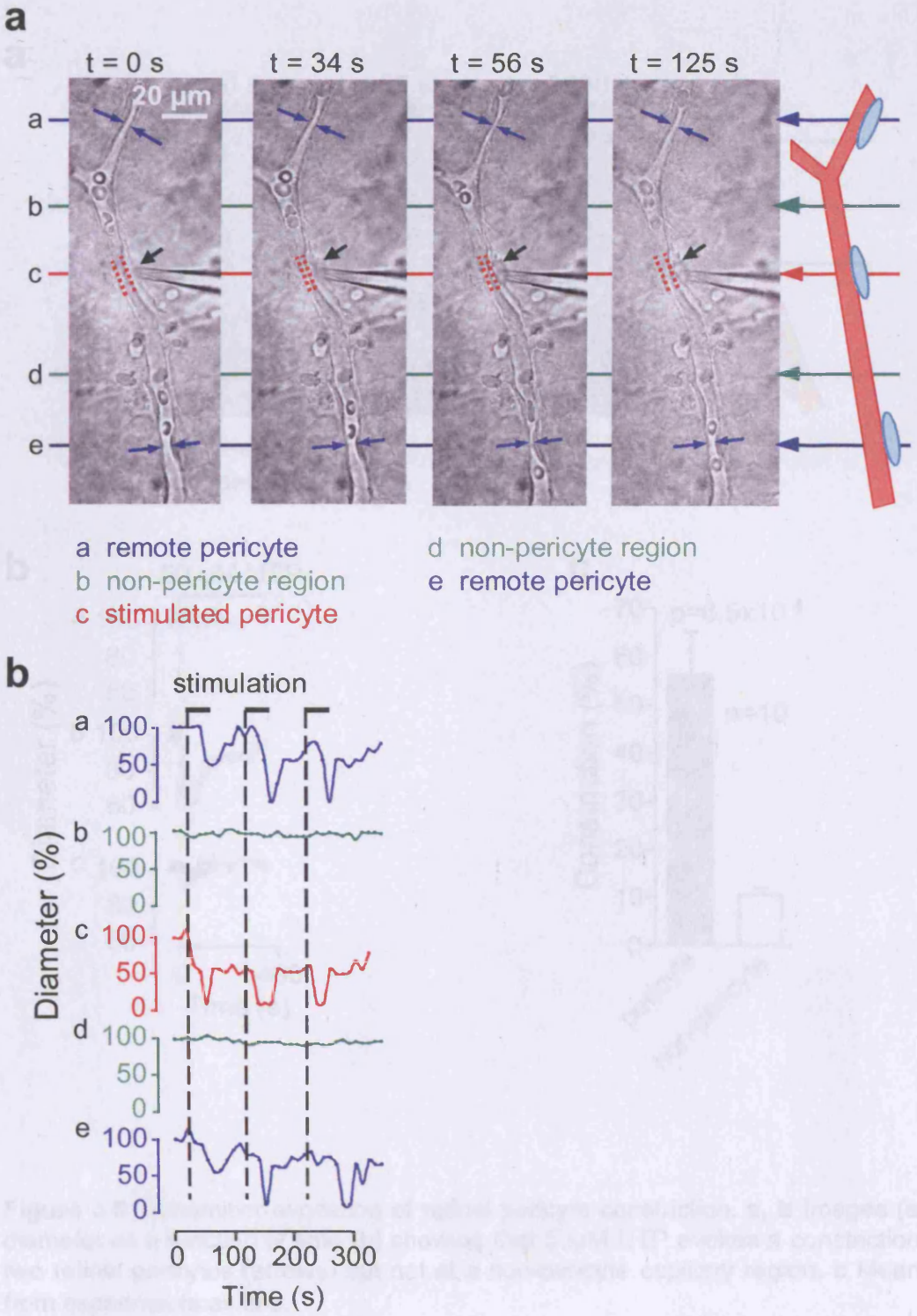

Figure 3.5 Propagation of retinal pericyte constriction. **a** Electrical stimulation of a pericyte (black arrow) evokes a local constriction (red dashed lines show vessel diameter, red trace in b) followed by a later constriction of distant pericytes (blue arrows in a and traces in b). **b** No constriction occurred at intervening non-pericyte regions (green arrows in a and traces in b; responses to 3 repeated stimuli).

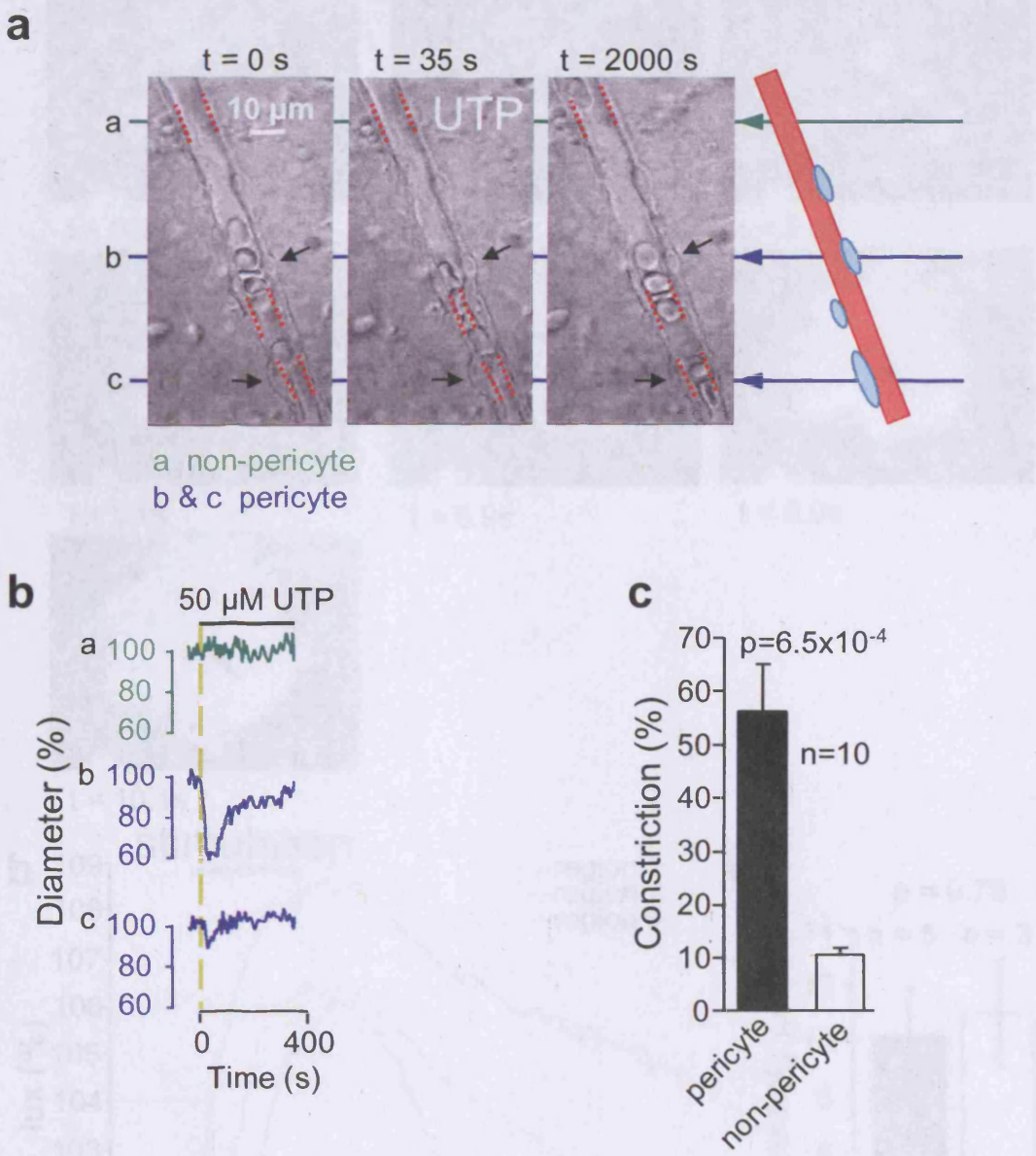

Figure 3.6 Transmitter-evocation of retinal pericyte constriction. **a, b** Images (a) and diameter as a function of time (b) showing that 50µM UTP evokes a constriction near two retinal pericytes (arrows) but not at a non-pericyte capillary region. **c** Mean data from experiments as in b.

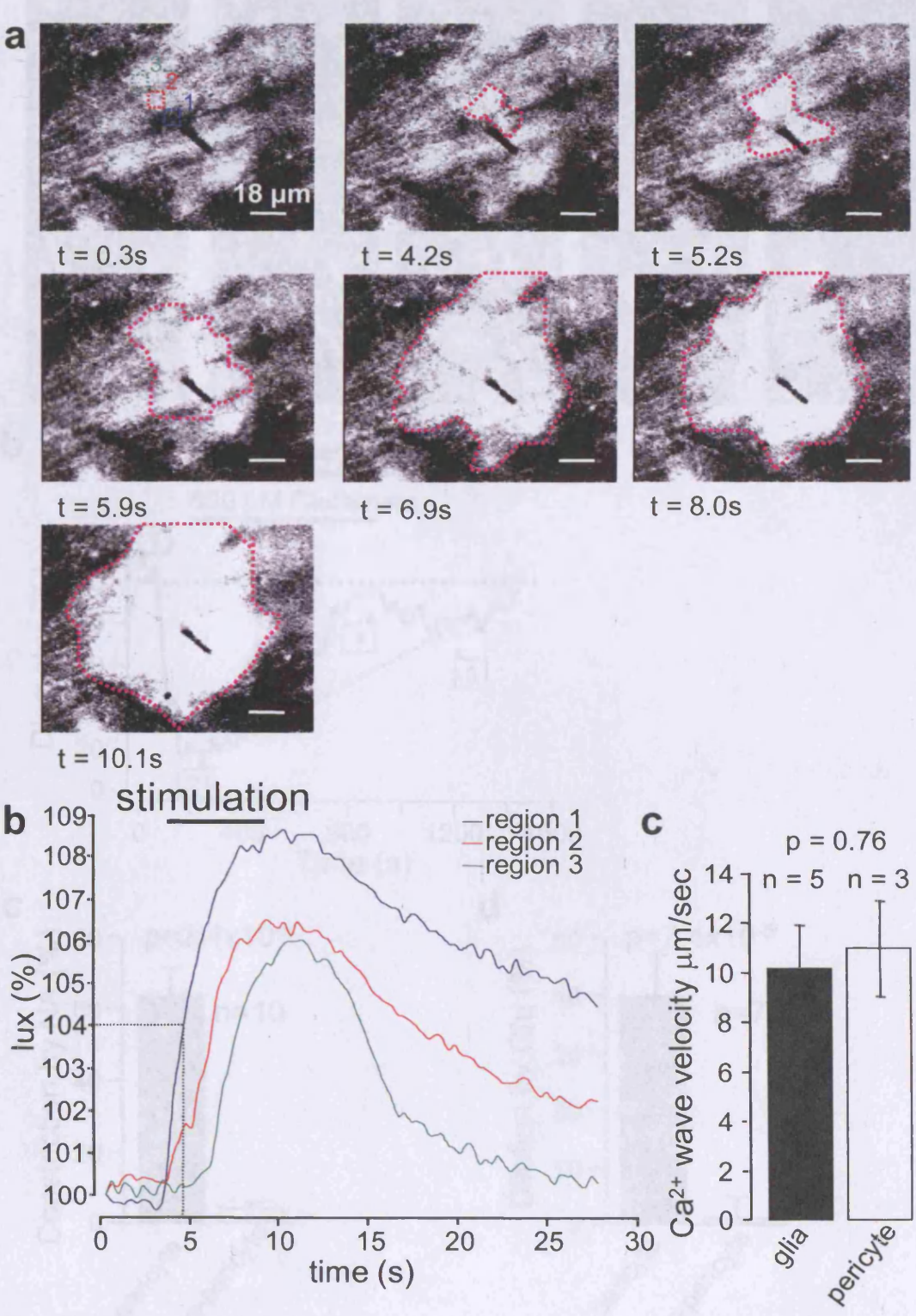

Figure 3.7 Stimulation of pericytes or glia evokes a Ca^{2+} wave. **a** Images showing spread of a Ca^{2+} wave (whiter area) evoked by pericyte stimulation. **b** Time course of fluorescence at three points shown in a. Velocity of wave was calculated as distance to the centre of the area, divided by the time to half maximum of the peak response (indicated for one trace by a dotted line). **c** Average velocity of Ca^{2+} wave evoked by glial or pericyte stimulation, not significantly different.

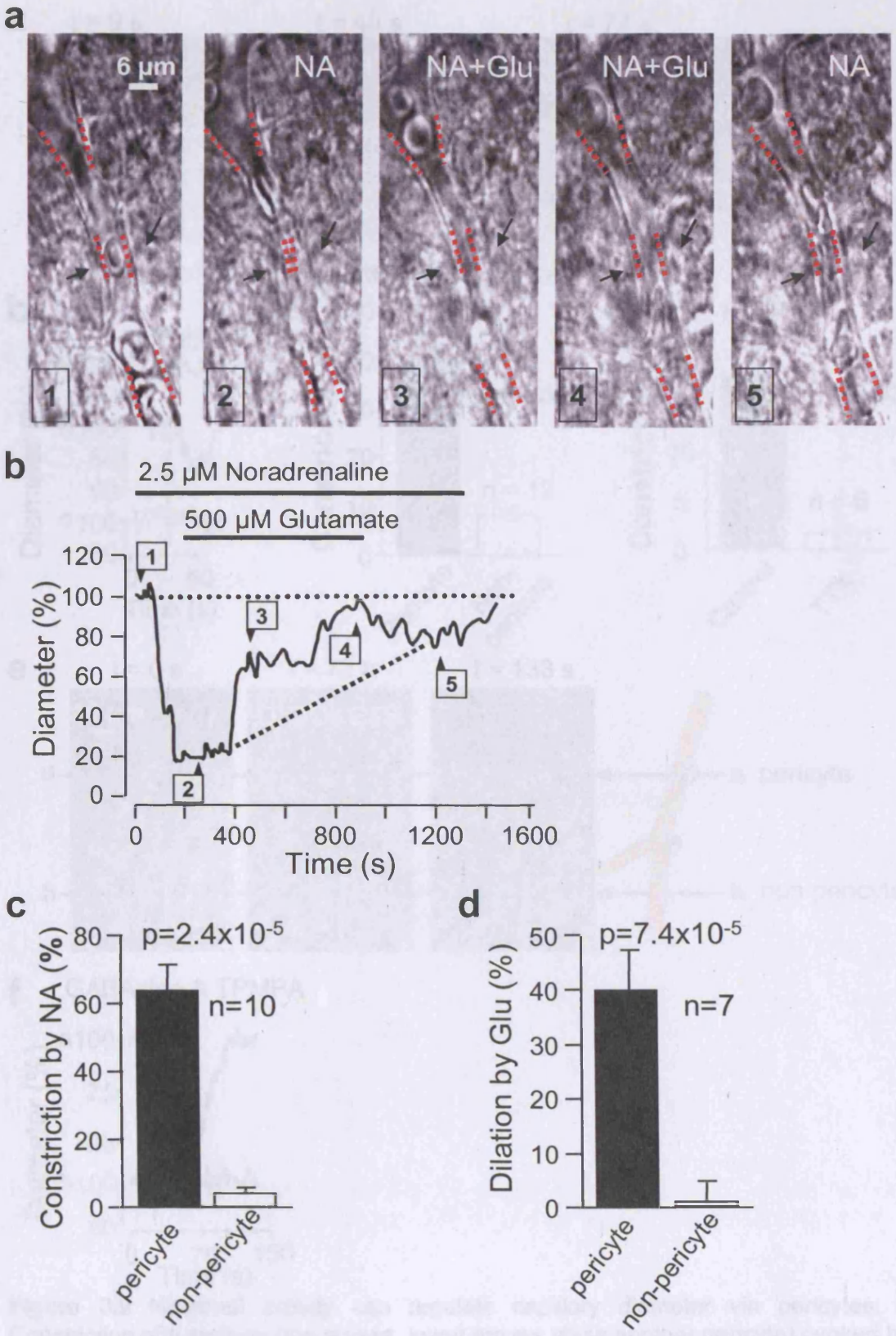

Figure 3.8 Transmitter-evocation of pericyte constriction and dilation in cerebellar slices. **a** Images showing localized constriction near pericytes on cerebellar molecular layer capillaries (black arrows, best seen in panel 4) in response to 2.5 µM noradrenaline, and dilation by superimposed 500 µM glutamate. **b** Diameter at pericyte; numbers show times of images in a. **c** Mean constriction by noradrenaline in 10 responding capillaries, at pericyte and non-pericyte sites. **d** Mean dilation (reduction of noradrenaline-evoked constriction) by 100-500 µM glutamate in 7 capillaries (relative to pre-noradrenaline diameter).

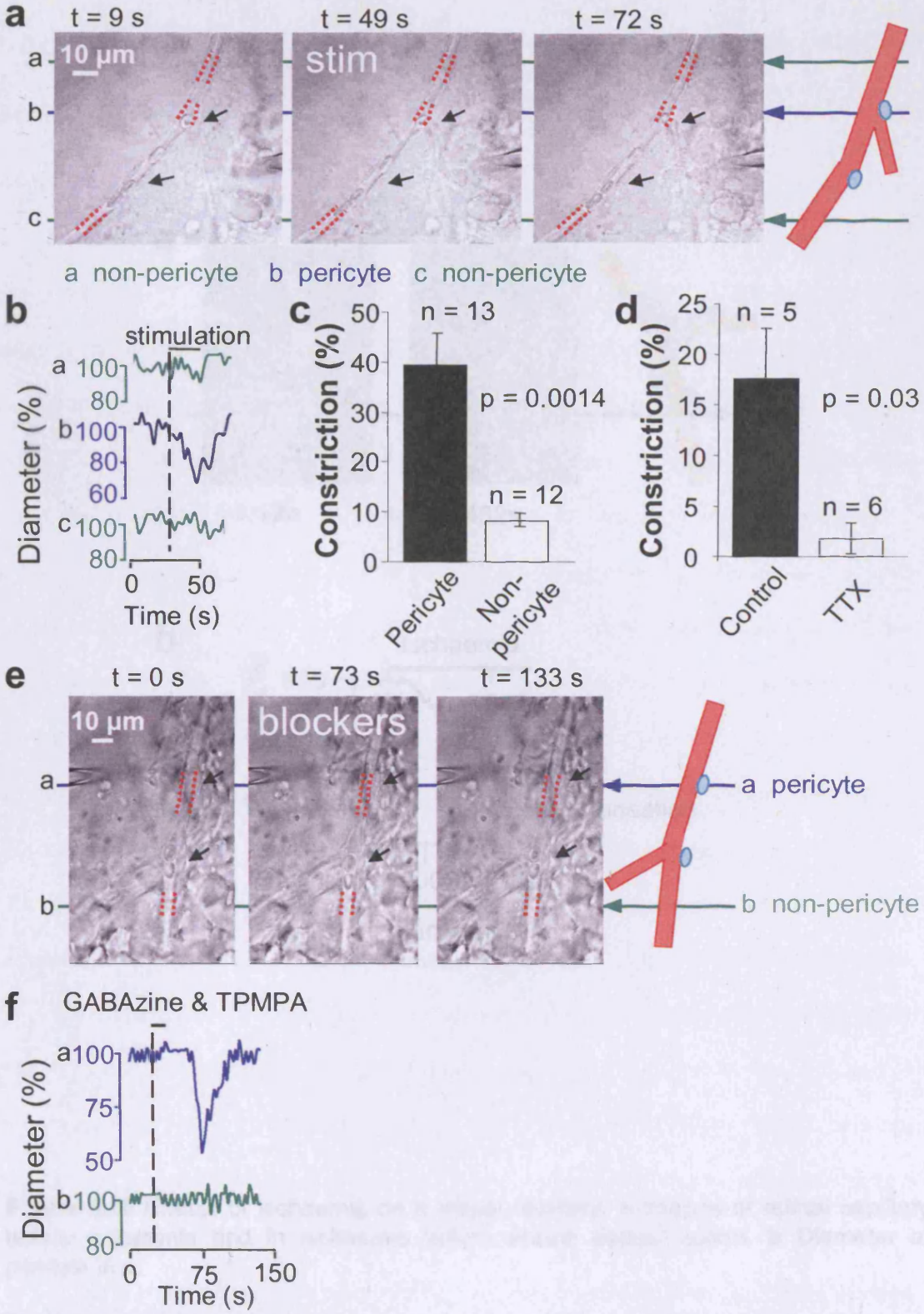

Figure 3.9 Neuronal activity can regulate capillary diameter via pericytes. **a** Constriction of a pericyte (top arrows, lower arrows show another pericyte) evoked by electrical stimulation (electrode on right) near the inner plexiform layer. **b** Time course of constriction in a at pericyte and non-pericyte sites. **c** Mean constriction at pericyte and non pericyte locations in response to electrical stimulation in the inner plexiform layer of the retina. **d** Mean constriction in response to second stimulus when stimulating in absence and presence of 1 µM TTX. **e** Constriction of pericyte (top arrows; lower arrows show another pericyte) evoked by puffing GABA receptor blockers (puff electrode top left) near the inner plexiform layer. **f** Time course of constriction in e at pericyte and non-pericyte site.

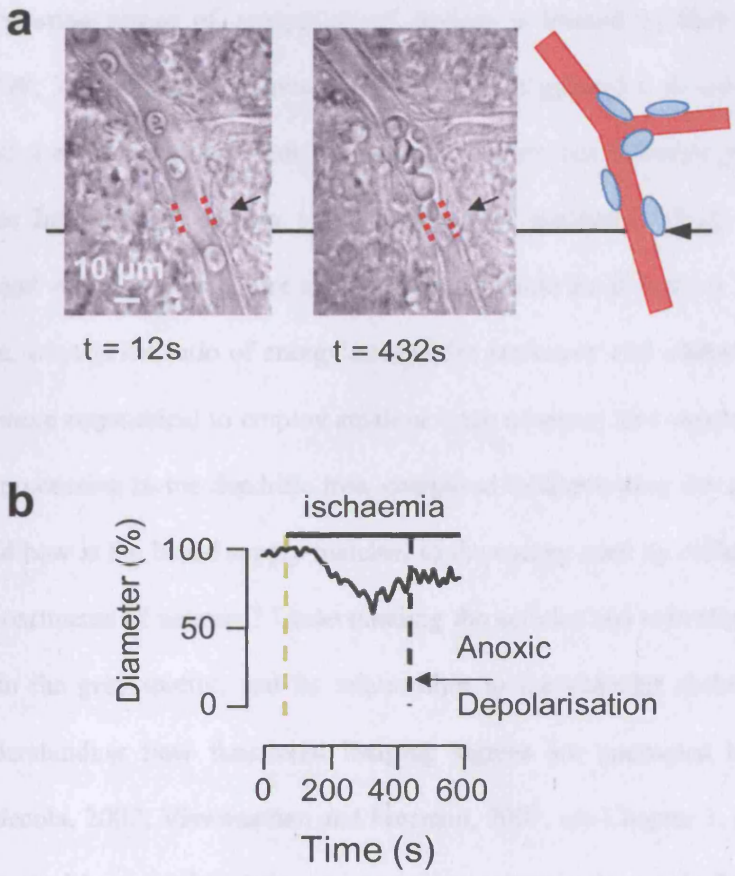

Figure 3.10 Effects of ischaemia on a retinal capillary. **a** Images of retinal capillary before ischaemia and in ischaemia before anoxic depolarization. **b** Diameter at pericyte in a.

Chapter 4: Matching energy supply and expenditure to computation in the cerebellum

4.1 Introduction

The processing power of computational devices is limited by their energy supply (Sarpeshkar, 1998; Laughlin and Sejnowski, 2003), but in general it is unknown how the energetic resources available to the brain are allotted to carry out different parts of a neural computation (see Introduction, section 1.2). Fundamental questions, which will determine how the neural and vascular architecture are structured, include the following: for a particular neural algorithm, what is the ratio of energy needed for excitatory and inhibitory neurons; is it energetically more economical to employ small or large neurons; how much energy is used on information processing in the dendritic tree, compared to distributing the computed result along axons; and how is the blood supply matched to the energy used by different neurons or subcellular compartments of neurons? Understanding the cellular and subcellular distribution of energy use in the grey matter, and its relationship to the vascular architecture, is also relevant to understanding how functional imaging signals are generated by brain tissue (Attwell and Iadecola, 2002; Viswanathan and Freeman, 2007, see Chapter 1, section 1.7). To address these issues I have analysed the energy use expected in the cerebellar cortex of the rat: a brain area for which the cellular properties and computations performed have been well studied (Tyrell and Willshaw, 1992), and which is thought to be used to store patterns of motor behaviour (Marr, 1969; Albus, 1971; Ito, 1972; Tyrell and Willshaw, 1992). I used the measured properties of each cerebellar cell type to investigate the relationship between energy expenditure and neural computation in the cerebellar cortex.

The cerebellar cortex receives information on the environment and body position from sensory receptors, and on the desired motor output from the cerebral cortex. By comparing this information to stored patterns of sensorimotor function it modulates the motor output to make movements smoother and more accurate. Information arrives along mossy fibres, each of which sends excitatory synapses onto about 150 cerebellar granule cells (Fig.

4.1). The granule cells are the smallest and most numerous neurons in the brain. They recode information they receive on ~4 small dendrites (each with an input from one mossy fibre) into action potentials which pass along their axons, the parallel fibres, to excite the output cells of the cerebellar cortex, the Purkinje cells. These are large cells, with an extensive dendritic tree, that send axons to inhibit neurons in the deep cerebellar nuclei. In this circuit, information arriving on ~13,000 mossy fibres is recoded into action potentials on a much larger number (~174,000) of parallel fibres, which synapse onto the single output Purkinje cell. Purkinje cells also receive a single powerful excitatory synapse from a climbing fibre arising in the inferior olive: this input is commonly assumed to instruct active parallel fibre synapses to decrease their strength during learning of motor patterns (Marr, 1969; Albus, 1971; Tyrell and Willshaw, 1992), although this is disputed (De Schutter, 1995). Inhibitory interneurons, the Golgi, basket and stellate cells (Fig. 4.1) moderate the activity of the whole network.

Most signalling-related energy in the brain is expended on pumping of Na^+ ions out of the cell (Siesjo, 1978; Attwell and Laughlin, 2001, see Chapter 1, section 1.2). I estimated the signalling energy expended on different cellular processes in the rat cerebellum as follows. Published anatomical and electrophysiological data on the properties of the different cerebellar cells were employed to calculate the ATP used to reverse the Na^+ influx producing excitatory synaptic currents and action potentials, the Na^+ influx occurring at the resting potential, the Ca^{2+} entry driving excitatory and inhibitory transmitter release (Attwell and Laughlin, 2001), and the ATP expended on other less energy consuming processes inherent in cerebellar information processing which are described in detail in the Results. My analysis differs significantly from previous energy budgets for the cerebral neocortex (Attwell and Laughlin, 2001) and olfactory cortex (Nawroth et al., 2007) in that it employs the experimentally measured parameters specific to each cell type being considered, rather than using average values obtained from a range of cell types. This is possible solely because the cerebellum has been more intensively studied electrophysiologically and anatomically than other brain areas. Only one parameter for my analysis was not available from the literature, the mean firing rate of granule cells, so I set this rate (to 6 Hz) to reproduce the measured

action potential dependent consumption of the cerebellar cortex (see section 4.2.2), and then investigated the effect of varying this parameter.

4.2 Methods

4.2.1 General strategy for calculations

Na^+ or Ca^{2+} entry into each cell, associated with synaptic, action or resting potentials, were estimated as detailed below and converted to the amounts of ATP needed to extrude them (Attwell and Laughlin, 2001) using the fact that the Na^+/K^+-ATPase consumes one ATP for each 3 Na^+ extruded, while the Ca^{2+}-ATPase (or $3Na^+/Ca^{2+}$ exchange followed by Na^+ extrusion) uses 1 ATP per Ca^{2+} extruded. Similarly, the ATP needed to restore Ca^{2+} to intracellular stores, and the ATP expended on transmitter and vesicle recycling, were estimated (Attwell and Laughlin, 2001). The energy expended on reversing Cl^- entry at inhibitory synapses is sufficiently small that it can be ignored (estimated to be <1% of that needed to restore an equivalent change of the Na^+ gradient, see section 4.2.8). These ATP costs per ion entering are justified in section 4.2.8 below, which can, however, be omitted without loss of continuity on a first reading.

I analysed the energy used on each cerebellar cell type, with all the cells firing action potentials at their measured physiological rates (see Results, below), i.e. the mossy fibre input firing at 40 Hz, the granule cells firing at 6 Hz (see section 4.2.2), Purkinje cells firing at 41 Hz (simple spikes) and 1 Hz (complex spikes), Golgi cells firing at 10 Hz, stellate and basket cells firing at 12 Hz and the climbing fibre input firing at 1 Hz. Full details of the calculations, and an analysis of the sensitivity of the predictions to uncertainties in the values of the parameters used, are given in the Results and in section 4.5.6, respectively. In what follows I consider only the energy used on signalling (including the resting potential), and ignore ATP use on housekeeping tasks.

4.2.2 Choosing parameters from the literature

Where possible the calculations are based on parameters for adult rat cerebellum, however much of the electrophysiological data had to be taken from studies on younger rats. If no data were available for rat, I used data from mice, and if not available from mice then from other mammalian species. The number or density of each cell type was taken from anatomical values in the literature, as detailed below. Where necessary, ion channel gating rates and conductances were adjusted to 37°C using Q_{10} values of 1.7 (AMPA and mGluR receptor gating rate: Marcaggi et al., 2003), 3.48 (NMDA receptor gating rate, the mean value obtained from 22 papers in the literature on the properties of NMDA receptors in a variety of cells: A. Gibb, personal communication) and 1.4 (for synaptic current amplitudes: Marcaggi et al., 2003). Input resistances were taken from data with K^+ (rather than Cs^+) in the recording pipette.

The Na^+ and Ca^{2+} entry generating excitatory synaptic currents were calculated at each cell's resting potential from values in the literature for current or conductance amplitudes and time courses measured electrophysiologically, as detailed below. To convert synaptic currents measured at a particular voltage to the current mediated by Na^+ entry, I assumed the synaptic current was carried by ohmic Na^+ and K^+ conductances with a reversal potential of 0 mV for the summed Na^+ and K^+ currents (so the potassium conductance was half the sodium conductance, assuming Nernst potentials of +50 mV and -100 mV for Na^+ and K^+ respectively) and calculated the resulting Na^+ component of the current. For example, for data at -70 mV the Na^+ current is thus 1.14-fold larger than the measured synaptic current (because K^+ efflux opposes it). Having obtained the Na^+ current at the measured voltage, it was then converted to an Na^+ current at the resting potential of the cell under consideration by using the ohmic dependence of Na^+ current on $(V - V_{Na})$.

It was not feasible to model the ion fluxes underlying the action potentials in all cell types in the cerebellum. Instead I usually followed the approach used previously (Attwell and Laughlin, 2001), by first calculating the minimum Na^+ entry needed to produce the voltage

change occurring during the action potential (given by the voltage change occurring multiplied by the capacitance of the area of cell being considered) and then quadrupling this to take account of simultaneous activation of Na^+ and K^+ channels (Hodgkin, 1975): in earlier work (Attwell and Laughlin, 2001) this 4-fold increase was validated by calculations by A. Roth and M. Hausser based on cell morphology and ionic current properties for cortical and hippocampal pyramidal cells. For all cells the capacitance per area of membrane was taken as $7.7x10^{-3}$ Fm^{-2} (Roth and Hausser, 2001). Energy used to pump out Na^+ entry at the resting potential was calculated from the cell's input resistance and resting potential, using equation (4.4) below. Each vesicle was assumed to contain 4000 molecules of glutamate or GABA, and to recycle each transmitter molecule after release it was assumed that 2.67 ATP were needed (Attwell and Laughlin, 2001), of which 12.5% (0.33 ATP) was used for vesicle uptake in the releasing cell. To pump out the Ca^{2+} triggering the release of one vesicle, it was assumed that $1.2x10^4$ ATP are needed (Attwell and Laughlin, 2001), and 821 ATP were needed to recycle each vesicle released (Attwell and Laughlin, 2001).

As detailed below, data are available in the literature for essentially all the parameters that comprise my model of cerebellar information processing (e.g. the action potential firing rates of the cells, the number of vesicles their synapses release, the conductances activated postsynaptically, etc.) with one important exception: the mean firing rate of granule cells. To constrain this parameter, I made use of the fact that the total energy consumption of the cerebellar cortex has been measured in conscious rats as 20 μmoles ATP/g/min (Sokoloff et al., 1977). Of this, I assume that ~68% is used on action potential driven processes (since in rat neocortex there is an average 68% reduction of energy use produced by deep anaesthesia (Nilsson and Siesjo, 1975; Sibson et al., 1998), compared to the energy expenditure in awake animals), i.e. 13.6 μmoles ATP/g/min. To reproduce this expenditure on pumping out the Na^+ entry associated with synaptic and action potential signalling in the cerebellar cortex, I had to set the mean firing rate of granule cells in my model to be 6 Hz. I then tested the effect of

varying the mean granule cell firing rate in the model (the results of this exploration are shown in Fig. 4.4a).

4.2.3 Calculating the energy use for each cell type

The energy use for each cell type was calculated by summing all the energy costs for that cell within the cerebellar cortex. For example, for the granule cell the ATP used on the resting potential, on action potentials, on synaptic currents generated by mossy fibre input, on transmitter release and vesicle recycling, and on the presynaptic component of glutamate recycling at the parallel fibre synapses, were summed. However, energy expended on postsynaptic currents in Purkinje cells or interneurons was ignored (it was allotted to the Purkinje cells or interneurons) even though these currents were generated by transmitter release from granule cells. Similarly, the energy expended on recycling glutamate (released from granule cells) in Bergmann glia and Purkinje cells (see Results) was also not attributed to granule cells. Only the grey matter was considered: energy use in axons in the white matter was ignored when calulating the energy usage of Purkinje cells, mossy and climbing fibres.

4.2.4 Calculating the total energy use of the cerebellar cortex

To calculate the total energy usage of the cerebellar cortex, the energy used per cell type was weighted by the number of cells present, and summed over all cells. To convert to an energy use per weight of tissue, I used a cerebellar density of 1.04 g/ml (Sundstrom et al., 1985). To partition the energy use between different cerebellar layers, the energy consumed in the part of each cell type in each layer was calculated, multiplied by the number of cells present, and summed over all cell types. Half of the Purkinje cell soma was attributed to the molecular layer and half to the granular layer. To compare the energy use on excitatory and inhibitory neurons, I summed the energy consumed in all excitatory neurons, and added on as an excitatory cost the energy expended on recycling glutamate in glial cells and Purkinje cells. I compared this with the sum of all the energy used on inhibitory neurons (excluding

the glutamate recycling energy in Purkinje cells); below I assume that GABA is recycled through the synaptic terminals of the releasing cell so that no glial component needs to be added to the inhibitory energy expenditure; ATP expended on glial resting potentials (only 1.9% of the total energy use) was excluded from this calculation.

4.2.5 Calculating the energy used on different stages of cerebellar computation

To compare the energy used on different stages of cerebellar computation I proceeded as follows. The energy used on remapping of information from the mossy fibre input action potentials to action potentials in the granule cell soma was calculated by summing the energy used on the mossy fibre resting and action potentials, and on vesicle release, recycling and refilling in the mossy fibres, on the resting, synaptic and action potentials in the granule cell dendrites and soma, on all aspects of the function of Golgi cells, and on the resting potential and transmitter recycling in granular layer astrocytes. (The contributions of Golgi cells and astrocytes were 13% of the total thus produced). The energy used on propagation of the recoded information to Purkinje cells was calculated by summing the energy used on the granule cell axon resting and action potentials, on vesicle release, recycling and refilling at the parallel fibre synaptic terminals, on all aspects of the function of stellate and basket cells, and on the resting potential and transmitter recycling in Bergmann glia (the contributions of the stellate and basket interneurons and of Bergmann glia were 16% of the total). The energy used on the computation of motor output by the Purkinje cells was obtained by summing the ATP used by the Purkinje cells on all processes.

4.2.6 Quantifying the blood vessel distribution in cerebellum

As described in Chapter 2, section 2.6, blood vessels in cerebellar slices from P21 rats were labelled with isolectin B4 conjugated to FITC (Sigma) and confocal stack images taken of the molecular and granular layers. Isolectin B4 labels the endothelial cells on the outside surface of the blood vessel, and so delineates the blood vessel surface area available

for O_2 and glucose exchange, which I assume is a measure of the potential O_2 and glucose supply to the tissue. An approximate quantification of the relative blood vessel surface area in the molecular and granular layers was obtained as described in Chapter 2, section 2.8.

4.2.7 The energy cost of reversing Na^+, K^+ and Cl^- movements

This section concludes that approximately 1 ATP is used to pump out each 3 Na^+ ions that enter the cell, while much less ATP is used to pump out each Cl^- that enters.

This treatment generalizes an earlier analysis (Attwell and Laughlin, 2001) which ignored Cl^- movements. The gas constant, R, Faraday, F, and absolute temperature, T, have their standard values (8.314 J/mole/K, 96495 Coulombs/mole, and 310K respectively), and for all cells the sodium and potassium reversal potentials will be assumed to be V_{Na}= +50 mV and V_K = -100 mV respectively.

The resting membrane of cells is assumed to be permeable to K^+ and Na^+ alone, with conductance g_K and g_{Na}, but during inhibitory synaptic transmission Cl^- influx is assumed to occur. In the absence of action potentials or synaptic currents, on a time scale longer than the membrane time constant the net membrane current is zero and

$$g_{Na}(V_{Na}-V) + g_K(V_K-V) = I_{pump} \quad (4.1)$$

where V is membrane potential, and the pump current, I_{pump}, is 1/3 of the Na^+ extrusion rate since the pump extrudes 3 Na^+ and imports 2 K^+ for each ATP hydrolysed. ATP is therefore consumed at a rate I_{pump}/F (F is the Faraday). At the resting potential when $d[Na^+]_i/dt$ = $d[K^+]_i/dt$ = 0,

$$I_{pump} = g_{Na}(V_{Na}-V)/3 \quad (4.2)$$

Solving (4.1) and (4.2) gives the resting potential as

$$V_{rp} = (2g_{Na}V_{Na} + 3g_KV_K)/(2g_{Na} + 3g_K) \quad (4.3)$$

From (4.1) and (4.2), the current produced by Na^+ influx at the resting potential, V_{rp}, is

$$g_{Na}(V_{Na}-V_{rp}) = 3(V_{Na}-V_{rp})(V_{rp}-V_K)/\{R_{in}(V_{rp}+2V_{Na}-3V_K)\}$$

where the input resistance, R_{in} is $1/(g_{Na}+g_K)$, so the rate of ATP consumption on the resting potential is

$$(V_{Na}-V_{rp})(V_{rp}-V_K)/\{FR_{in}(V_{rp}+2V_{Na}-3V_K)\} \quad (4.4)$$

Suppose now that a series of action potentials or synaptic currents suddenly raises $[Na^+]_i$ and/or $[Cl^-]_i$ and lowers $[K^+]_i$. The sum of these charge movements is assumed to be zero because after the activity the cell is approximately back at the resting potential (the deviation from the original resting potential is determined by how much the ion fluxes have altered the intracellular ion concentrations, and can be made small by assuming a large intracellular volume). Thus,

$$\Delta[Na^+]_i + \Delta[K^+]_i = \Delta[Cl^-]_i \quad (4.5)$$

If I first ignore Cl^- fluxes, equal rises of $[Na^+]_i$ and falls of $[K^+]_i$ produced by action potentials or excitatory synaptic currents will be corrected in part by the Na^+ pump. However, the pump extrudes more Na^+ than it transfers K^+ in so, for an equal and opposite change of the concentrations of these ions induced by action or synaptic potentials, how should one calculate the energy used: does one divide the number of Na^+ transferred by 3 or divide the K^+ transferred by 2? If the pump extrudes all the Na^+ that has entered, then 33% less K^+ than left the cell will have been pumped back in, and more K^+ will tend to enter again passively through the cell's K^+ conductance. Thus, part of the restoration of ion gradients is achieved by passive ion movements through ion channels, powered by the transmembrane ion gradients themselves. The analysis below shows that the relative contribution of pumping and passive ion movement to this restoration, and hence the total energy used on restoring the ion gradients, depends on the g_{Na}/g_K ratio for the cell.

Rises of $[Cl^-]_i$ produced by synaptic inhibition are assumed to be corrected by Cl^- extrusion (or a reduction of the Cl^- influx) carried out by the electroneutral KCC2 K-Cl co-transporter (Rivera et al., 1999). This will result in net K^+ loss from the cell which will need to be reversed by a reduction of passive efflux of K^+ through the cell's g_K or by active pumping of K^+ into the cell.

To calculate the energy needed to restore the ion gradients after action and synaptic potentials I proceed as follows. Rewriting (4.1) in terms of changes (Δ) from the resting values, the change of membrane potential is

$$\Delta V = (g_{Na}\Delta V_{Na} + g_K\Delta V_K - \Delta I_{pump})/(g_{Na}+g_K) \quad (4.6)$$

The rates of change of $[Na^+]_i$, $[K^+]_i$ and $[Cl^-]_i$ in a cell of volume U are

$$UF\ d[Na^+]_i/dt = g_{Na}(\Delta V_{Na}-\Delta V) - 3\Delta I_{pump} \quad (4.7)$$

$$UF\ d[K^+]_i/dt = g_K(\Delta V_K-\Delta V) + 2\Delta I_{pump} - \Delta T_{KCC2} \quad (4.8)$$

$$UF\ d[Cl^-]_i/dt = -\Delta T_{KCC2} \quad (4.9)$$

where $\Delta T_{KCC2}/F$ is the change in the rate at which K^+ and Cl^- are transported out by KCC2. From (4.6)-(4.9), $d[Na^+]_i/dt = -\,d([K^+]_i-[Cl^-])/dt$, and initially $\Delta[Na^+]_i = -(\Delta[K^+]_i-\Delta[Cl^-]_i)$ (from eqn. 4.5) so that

$$\Delta[Na^+]_i = -(\Delta[K^+]_i-\Delta[Cl^-]_i) \quad (4.10)$$

at all times. I solve (4.7) – (4.9) by assuming that the Na^+ pump rate varies linearly with small changes of $[Na^+]_i$ around the resting value so that

$$\Delta I_{pump} = \lambda_{Na}\Delta[Na^+]_i \quad (4.11)$$

and assuming (for simplicity) that the transport rate of KCC2 is independent of $[K^+]_i$ (because $[K^+]_i$ is high and its fractional changes will be small) but varies linearly with $[Cl^-]_i$ as

$$\Delta T_{KCC2} = \lambda_{Cl}.\Delta[Cl^-]_i \quad (4.12)$$

where λ_{Cl} is a constant. Eqns. (4.9) and (4.12) give

$$\Delta[Cl^-]_i = \Delta[Cl^-]_i(t=0).\exp(-t/\tau_{Cl}) \quad (4.13)$$

where $\tau_{Cl} = UF/\lambda_{Cl}$ is the time constant with which KCC2 restores $[Cl^-]_i$ to its initial value. Next I linearize eqns. (4.6) and (4.7) by using (for small concentration changes)

$\Delta V_{Na} = -(RT/F)\ln([Na^+]_{i,new}/[Na^+]_{i,old}) \sim -(RT/F)(\Delta[Na^+]_i/Na_i)$; $\Delta V_K \sim -(RT/F)(\Delta[K^+]_i/K_i)$

where Na_i and K_i are resting values. Eqn. (4.7) then becomes, using eqns. (4.10) and (4.13)

$$UF\ d[Na^+]_i/dt = \Delta[Cl^-]_i(t=0).\exp(-t/\tau_{Cl}).[g_{Na}g_K/(g_{Na}+g_K)].(RT/F)/[K^+]_i$$
$$-\Delta[Na^+]_i\{\ \lambda_{Na}(2g_{Na}+3g_K)/(g_{Na}+g_K) +$$
$$[g_{Na}g_K/(g_{Na}+g_K)].(RT/F).[(1/Na_i)+(1/K_i)]\ \} \quad (4.14)$$

If I define the time constant, τ_{Na}, with which $\Delta[Na^+]_i$ recovers if there is no Cl^- influx, as

$$1/\tau_{Na} = \{ \lambda_{Na}(2g_{Na}+3g_K)/(g_{Na}+g_K) + [g_{Na}g_K/(g_{Na}+g_K)].(RT/F).[(1/Na_i)+(1/K_i)] \}/UF$$

$$\text{then } \Delta[Na^+]_i(t) = C_1.\exp(-t/\tau_{Na}) + C_2.\exp(-t/\tau_{Cl}) \quad (4.15)$$

where C_1 and C_2 are constants set by the boundary condition $C_1+C_2 = \Delta[Na^+]_i(t=0)$ (4.16)

From (4.14) – (4.16)

$$C_2 = \Delta[Cl^-]_i(t=0)\ [g_{Na}g_K/(g_{Na}+g_K)].(RT/F)/\{UF.[K^+]_i.[(1/\tau_{Na})-(1/\tau_{Cl})]\} \quad (4.17)$$

and

$$C_1 = \Delta[Na^+]_i(t=0) - \Delta[Cl^-]_i(t=0).[g_{Na}g_K/(g_{Na}+g_K)].(RT/F)/\{UF.[K^+]_i.[(1/\tau_{Na})-(1/\tau_{Cl})]\} \quad (4.18)$$

The ATP use by the sodium pump is

$$\int_0^\infty \Delta I_{pump}/F\ dt = \int_0^\infty \lambda_{Na}\Delta[Na^+]_i(t)/F = (\lambda_{Na}/F)[C_1\tau_{Na} + C_2\tau_{Cl}] \quad (4.19)$$

Evaluating eqn. (4.19) I find the energy used is the sum of two independent terms, one proportional to the sodium load, $U\Delta[Na^+]_i$, imposed on the cell:

$$U\Delta[Na^+]_i(t=0))/[\ (2g_{Na}+3g_K)/(g_{Na}+g_K) + \{g_{Na}g_K/(g_{Na}+g_K)\}.\{RT/F\}\{(1/Na_i)+(1/K_i)\}/\lambda_{Na}\ ] \quad (4.20)$$

and the other proportional to the chloride load, $U\Delta[Cl^-]_i$:

$$U\Delta[Cl^-]_i(t=o)/\{\lambda_{Cl}.[\{(2g_{Na}+3g_K)/(g_{Na}g_K)\}.K_i/(RT/F) + \{(K_i/Na_i)+1)/\lambda_{Na}\ ]\} \quad (4.21)$$

I first consider the energy expended on pumping out Na^+. The value of λ_{Na} ($dI_{pump}/d[Na^+]_i$ from eqn. 4.11) is set by the sensitivity of the sodium pump to $[Na^+]_i$ changes. If the rate of pumping out of Na^+ is given (in moles/sec) by the Hill equation

$$P_{max}.[Na^+]_i^h/([Na^+]_i^h + EC_{50}^h) \quad (4.22)$$

where P_{max} is the maximum pump rate, EC_{50} is the $[Na^+]_i$ that produces a half-maximal pump rate, and h is the Hill coefficient, then at equilibrium at the resting potential, when $[Na^+]_i = Na_i$,

$$g_{Na}(V_{Na}-V_{rp}) = F.P_{max}.Na_i^h/(Na_i^h + EC_{50}^h)$$

$$\text{so} \qquad P_{max} = g_{Na}(V_{Na}-V_{rp}).(Na_i^h + EC_{50}^h)/(F.Na_i^h) \quad (4.23)$$

The pump current is

$$I_{pump} = (F/3).P_{max}.[Na^+]_i^h/\{[Na^+]_i^h + EC_{50}^h\}$$

so $$\lambda_{Na} = dI_{pump}/d[Na^+]_i = (F/3).P_{max}.EC_{50}^h.h.[Na^+]_i^{h-1}/([Na^+]_i^h + EC_{50}^h)^2 \quad (4.24)$$

Substituting in P_{max} from (4.23) and V_{rp} from (4.3) gives, (with $[Na^+]_i = Na_i$ at the resting potential)

$$\lambda_{Na} = g_{Na}g_K(V_{Na}-V_K).EC_{50}^h.h/\{([Na^+]_i^h + EC_{50}^h).Na_i.(2g_{Na}+3g_K)\} \quad (4.25)$$

Inserting this into (4.20) gives the energy used on Na^+ pumping as

$$\frac{U\Delta[Na^+]_i(t=0))}{[\{(2g_{Na}+3g_K)/(g_{Na}+g_K)\}.\{1+[(RT/hF)/(V_{Na}-V_K)]\{1+(Na_i/K_i)\}.\{1+(Na_i/EC_{50})^h\}]} \quad (4.26)$$

When $Na_i<EC_{50}$, and the sensitivity of the pump to changes in $[Na^+]_i$ is made high by having a very large Hill coefficient, h, this simplifies to

$$U\Delta[Na^+]_i(t=0)).(g_{Na}+g_K)/(2g_{Na}+3g_K) \quad (4.27)$$

which, for a cell with little permeability to Na^+ ($g_{Na}\sim0$) predicts an energy use of

(Na^+ load)/3,

the approximation I use in the rest of the paper. This reflects the fact that one ATP molecule is used to extrude each 3 Na^+ which entered and, although this will result in the import of 33% less K^+ than left the cell, the fact that the membrane is K^+-selective means that the simultaneous passive entry of K^+ that is needed to completely restore the K^+ ions can occur with no significant energy use because the membrane potential is close to the Nernst potential for K^+. Similarly, if the membrane were Na^+-selective ($g_K=0$) eqn. (4.27) predicts that the energy used would be

(Na^+ load)/2, or (K^+ lost)/2

because, after the lost K^+ has been pumped back in with an expenditure of one ATP per 2 K^+ imported, the 50% extra Na^+ which is pumped out will be able to diffuse back in through the membrane Na^+ conductance. Thus, because part of the restoration of ion gradients is achieved by passive diffusion through ion channels, and the contribution of this depends on the membrane's relative permeability to Na^+ and K^+, the ATP expended on pumping also depends on the g_{Na}/g_K ratio. Eqn. (4.27) describes the transition between the extreme values

of 1/3 and 1/2 of the sodium load as the membrane permeability ratio shifts from being K^+-specific to being Na^+-specific.

If the pump is not highly responsive to $[Na^+]_i$ changes, the second term in the denominator of eqn. (4.26) generates a reduction of ATP usage which results from the fact that I am calculating the *change* in usage from its resting value, and the rise in $[Na^+]_i$, fall in $[K^+]_i$ and altered potential decrease the ATP expenditure on reversing the ion fluxes which occur at the resting potential (this term is zero if the sodium pump is extremely sensitive to change of $[Na^+]_i$ (h and $\lambda_{Na} = \infty$) because then the reversal of ion gradients is achieved instantaneously ($\tau_{Na} = 0$) and the duration over which the resting ion fluxes are altered becomes zero). For a pump rate that depends on $[Na^+]_i$ according to eqn. (4.22) with a Hill coefficient (Hasler et al., 1998) of 3 and an EC_{50} (Crambert et al., 2000) of 20 mM, with $[Na^+]_i$ = 20 mM, $[K^+]_i$ = 140 mM, and using the resting and Nernst potentials assumed in the calculations below (which define the ratio of g_{Na} to g_K), this predicts ATP consumption values that are within 1-3% (for neurons) or 5-6% (for glia) of the (Na^+ load)/3 value, and so the latter was used for simplicity.

To assess the energy expended on extruding Cl^- it is convenient to take the ratio of eqns. (4.20) and (4.21) to obtain the ATP usage per Cl^- extruded relative to that per Na^+ pumped, as:

$$(\text{ATP per } Cl^-)/(\text{ATP per } Na^+) = [g_{Na}g_K/(g_{Na}+g_K)].(RT/F)/([K^+]_i.\lambda_{Cl}) \quad (4.28)$$

$$= (1/R_{in}).\{(V_{rp}-V_K)/(V_{Na}-V_K)\}.\{(V_{Na}-V_{rp})/(V_{Na}-V_K)\}.(RT/F)/([K^+]_i.\lambda_{Cl}) \quad (4.29)$$

For a K^+-specific membrane (g_{Na}=0), no energy is needed to extrude Cl^- (because no energy is expended on re-accumulating the K^+ which leaves with the Cl^-), but in general this is not true. To gain insight into the energy needed for Cl^- pumping, note that if g_{Na} is small so that $g_K/(g_K+g_{Na})\sim1$, then the ratio in eqn. (4.28) is the passive Na^+ influx generated by a 60mV driving force (i.e. g_{Na}.RT/F, which is of the same order of magnitude as the pumped Na^+ flux at the resting potential), divided by the current that Cl^- extrusion would generate (for a KCC2 rate proportional to $[Cl^-]_i$) if $[Cl^-]_i$ were equal to $[K^+]_i$ and if pumping out of Cl^- were not

accompanied by K^+ extrusion (i.e. were not electroneutral). This ratio is therefore, roughly, a measure of the ratio of the pumping capacity of the cell for Na^+ to that for Cl^-. A quantitative estimate of this ratio was obtained using data on Cl^- extrusion in neocortical neurons (Jin et al., 2005). After Cl^- loading, into an intracellular volume of $U= 3.2x10^{-15} m^3$, Cl^- was pumped out by KCC2 with a time constant of $\tau_{Cl}= 6.7$ sec. From eqn. (4.13) $\lambda_{Cl} = UF/\tau_{Cl} = 4.6x10^{-11}$ m^3.amps/mole. Using a resting potential (Jin et al., 2005) of -59 mV, and an input resistance (Jin et al., 2005) of 173 MΩ, with V_{Na}=50 mV, V_K=-100 mV and $[K^+]_i$ = 140 mM, eqn. (4.29) gives

$$(\text{ATP per } Cl^-)/(\text{ATP per } Na^+) = 4.8x10^{-3}$$

implying that the cost of extruding each Cl^- is much less than that needed to extrude a Na^+. Assuming that this result can be extended to the cerebellar cells I am considering, I therefore ignored the ATP needed to extrude Cl^- entering during synaptic inhibition (however the ATP used presynaptically at inhibitory synapses, and on action potentials in inhibitory neurons, was calculated, as described in the Results below).

4.3 Results: Detailed energy use calculations for each cell type

The ATP consumption needed to sustain the signalling activity of each cell type in the cerebellar cortex is assessed in the sections below.

4.3.1 Purkinje cells

4.3.1.1 Action potentials

Purkinje cells were treated as a soma of diameter 40 μm (Bordey and Sontheimer, 2003) attached to an axon of diameter 0.66 μm (Roth and Hausser, 2001) that runs for 145 μm through the granular layer (Harvey and Napper, 1988) (energy expended in the white matter was ignored), and to dendrites with a total length of 9.85 mm (Roth and Hausser, 2001) and mean diameter 1.78 μm (Gundappa-Sulur et al., 1999). To calculate the minimal charge entry to produce a single action potential (simple spike) in the cell, the areas of these

cell components were multiplied by the cell capacitance per unit area (see section 4.2.2, above) and by the voltage change occurring during the action potential, i.e. 97 mV for the axon and soma (Vetter et al., 2001) and 12.7 mV for the dendrites (Vetter et al., 2001: (the mean amplitude weighted by the area at each point). This was then multiplied by 4 to give a more realistic value for the Na^+ entry (Hodgkin, 1975, see section 4.2.2, above) and divided by 3 to obtain the ATP consumed to pump this Na^+ out ($7.8x10^7$ ATP molecules). The rate of ATP expenditure on simple spikes was calculated by multiplying this by the simple spike rate (41.3 Hz in awake rats (LeDoux and Lorden, 2002)). Complex spikes evoked by climbing fibre input are longer than simple spikes. In the soma and dendrites they consist of an initial spike of 70-90 mV (Stuart and Hausser, 1994; Monsivais et al., 2005) followed by a prolonged (~13 ms (Monsivais et al., 2005)) depolarization, sometimes with superimposed spikes, with a time-averaged amplitude of ~ 42.7 mV (Stuart and Hausser, 1994; Monsivais et al., 2005). In the axon the complex spike propagates as (on average) 1.7 simple-like spikes, with an assumed amplitude of 97 mV (Monsivais et al., 2005). The Na^+ entry, and hence ATP consumption, for a complex spike was calculated for the axon by assuming it was equivalent to that needed for 1.7 simple spikes. For the soma plus dendrites the ATP needed was calculated from the Na^+ entry needed to produce an initial 80 mV depolarization (calculated as above for the simple spike) plus the synaptic current (860 pA) needed to be injected into an input resistance of 49.5 MΩ (Hausser and Clark, 1997) to produce a 13 ms depolarization (Stuart and Hausser, 1994; Monsivais et al., 2005) of 42.7 mV: this charge entry (assumed for simplicity to be all Na^+) was allotted to the dendrites and soma in proportion to their capacitance. The total ATP usage per complex spike was thus estimated to be $3.4x10^8$ ATP molecules. Complex spikes occur at a rate of ~1 Hz in awake rats (Lang et al., 1999).

4.3.1.2 Resting potential

The ATP usage needed to maintain the resting potential ($1.76x10^9$ ATP/sec) was calculated from eqn. 4.4, using a resting input resistance (Hausser and Clark, 1997) of 49.5

MΩ (assumed to reflect the properties of the whole cell in the cerebellar cortex) and resting potential of -53 mV. (This resting potential is a time-weighted average over "up" and "down" states (Loewenstein et al., 2005), and ignores the fact that switching to "up" states may be produced by excitatory input, the energy use on which is calculated below; if the resting potential were set to -70 mV the ATP used to maintain it would be reduced by 22%, and the total predicted energy expenditure by the cell would be reduced by 3.3%). This energy usage was partitioned among the different cerebellar layers in proportion to the capacitance of the cell in each layer, i.e. by assuming for simplicity that the input resistance reflects a uniform conductance all over the cell membrane.

4.3.1.3 AMPA receptor current at the parallel fibre synapse

Na^+ entry per vesicle released at parallel fibre synapses was calculated from the 6 pA value (Marcaggi and Attwell, 2005) for (single vesicle current)x(1-release probability in 3 mM $[Ca^{2+}]_o$) using a release probability in 3 mM $[Ca^{2+}]_o$ of 0.48 (Marcaggi et al., 2003). It was then corrected from a holding potential of -70 mV to a resting potential of -53 mV as described above and corrected to 37°C by a factor of 1.4 (Marcaggi et al., 2003); this was then multiplied by a decay time constant of 4 ms (Marcaggi et al., 2003), corrected to 37°C by a factor of 2.5/3.3 (Marcaggi et al., 2003), to obtain an entry of $3x10^5$ Na^+. To calculate the total Na^+ entry from all 174,000 parallel fibres (Napper and Harvey, 1988), this Na^+ entry was multiplied by the number of fibres, by a release probability (Marcaggi et al., 2003) of 0.36 (for 2 mM $[Ca^{2+}]_o$) assuming there is only one release site/fibre, and by the fraction of parallel fibres which actually generate functional synapses in adult rat (0.15 (Isope and Barbour, 2002), see section 4.5.6, below on sensitivity of the predictions to the parameters assumed), and by the frequency of firing of granule cells. The mean granule cell firing rate (which may vary in different cerebellar regions dealing with different sensory afferents) is not well defined by papers in the literature. Sensory input evokes bursts of granule cell firing (at least in anaesthetised rats), with whisker stimulation typically generating 3.3 action potentials

at a mean frequency of 77 Hz (Chadderton et al., 2004): how often this activation occurs during normal movement is unknown, but most movements should activate granule cells e.g. as a result of air movement stimulating skin hairs. Experiments on decerebrate cat granule cells (Jorntell and Ekerot, 2006) show that granule cells controlling the forelimb that receive cutaneous input from the cuneate nucleus do not fire in the absence of sensory input, whereas those receiving proprioceptive input from the cuneate area, or somatosensory input and motor cortical output from the lateral reticular nucleus, fire tonically at up to 20 Hz. With uncertainty over the mean firing rate, I set the mean rate at 6 Hz in order to reproduce the measured energy expenditure on action potential driven processes (as described above). I also explored the consequences of varying this rate (see section 4.4.3, below).

4.3.1.4 mGluR activation at the parallel fibre synapse

Each vesicle released was assumed to require 3000 ATP to reverse Ca^{2+} release from internal stores evoked by G protein coupled receptors (Attwell and Laughlin, 2001). The data of Marcaggi et al. (2005) imply that releasing a vesicle from a single parallel fibre synapse 10 times evokes an mGluR-mediated current (assumed for simplicity to be generated by a channel permeable to Na^+ and K^+ with a reversal potential of 0mV) of $1.13x10^4$ ions, calculated (assuming a constant release probability and one release site per parallel fibre) as (amplitude of 34 fA from Fig. 2f of Marcaggi and Attwell (2005))/10 vesicles/(release probability in 3 mM $[Ca^{2+}]_o$ of 0.48 (Marcaggi et al., 2003))x(effective duration of 317 ms from Fig. 2a of Marcaggi and Attwell (2005) at 27°C, which becomes 186 ms at 37°C) and then corrected from a holding potential of -70mV to the resting potential of -53 mV as above. For a single action potential, and a release probability of 0.36 in 2 mM $[Ca^{2+}]_o$, this becomes 4068 ions, corresponding to 1356 ATP used. The total ATP used/vesicle on mGluR signalling is therefore 4356 (3000 + 1356) molecules.

4.3.1.5 AMPA receptor current at the climbing fibre synapse

Activating the climbing fibre evokes an influx of $6.7x10^8$ Na^+ ions, requiring $2x10^8$ ATP molecules to be pumped out. This was calculated for the resting potential of -53 mV from the 200 nS conductance measured (Silver et al., 1998) at postnatal day 12-14 using 0.2 Hz stimulation (decreased by a factor of 1.47 to correct to the 1 Hz occurrence rate of complex spikes from Fig. 7 of Silver et al. (1998), adjusted to 37°C with a Q_{10} of 1.4, and increased by a factor of 1440/510 to correct for the larger number of release sites (Strata and Rossi, 1998) in adult climbing fibres), and the decay time constant of 3.17 ms (measured at postnatal day 8-16 at 35°C, corrected to 37°C as above). All the climbing fibre Na^+ entry was assumed to occur in the molecular layer. There is no significant mGluR activation normally at the climbing fibre synapse (Tempia et al., 1998).

4.3.1.6 Glutamate recycling

Of the glutamate released at the climbing and parallel fibre synapses, 17% is assumed to be taken up by transporters in the Purkinje cell (Brasnjo and Otis, 2004), and the remainder is presumably taken up into Bergmann glia. Since each vesicle requires 11,000 ATP to recycle its glutamate (Attwell and Laughlin, 2001), the 56,376 vesicles released/sec from the parallel fibres/sec (calculated as (174,000 fibres (Napper and Harvey, 1988)) x (release probability (Marcaggi et al., 2003) of 0.36) x (fraction (0.15) of parallel fibres which actually generate functional synapses in adult rat (Isope and Barbour, 2002))) x (6 Hz frequency of firing of granule cells, see above) therefore need $6.2x10^8$ ATP/sec for recycling. (If the non-function of 85% of parallel fibre synapses (Isope and Barbour, 2002) responsible for the factor 0.15 were produced by an absence of postsynaptic receptors, and glutamate was still released, then the glutamate recycling cost for parallel fibres would increase by a factor of 1/0.15, but would still only be 5% of the total Purkinje cell energy use). For the climbing fibres, the 4680 vesicles released/second (3.25 vesicles per release site (Brasnjo and Otis, 2004) multiplied by 1440 release sites in adult (Strata and Rossi, 1998)) require a total of

$5.15x10^7$ ATP/sec to recycle. Of the energy used for recycling, 87.5% of it is used in the cell taking the glutamate up, and the remaining 12.5% is used in the presynaptic cell to which the glutamate is recycled (Attwell and Laughlin, 2001). Thus, of this total ATP consumption, 0.875x17% =15% is used in Purkinje cells, 0.875x83% = 72.6% is used in Bergmann glia, and the rest is used in the presynaptic parallel and climbing fibre terminals.

4.3.1.7 Scaling to whole cerebellum

After summing the ATP usage on all the cellular processes contributing to signalling, the sum was converted to an energy use per m^2 of cerebellar cortex, using the fact that there are $1.02x10^9$ Purkinje cells per m^2 (Harvey and Napper, 1988).

4.3.2 Granule cells

4.3.2.1 Action potentials

Granule cells were treated as a 6 μm diameter soma (Palay and Chan-Palay, 1974), attached to 4 dendrites (Eccles, Ito, and Szentagothai, 1967) of length (Berends et al., 2004) 13.6 μm and diameter 1 μm (Fiala and Harris, 1999), and to an axon which (on average) runs for 226.5 μm (Harvey and Napper, 1988) (72.5 μm across half the granular layer, 40 μm across the Purkinje cell layer, and 114 μm across half the molecular layer) before bifurcating into a parallel fibre running 2.2 mm in either direction (Berends et al., 2004), of diameter 0.17 μm (Wyatt et al., 2005). The energy expended on pumping out the Na^+ generating each action potential was calculated as above, using an action potential amplitude (D'Angelo et al., 1997) of 100 mV throughout the axon, soma and dendrites, and gave a usage of $1.8x10^7$ ATP per action potential, 89% of which was consumed in the axon. As discussed above, the mean granule cell firing rate is uncertain, so it was initially set at 6 Hz. The effect was also explored of changes in this value (see section 4.4.3 and Fig. 4.4a).

4.3.2.2 Resting potential

The input resistance of granule cells at the soma is 1.1 GΩ (Chadderton et al., 2004), which I took to represent the resting conductance of the soma, dendrites and the part of the axon in the granular layer (assuming, simplistically, that the rest of the axon is too electrotonically distant to contribute to the soma input resistance). For a resting potential of -64 mV (Chadderton et al., 2004), eqn. 4.4 predicts usage of 6.9×10^7 ATP/sec. The rest of the axon has an area 7.5 fold larger than the area of the soma, dendrites and part of the axon in the granular layer. To estimate the ATP used to maintain the resting potential in this part of the cell, I used the measured space constant of hippocampal mossy fibre axons (Alle and Geiger, 2006), to calculate the specific membrane resistance of the axon. The total granule cell axon membrane resistance was then calculated as 3.02×10^9 Ω, for an axon of 4.5 mm length (40 μm across the Purkinje cell layer, 114 μm across half the molecular layer and 2.2 mm in either direction (Berends et al., 2004)) and diameter (Wyatt et al., 2005) 0.17 μm. For this resistance, and a resting potential of -64 mV, eqn. 4.4 predicts usage of 2.5×10^7 ATP/sec. (The membrane resistivity calculated in this way was 20.7-fold higher than that obtained for the soma and dendrites by using the input resistance at the soma: if the axon had the same properties as the membrane contributing to the input resistance measured at the soma, then the energy use of individual granule cells would be dominated by the cost of maintaining the axonal resting potential, and 64% of the signalling energy consumption of the whole cerebellar cortex would be used on this).

4.3.2.3 AMPA and NMDA receptor current at the mossy fibre synapse

The Na^+ entry via AMPA receptors when a vesicle is released at the mossy fibre synapse is 9.4×10^4 ions (calculated from Silver et al. (1996b) and Silver et al. (1996a) as in Attwell and Laughlin (2001), but corrected for the K^+ component of the current and adjusted to a resting potential of -64 mV as above). Mossy fibres fire at ~ 40 Hz (Maex and De Schutter, 1998), and release vesicles with a release probability of 0.48 from a mean of 4.7

release sites on each of the 4 granule cell dendrites (Sargent et al., 2005), giving a total release of 361 vesicles onto each granule cell/second and a corresponding ATP usage per second on pumping out the Na^+ entering through AMPA receptors of $1.13x10^7$ ATP molecules. The corresponding ATP consumption on extruding Na^+ and Ca^{2+} entering through NMDA receptors was calculated as in Attwell and Laughlin (2001) from the ratio of charge transfer in the NMDA and AMPA components of the synaptic current (assuming Mg^{2+}-block reduces NMDA receptor current 4.4-fold at -70 mV at cerebellar synapses (Jahr and Stevens, 1990)) and found to be $1.07x10^7$ ATP/sec.

4.3.2.4 Presynaptic ATP use on vesicle release and recycling

This was calculated for 56,376 vesicles released per second at the parallel fibre synapses onto one Purkinje cell (see above) by noting that each vesicle released requires an ATP expenditure of 12,000 molecules to reverse the Ca^{2+} entry controlling exocytosis, 21 molecules for the activation energy of vesicle membrane fusion with the plasma membrane, 400 molecules to control endocytosis and 400 to control exocytosis (Attwell and Laughlin, 2001). This usage was apportioned to single granule cells by scaling from the area density of Purkinje cells (Harvey and Napper, 1988) ($1.02x10^9/m^2$) to that of granule cells ($2.79x10^{11}$ $/m^2$, calculated from the density of Purkinje cells above and the fact that there are 274 granule cells / Purkinje cell (Harvey and Napper, 1988)). In addition, presynaptic ATP use at the parallel fibre to stellate, basket and Golgi cells was calculated in a similar manner and allotted to granule cells (details of energy use at these synapses are given in the section for each postsynaptic cell below).

4.3.2.5 Presynaptic ATP use on glutamate recycling

This was calculated as described above for the synapses onto Purkinje cells, and as described below for the synapses onto inhibitory interneurons.

4.3.2.6 Scaling to whole cerebellum

After summing the ATP usage on all the cellular processes contributing to signalling, the sum was converted to an energy use per m^2 of cerebellar cortex, using the area density of granule cells of $2.79x10^{11}/m^2$ given above (Harvey and Napper, 1988).

4.3.3 Mossy fibres

4.3.3.1 Resting potential

Energy expenditure on the resting potential was calculated from a total membrane resistance of 108 GΩ, which was derived from the hippocampal space constant, as for the granule cell axon above, using a fibre diameter (Shinoda et al., 1992) of 0.3 μm and length of 72.5 μm (half the width of the granular layer).

4.3.3.2 Action potential

Energy expenditure on the action potential was calculated as described in section 4.2.2, assuming a voltage change of 100 mV, using the dimensions above, and a firing rate of 40 Hz (Maex and De Schutter, 1998).

4.3.3.3 Glutamate recycling

The glutamate released at the mossy fibre synapses was assumed to be taken up into astrocytes for recycling to mossy fibre terminals. Per granule cell, the resulting energy cost to mossy fibres (expended on repackaging glutamate into vesicles) is 12.5% of the total recycling cost of 11,000 ATP/vesicle released (Attwell and Laughlin, 2001), multiplied by the 361 vesicles released/second onto each granule cell. This was converted to a cost per mossy fibre by scaling by the ratio of the densities of granule cells ($2.79x10^{11}/m^2$, see above) and mossy fibres ($4.07x10^{9}/m^2$, calculated from the density of Purkinje cells above and the fact that there are 4 mossy fibres/Purkinje cell (in cat: Ito, 1984)).

4.3.3.4 Presynaptic ATP use

For one granule cell 361 vesicles are released/sec from the mossy fibres (see above). Each vesicle released requires an ATP expenditure of 12,000 molecules to reverse the Ca^{2+} entry controlling exocytosis, 21 molecules for the activation energy of vesicle membrane fusion with the plasma membrane, 400 molecules to control endocytosis and 400 to control exocytosis (Attwell and Laughlin, 2001). This usage was scaled to the value for a single mossy fibre by scaling from the area density of granule cells to that of mossy fibres (which was calculated as $4.07 \times 10^9/m^2$ from the density of Purkinje cells and the ratio of the number of mossy fibres to the number of Purkinje cells (in cat: Ito, 1984). A similar calculation was done for the mossy fibre to Golgi cell synapses.

4.3.4 Climbing fibres

4.3.4.1 Resting potential

Energy expenditure on the resting potential was calculated from a total membrane resistance of 17.5 GΩ, which was derived from the hippocampal space constant as for the granule cell axon above, using a fibre diameter (van der Want et al., 1985) of 0.45 μm and length of 299 μm (the 145 μm width of the granular layer plus the 40 μm width of the Purkinje cell layer plus half the 228 μm width of the molecular layer). Expenditure was allocated to the different layers in proportion to the membrane area in each layer.

4.3.4.2 Action potential

Energy expenditure on the action potential was calculated as described in section 4.2.2, assuming a voltage change of 100 mV, using the dimensions above. Expenditure was allocated to the different layers in proportion to the membrane area in each layer.

4.3.4.3 Glutamate recycling

The glutamate released at the climbing fibre synapses was assumed to be taken up into Bergmann glia and Purkinje cells for recycling to climbing fibre terminals (energy use on this is dealt with in the sections on Bergmann glia and Purkinje cells). Per Purkinje cell, the resulting energy cost to climbing fibres (expended on repackaging glutamate into vesicles) is 12.5% (Attwell and Laughlin, 2001) of the total recycling cost of 11,000 ATP/vesicle released (Attwell and Laughlin, 2001), multiplied by the 4680 vesicles released/second (see above) onto each Purkinje cell. This was converted to a cost per climbing fibre by assuming that effectively one climbing fibre projects to each Purkinje cell (although in fact each olivary neuron innervates 7 Purkinje cells I consider only the part of the fibre within the cerebellar cortical grey matter as a single climbing fibre). All of this energy was allocated to the molecular layer.

4.3.4.4 Presynaptic ATP use

For each climbing fibre 4680 vesicles are released/sec (see above), each of which requires an ATP expenditure of 12,000 molecules to reverse the Ca^{2+} entry controlling exocytosis, 21 molecules for the activation energy of vesicle membrane fusion with the plasma membrane, 400 molecules to control endocytosis and 400 to control exocytosis (Attwell and Laughlin, 2001). All of this energy was allocated to the molecular layer.

4.3.5 Bergmann glia

4.3.5.1 Resting potential

The ATP usage needed to maintain the resting potential (2.19×10^8 ATP/sec) was calculated from eqn. 4.4, using an input resistance of 213 MΩ (calculated assuming that a 61 MΩ input resistance (Clark and Barbour, 1997) (subtracting a 9 MΩ series resistance (Clark and Barbour, 1997)) reflects one central cell coupled to 7 more through coupling resistances (Clark and Barbour, 1997) of 385 MΩ) and a resting potential (Clark and Barbour, 1997) of

-82 mV. Energy use in Bergmann glia was assigned to the molecular layer, although the somata merge slightly into the Purkinje cell layer (Clark and Barbour, 1997).

4.3.5.2 Glutamate recycling

The ATP cost to a Bergmann glial cell of recycling glutamate released at the parallel and climbing fibre synapses ($1.03x10^8$ ATP/sec) was calculated from the values obtained above for the cost of uptake of glutamate into Purkinje cells, multiplied by a factor of 4.88 (the ratio of the amount of uptake into Bergmann glia to that into Purkinje cells (Brasnjo and Otis, 2004)), and then scaled to the value for a single Bergmann glial cell using the fact that there are 4.75 Bergmann glia per Purkinje cell (Legrand et al., 1983). The ATP cost of recycling glutamate released at the parallel fibre to stellate/basket/Golgi cell synapses ($4.83x10^7$ ATP/sec) was calculated from the values obtained for the cost of uptake of glutamate into these cells, multiplied by a factor of 7.02 (the ratio of the amount of uptake into Bergmann glia to that into granule cells (Attwell and Laughlin, 2001)) and then scaled to the value for a single Bergmann glial cell using the fact that there are $1.73x10^{-2}$ Bergmann glia per granule cell (assuming there are 4.75 Bergmann glia per Purkinje cell (Legrand et al., 1983)).

4.3.5.3 Scaling to whole cerebellum

After summing the ATP usage on all cellular processes, the sum was converted to an energy use per m^2 of cerebellar cortex, using an area density for Bergmann glia of granule cells of $4.84x10^9/m^2$ calculated from the Purkinje cell density and the fact that there are 4.75 Bergmann glia per Purkinje cell (Legrand et al., 1983).

4.3.6 Astrocytes

4.3.6.1 Resting potential

The ATP usage needed to maintain the resting potential ($1.01x10^8$ ATP/sec) was calculated from eqn. 4.4, using an assumed input resistance (Attwell and Laughlin, 2001) of 500 MΩ and resting potential (Attwell and Laughlin, 2001) of -80 mV.

4.3.6.2 Glutamate recycling

The ATP cost to an astrocyte of recycling glutamate released at the mossy fibre-granule cell synapses ($1.62x10^8$ ATP/sec) was calculated by multiplying the number of vesicles released onto one granule cell (361/sec, see above) by the total ATP cost of recycling one vesicle (11,000 ATP (Attwell and Laughlin, 2001)) and by the fraction of that cost which is incurred in the cell taking the glutamate up (0.875 (Attwell and Laughlin, 2001)), and then scaling to the value for a single astrocyte using the fact that there are 45 granule cells per astrocyte (deduced from a density, in mouse, of 2142 astrocytes/mm^2 in 50 μm sections (Delaney et al., 1996), corresponding to a volume density of $4.28x10^4$ /mm^3, and thus to an area density in a 145 μm thick (Harvey and Napper, 1988) granular layer of $6.2x10^9$ /m^2, which is 45-fold less than the granule cell density). Glutamate recycling at the mossy fibre to Golgi cell synapse is dealt with in the Golgi cell section below.

4.3.7 Stellate cells

There is debate in the literature over whether stellate and basket cells can be absolutely distinguished (Sultan and Bower, 1998); I treated all the interneurons in the upper half of the molecular layer as being stellate cells, and those in the lower half to be basket cells and assumed that the area density of interneurons in each half was the same. Where necessary, as described below, if parameters have not been measured for one cell type, I used values measured for the other cell type.

4.3.7.1 Action potentials

Stellate cells were treated as a soma of diameter (Auger et al., 1998) 8 μm, attached to 3.1 (Sultan and Bower, 1998) dendrites of mean diameter 0.55 μm (Sultan and Bower, 1998) and total length 1189 μm (Sultan and Bower, 1998), and a 1393 μm long axon (Sultan and Bower, 1998) of diameter 2 μm (the value for basket cells (Palay and Chan-Palay, 1974)). Energy expenditure on the action potential was calculated as described in the section above on Choosing parameters from the literature (section 4.2.2), assuming a voltage change of 100 mV throughout the cell, using these dimensions, and multiplied by a mean firing rate (Hausser and Clark, 1997) of 12.3 Hz to obtain an expenditure on action potentials of 8.7×10^8 ATP/sec.

4.3.7.2 Resting potential

The ATP usage needed to maintain the resting potential (3.77×10^8 ATP/sec) was calculated from eqn. 4.4, using an input resistance (Loewenstein et al., 2005) of 224 MΩ and resting potential (Loewenstein et al., 2005) of -56 mV.

4.3.7.3 AMPA receptor current and mGluR effects at the parallel fibre to stellate cell synapse

Na^+ entry per vesicle released at parallel fibre synapses was calculated as 4.52×10^5 ions from the mEPSC amplitude and half-decay time of 79 pA and 0.57 ms measured (Carter and Regehr, 2002) at 34°C, corrected to 37°C using a Q_{10} of 1.7 for the decay time (Marcaggi et al., 2003), and a factor of 1.4 for the amplitude (Marcaggi et al., 2003), and with the amplitude corrected for K^+ movement and to the resting potential as described above. Stellate cells receive 1500 synaptic boutons from parallel fibres (Harvey and Napper, 1991), with a release probability (Rancillac and Barbara, 2005) of ~0.72, so that for granule cells firing at 6 Hz 6480 vesicles are released onto the stellate cells per sec (I ignore, for simplicity, the possibility that only a small fraction of the synapses are active, as occurs for transmission to

Purkinje cells (Isope and Barbour, 2002)). Multiplying this by the ATP needed to pump out the Na^+ entering/vesicle, I find $9.76x10^8$ ATP/sec are expended on the effects of AMPA receptor activation. Metabotropic glutamate receptor activation was treated assuming that each vesicle released requires 3000 ATP to reverse the intracellular Ca^{2+} release produced (Attwell and Laughlin, 2001); the mGluR-activated current (Karakossian and Otis, 2004), and activation of NMDA receptors, that can be produced by stimulating many adjacent synapses (Clark and Cull-Candy, 2002) are unlikely to occur in vivo when the synaptic input to Purkinje cells is likely to be spatially dispersed (Marcaggi and Attwell, 2005), and so they were neglected here.

4.3.7.4 Glutamate recycling at the parallel fibre to stellate cell synapse

The glutamate in the 6480 vesicles released/sec onto each stellate cell was assumed to be recycled at a total cost of 11,000 ATP/vesicle (Attwell and Laughlin, 2001), with 87.5% of the cost being expended in the Bergmann glia that take the glutamate up and 12.5% in the presynaptic parallel fibre terminals when the glutamate is repackaged into vesicles (Attwell and Laughlin, 2001). These costs were adjusted to the ATP usage per granule cell or Bergmann glial cell using a density for stellate cells of $1.22x10^9/m^2$ (the same as for basket cells, i.e. 15-20% higher than that of Purkinje cells (Eccles, Ito, and Szentagothai, 1967)).

4.3.7.5 Presynaptic ATP use at the parallel fibre to stellate cell synapse

This was calculated for the 6480 vesicles released per second at the parallel fibre synapses onto one stellate cell (see above) by noting that each vesicle released requires an ATP expenditure of 12,000 molecules to reverse the Ca^{2+} entry controlling exocytosis, 21 molecules for the activation energy of vesicle membrane fusion with the plasma membrane, 400 molecules to control endocytosis and 400 to control exocytosis (Attwell and Laughlin, 2001). This usage was apportioned to single granule cells by scaling from the area density of stellate cells to that of granule cells.

4.3.7.6 Presynaptic ATP use at the stellate cell to Purkinje cell synapse

Each stellate cell has an average of 149 output boutons (Sultan and Bower, 1998) onto Purkinje cells. Assuming there is a single release site from one stellate cell to a given Purkinje cell (there is no information in the literature on this), measurement of transmission failures suggests the release probability (at room temperature) is 0.67 (Pouzat and Hestrin, 1997). For a stellate firing rate (Hausser and Clark, 1997) of 12.3 Hz this gives a release of 1,228 vesicles of GABA per stellate cell. The ATP use needed to release and recycle these vesicles was calculated using the ATP expenditures per vesicle listed in the previous paragraph.

4.3.7.7 GABA recycling at the stellate to Purkinje cell synapse

It was assumed that the 1228 vesicles/sec of released GABA was taken up into the releasing terminals by presynaptic GAT1 transporters, and recycled at an energy cost (calculated for glutamate (Attwell and Laughlin, 2001) of 11,000 ATP/vesicle) of 1.35×10^7 ATP/sec.

4.3.7.8 Stellate-stellate cell synapses

Each stellate cell receives on average 4.25 synapses (Kondo and Marty, 1998) from other stellate cells, which each release ~1.3 vesicles (Auger et al., 1998) with a probability (Kondo and Marty, 1998) of ~0.315. Postsynaptic energy use on pumping back Cl^- ions at these synapses was neglected because it is so small (see section 4.2.8 on the energy needed to restore ion movements). The presynaptic ATP use on vesicle recycling and the GABA recycling energy cost were calculated as in the preceding sections, and together they were only 0.02% of the cell's total energy use.

4.3.7.9 Scaling to whole cerebellum

After summing the ATP usage on all the cellular processes contributing to signalling, the sum was converted to an energy use per m^2 of cerebellar cortex, using an area density for stellate cells that was 20% higher than for Purkinje cells (Eccles, Ito, and Szentagothai, 1967), i.e. $1.22 \times 10^9/m^2$.

4.3.8 Basket cells

4.3.8.1 Action potentials

Basket cells were treated as a soma of diameter (Southan and Robertson, 1998) 12.5 μm, attached to dendrites of mean diameter 1 μm (Llano et al., 1997) and total length 338 μm (from Fig. 5A of Llano et al. (1997)), and a 500 μm long axon (Ito, 1984) of diameter (Palay and Chan-Palay, 1974) 2 μm. Energy expenditure on the action potential was calculated as described in section 4.2.2, assuming a voltage change of 100 mV, using these dimensions, and multiplied by a mean firing rate (Hausser and Clark, 1997) of 12.3 Hz to obtain an expenditure on action potentials of 3.7×10^8 ATP/sec. To apportion this usage to the cerebellar layers, half the axon was assumed to lie in the molecular layer and half in the Purkinje cell layer (Fig. 2 of Southan and Robertson (1998)), and the rest of the cell in the molecular layer.

4.3.8.2 Resting potential

The ATP usage needed to maintain the resting potential (3.77×10^8 ATP/sec) was calculated from eqn. 4.4, using an input resistance (Loewenstein et al., 2005) of 224 MΩ and resting potential (Loewenstein et al., 2005) of -56 mV.

4.3.8.3 AMPA receptor current and mGluR effects at the parallel fibre to basket cell synapse

These were calculated exactly as at the parallel fibre to stellate cell synapse.

4.3.8.4 Glutamate recycling at the parallel fibre to basket cell synapse

This was calculated exactly as at the parallel fibre to stellate cell synapse to calculate the ATP use in Bergmann glia and granule cell (parallel fibre) terminals.

4.3.8.5 Presynaptic ATP use at the parallel fibre to basket cell synapse

This was calculated as at the parallel fibre to stellate cell synapse to calculate the ATP used in granule cell (parallel fibre) terminals.

4.3.8.6 Presynaptic ATP use at the basket cell to Purkinje cell synapse

This was calculated as at the stellate cell to Purkinje cell synapse, except that a release probability of 0.96 was assumed, based on the failure rate seen by Galante and Marty (2003) for basket cell to Purkinje cell transmission and assuming simplistically that there is only one release site from each stellate cell onto a Purkinje cell. This energy use was allotted to the Purkinje cell layer (reflecting the location of the output synapses from basket cells on the initial segment of the Purkinje cell axon where it leaves the Purkinje cell soma).

4.3.8.7 GABA recycling at the basket cell to Purkinje cell synapse

This was calculated as at the stellate cell to Purkinje cell synapse, except that a release probability of 0.96 was assumed, and was allotted to the Purkinje cell layer.

4.3.8.8 Basket-basket and stellate-basket cell synapses

These were ignored because of an absence of electrophysiological data and because the calculated energy use of stellate-stellate cell synapses was completely negligible (see above).

4.3.8.9 Scaling to whole cerebellum

After summing the ATP usage on all the cellular processes contributing to signalling, the sum was converted to an energy use per m^2 of cerebellar cortex, using an area density for basket cells that was 20% higher than for Purkinje cells (Eccles, Ito, and Szentagothai, 1967), i.e. $1.22 \times 10^9/m^2$.

4.3.9 Golgi cells

4.3.9.1 Action potentials

Golgi cells were treated as a soma of diameter 25.8 μm (the mean of the values in Dieudonne (1998) and Misra et al. (2000)), attached to dendrites of mean diameter 1 μm (Dieudonne, 1998) and total length 1350 μm (from Fig. 1 of Misra et al. (2000)), and a 3190 μm long axon (calculated from the charge transfer of the axonal capacity transient in Dieudonne (1998), assuming a diameter of 1 μm). No information is available in the literature on how the action potential spreads through the Golgi cell dendritic tree, so the energy expenditure on the action potential was calculated as described in section 4.2.2, assuming a voltage change of 100 mV, using these dimensions, and multiplied by a mean firing rate of 10 Hz (the mean of the active and resting rates in Vos et al. (1999)), to obtain an expenditure on action potentials of 1.05×10^9 ATP/sec. To apportion this usage to the cerebellar layers, 45% of the dendrites were assumed to lie in the molecular layer, 10% in the Purkinje cell layer and 45% in the granular layer, with the soma and axon being entirely in the granular layer (Fig. 1 of Misra et al. (2000)).

4.3.9.2 Resting potential

I assumed a resting potential of -65 mV, in the middle of the pacemaking range of these cells (Forti et al., 2006), and an input resistance of 522 MΩ (Forti et al., 2006). This gave an energy consumption on the resting potential of 1.4×10^8 ATP/sec.

4.3.9.3 AMPA receptor current at the parallel fibre to Golgi cell synapse

Single vesicles released from parallel fibres evoke an AMPA receptor current of ~30 pA at +61 mV and 25°C (Dieudonne, 1998). Converting this to -69 mV using a rectification index of 0.49 (Dieudonne, 1998), adjusting the amplitude to 37°C with a Q_{10} of 1.4, and correcting for the K^+ component of the current and to the assumed resting potential of -64 mV as described above, gives an amplitude of 97 pA. Since the current decay time constant was 1.06 ms at 25°C, giving 0.56 ms when corrected to 37°C using a Q_{10} of 1.7, this leads to a Na^+ entry of 3.41×10^5 ions per vesicle. Each Golgi cell was assumed to receive input from 4788 (Pellionisz and Szentagothai, 1973) parallel fibres (I ignore, for simplicity, the possibility that only a small fraction of the synapses are active, as occurs for transmission to Purkinje cells (Isope and Barbour, 2002)), with a release probability of 0.72 as for stellate cells (Rancillac and Barbara, 2005), so that 20684 vesicles are released/sec, giving a total ATP used on reversing the resulting Na^+ entry of 2.35×10^9/sec for parallel fibres firing at 6 Hz.

4.3.9.4 NMDA receptor current at the parallel fibre to Golgi cell synapse

Na^+ and Ca^{2+} entry via NMDA receptors at the parallel fibre to Golgi cell synapse were calculated using a weighted time constant for the current (adjusted to 37°C) of 28 ms (Dieudonne, 1998), and an amplitude for the current derived as follows. The amplitude at +61 mV is ~15 pA (Dieudonne, 1998), giving an inward current of 17 pA at -69 mV (at 25°C), which was then corrected to 37°C using a Q_{10} of 1.4 (Marcaggi et al., 2003), and corrected for K^+ entry and to a resting potential of -64 mV. Then Mg^{2+} block of the current was assumed to reduce the current 60-fold, based on the synapses expressing NMDA receptors composed of NR1 and NR2B subunits (Misra et al., 2000). The resulting current amplitude was 0.46 pA. This was divided between Na^+ and Ca^{2+} assuming the same relative permeability as for the receptors at the mossy fibre to granule cell synapse (see above), and used to calculate the ATP needed to pump out the Na^+ and Ca^{2+}, which was approximately 3×10^4 ATP/vesicle released, giving an ATP expenditure on NMDA receptors of 5.78×10^8/sec.

4.3.9.5 mGluR activation at the parallel fibre to Golgi cell synapse

Release of each vesicle was assumed to require 3000 ATP to reverse its effects (Attwell and Laughlin, 2001).

4.3.9.6 Glutamate recycling at the parallel fibre to Golgi cell synapse

The glutamate in the 20684 vesicles released onto Golgi cells/sec was assumed to be taken up into Bergmann glia, and recycled to parallel fibre terminals. The total energy cost/vesicle is 11,000 ATP molecules, split 87.5% in the Bergmann glia and 12.5% in the parallel fibre terminals (Attwell and Laughlin, 2001). These costs were allocated to each Bergmann glial cell and granule cell by scaling by the density of those cells relative to that of Golgi cells (calculated as $4.07 \times 10^8 /m^2$, from a mean volume density of 985.48 $/mm^3$ (Lange, 1974) using the fact that the cerebellar cortex is 413 μm wide (Harvey and Napper, 1988; Bordey and Sontheimer, 2003)).

4.3.9.7 Presynaptic ATP use at the parallel fibre to Golgi cell synapse

This was calculated as for the parallel fibre to stellate cell synapse, except using the number of vesicles released/sec onto Golgi cells and using the Golgi cell density to convert to a value per granule cell.

4.3.9.8 AMPA receptor current at the mossy fibre to Golgi cell synapse

Stimulating a single mossy fibre evokes an AMPA receptor mediated current (but no NMDA or mGluR mediated current) in the Golgi cell with a mean amplitude at -68 mV of 66 pA, and a weighted decay time constant of 1.14 ms (Kanichay and Silver, 2007) (all at 35°C). Correcting to 37°C as above, correcting the amplitude for K^+ efflux and to the resting potential of -64 mV as above, and multiplying by the estimated (Pellionisz and Szentagothai, 1973) 228 mossy fibres that are believed to project to each Golgi cell, for a mossy fibre firing

rate (Maex and De Schutter, 1998) of 40Hz this requires $1.71x10^9$ ATP/sec to pump out the Na^+ entering. NMDA and mGluR components of the mossy fibre to Golgi cell EPSC have not been reported.

4.3.9.9 Glutamate recycling at the mossy fibre to Golgi cell synapse

The 228 mossy fibres contacting each Golgi cell were assumed to have two release sites with a release probability of 0.5 (Kanichay and Silver, 2007 and personal communication). For a firing rate of 40 Hz (Maex and De Schutter, 1998), therefore, 9120 vesicles will be released/sec onto each Golgi cell. The glutamate in these vesicles was assumed to be taken up into astrocytes, and recycled to the mossy fibre terminals. The total energy cost/vesicle is 11,000 split 87.5% in the astrocytes and 12.5% in the mossy fibre terminals. These costs were allocated to each astrocyte and mossy fibre by scaling by the density of those cells relative to that of Golgi cells.

4.3.9.10 Presynaptic ATP use at the mossy fibre to Golgi cell synapse

This was calculated as for the mossy fibre to granule cell synapse, except using the number of vesicles released/sec onto Golgi cells and using the mossy fibre density to convert to a value per mossy fibre.

4.3.9.11 Presynaptic ATP use at the Golgi cell to granule cell synapse

Each granule cell receives synaptic input from its 4 nearest Golgi cells (Volny-Luraghi et al., 2002), so the number of Golgi to granule cell inputs per Golgi cell is given by 4x(the number of granule cells)/(the number of Golgi cells), where the number of Golgi cells was calculated from the ratio of the densities of Golgi cells (Lange, 1974) to Purkinje cells (Harvey and Napper, 1988) x (the number of Purkinje cells). Each input has on average 2.6 release sites (Jakab and Hamori, 1988), with a release probability of 0.387 (based on the

failure rate seen by Farrant and Brickley (2003)). Presynaptic ATP use was calculated, using these parameters, as for the stellate cell to Purkinje cell synapse.

4.3.9.12 GABA recycling at the Golgi cell to granule cell synapse

This was calculated as at the stellate cell to Purkinje cell synapse, using the parameters described in the previous paragraph.

4.3.10 Lugaro and unipolar brush cells

These cells were ignored, assuming that in most previous estimates of Golgi cell density they were counted as Golgi cells.

4.4 Results: Conclusions based on the calculations

4.4.1 The cellular distribution of energy use

Analysis of the energy used on each cerebellar cell type revealed that larger cells use more ATP/sec than small cells. This reflects the fact that, in general, larger areas of membrane mediate larger ion fluxes that require more ATP to pump back. Thus, each of the largest cerebellar neurons, the Purkinje cells, uses 1.15×10^{10} moles of ATP/sec, which is far greater than the 2.27×10^{8} moles of ATP/sec used by each of the smallest, granule, neurons, and the intermediate size inhibitory interneurons are in between (Fig. 4.2a). Nevertheless, when multiplied by the number of neurons present, the 274-fold higher density of granule cells results in them dominating the energy use of the whole cerebellar cortex (Fig. 4.2b), consuming 72% of the total signalling energy, while the principal Purkinje neurons use only 13% of the total.

4.4.2 The subcellular distribution of energy consumption

The predicted distribution of energy expenditure on subcellular tasks in the cerebellar cortex was calculated by summing the energy used on action potentials, synaptic currents, the

resting potential, etc., over all cells, weighted by their area density (Fig. 4.2c). In the cerebellum this distribution differs substantially from that in the cerebral cortex (Attwell and Laughlin, 2001). Although in both areas 40-50% of signalling energy goes on action potentials, and only a small fraction goes on transmitter release and recycling, much more energy is used on resting potentials in the cerebellum than in the cerebral cortex (35% versus 13%, respectively), and much less on postsynaptic currents (19% versus 34%). Furthermore, the subcellular distribution of energy use varies dramatically between different cerebellar neuron types (Fig. 4.3). Purkinje cells, which receive about 174,000 excitatory synaptic inputs, and have only a short output axon within the cerebellar cortex, use most (53%) of their signalling energy on postsynaptic receptors. By contrast, for the much smaller granule cells, which receive only 4 excitatory synaptic inputs, but have to propagate their action potential along, and maintain the resting potential of, a very long (~4.5 mm) axon, most of the energy goes on the action potentials (47%) and the resting potential (42%). The subcellular energy distribution of the inhibitory interneurons has characteristics more similar to those of the Purkinje cells (Fig. 4.3).

4.4.3 Effect on energy use of altering firing rates

Because most cerebellar energy is expended on granule cells and the postsynaptic currents they evoke in Purkinje cells, if the firing frequency of granule cells alone is varied in the model then the total cerebellar energy expenditure is predicted to vary dramatically (Fig. 4.4a). By contrast, varying the assumed (simple spike) firing rate of Purkinje cells alone has very little effect on energy consumption. Thus, the total energy use need not correlate well with the firing rate of the principal neurons in this part of the brain.

4.4.4 Energy use by excitatory and inhibitory neurons

To examine the allocation, by evolution, of energy use to excitatory and inhibitory neurons, I summed the energy used on mossy fibres, climbing fibres and granule cells, and on

Purkinje, stellate, basket and Golgi neurons, respectively (and I included as an excitatory cost the much smaller ATP consumption on recycling glutamate in glia; ATP use on glial resting potentials was ignored). Excitatory neurons were found to consume 6.68 x 10^{19} moles ATP/sec/m^2 of cerebellum, while inhibitory neurons consumed only 1.92 x 10^{19} moles ATP/sec/m^2 of cerebellum (Fig. 4.4b).

4.4.5 Energy use on different stages of cerebellar computation

One can conceptualize the retrieval of motor patterns from the cerebellar cortex as occurring in three stages: remapping from mossy fibre input action potentials to action potentials in the granule cell soma (involving energy use in mossy fibres, in the granule cell dendrites and soma, in Golgi cells, and in granular layer astrocytes); propagation of the remapped sensorimotor information to Purkinje cells as a sparse code (involving energy use in the granule cell axon, molecular layer interneurons and Bergmann glia); and computation by the Purkinje cells of an output signal (using energy in the Purkinje cell) (Tyrell and Willshaw, 1992). By summing the energy used in the different cell types participating in these different stages of cerebellar computations, the relative amounts of ATP used on these processes were predicted to be 37%:49%:14% (Fig. 4.4c). Thus, most cerebellar signalling energy is used on intra-cerebellar processing of the incoming information.

4.4.6 The laminar distribution of energy use and supply are matched in the cerebellum

The predicted laminar distribution of energy use across the cerebellar cortex was calculated by summing energy consumed in the parts of the neurons and glial cells in the molecular layer and the granular layer (including half of the Purkinje cell somata in each layer). The large amount of ATP consumed by the granule cell action and resting potentials, and on postsynaptic currents in Purkinje cells, results in the molecular layer being predicted to use 60% of the total ATP consumption, and the granular layer 40% (Fig. 4.5c), a ratio of

1.5. Adding to the signalling energy a small amount of housekeeping energy would not alter this ratio significantly if housekeeping energy is proportional to tissue volume, since the relative thickness of the molecular and granular layers (with half of the Purkinje cell layer allotted to each) is also 1.50 (Harvey and Napper, 1988). To test how the laminar distribution of energy use was served by the energy supply provided by blood vessels, I used confocal imaging of the blood vessel (labelled with FITC-conjugated isolectin B_4) to measure the surface area available for oxygen diffusion and glucose transport in each lamina. The predicted energy use showed a good correlation with the vessel surface area available for oxygen diffusion and glucose transport in each lamina, which were 58 $\pm$ 9% and 42 $\pm$ 4% in the molecular and granular layers respectively (number of lobes measured = 26, Fig. 4.5a,b).

4.5 Discussion

I have constructed an energy budget for the cerebellum from the bottom up, based on the properties of the ion channels and transporters in each cell type mediating the ion fluxes underlying synaptic and action potentials. Comparing this predicted energy usage, with the computations being carried out by different cells in the cerebellar circuit, reveals important features of how the cerebellum has been "designed" by evolution.

4.5.1 Excitatory cells use more energy than inhibitory cells

Energy use is split between excitatory and inhibitory cells in a roughly 3.5:1 ratio (Fig. 4.4b). This partly reflects the relative numbers of excitatory and inhibitory cells present, but is also affected by their relative size. For example each Purkinje cell consumes 51 times as much energy as each granule cell (Fig. 4.2a), because of the larger ion fluxes across its much larger membrane area.

4.5.2 Energy use need not correlate with principal neuron firing

Although it was earlier assumed that the energy use of a brain area, and functional imaging signals based on this, mainly reflect the spiking activity in the principal neurons of that area, more recent findings have questioned this (Logothetis et al., 2001; Viswanathan and Freeman, 2007), and I find that the principal neurons in the cerebellum use only a small fraction of the energy consumed by the cerebellar cortex (Fig. 4.2b). This is because the much larger number of granule cells results in their energy consumption dominating that of the Purkinje cells (Fig. 4.2b). Furthermore, in the Purkinje cells more of the energy is employed to reverse ion entry at the input synapses from the parallel fibres, than is used on action potentials (Fig. 4.3b). Consequently, if I examine how altering the firing rate of the Purkinje cells alone affects the total energy consumption of the cerebellar cortex, I find that it has very little effect, whereas altering the mean firing rate of granule cells alone has a profound effect on the total energy consumption (Fig. 4.4a).

4.5.3 Granule cells use most cerebellar energy

If I divide cerebellar computation into the three stages of remapping from mossy fibre input action potentials to action potentials in the granule cell somata, propagation of the remapped information to Purkinje cells, and computation by the Purkinje cells of an output signal, the relative amounts of ATP used on these processes are 37%: 49%: 14% (Fig. 4.4c). Thus, most ATP is consumed by the granule cells as they remap incoming information into a sparsely coded signal and distribute it to Purkinje cells. The high ATP usage in granule cells suggests that the ability to store a large number of motor patterns, which is conferred by their remapping of information (Marr, 1969; Tyrell and Willshaw, 1992), provided a sufficient advance in motor performance for evolution to allocate blood vessels to supply the associated energy expenditure in these cells.

4.5.4 Energy efficiency is improved by some aspects of cerebellar design

Despite the fact that granule cells use most of the energy supplied to the cerebellar cortex, my analysis reveals that this energy consumption would be much higher were it not for two key features of how evolution has "designed" the cerebellum. First, once the cerebellum has stored patterns of motor information, 85% of its parallel fibre synapses generate no synaptic current (Isope and Barbour, 2002). This is predicted for optimal information storage by Purkinje cells (Brunel et al., 2004), but in addition reduces the predicted total signalling energy consumption of the cerebellar cortex by 32% (see section 4.5.6). Second, I predict, based on measurements of the electrical space constant of other CNS axons (Alle and Geiger, 2006; Kole et al., 2007), that the axon of granule cells has a much higher specific resistance than the soma and dendrites, which reduces 20.7-fold the energy expended on maintaining the resting potential of the axon (see section 4.5.6). As a result the energy consumption of the molecular layer is reduced by 73%. A lower Na^+ influx per membrane area of the axon, compared to the soma and dendrites, might reflect a design principle setting the specific conductance in the two subcellular areas. The time scale of processing of subthreshold signals in dendrites is partly limited by the membrane time constant, τ_m, which is the product of cell resistance and capacitance. In the dendrites and soma the membrane resistance cannot be too high as this will raise the time constant and limit the speed with which synaptic currents can change the membrane potential (Attwell and Gibb, 2005), but this is not a constraint in the axon, where the conductance will increase dramatically as the action potential approaches. Indeed, two recent papers (Alle and Geiger, 2006; Kole et al., 2007) have shown that the space constant in axons is much longer than that in dendrites (Ulrich and Stricker, 2000).

4.5.5 Energy supply is matched to energy use in the cerebellar layers

The neuronal and computational architecture differs dramatically between the granular layer, where there are many tiny granule cells each receiving very few input

synapses, and the molecular layer, where the much smaller number of much larger Purkinje cells each receive a very large number of inputs. I tested whether the energy supply to these different layers was matched to the energy expenditure in the layers, as might arise through evolution since different brain areas consume different amounts of energy (Sokoloff et al., 1977) and the blood vessel density is correlated with glucose use in different neocortical areas (Borowsky and Collins, 1989). Comparing the signalling energy consumption values of my model for the molecular and granular layers, with the measured surface area of blood vessels available for the supply of oxygen and glucose, revealed an extremely good match (Fig. 4.5). Thus, the distribution of blood vessels may have evolved to match the large ATP usage of granule cells. Interestingly, the predicted signalling energy use per tissue volume in the molecular and granular layers is identical, since the ratio of predicted energy uses, 1.5, is the same as the measured ratio (1.5) of the thicknesses of the two layers (with half the Purkinje cell layer allotted to each) (Harvey and Napper, 1988).

4.5.6 Sensitivity of the predictions to the parameters assumed

As detailed above, the great majority of the parameters needed to make these energy use predictions have been measured for each of the cerebellar cell types and synapses. My predictions are most sensitive to uncertainties in the values of three parameters, as follows. First, a detailed analysis of parallel fibre to Purkinje cell connectivity concluded that, in the adult, after learning of motor programmes has occurred, 85% of the weights of parallel fibre to Purkinje cell synapses have been reduced to zero (Isope and Barbour, 2002). The fact that only a small fraction (0.15) of these synapses is active is a consequence of optimizing information storage in the cerebellum (Brunel et al., 2004), and has a major effect on the predicted total energy consumption, lowering it from 30 to 20μmoles ATP/g/min. An error in the measurement of the fraction of inactive synapses would have a correspondingly large effect on my predicted total energy use. I assumed that this zero synaptic weight reflects an absence of glutamate release. However, if the synapses have zero weight because glutamate is

released in the absence of postsynaptic receptors, the increase in total energy consumption of the cerebellar cortex due to glutamate release and recycling would be only 4%.

Secondly, the resting membrane properties of the long granule cell axon are unknown, because measuring the input resistance at the soma probably only determines the mean conductance of the soma, the short dendrites and the part of the axon near the soma: most of the axon is too electrotonically distant to contribute. I therefore calculated the axon membrane conductance from measurements of the space constant of hippocampal axons (Alle and Geiger, 2006) (scaled appropriately for the diameter and length of the parallel fibres: see above). Using this value gave a specific resistance for the axon membrane that was 20.7-fold higher than that of the soma and dendrites. If I assumed the axon membrane had the same specific resistance as the membrane around the soma, then this would increase the ATP consumption on the resting potential by a factor of 20.7 over the value I actually use in the model, which would increase the total signalling energy expenditure to 55 μmoles ATP/g/min, 2.8-fold larger than the total cerebellar energy expenditure that has been measured (Sokoloff et al., 1977).

The final uncertain parameter in my analysis is the mean firing rate of granule cells. Sensory stimulation produces brief bursts of ~ 3 action potentials at ~ 80Hz (Chadderton et al., 2004), but it is not known how often this occurs *in vivo* (see above), although movement through the environment should often stimulate sensory input. I therefore assumed a mean firing rate of 6 Hz in order to produce an action potential driven energy consumption of 13.6 μmoles ATP/g/min (which is the value expected for the measured total energy consumption (Sokoloff et al., 1977) of 20 μmoles ATP/g/min if a mean value (Nilsson and Siesjo, 1975; Sibson et al., 1998) of 68% of the energy is action potential driven), and explored the effect of varying this parameter in Fig. 4.4a. Again, if this parameter were chosen wrongly it would have a large effect on the predicted energy use of the cerebellar cortex.

4.5.7 Cost of information storage

From my analysis I calculate that ~10^{11} ATP molecules are used on signalling per second for each Purkinje cell (and associated other neurons and glia) in the cerebellar cortex. Each Purkinje cell can store approximately 40,000 input-output associations, corresponding to ~5kB of information ((Brunel et al., 2004), but see Steuber et al. (2007) which suggests a lower number of patterns stored). Using a standard energy production per mole of ATP hydrolysed of 31kJ, this translates into a resting energy consumption of 1mW/GB of stored motor patterns. For comparison, modern hard disks consume ~5mW/GB of stored information.

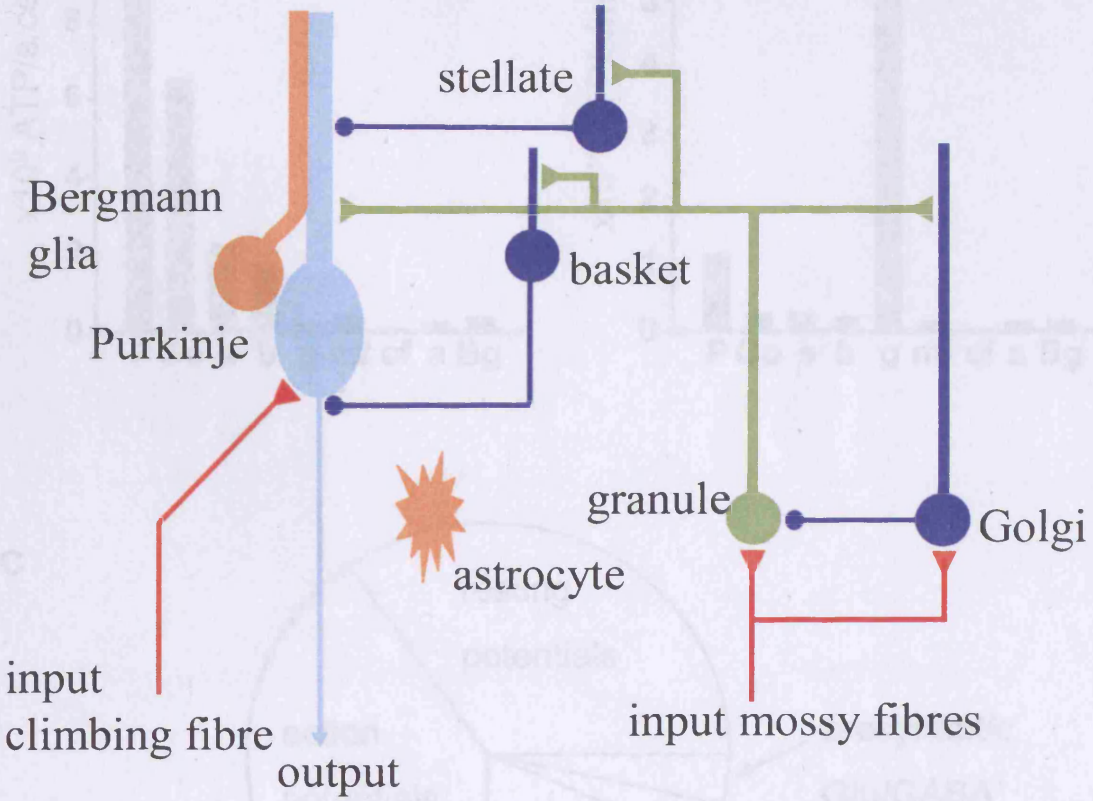

Figure 4.1 Schematic diagram of the cerebellar cortex showing the cell types considered.

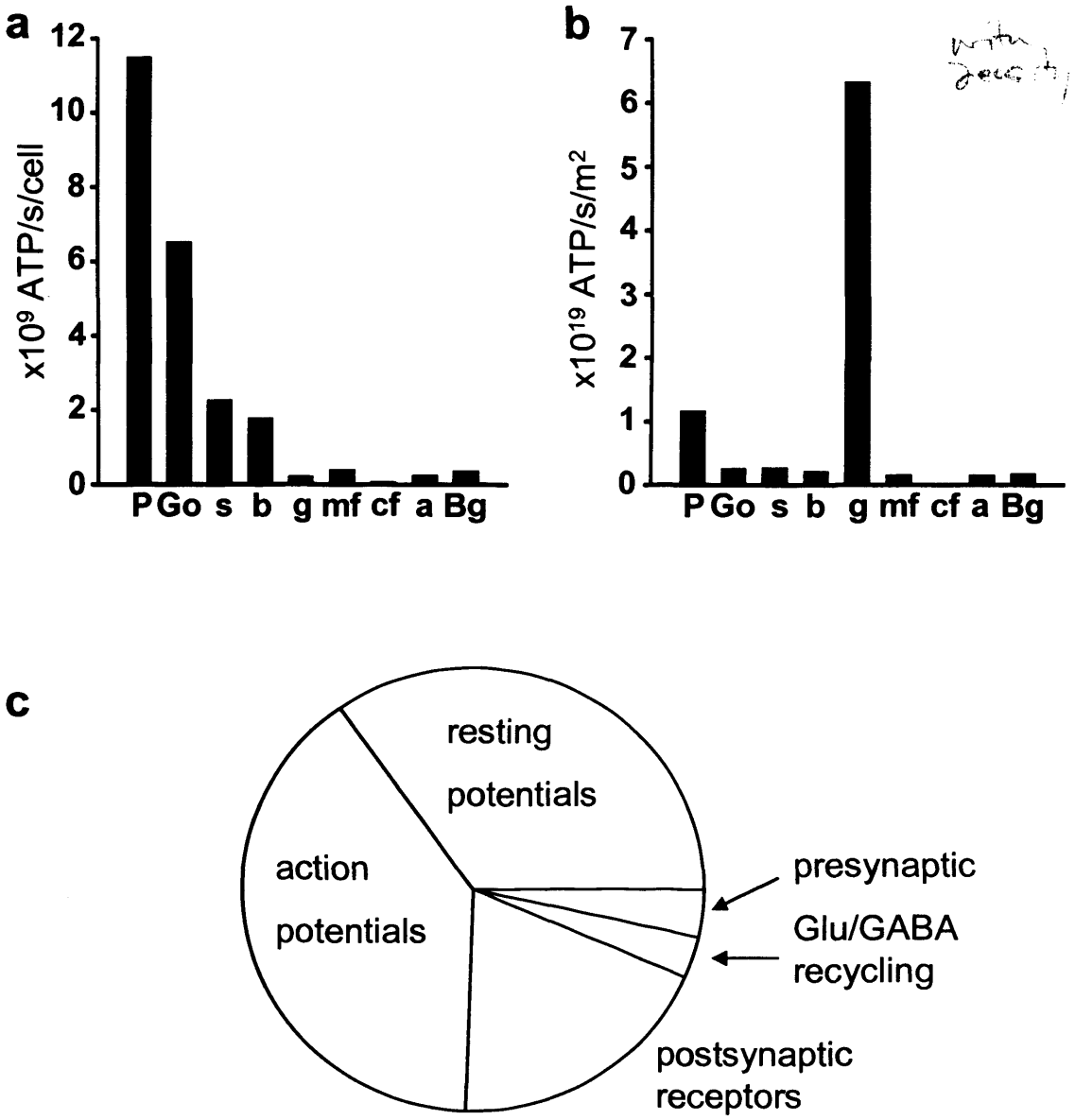

Figure 4.2 Predicted energy use for the cerebellar cortex with all cell types firing at their physiological rates. **a**: Cellular distribution of predicted energy use (ATP used per cell). Key: P Purkinje cell, Go Golgi cell, s stellate cell, b basket cell, g granule cell, mf mossy fibre, cf climbing fibre, a astrocyte, Bg Bergmann glia. **b**: Cellular distribution of energy use, taking density of cells into account (ATP use per class of cell). The far greater density of granule cells results in them dominating the cerebellar energy use. **c**: Energy distribution among subcellular processes in the cerebellum (summed over all cell types, weighted by cell densities). Resting potentials account for 35% of the energy use, action potentials 40%, postsynaptic receptors 19%, neurotransmitter recycling (ATP used in glia and on packaging transmitter into vesicles in the releasing cell) 3%, and presynaptic Ca^{2+} entry and vesicle cycling 3%.

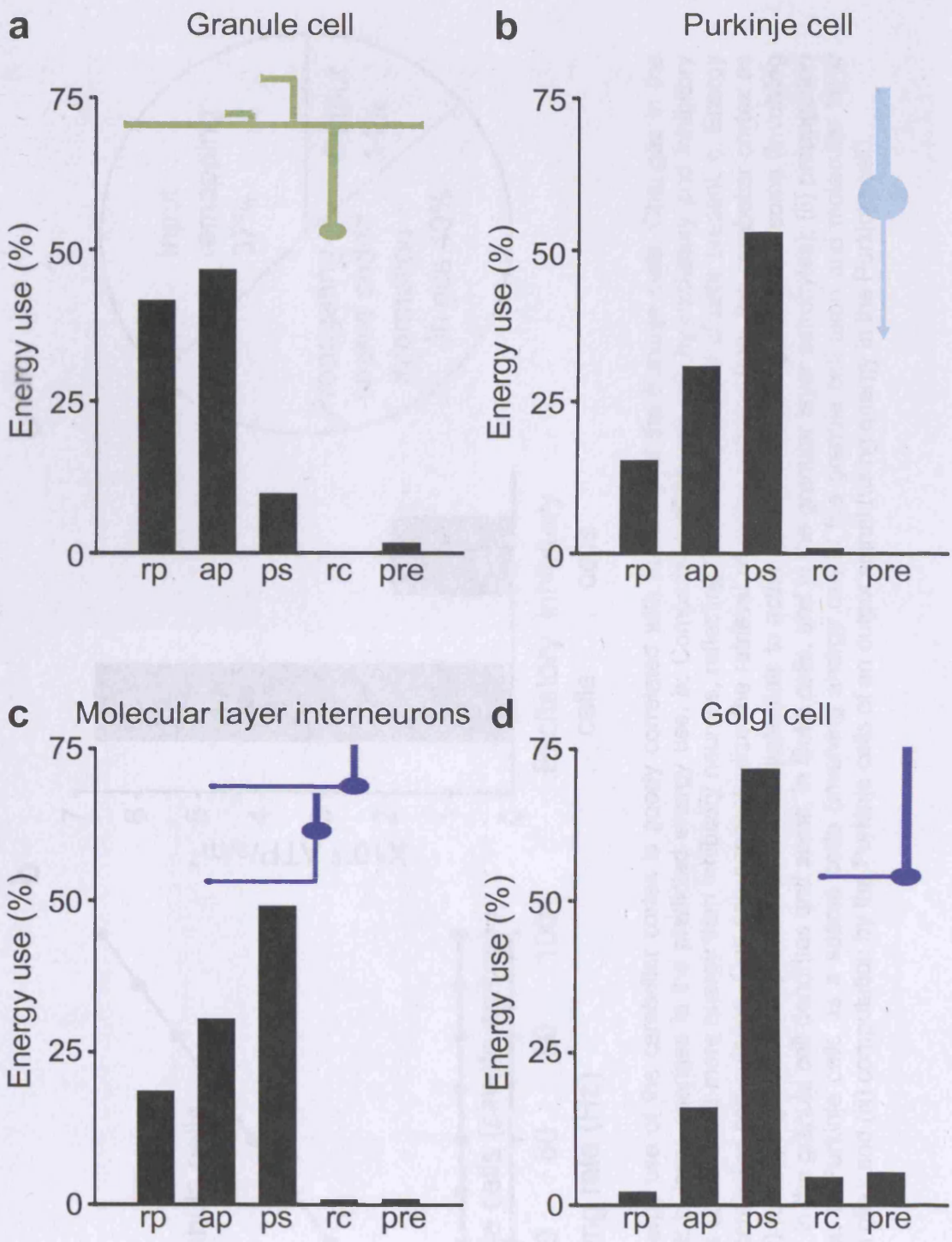

Figure 4.3 The subcellular distribution of energy use varies according to cell type. **a**: Granule cells. Most energy is used to propagate action potentials and maintain the resting potential along the long parallel fibres. **b**: Purkinje cells. These cells have around 174,000 synaptic inputs; most energy is used on postsynaptic receptors. **c,d**: Inhibitory neurons have a distribution more similar to Purkinje cells. **c**: Molecular layer interneurons. **d**: Golgi cells. Key: rp: resting potential, ap: action potential, ps: postsynaptic receptors, rc: transmitter recycling (ATP used on glial uptake of transmitter and its metabolic processing, and on packaging transmitter into vesicles in the releasing cell), pre: presynaptic Ca^{2+} entry and vesicle cycling.

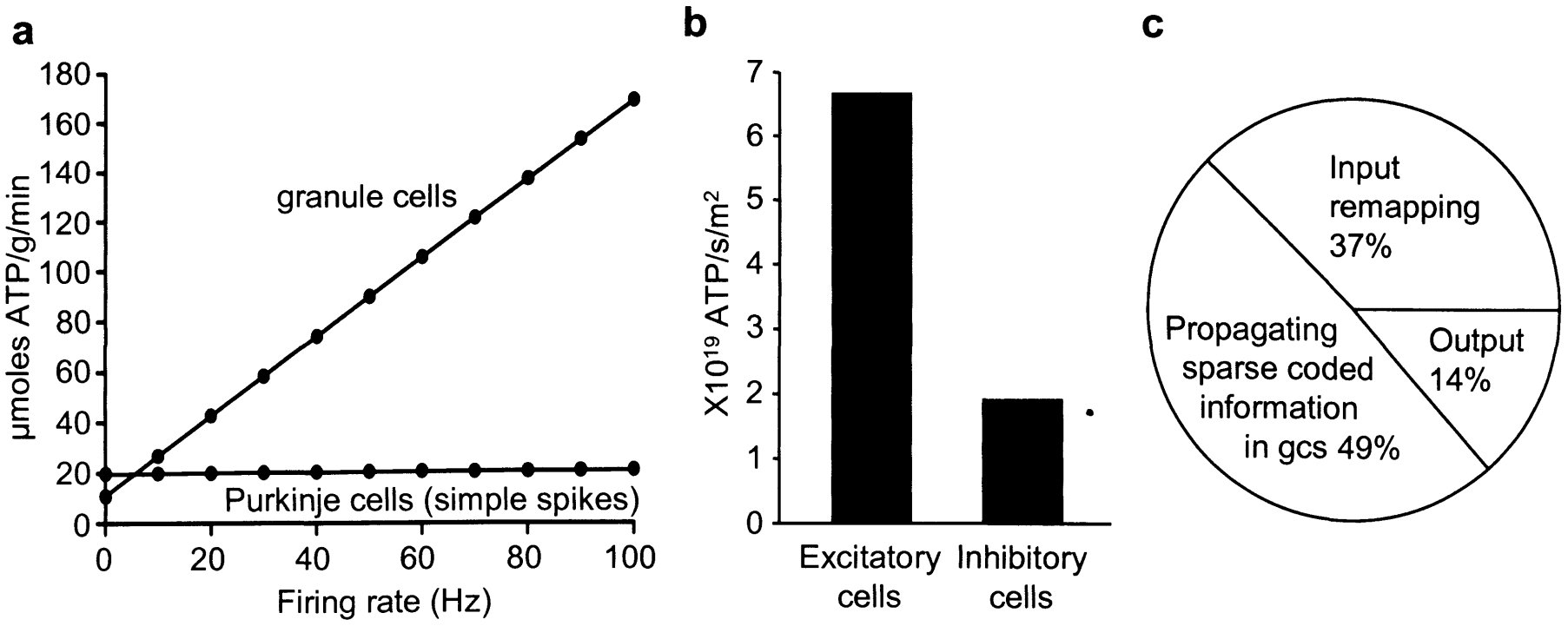

Figure 4.4 a: Predicted energy use of the cerebellar cortex is poorly correlated with the firing of the Purkinje cells. Changes in the granule cell firing rate result in large changes in the predicted energy use. **b**: Comparison of energy use by excitatory and inhibitory neurons. Excitatory neurons use 3.5-fold more energy than inhibitory neurons, reflecting the relative number of cells present. **c**: Energy use on different stages of cerebellar computation. One can conceptualize the retrieval of motor patterns from the cerebellar cortex as occurring in three stages: (i) remapping from mossy fibre input action potentials to action potentials in the granule cell soma (involving energy use in mossy fibres, in the granule cell dendrites and soma, in Golgi cells, and in the granular layer astrocytes); (ii) propagation of the remapped information to Purkinje cells as a sparse code (involving energy use in the granule cell axon and molecular layer interneurons and Bergmann glia); and (iii) computation by the Purkinje cells of an output signal (using energy in the Purkinje cell).

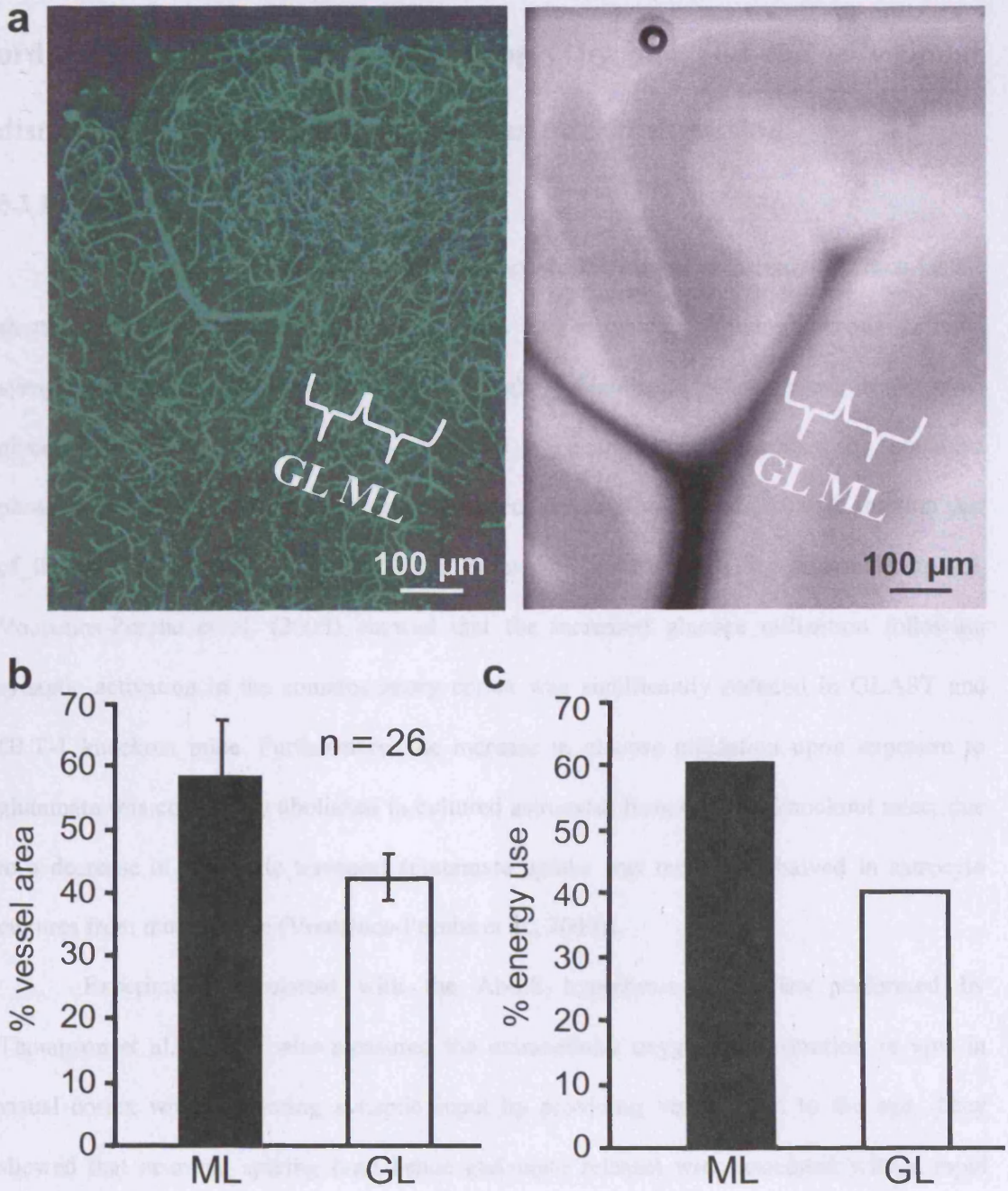

Figure 4.5 a,b: Comparing the predicted laminar distribution of energy use with the observed distribution of blood vessels. **a**: Cerebellar slice from a P21 rat, with blood vessels labelled with FITC-conjugated isolectin B4. Projection image of a confocal FITC z stack (left) and grey scale image (right). The molecular layer (ML) and granular layer (GL) are labelled. **b**: Measured distribution of blood vessel surface area (±s.e.m) between layers in 26 lobules from 17 brain slices. **c**: The predicted energy use in the molecular and granular layers reflects the large amount of ATP consumed by the granule cell action and resting potentials, and on postsynaptic currents in Purkinje cells.

Chapter 5: Measuring oxygen consumption to investigate the co-ordination of neuronal energy supply by glia and the subcellular distribution of energy use during synaptic transmission

5.1 Introduction

Pellerin and Magistretti (1994) have proposed the idea of an astrocyte-neuron lactate shuttle (ANLS, see Chapter 1, section 1.5, Fig. 1.4) in which, following neuronal activity, synaptically released glutamate is taken up by glia, which leads to an increase in astrocytic glycolysis. The resulting lactate is taken up by neurons and consumed by oxidative phosphorylation, resulting in an increased oxygen consumption. Consistent with the first part of the ANLS hypothesis, i.e. glycolysis is evoked in astrocytes by glutamate uptake, Voutsinos-Porche et al. (2003) showed that the increased glucose utilization following synaptic activation in the somatosensory cortex was significantly reduced in GLAST and GLT-1 knockout mice. Furthermore, the increase in glucose utilisation upon exposure to glutamate was completely abolished in cultured astrocytes from GLAST knockout mice, due to a decrease in glutamate transport (glutamate uptake was more than halved in astrocyte cultures from mutant mice (Voutsinos-Porche et al., 2003)).

Experiments consistent with the ANLS hypothesis were also performed by Thompson et al. (2003), who measured the extracellular oxygen concentration *in vivo* in visual cortex while activating synaptic input by providing visual input to the eye. They showed that neuronal spiking (and hence glutamate release) was associated with a rapid decrease in local oxygen concentration, reflecting oxygen consumption. On the ANLS hypothesis, this oxygen would be used in neurons to oxidize lactate provided by astrocytes to the neurons.

However, as discussed in Chapter 1, section 1.5, the ANLS hypothesis remains controversial; and has been challenged by data from Cerdan et al. (2006), who proposed reversible rather than unidirectional exchange of lactate between astrocytes and neurons, and by Kasischke et al. (2004), who used changes in NADH fluorescence to suggest that neuronal

oxygen use occurs before astrocytic glycolysis rather than after it as expected on the ANLS hypothesis, (see Chapter 1, section 1.5).

I further tested Pellerin and Magistretti's theory, by measuring oxygen use when glutamate uptake was blocked. On their theory there should be little oxygen use evoked by neural activity with uptake blocked, because blocking uptake will prevent the signalling-induced increase in ATP consumption in astrocytes and hence prevent the export to neurons of lactate produced by astrocyte glycolysis.

As an essential prelude to those experiments, I carried out modelling studies, in order to find the expected effect of various uptake block strategies on the ATP use evoked in glia by glutamate released from neurons. The aim was to examine by how much transporter knockout would be expected to reduce glutamate uptake into, and ATP use by, astrocytes in the experiments of Voutsinos-Porche et al. (2003), and to determine the best blocking strategy to use in my experiments on cerebellum.

As an extension of looking at the importance of glutamate uptake for controlling CNS oxygen use, I also assessed the contribution of various cellular processes to the oxygen consumption evoked by neural activity. In general it is unknown how the energy resources available to the brain are allotted to carry out different parts of a neural computation (see Chapter 1, section 1.2 and Chapter 4, section 4.1). Offenhauser et al. (2005) found that, at the climbing fibre – Purkinje cell synapse, where many AMPA receptors on an extensive dendritic tree are activated, the oxygen consumption is mainly driven by activation of postsynaptic receptors. I monitored oxygen consumption while pharmacologically blocking various processes during synaptic transmission at the parallel fibre – Purkinje cell synapse.

5.2 Methods

5.2.1 O_2 electrode measurements

Transverse cerebellar slices 200 μm thick were prepared as described in Chapter 2, section 2.1. These have the Purkinje cell dendritic tree perpendicular to the plane of the slice,

allowing stimulation of the parallel fibres at some distance from the Purkinje cell. Slices were obtained from 18-21 day old rats or 17-21 day old GLAST knockout and wild-type mice, and were superfused with either bicarbonate Ringer's or HEPES Ringer's solution at room temperature as previously described in Chapter 2, section 2.1. Drugs were added to the superfusion solution as described previously in Chapter 2, section 2.2 and, for experiments using mouse tissue, solutions were bubbled with air for approximately 1 hour prior to use in order to become air equilibrated. In the experiments on rats, solutions were gassed with 95% O_2/5% CO_2 for bicarbonate Ringer's or with 100% O_2 for HEPES Ringer's). An oxygen electrode (placed in the molecular layer) was used to measure changes in the extracellular oxygen concentration, as an index of changes in oxygen consumption, close to the dendritic tree of the Purkinje cells, as previously described in section 2.11. The stimulating electrode (described in Chapter 2, section 2.9) was placed in the molecular layer ~100 μm along the parallel fibres from the oxygen electrode. Stimulation with a 10 second, 20 Hz train of pulses (75 V, 0.06 ms) was applied to the parallel fibres. Solutions were bath perfused onto the slice and the changes in oxygen concentration occurring in response to stimulation were recorded.

5.2.2 Analysis of oxygen electrode data

Applying a stimulation train to the parallel fibres caused a sharp decrease in the measured extracellular oxygen concentration which is a useful indicator of oxygen consumption (as discussed in Offenhauser et al. (2005)), followed by a slow recovery (Fig. 5.5b). The difference between the slope of the graph of [O_2] against time during stimulation and the slope over a similar time period just before stimulation was calculated. In control conditions, this difference was set to be 100% and all the values during drug exposure were calculated as percentages of the slope difference in control conditions.

5.3. Results

5.3.1 Aims of modelling glutamate uptake

Initially I will consider several models for glutamate removal in cerebellar slices. Then I will extend these models to the neocortical experiments of Voutsinos-Porche et al. (2003). All models were built in Mathcad 8 Professional (MathSoft Inc).

The aims of the modelling reported below were:

(1) To determine how well GLAST or GLT-1 knockout (as used by Voutsinos-Porche et al. (2003)) is expected to reduce glutamate uptake, and associated ATP use, in neocortical glia.

(2) To predict the effects on the ATP consumption stimulated by glutamate uptake at the parallel fibre – Purkinje cell synapse when GLAST is knocked out, and when glial glutamate transporters are inhibited pharmacologically with TBOA (the glutamate analogue, DL-threo-β-benzyloxyaspartate, a non-transportable competitive inhibitor of excitatory amino acid transporters (Shimamoto et al., 1998)) and DHK (dihydrokainate, a glutamate analogue which is a non-transported blocker of GLT-1 transporters (Arriza et al., 1994; Levy et al., 1998)).

(3) To test whether a larger fractional reduction of glial glutamate uptake and downstream ATP use in astrocytes can be achieved by superimposing DHK on GLAST knockout.

The motivation for this modelling was the realisation that knocking out or inhibiting one glial transporter type need not have a large effect on the overall uptake of glutamate into glia, because when uptake by one transporter is reduced the extracellular glutamate concentration stays higher for longer, increasing uptake by the remaining transporters. If we ignore loss of glutamate by diffusion out of the slice (in my experiments) or to the blood (in vivo) then a decrease in glial uptake (and associated ATP consumption, which is what is supposed to drive lactate export to neurons) can only occur if there is a shift towards uptake by neuronal transporters. This is hard to achieve because neuronal transporters provide only a

small fraction of the total transport capacity present. Thus, although the experiments of Voutsinos-Porche et al. (2003) apparently gave results compatible with the ANLS hypothesis, I questioned whether they could actually have significantly decreased the ATP consumption (and lactate production) occurring in astrocytes as a result of glutamate uptake. As will be seen below, quantitative modellling revealed that this is a serious concern with the pure knockout approach used by Voutsinos-Porche et al. (2003).

5.3.2 Single compartment cerebellar model with peak glutamate concentration of 1 mM.

The aim of the cerebellar simulations carried out was to calculate the amount of glutamate taken up into astrocytes (Bergmann glia) surrounding a parallel fibre synapse, since this will be proportional to the ATP consumed as a result within the glial cell (the ATP is used to pump out the ions powering glutamate uptake and to convert glutamate to glutamine). Initially a single compartment model was built, assuming that glutamate was released into the extracellular space and then taken up by GLAST (denoting "glutamate-aspartate transporter", the major transporter in the cerebellum which is present in the Bergmann glia wrapping the parallel fibre synapses (Lehre and Danbolt, 1998)), by GLT-1 (denoting "glutamate transporter", also present in Bergmann glia), and by EAAT4 ("excitatory amino acid transporter", expressed in Purkinje cell dendritic spines) transporters within the single compartment (Fig. 5.1a).

The release of glutamate was assumed to occur for 0.001s with the peak glutamate concentration reaching 1mM in the compartment, as the peak glutamate concentration reached at the climbing fibre synapse is in the millimolar range (Wadiche and Jahr, 2001). The K_M values for uptake of this glutamate by GLAST, GLT-1 and EAAT4 are 77 μM (Storck et al., 1992), 16.5 μM (Levy et al., 1998) and 1.3 μM (Shigeri et al., 2001), respectively. Using Michaelis-Menten kinetics for competitive inhibitors, the rate of uptake

by GLAST (U_{glast}) in the presence of the blocker TBOA can be expressed in the following way:

$$U_{glast}([glu],[TBOA]) = \frac{V_{glast}[glu]}{[glu] + K_{glast}(1 + \frac{[TBOA]}{K_{tboaglast}})} \quad (5.1)$$

where V_{glast} is the V_{max} of GLAST, $[glu]$ is the concentration of glutamate present, K_{glast} is the K_M value for GLAST, $[TBOA]$ is the concentration of TBOA applied and $K_{tboaglast}$ is the K_i value of TBOA for GLAST. A similar equation was used to calculate the uptake by EAAT4 within the model. No modification of eqn. (5.1) is needed in the presence of DHK because this compound does not act on GLAST or EAAT4.

The uptake by GLT-1 transporters in the presence of the blockers DHK and TBOA was calculated from the following expression, again derived through Michaelis-Menten kinetics:

$$U_{glt}([glu],[TBOA],[DHK]) = \frac{V_{glt}[glu]}{[glu] + K_{glt}(1 + \frac{[DHK]}{K_{dhk}} + \frac{[TBOA]}{K_{tboaglt}})} \quad (5.2)$$

where the symbols have similar meanings to equation (5.1), $[DHK]$ is the concentration of DHK applied, and K_{dhk} is the K_i value of DHK for GLT-1. The K_i values of TBOA for GLAST, GLT-1 and EAAT4 are 42 μM (Shimamoto et al., 1998), 5.7 μM (Shimamoto et al., 1998) and 4.4 μM (Shigeri et al., 2001) respectively. The K_i value of DHK for GLT-1 was taken as 15.5 μM (the average of 8 μM (Wang et al., 1998) and 23 μM (Arriza et al., 1994)).

In the cerebellar molecular layer the concentration of GLAST is 18000 GLAST molecules per μm^3 of tissue (Lehre and Danbolt, 1998), and of GLT-1 is 2800μm^{-3} (Lehre and Danbolt, 1998). The average concentration of EAAT4 in the molecular layer of the adult rat is 1900 molecules per μm^3 of tissue (Dehnes et al., 1998). The V_{max} value for each transporter type was assumed to be proportional to the number of transporters present i.e. the cycle time was assumed to be the same for each type of transporter: experimental cycle times are 70 ms for EAAT2 (Wadiche et al., 1995) and 77 ms for EAAT4 (Otis and Jahr, 1998). In

control conditions (with no blockers or knockout of glutamate transporters) the total amount of glutamate uptake was set so that for small elevations of [glu], the decay time constant, τ (see equation 5.6), was approximately 10ms in the linear phase of equation (5.5) below, as synaptically released glutamate is cleared from the synaptic cleft on a millisecond time scale (Attwell and Gibb, 2005).

The concentration of glutamate ([glu]) in the extracellular space was calculated by solving the differential equation (5.3) where R is the release of glutamate, U_x is the glutamate uptake by transporter x and *Volume* is the volume into which the glutamate is released (note that GLAST and EAAT4 are not affected by DHK).

$$\frac{d[glu]}{dt} = \frac{R(t) - U_{glast}([glu],[TBOA]) - U_{glt}([glu],[TBOA],[DHK]) - U_{eaat4}([glu],[TBOA])}{Volume} \tag{5.3}$$

The diffusion of glutamate out of the compartment was ignored as the time taken to diffuse out of the slice in my experiment would be on the order of 16s (estimated as $t = x^2/2D$, assuming diffusion from the centre of a slice of thickness $2x = 200$ μm with a diffusion constant, $D \sim 3\times10^{-10} m^2 s^{-1}$ (Barbour, 2001)).

In the absence of blockers, equation (5.3) can be expressed as:

$$\frac{d[glu]}{dt} = \frac{R(t) - \frac{V_{glast}[glu]}{[glu]+K_{glast}} - \frac{V_{glt}[glu]}{[glu]+K_{glt}} - \frac{V_{eaat4}[glu]}{[glu]+K_{eaat4}}}{Volume} \tag{5.4}$$

In the case of a low glutamate concentration, all of the K values are >>[glu], and

$$\frac{d[glu]}{dt} = \frac{R(t) - \frac{V_{glast}[glu]}{K_{glast}} - \frac{V_{glt}[glu]}{K_{glt}} - \frac{V_{eaat4}[glu]}{K_{eaat4}}}{Volume} \tag{5.5}$$

The solution of this equation is $[glu] = G_0 e^{-t/\tau}$, with G_0 the initial value of [glu], which gives:

$$\tau = \frac{Volume}{\frac{V_{glast}}{K_{glast}} + \frac{V_{glt}}{K_{glt}} + \frac{V_{eaat4}}{K_{eaat4}}} \tag{5.6}$$

where, from the relative transporter concentrations above, in control conditions

$V_{glt} = V_{glast}\frac{2800}{18000}$, and $V_{eaat4} = V_{glast}\frac{1900}{18000}$. As stated above the value of V_{glast} (and hence of V_{glt} and V_{eaat4}) was set to give a decay time constant, τ, of approximately 10ms (using V_{glast} = 1.4 moles/s).

In the single compartment model with a peak glutamate concentration of 1 mM, in control conditions, GLAST takes up 75% of the glutamate released, GLT-1 takes up 14% while EAAT4 accounts for the remaining 11%. As can be seen in Fig. 5.2a (rightmost bars for GLAST + GLT-1), the glial transporters together take up 89% of the glutamate. When a GLAST knockout was modelled, GLT-1 and EAAT4 uptake increased to 58% and 42% respectively, but the total time-integrated glial uptake (now occurring by GLT-1 alone) decreased by only 35% compared to control conditions (compare yellow and dark blue rightmost bars in Fig. 5.2a). Although GLAST is the dominant cerebellar glutamate transporter, when GLAST is knocked out (as in my experiments) the glutamate has to be taken up by the remaining transporters, as there is no diffusion to the bulk solution in this model. Thus the total amount of glutamate taken up is not altered (in vivo this will also be true, except that some glutamate could conceivably be lost to the blood) and relatively little of the glutamate is switched to being taken up by neurons.

When 200 μM DHK, a selective, non-transported blocker of GLT-1 transporters (Arriza et al., 1994; Levy et al., 1998), was added to the GLAST knockout model it was found that glial uptake fell by only 20% (compared to GLAST knockout alone) from 58% to 46% (compare pale blue and yellow rightmost bars in Fig. 5.2a). Although this concentration of DHK is expected (from equation 5.2) to block the uptake by GLT-1 of 1 mM glutamate by 82%, the slowed uptake results in glutamate remaining present for longer, so the time integral of the uptake by GLT-1 is little changed and only a small fraction of the glutamate is taken up by EAAT4 instead (because the very high affinity EAAT4 is already almost saturated for much of the time). A higher concentration of DHK was needed to block the residual glial uptake by over 50%. When 1 mM DHK was added to the GLAST knockout model, uptake by GLT-1 decreased to 29% of the total uptake (i.e. 50% of the uptake by GLT-1 when GLAST

is knocked out alone: yellow and dark magenta bars in Fig. 5.2a). However, in the experiments below a concentration of 200 μM, rather than 1 mM, DHK was used to avoid any untested, unspecific, effects of a higher concentration of DHK which, at higher concentrations, is also a weak inhibitor of AMPA/kainate glutamate receptors. If GLAST knockout was not used, blocking glial glutamate uptake solely with 200 μM DHK and 200 μM TBOA only resulted in a 6% decrease in time-integrated glial uptake, compared to control conditions (pale orange bar in Fig. 5.2a).

Thus, on this model, using 200 μM TBOA and 200 μM DHK to pharmacologically block glial glutamate transport changes the total glial glutamate uptake negligibly. Furthermore, even though GLAST is the dominant transporter in the cerebellum, a simple GLAST knockout will only decrease time-integrated glial glutamate uptake and consequent ATP use by 35%. However, combining 200 μM DHK with the GLAST knockout reduces total glial glutamate uptake by 48% (from 89% of the total to 46%).

5.3.3 Single compartment cerebellar model with peak glutamate concentration of 175 μM.

Using the same single compartment model, another simulation was performed using a glutamate concentration of 175 μM to reflect the peak concentration reached outside the climbing fibre – Purkinje cell synapse near glial cells (Dzubay and Jahr, 1999). In this model the transporters are less saturated initially. In control conditions, GLAST takes up 65% of the glutamate released, GLT-1 takes up 18% while EAAT4 accounts for the remaining 17%. As can be seen in Fig. 5.2b, the glial transporters (GLAST + GLT-1) together take up 83% of the glutamate. When a GLAST knockout was modelled, the GLT-1 and EAAT4 uptake rose to 53% and 47% respectively, so total time-integrated glial uptake was only reduced by 36% (from 83% to 53% of the total). When 200 μM DHK was added to the GLAST knockout it was found that glial uptake (now by GLT-1 alone) fell to 27% as a fraction of the total glutamate taken up (the balance being taken up by EAAT4), so total glial uptake was reduced

by 49% (compared to GLAST knockout alone) leaving only 33% of the total glial uptake in control conditions. With the lower peak glutamate concentration used in this model, 200 μM DHK is a high enough concentration to halve the remaining glial uptake of glutamate in a GLAST knockout. When 1 mM DHK was added to the GLAST knockout model, uptake by GLT-1 decreased to only 12% of the total glial uptake in control conditions. When glial glutamate uptake was blocked with 200 μM DHK and 200 μM TBOA, glial uptake accounted for 73% of total glutamate uptake, compared to 83% in control conditions (i.e. dual pharmacological block of glial glutamate uptake resulted in only a 12% decrease in total glial uptake, compared to control).

Thus, on this model, combining GLAST knockout with 200 μM DHK produces a substantial (67%) reduction of total glial glutamate uptake.

5.3.4 Two compartment cerebellar model with all glial transporters in the second compartment.

Next, the single compartment model was adapted into a more realistic two compartment model, to allow glutamate release and uptake by EAAT4 to occur within the first compartment (representing the synapse) where the maximum glutamate concentration reached 2 mM (Wadiche and Jahr, 2001), and with uptake by GLAST and GLT-1 being from a second compartment (representing the surrounding extrasynaptic tissue) where the maximum concentration reached (in control conditions) was 175 μM (concentration taken from Dzubay and Jahr (1999)). The volumes of the two compartments were identical. This model reflects the distribution of transporters seen at the parallel fibre – Purkinje cell synapses, where GLAST and GLT-1 are found in the surrounding Bergmann glia (Danbolt et al., 1992; Rothstein et al., 1994; Chaudhry et al., 1995; Lehre et al., 1995) while EAAT4 is found on the Purkinje cell dendrites (Yamada et al., 1996; Nagao et al., 1997; Dehnes et al., 1998). The glutamate passed from the first to the second compartment across a diffusion barrier with a permeability, P (Fig. 5.1b). This model takes into account the fact that many

glial transporters are further from the synaptic cleft and see a lower concentration of glutamate than the EAAT4 transporters which are situated on the dendrites.

The permeability, P, was set to a value which allowed the concentration in the surrounding tissue (compartment 2) to reach 175 μM in control conditions. The differential equations which must be solved for compartments 1 and 2 are, respectively,:

$$\frac{d[glu]_1}{dt} = \frac{R(t) - U_{eaat4}([glu],[TBOA]) - P([glu]_1 - [glu]_2)}{Volume_1} \tag{5.7}$$

$$\frac{d[glu]_2}{dt} = \frac{P([glu]_1 - [glu]_2) - U_{glast}([glu],[TBOA]) - U_{glt}([glu],[TBOA],[DHK])}{Volume_2} \tag{5.8}$$

where $[glu]_1$ and $[glu]_2$ are the glutamate concentrations in the 2 compartments of $Volume_1$ and $Volume_2$.

This model consisted of two compartments: the first compartment containing the neuronal EAAT4 transporters in the postsynaptic spine, and the second compartment, representing the surrounding extrasynaptic tissue, containing all the glial transporters (Fig. 5.1b). In control conditions, GLAST takes up 66% of the glutamate released, GLT-1 takes up 17%, while EAAT4 accounts for the remaining 16%. As can be seen in Fig. 5.2c, the glial transporters together take up 84% of the glutamate. When a GLAST knockout was modelled, the GLT-1 and EAAT4 uptake increased to 58% and 42% respectively, but the total glial uptake (now by GLT-1 alone) was only reduced by 31%, from 84% to 58% of the total. When 200μM DHK was added to the GLAST knockout model, glial uptake fell from 58% (in the knockout) to 47%, implying that total glial uptake was reduced by 44% compared to the control (wild type) situation. However, when 1 mM DHK was added to the GLAST knockout model, uptake by GLT-1 decreased to 29% of the total time-integrated glutamate uptake (i.e. 50% of the uptake by GLT-1 when GLAST is knocked out and only 35% of the glial uptake in control conditions). Blocking glial glutamate uptake with 200 μM DHK and 200 μM TBOA resulted in only a 10% decrease in glial uptake, compared to control conditions.

On this more realistic model, therefore, pharmacological block of transporters with 200 μM DHK and 200 μM TBOA is ineffective at reducing total glial glutamate uptake and ATP use, while combining GLAST knockout and 200 μM DHK reduces it by 44%.

5.3.5 Two compartment cerebellar model with 50% of GLAST transporters in the first compartment.

An even more realistic two compartment model was then produced in which the first compartment contained the EAAT4 transporters and 50% of the GLAST transporters and the second compartment contained all GLT-1 and 50% GLAST transporters (Fig. 5.1c), reflecting the transporter distribution reported in Fig. 13a of Danbolt (2001). In control conditions, GLAST takes up 74% of the glutamate released, GLT-1 takes up 13% while EAAT4 accounts for the remaining 13%. As can be seen in Fig. 5.2d, the glial transporters together take up 87% of the glutamate. When a GLAST knockout was modelled, the GLT-1 and EAAT4 uptake increased to 57% and 43% respectively, and total glial uptake was inhibited by 34%. When 200 μM DHK was added to the GLAST knockout model it was found that GLT-1 uptake fell from 57% (in the knockout) to 47%, and glial uptake was reduced by 46% compared to normal (wild type) conditions. However, when 1 mM DHK was added to the GLAST knockout model, uptake by GLT-1 decreased to 29% of the total time-integrated glutamate uptake (i.e. 51% of the uptake by GLT-1 when GLAST is knocked out and 33% of the glial uptake in normal conditions). Blocking glial glutamate uptake with 200 μM DHK and 200 μM TBOA resulted in a 5% decrease in glial uptake, compared to control conditions.

Again, pharmacological block of transporters with 200 μM DHK and 200 μM TBOA is ineffective at reducing total glial glutamate uptake and ATP use, while combining GLAST knockout and 200 μM DHK reduces it by 46%.

5.3.6 Predicted glutamate time courses vary under each condition.

Under control conditions the transporter density was set to clear low concentrations of glutamate with a time constant of 10 ms for the one compartment model (see section 5.3.2, above). For the millimolar glutamate concentration reached during synaptic transmission, clearance is slower because the transporters are saturated. As expected, the glutamate takes longer to clear when GLAST is knocked out and/or transporters are blocked using DHK and TBOA (Fig. 5.3a-f). In the case of the two compartment model, when transporters are knocked out or blocked, the glutamate in the second compartment rises above 175 μM and requires longer to be taken up by the remaining active transporters (Fig. 5.3d,f).

5.3.7 Predicted glutamate uptake in postnatal day 10 rat cortex.

5.3.7.1 Postnatal day 10 cortical two compartment model

The modelling above was carried out for cerebellum. In order to assess whether knocking out one of the glial glutamate transporters (GLT-1 or GLAST) would have a large effect on the time integrated glutamate uptake in cerebral cortex, as suggested by Voutsinos-Porche et al. (2003), the two compartment models were adjusted to reflect the distribution and density of glutamate transporters present in the neocortex at postnatal day 10 (P10, as used by Voutsinos-Porche et al. (2003)).

Glutamate was assumed to be released and then taken up by GLT-1 (the dominant transporter in the cortex, see references in Danbolt (2001)), GLAST, EAAT4 and EAAC1 (excitatory amino-acid carrier 1). EAAC1 transporters are located on neuronal cell bodies and dendrites (Rothstein et al., 1994) and so were placed in the first compartment along with EAAT4 transporters (which appear transiently in the rat forebrain, reaching a peak around P10 (Furuta et al., 1997)), while GLT-1 and GLAST were present in the second compartment. The K_M values for uptake of glutamate by all transporters were as used for the previous models (sections 5.3.2) with the addition of a K_M value for uptake of glutamate by EAAC1 of 15.2 μM (Dowd et al., 1996). K_i values of TBOA for GLAST, GLT-1 and EAAT4

were as above (section 5.3.2) and for EAAC1 was 4.9 μM (Grewer et al., 2000). The Ki value of DHK for GLT-1 was also taken as above (section 5.3.2).

The average concentrations of GLAST, GLT-1 and EAAT4 in the cerebral cortex of a P10 rat were calculated from Fig. 1b of Furuta et al. (1997) using the known concentrations of transporters in adult cerebellum (Lehre and Danbolt, 1998; Dehnes et al., 1998, see section 5.3.2, above). The concentration of EAAC1 in P10 cortex was also calculated from Fig. 1b of Furuta et al. (1997) using the fact that the concentration of EAAC1 in adult cortex is ~ 1% (Danbolt, personal communication) of that of GLT-1, which is ~ 9360 μm^{-3} (calculated as 78% of the GLT-1 level in adult rat hippocampus, 12000 μm^{-3} (Lehre et al., 1995; Lehre and Danbolt, 1998)). Therefore, the ratio of GLT-1: GLAST: EAAC1: EAAT4: in P10 rat cortex was taken as 4800: 2040: 273: 252 per μm^3.

This model predicts that under control conditions glial glutamate uptake accounts for 66% of total time integrated glutamate uptake: GLT-1 takes up 59% while GLAST takes up 7% of the glutamate released. Neuronal uptake accounts for the remaining 34% with EAAT4 and EAAC1 each taking up 17% of the glutamate released (Fig. 5.4a). When a GLT-1 knockout was modelled, the GLAST uptake increased to 63% of the total (a 9-fold increase compared to control conditions) while EAAT4 and EAAC1 uptake each increased to 18% (Fig. 5.4a). The small size of the increase in the fraction of glutamate uptake by neuronal transporters reflects the fact that these high affinity transporters are already almost saturated for much of the time. In this condition glial glutamate uptake accounts for 63% of total glutamate uptake, ie only a 5% decrease compared to the 66% predicted in control conditions. Voutsinos-Porche et al. (2003) also used GLAST knockouts. When a GLAST knockout was modelled, glutamate uptake by GLT-1 increased to 66% while EAAT4 and EAAC1 uptake each remained at 17% (Fig. 5.4a). Thus, knocking out GLAST has no effect on the total time-integrated glial glutamate uptake compared to control conditions: glial uptake accounts for 66% of the total glutamate uptake in both cases.

Thus, knocking out either GLT-1 (the dominant transporter in the forebrain) or GLAST is not predicted to have a large effect on glial glutamate uptake and downstream ATP use and glucose uptake, apparently contradicting the experiments of Voutsinos-Porche et al. (2003), who attributed a 60% and 68% decrease of glucose uptake in the GLT and GLAST knockouts, respectively, to less energy expenditure on glutamate uptake.

5.3.7.2 Two compartment model for P10 cortex with GLAST in both compartments

The two compartment model (section 5.3.7.1) was then adjusted so that EAAT4, EAAC1 and 50% of GLAST transporters were present in the first compartment, with GLT-1 and the remaining GLAST transporters in the second compartment. This model predicts that under control conditions glial glutamate uptake accounts for 76% of the total glutamate uptake. GLAST takes up 41% of the glutamate released, GLT-1 takes up 35%, while EAAT4 and EAAC1 each account for 12% (Fig. 5.4b). When a GLT-1 knockout was modelled, the GLAST uptake increased to 74% while EAAT4 and EAAC1 uptake each increased to 13% (Fig. 5.4b). Glial glutamate uptake then accounted for 74% of total glutamate uptake, ie a negligible 3% decrease compared to in control conditions. When a GLAST knockout was modelled, glutamate uptake by GLT-1 increased to 59%, while EAAT4 and EAAC1 uptake increased to 20% and 21%, respectively (Fig. 5.4b). Knocking out GLAST decreased the glial glutamate uptake to 59%, a 22% decrease compared to control conditions. Surprisingly, therefore, although GLT-1 is the dominant transporter in the cerebral cortex, knocking out GLAST, rather than GLT-1, is predicted to have a larger effect on the time integrated glial glutamate uptake (but even then only a 22% effect). This reflects both the higher affinity of GLT-1 (it is more saturated and cannot increase its uptake much when GLAST is knocked out) and the fact that GLAST is present in both compartments in this model.

In contrast to the large effect expected from the results of Voutsinos-Porche et al. (2003), knocking out either GLT-1 or GLAST results in only a 3% or 22% reduction in glial

glutamate uptake and so would be expected to have a correspondingly small effect on the associated ATP use and glucose uptake into astrocytes.

5.3.8 Blocking glial glutamate transport does not cause a large reduction in oxygen consumption in response to neural stimulation

When glutamate was applied to cerebellar slices, a decrease in the extracellular oxygen concentration (indicating an increased oxygen consumption) was observed (Fig. 5.5a). Stimulating the parallel fibres also led to a transient decrease in extracellular oxygen concentration near the Purkinje cells that the parallel fibres project to, confirming that a change in oxygen consumption due to increased neural activity was detectable by the electrode (Fig. 5.5b,c).

According to the ANLS hypothesis, if glutamate uptake and downstream ATP use and glycolysis in astrocytes were blocked, then neurons would not receive lactate for oxidation in their mitochondria. In this case we would expect that blocking glial glutamate uptake should reduce the oxygen use associated with neural activity.

Initially, glial glutamate transporters were blocked using TBOA and DHK. However, blocking glutamate uptake with 200 μM TBOA alone or 200 μM TBOA and 200 μM DHK combined had no significant effect on the oxygen consumption in response to electrical stimulation of parallel fibres ($p = 0.90$, $n = 2$ and $p = 0.22$, $n = 2$, respectively). Although the numbers of slices studied are small, this is in agreement with my model (see sections 5.3.2 – 5.3.5), which predicts that using 200 μM TBOA and 200 μM DHK to pharmacologically block glial glutamate transport leads to a decrease in time integrated glial glutamate uptake of only 5 - 12% and, therefore, one would not expect to see a large effect on ATP consumption, nor on downstream lactate-fuelled oxygen consumption. Although the uptake rate is slowed in the presence of pharmacological blockers, the persisting glutamate is still mostly taken up into glia (both because EAAT4 is largely saturated and because of the low density of EAAT4).

Glial glutamate uptake was then reduced by combining genetic knockout of the GLAST glutamate transporters with pharmacological block of the GLT-1 glutamate transporters using 200 μM DHK. The models described above predict that this strategy will reduce glial glutamate uptake by 44 – 67%.

The initial resting oxygen level in slices from GLAST knockout mice was 5.5 ± 0.8% (n = 11), which was similar to the initial concentration measured in wild type slices (6.1 ± 0.7%, n = 3, not significantly different, p = 0.58). This suggests that the basal oxygen consumption of slices taken from both animals is similar. The gradient of the transient decrease produced by parallel fibre stimulation (Fig. 5.5b,c) was not significantly different in knockout and wild type slices (p = 0.47, Fig. 5.5d). In addition, the oxygen response to parallel fibre stimulation was not significantly different in slices from GLAST knockout mice in the presence of 200 μM DHK to that in slices from wildtype mice in control conditions (p = 0.75, Fig. 5.5d). These data suggest no effect of uptake block on O_2 consumption, apparently contradicting the ANLS hypothesis.

However, in slices from GLAST knockout mice, application of 200 μM DHK led to a small decrease in the oxygen consumption in response to parallel fibre stimulation which approaches significance (p = 0.06, n = 11, Fig. 5.5e, striped bars), although 83 ± 8% of the oxygen response was preserved in the presence of DHK compared to control conditions (in knockout slices). This suggests that interslice variability may be masking an effect of knocking out GLAST and that the number of slices studied should be increased to assess whether the variability can be reduced. In comparison to the results obtained in knockout slices, in slices from wild type littermates application of 200 μM DHK did not result in a significant change in oxygen consumption in response to the electrical stimulation of parallel fibres (p = 0.84, n = 3, Fig. 5.5e, white bars). This is not surprising as GLAST, which remains active in this condition, is the major glutamate transporter in the cerebellum (Lehre and Danbolt, 1998).

5.3.9 Pre- and post-synaptic oxygen use in response to parallel fibre stimulation

To quantify the energy usage on different signalling processes, I applied different pharmacological blockers while stimulating the parallel fibres and monitoring oxygen concentration in the molecular layer.

Post-synaptic action potentials evoked by synaptic transmission were inhibited using 20 μM muscimol, a $GABA_A$ agonist which hyperpolarises the Purkinje cells (Caesar et al., 2003). In the presence of muscimol, 80 ± 7% of the oxygen consumption in response to parallel fibre stimulation was preserved (n = 4, significantly reduced, p = 0.05, Fig. 5.6a,b), implying that post-synaptic action potentials evoked by synaptic transmission account for 20% of the oxygen usage at the parallel fibre - Purkinje cell synapse following parallel fibre stimulation (Fig. 5.6c). NBQX (10 μM), which blocks post-synaptic AMPA receptors (and downstream action potentials), reduced the oxygen response to 41 ± 7% (n = 11, significantly reduced, $p = 1.2 \times 10^{-5}$, Fig. 5.6a,b) of the original response. This suggests that AMPA receptor mediated effects of synaptic transmission account for 39% (80% - 41%) of oxygen usage (Fig. 5.6c). Application of 250 μM cadmium, which blocks glutamate release by directly blocking presynaptic Ca^{2+} channels, had the strongest effect of all drugs used, blocking all except 7 ± 4% (n = 5, significantly reduced, p = 0.0003, Fig. 5.6a,b) of the oxygen response to parallel fibre stimulation. This suggests that pre-synaptic action potentials account for 7% of the oxygen usage (Fig. 5.6c), and that voltage-gated calcium entry, vesicle recycling and transmitter uptake use 34% of the oxygen usage (the difference between the 41% and 7% responses remaining in the presence of NBQX and cadmium: Fig. 5.6c).

5.4 Discussion

5.4.1 Modelling glutamate uptake at the parallel fibre – Purkinje cell synapse

I produced a Mathcad model of glutamate uptake at a parallel fibre – Purkinje cell synapse, in order to suggest possible experiments to test the astrocyte-neuron lactate shuttle theory (see section 5.3.8). Model-dependent differences in predicted glutamate uptake were

minimal. The best strategy for reducing glial glutamate uptake was predicted to be to use a GLAST knockout, and then add DHK to reduce uptake by the remaining glial GLT-1 transporters. DHK is a selective inhibitor of the GLT-1 glutamate transporter but, at higher concentrations, it is also a weak inhibitor of AMPA/kainate glutamate receptors, so 200 μM DHK was used in all experiments as opposed to the 1 mM that was also considered in the modelling study (sections 5.3.2-5.3.5, above) in order to avoid any untested effects of a higher concentration of DHK. For all the models considered, the combination of GLAST knockout and 200μM DHK is predicted to reduce total glial glutamate uptake by at least 44%.

Experimentally, P21 mice were used, while the model of glutamate uptake used the transporter density ratios of adult animals (Lehre and Danbolt, 1998; Dehnes et al., 1998). During development GLAST and GLT-1 concentrations increase until reaching adult levels around postnatal day 35 (Furuta et al., 1997; Ullensvang et al., 1997). Furthermore, the largest increase in GLT-1 levels occurs between postnatal days 21 and 35 (Ullensvang et al., 1997). Considering this alone suggests that the model may predict a smaller effect of knocking out GLAST transporters on glial glutamate uptake than may occur experimentally using P21 animals. The lower levels of GLT-1 present at P21 may lead to a slight decrease in the amount of glial uptake present and a slight increase in the amount of neuronal uptake present when GLAST is knocked out, compared to that predicted by the model. This implies that a greater effect on glial glutamate uptake, and the accompanying ATP use, should be seen experimentally than is predicted by the model. However, the levels of EAAT4 also increase during development, reaching their adult level between postnatal days 10 and 24 (Furuta et al., 1997), so there may be a slight reduction (compared to the model) in uptake by EAAT4 in the P21 animals used due to a lower concentration of neuronal transporters at this age. Overall, therefore, the glial glutamate uptake at P21 is likely to be similar to that predicted by the model using an adult distribution of transporters.

5.4.2 Modelling glutamate uptake in the P10 rat cortex

I also produced a model of glutamate uptake in P10 rat cortex in order to assess the results of Voutsinos-Porche et al. (2003). The model for cerebellum was adjusted to account for the different relative number of transporters present in the cortex. The presence of an extra transporter, EAAC1, had to be taken into account, as did the difference in age as the contribution of each transporter varies with development. By incorporating these data into the two compartment models above I was able to predict how well GLT-1 or GLAST knockout (as used by Voutsinos-Porche et al. (2003)) would be expected to reduce glial glutamate uptake in a P10 animal. My results suggest that using a GLT-1 knockout does not have the large effect on glial uptake that was proposed by Voutsinos-Porche et al. (2003). Results from the two compartment model (with all glial glutamate transporters in the second compartment) predicted that knocking out GLT-1 would only reduce total glial glutamate uptake by 5% (Fig. 5.4a). Similarly, results from the two compartment model where half the GLAST transporters are in the first compartment predicted that knocking out GLT-1 would reduce total glial glutamate uptake by only 3% (Fig. 5.4b). These results predict a much smaller effect of GLT-1 knockout on glial glutamate uptake and hence, associated ATP use, than the ~ 60% reduction in glucose utilisation measured by Voutsinos-Porche et al. (2003).

In addition to using GLT-1 knockout mice, Voutsinos-Porche et al. (2003) also used GLAST knockout mice. They found that in slices from GLAST knockout mice, as in slices from GLT-1 knockout mice, 2-deoxyglucose uptake (and hence glucose utilisation) was also reduced significantly (by ~ 68%). Again, the two compartment models contradict these results, predicting that glial glutamate uptake is reduced by, at most, 22% in a GLAST knockout animal (Fig. 5.4).

These modelling results raise the possibility that the decrease in activity-induced glucose uptake seen by Voutsinos-Porche et al. (2003) was in fact a side-effect of the transporter knockouts, rather than a direct effect on ATP consumption evoked by glutamate

uptake. They thus undermine the support given to the ANLS hypothesis by Voutsinos-Porche et al. (2003).

5.4.3 Co-ordination of the energy supply to neurons by glia

The ANLS hypothesis predicts that neural activity will cause (i) glucose use in astrocytes dependent on glutamate uptake, (ii) ATP production that occurs first in astrocytes, then in neurons, and (iii) oxygen use that is blocked by blocking glutamate uptake (see Chapter 1, Fig. 1.4). I performed experiments to test the third of these, whether oxygen use is blocked by blocking glutamate uptake, after first modelling the expected results of pharmacological block and genetic knockout approaches, as discussed above. Pharmacological block of glial glutamate uptake using TBOA and DHK was found to be ineffective both in the modelling and experimentally. In addition, the use of TBOA presents an interpretational problem as glutamate uptake in neurons will be blocked in addition to glial uptake. This could cause a rapid accumulation of glutamate in the synaptic cleft, which could desensitise glutamate receptors. As the optimal strategy for reducing glial glutamate uptake, to test the ANLS hypothesis, I therefore combined pharmacological block of GLT-1 transporters using DHK and genetic knockout of GLAST transporters in order to significantly reduce uptake, and tested whether oxygen use was reduced.

Simplistically, if the ANLS hypothesis was correct, one might expect a reduction of glutamate transport to produce a corresponding reduction in the generation of lactate and a proportional decrease in O_2 usage. Alternatively, if the ANLS idea is incorrect, and neuronal oxidative phosphorylation employs glucose taken up directly into neurons, then blocking glutamate uptake should not affect O_2 use (although, as discussed below, changes in synaptic charge entry caused by uptake block may then predict an *increase* of O_2 usage).

Experimentally, comparing wild type animals with the GLAST knockout in the presence of DHK there was no significant difference in the oxygen response evoked by

parallel fibre stimulation. Since the knockout plus DHK should reduce glial uptake by 50%, this argues against astrocyte glutamate uptake regulating neuronal oxidative phosphorylation.

There are two possible arguments against this conclusion, however. First, if neuronal lactate transporters are nearly saturated, then even a decrease of ~50% in lactate release from astrocytes (as a result of blocking glutamate uptake) may not much affect the lactate supply to neurons and so there may only be a small change in the amount of lactate-powered neuronal oxidative phosphorylation (if correct this would undermine the ANLS hypothesis, in that astrocyte lactate release would have only a weak control over the rate of neuronal oxidative phosphorylation). Secondly, applying 200 μM DHK to slices from GLAST knockout animals (a manoeuvre predicted by the modelling to reduce glial uptake by 20%) reduced the oxygen consumption seen in response to parallel fibre stimulation by 17% (an almost significant reduction, $p = 0.06$). This might suggest that glial glycolysis does indeed supply lactate to neuronal mitochondria, and that the lack of a difference seen when comparing wild-type slices with GLAST knockout slices in the presence of DHK is a result of the variability inherent in comparing data from different slices obscuring a difference which does actually exist.

Considering the changes in synaptic charge entry into Purkinje cells that are produced by uptake block leads to further interpretational problems. Marcaggi et al. (2003) found that knocking out GLAST transporters caused a 2.2-fold increase in the synaptic charge transfer in Purkinje cells in response to a train of parallel fibre stimuli (as used in these experiments: see section 5.2.1). Similarly, application of 200 μM DHK to slices from GLAST knockout animals caused a further 2.4-fold increase in the charge transfer (Marcaggi et al., 2003). This increased charge transfer will result in a greater metabolic load in the Purkinje cells in knockout slices than in the wild type slices and thus, if ions entering as a result of synaptic activity are pumped out using power provided by oxidative phosphorylation, one would expect a greater oxygen consumption to occur in knockout slices (and in the presence of DHK) than in wild type slices (although this would not be the case if

neurons use glycolytically produced ATP to pump the ions out). This increase in O_2 use could easily be provided if neurons regulate their oxidative phosphorylation autonomously, but could apparently not occur if neuronal oxidative phosphorylation is exclusively powered by astrocyte lactate, the amount of which is set by the amount of glutamate taken up and so will not have increased in this situation. This means that the experimentally observed lack of a significant difference in the O_2 responses in knockout and wild type slices to parallel fibre stimulation, and the lack of a significant difference seen when DHK was applied to slices in the knockout, could be explained by any of the following hypotheses:

(i) the ANLS hypothesis is incorrect (so lack of uptake and lactate release has no effect on O_2 use) and the extra ion pumping occurring in Purkinje cells is powered by neuronal glycolysis;

(ii) lack of uptake does reduce lactate export to neurons, tending to lower neuronal O_2 consumption, but there is a compensating increase of neuronal O_2 use due to the greater synaptic charge entry described above (resulting in no net change in O_2 use) – this extra neuronal oxidative phosphorylation would presumably need to be powered by neuronal glycolysis, again undermining the idea that neuronal mitochondria are fed solely by astrocyte lactate;

(iii) lack of uptake does reduce lactate export to neurons, but neuronal lactate transporters are saturated, so that this decreased export has little effect on neuronal oxidative phosphorylation – again this undermines the ANLS hypothesis.

In summary, although there are interpretational complications, my data do not support the ANLS hypothesis.

5.4.4 Relative contributions of synaptic processes to oxygen usage at the parallel fibre - Purkinje cell synapse

I investigated oxygen consumption at the glutamatergic synapse between parallel fibres and Purkinje cells. By applying selective blockers I have determined the relative oxygen usage of various subcellular processes of synaptic transmission. Blocking synaptic transmission at different points led to differential decreases in the extracellular oxygen

concentration and, hence, the oxygen consumption by the slice. From the results in transverse slices, the process accounting for the largest proportion (39%) of oxygen consumption in the Purkinje cell in response to parallel fibre stimulation were the AMPA receptor mediated effects of synaptic transmission. Presynaptic action potentials and postsynaptic action potentials accounted for 7 and 20% of oxygen usage respectively. The remaining 34% of oxygen consumption was due to voltage-gated calcium entry and vesicle recycling and uptake (Fig. 5.6c).

5.4.5 Conclusions

My simulations undermine the claim of Voutsinos-Porche et al. (2003) that transporter knockout decreases astrocyte ATP use and downstream export of lactate to neurons. Experimentally I find little change of activity induced O_2 consumption when uptake is blocked by ~50%, undermining the ANLS hypothesis. My data on the use of O_2 on different cellular processes extend the findings of Offenhauser et al. (2005) who measured oxygen consumption by Purkinje cells in vivo. Offenhauser et al. (2005) concluded that at the climbing fibre - Purkinje cell synapse, where many AMPA receptors on an extensive dendritic tree are activated, oxygen consumption was driven by postsynaptic responses (this includes the ATP used on reversing ion influx through synaptic AMPA receptors and also that used on reversing ions entering during action potentials). My findings show that this is also the case at the parallel fibre - Purkinje cell synapse (Fig. 5.6c) in cerebellar slices.

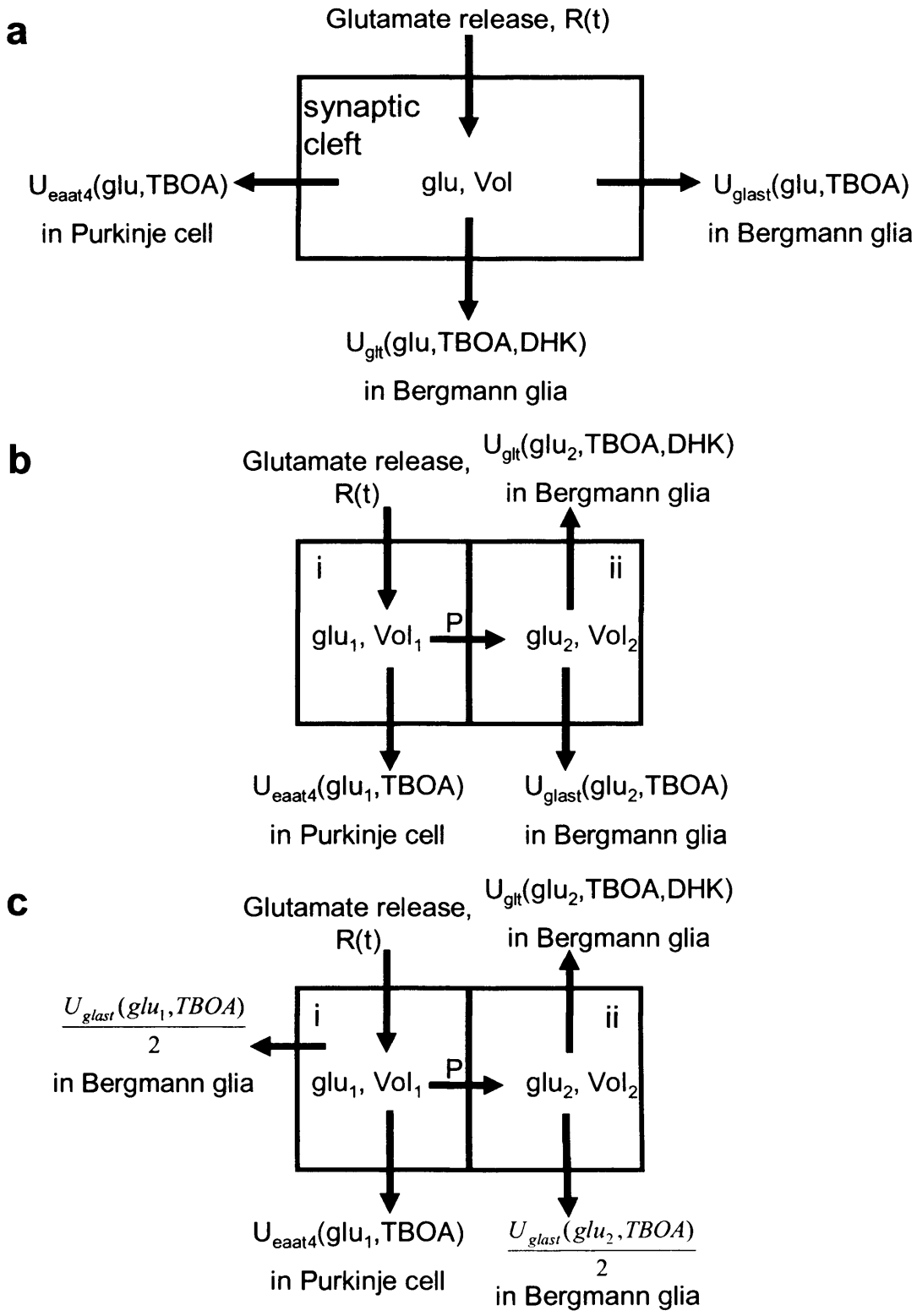

Figure 5.1 Diagrams of models of glutamate uptake at the parallel fibre – Purkinje cell synapse. **a** 1 compartment model with a peak glutamate concentration of 1 mM or 175 μM. **b** 2 compartment model. 1st compartment has a peak glutamate concentration of 2 mM and all glial transporters are situated in 2nd compartment. **c** 2 compartment model with 50% of GLAST located in the 1st compartment.

R(t) = glutamate release. U(glu,TBOA,DHK) = glutamate uptake (dependent on concentrations of glutamate, TBOA and DHK respectively). glu = glutamate concentration. Vol = volume of compartment. P = permeability between compartments. **i** = synaptic cleft. **ii** = surrounding extrasynaptic tissue.

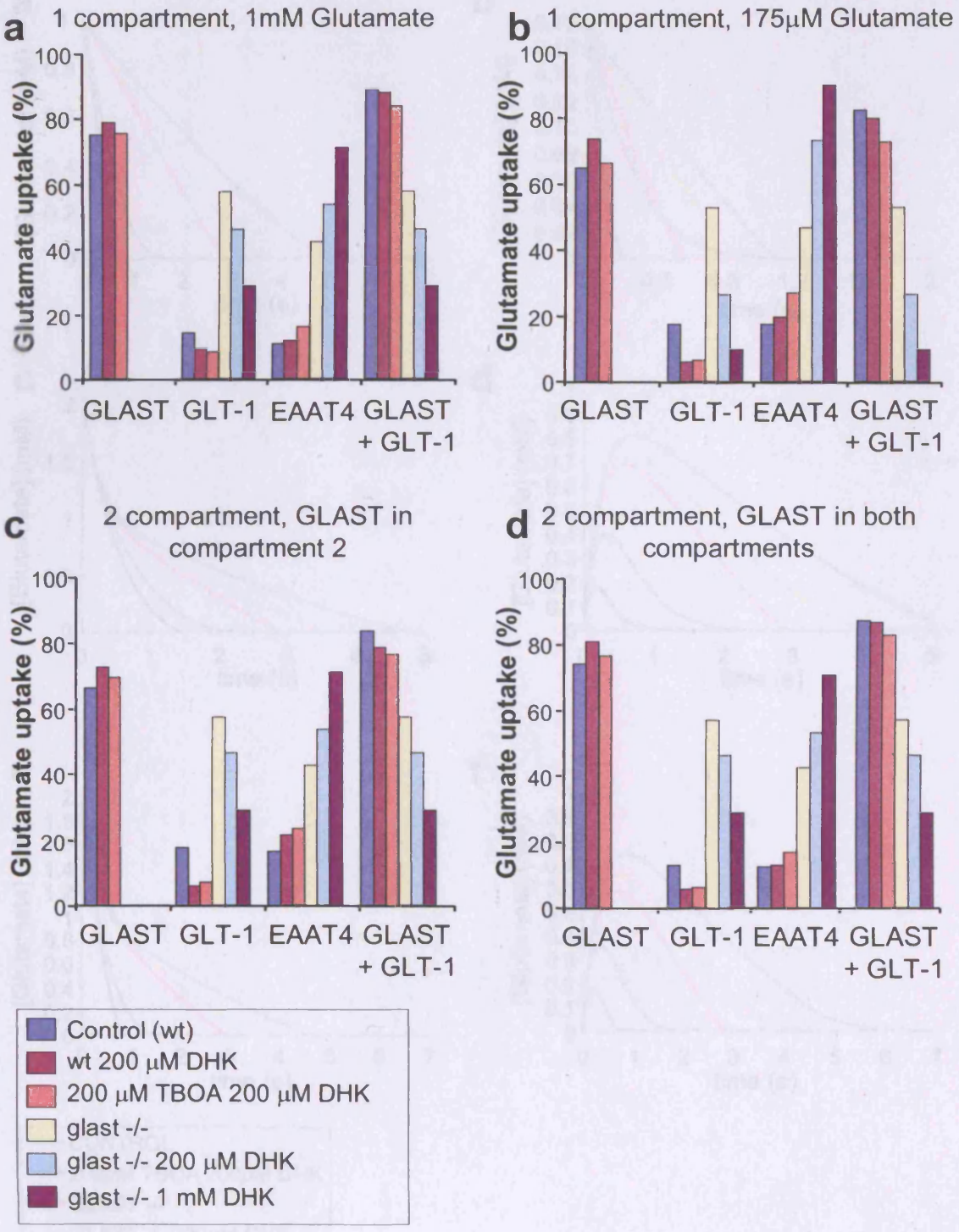

Figure 5.2 Comparison of predicted glutamate uptake by glutamate transporters in cerebellar models, integrated over time after glutamate release. Key applies to all panels. **a** Results for 1 compartment model with peak glutamate concentration of 1 mM. **b** Results for 1 compartment model with peak glutamate concentration of 175 μM. **c** Results for 2 compartment model with all GLAST transporters in 2nd compartment and a peak glutamate concentration in first compartment of 2 mM. **d** Results for 2 compartment model with 50% of GLAST in 1st compartment and a peak glutamate concentration in first compartment of 2 mM.

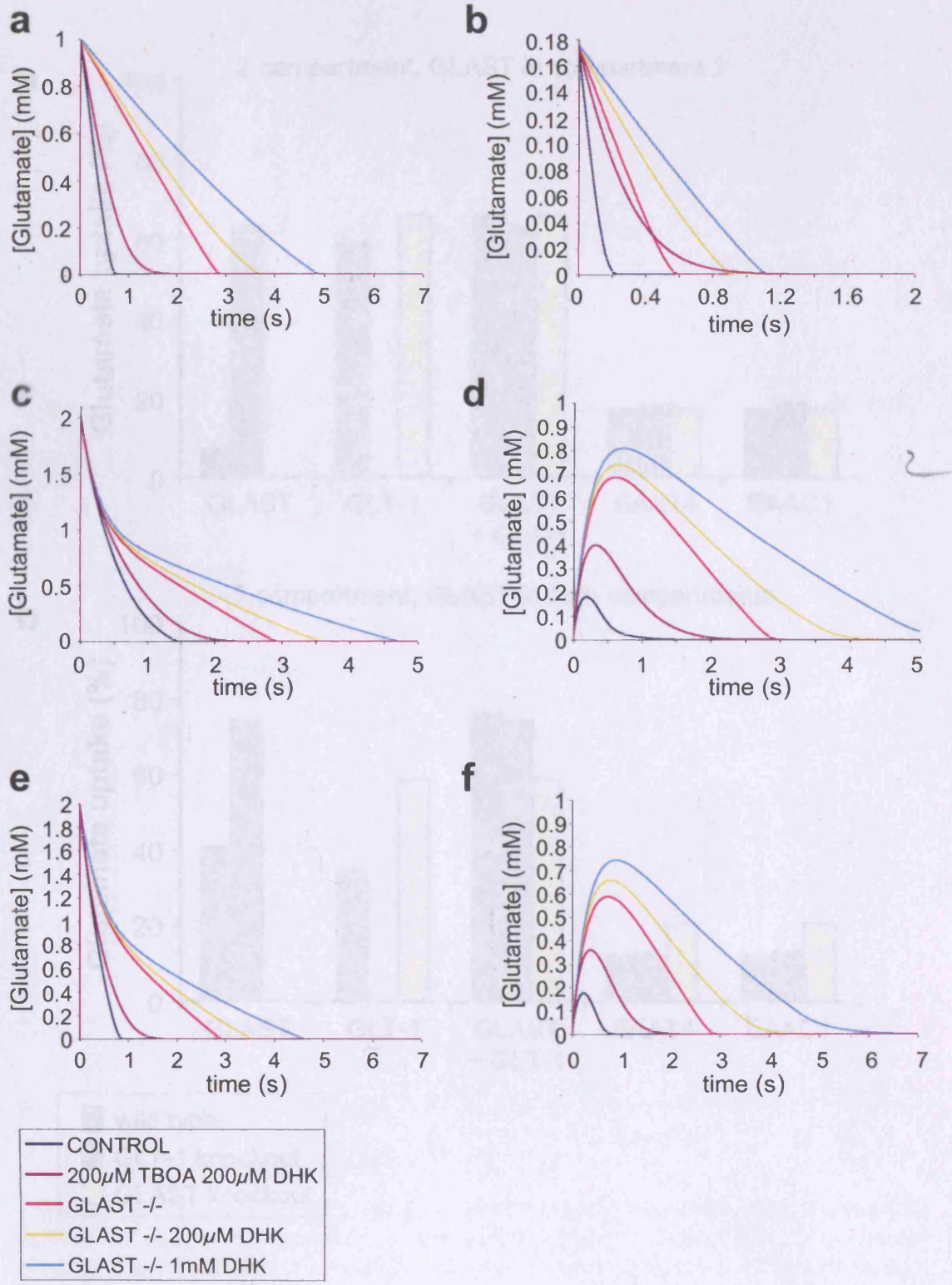

Figure 5.3 Predicted time course of glutamate concentration for cerebellar models. **a** Results for 1 compartment model with peak glutamate concentration of 1 mM. **b** Results for 1 compartment model with peak glutamate concentration of 175 μM. **c,d** Results for 2 compartment model with peak glutamate concentration of 1 mM, all GLAST transporters in 2nd compartment. **c** shows results for 1st compartment, **d** for 2nd compartment. **e,f** Results for 2 compartment model with peak glutamate concentration of 1 mM, 50% GLAST in 1st compartment. **e** results for 1st compartment, **f** results for second compartment.

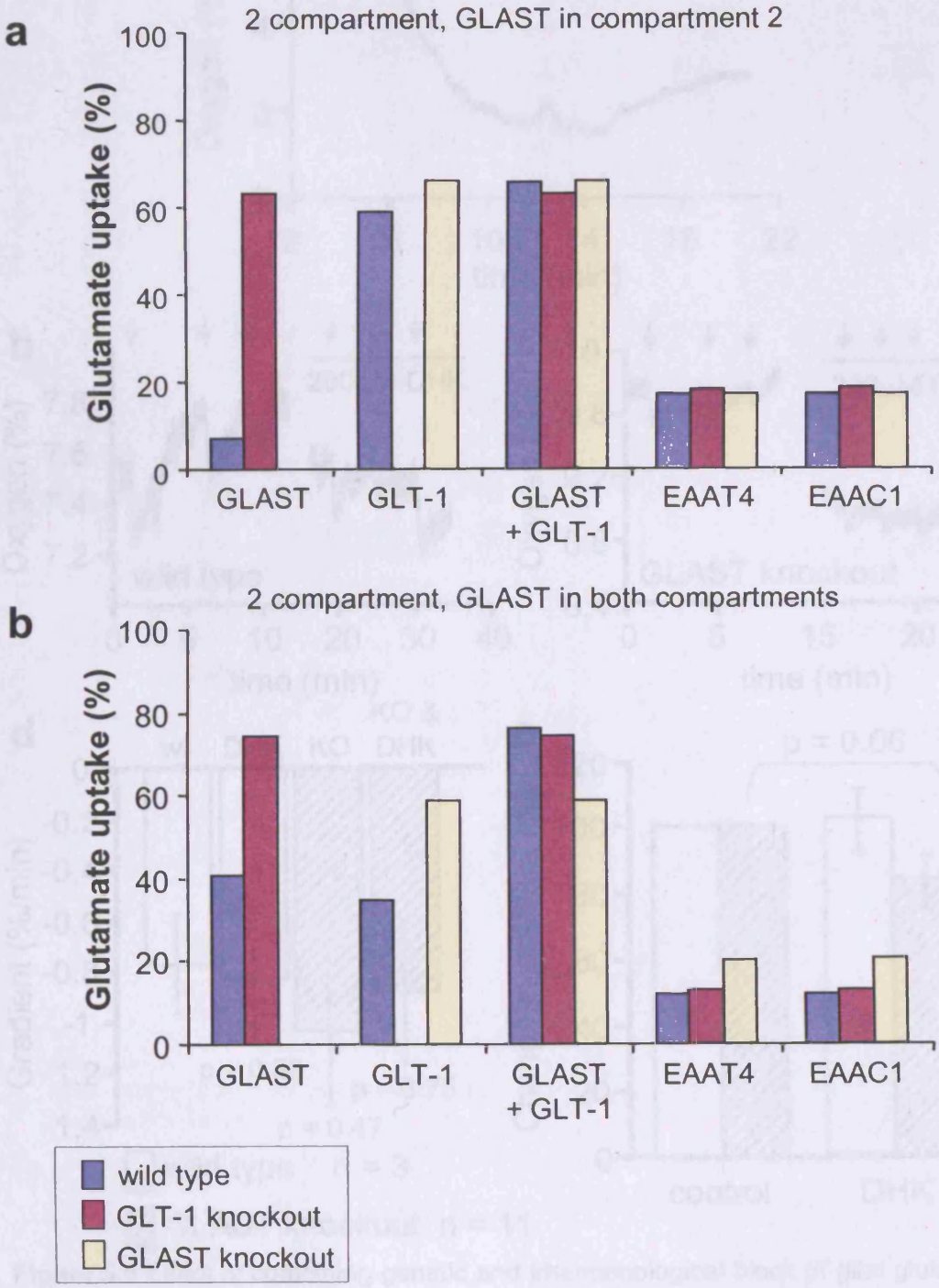

Figure 5.4 Comparison of predicted glutamate uptake by glutamate transporters in the cerebral cortex, integrated over time after glutamate release. Key applies to all panels. **a** Results for 2 compartment model with all GLAST transporters in 2nd compartment. **b** Results for 2 compartment model with 50% of GLAST in 1st compartment.

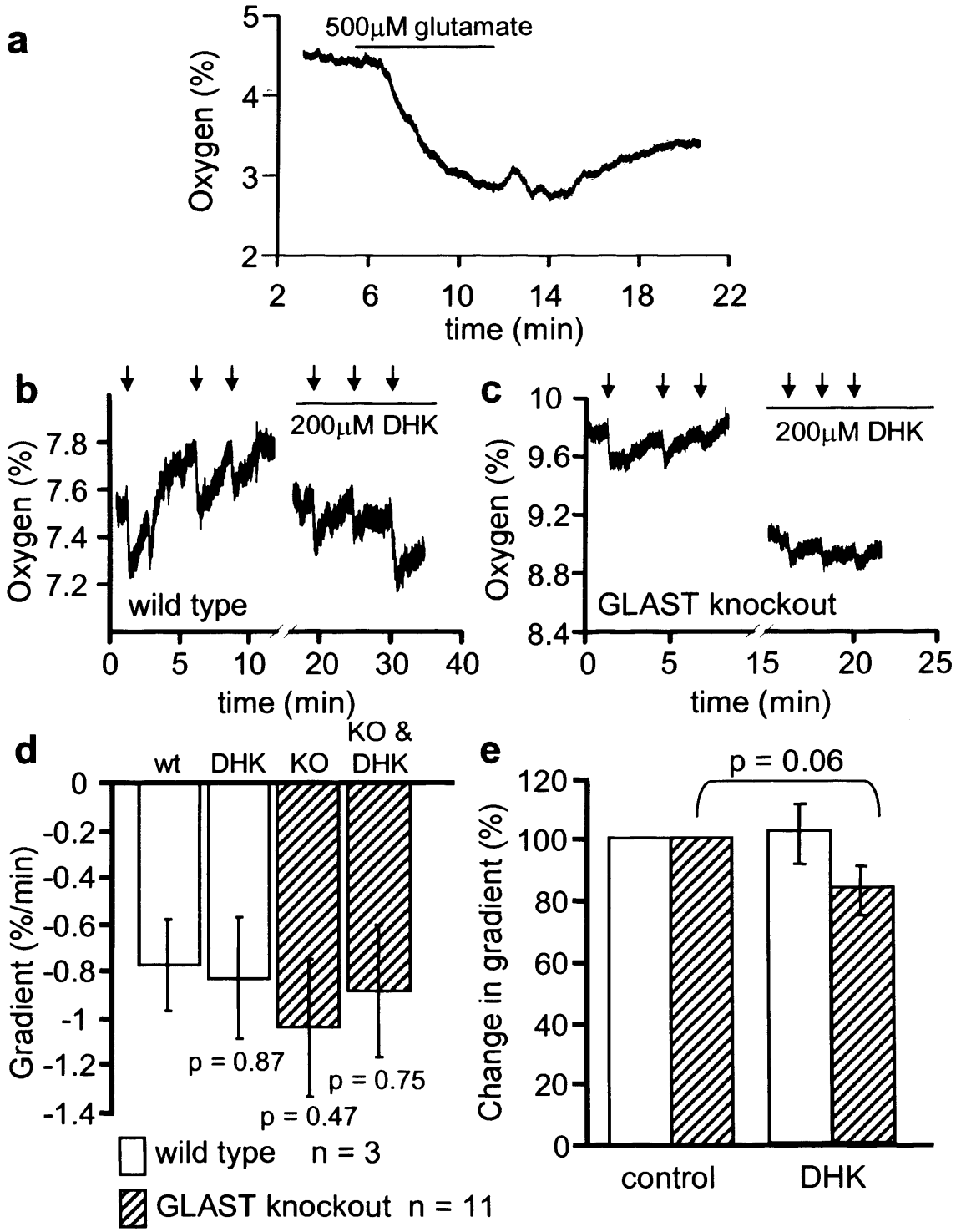

Figure 5.5 Effect of combining genetic and pharmacological block of glial glutamate uptake on oxygen consumption in cerebellar slices. **a:** Application of glutamate evoked a decrease in the extracellular oxygen concentration in a wild type slice. **b,c:** Parallel fibre stimulation (arrows) led to a transient decrease in extracellular oxygen concentration. In the presence of DHK this response was preserved in wild type (**b**) slices and was slightly reduced in GLAST knockout (**c**) slices. **d:** Applying 200μM DHK, knocking out GLAST (KO) and combining knockout and DHK caused no significant difference to the oxygen response to stimulation, compared to in wild type slices (wt) **e:** 200μM DHK has no significant effect on the oxygen consumption in response to parallel fibre stimulation in the wild type ($p = 0.84$, white bars). Application of 200μM DHK to transverse cerebellar slices from knockout animals causes a small but not quite significant decrease in oxygen consumption in response to parallel fibre stimulation ($p = 0.06$, striped bars).

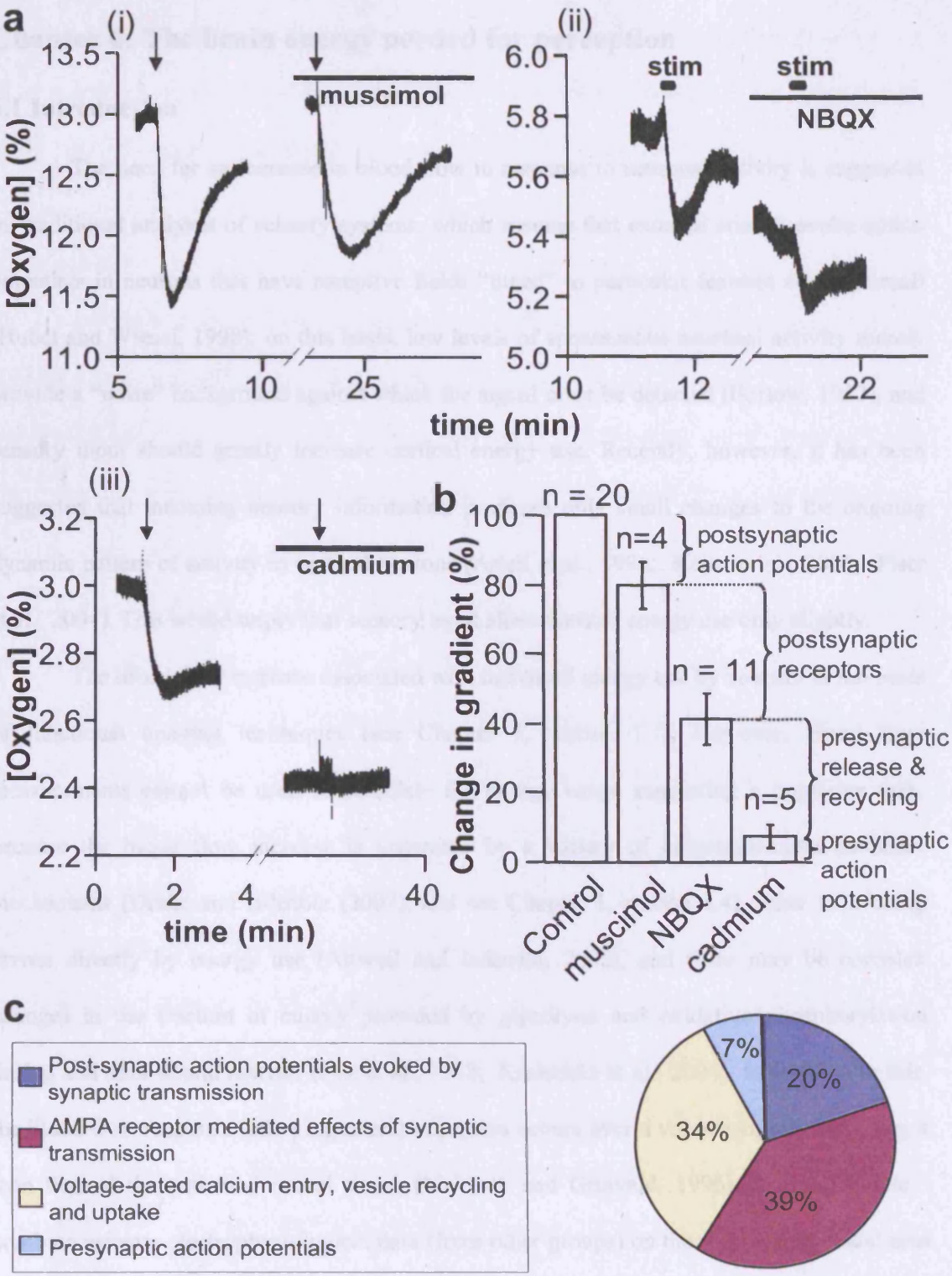

Figure 5.6 Separating pre- and post-synaptic oxygen use in response to parallel fibre stimulation in transverse cerebellar slices. **a:** Example data traces showing transient decreases in oxygen concentration in response to parallel fibre stimulation. In these examples 79%, 42% and 5% of the oxygen responses were preserved in the presence of muscimol (**i**), NBQX (**ii**) and cadmium (**iii**), respectively. **b:** On average, 80 ± 6.7%, 41 ± 7.3% and 7 ± 3.6% of the oxygen response to parallel fibre stimulation were preserved in the presence of muscimol, NBQX and cadmium, respectively. **c:** Relative contributions of synaptic processes to oxygen usage.

Chapter 6: The brain energy needed for perception

6.1 Introduction

The need for an increase in blood flow in response to neuronal activity is suggested by traditional analyses of sensory systems, which assume that external stimuli evoke action potentials in neurons that have receptive fields "tuned" to particular features of the stimuli (Hubel and Wiesel, 1998): on this basis, low levels of spontaneous neuronal activity merely provide a "noise" background against which the signal must be detected (Barlow, 1957), and sensory input should greatly increase cortical energy use. Recently, however, it has been suggested that incoming sensory information produces only small changes to the ongoing dynamic pattern of activity in cortical neurons (Arieli et al., 1996; Kenet et al., 2003; Fiser et al., 2004). This would imply that sensory input alters cortical energy use only slightly.

The blood flow increase associated with increased energy use by neurons is the basis of functional imaging techniques (see Chapter 1, section 1.7). However, blood flow measurements cannot be used to calculate the energy usage supporting a cognitive task, because the blood flow increase is generated by a variety of neurotransmitter-mediated mechanisms (Drake and Iadecola (2007), and see Chapter 1, section 1.4) rather than being driven directly by energy use (Attwell and Iadecola, 2002), and there may be complex changes in the fraction of energy provided by glycolysis and oxidative phosphorylation during and after neural activity (Fox et al., 1988; Kasischke et al., 2004). In addition to this, the blood flow response following neural activation occurs over a volume significantly larger than that of the activated neural tissue (Malonek and Grinvald, 1996). In this Chapter I combine primate electrophysiological data (from other groups) on the response of visual area MT neurons to movement, area S2 somatosensory neurons to touch, or auditory cortical neurons to tones, with a theoretical energy budget for the cerebral cortex (Attwell and Laughlin, 2001), to estimate the change of neuronal firing rate and local cortical energy use occurring when making a perceptual decision of the sort studied in human psychophysical and functional imaging experiments. I adopted a philosophy similar to that in functional

imaging experiments, by subtracting the energy use powering neural responses to two types of stimuli which differ only in the perception of a particular attribute of the stimulus (Tootell et al., 1995; Phillips et al., 1997; McKeefry and Zeki, 1997; Epstein and Kanwisher, 1998).

6.2 Methods

For three different sensory modalities, vision, touch and hearing, I identified tasks that have been studied psychophysically and electrophysiologically in monkeys, as well as psychophysically and by functional imaging in humans. Electrophysiological single unit data from monkeys were used to evaluate the change in mean neuronal firing rate occurring in cortical areas providing neural responses which can be used for the detection of visual motion, skin vibration frequency or sound frequency (Fig. 6.1), both at threshold when the percept was just detected, and under conditions when perception was highly reliable. This change in firing rate was then converted into an estimated fractional change of energy use in that area, using an energy budget for the cerebral cortex (Attwell and Laughlin, 2001) which predicts the energy consumed on different subcellular processes underlying neural information processing (largely the reversal of ion movements generating synaptic, action and resting potentials). For each task (and associated brain area) considered, the aim was to evaluate the change in action potential firing, and hence the extra energy needed, for perception, above that needed merely to represent stimuli which do not produce a percept, since this is the change in energy consumption between brain activation states that are commonly subtracted in functional imaging experiments (Tootell et al., 1995; Phillips et al., 1997; McKeefry and Zeki, 1997; Epstein and Kanwisher, 1998). To convert the altered firing rate to a change of energy usage, I employed the fact that the increase in energy used for signalling in the cells recorded from, and in the input neurons driving their firing, can be divided into two parts, proportional to postsynaptic and presynaptic action potential frequency respectively (Attwell and Laughlin, 2001). Energy used to reverse the ion movements generating postsynaptic action potentials is proportional to postsynaptic firing

rate (Attwell and Laughlin, 2001). Energy used on presynaptic action potentials and transmitter release, transmitter and vesicle recycling, and reversal of postsynaptic ion movements generated by transmitter release, is proportional to presynaptic firing rate (Attwell and Laughlin, 2001). For simplicity, in the Results I assume that the input-output relationship of the synapses impinging on the cells recorded from is linear, so that the fractional change of firing frequency in the recorded cells is equal to the fractional change of presynaptic frequency in their input neurons (this assumption is assessed in the Appendix to this Chapter). This implies that the fractional change in total firing-related energy use is equal to the fractional change in the firing rate of the recorded postsynaptic cells. However, in addition to these action potential driven processes, 25-50% of brain energy is also expended on the resting potentials of neurons and glia, and on non-signalling housekeeping tasks (Attwell and Laughlin, 2001), and this was taken into account when calculating the percentage change of total energy use evoked by a stimulus, as described below.

6.3 Results

6.3.1 Detection of visual motion

For the visual modality, I analysed detection of movement in random dot visual stimuli, which has been studied psychophysically and electrophysiologically at the single unit level in monkeys (Britten et al., 1992; Britten et al., 1993), as well as psychophysically (Britten et al., 1992) and by fMRI (Tootell et al., 1995; Rees et al., 2000) in humans. An array of moving dot stimuli is presented (Fig. 6.2a), with the dot intensity well above the threshold for visibility, in which all the dots may move in random directions (termed 0% coherence), or a certain percentage (X) of dots move in the same direction (X% coherence), and the observer has to decide what the general direction of motion is. A neural substrate contributing to this decision is likely to be the middle temporal visual area (MT or V5). This is the first area on the visual pathway in which the responses of most monkey neurons (up to 97%) are directionally selective (Dubner and Zeki, 1971; Zeki, 1974; Van Essen et al.,

1981), and is activated when humans view moving stimuli (Zeki et al., 1991; Heeger et al., 1999). The sensitivity of monkey MT neurons to such stimuli correlates well with the monkeys' psychophysically determined threshold and the psychometric function relating performance to strength (coherence) of the motion signal (Britten et al., 1992) (Fig. 6.2b). Furthermore, the psychophysical performance of human observers on this task is similar to that of monkeys (Britten et al., 1992), supporting extrapolation from the monkey neuronal firing data to the human cortex. From area MT, information is passed to the prefrontal cortex or lateral intraparietal area where behavioural decisions based on the perceived motion may be made (Kim and Shadlen, 1999; Huk and Shadlen, 2005; Zaksas and Pasternak, 2006) (Fig. 6.1).

To calculate the energy needed to support the perception of motion in area MT, I needed to know the action potential rate of the cells analysing the motion. Monkey MT neurons have a firing rate of ~8 Hz in darkness, and this increases to 20 Hz when the animal views a 0% coherence stimulus of moving dots (analysis by Huk and Shadlen (2005) of data in Britten et al. (1993)). Increasing the stimulus coherence increases the firing of cells tuned to respond to the direction of motion of the coherently moving dots, decreases the firing of cells tuned to the opposite direction (Fig. 6.2c) and makes it easier to detect the general direction of motion of the dots. Psychometric functions measured psychophysically, or "neurometric" functions derived by deducing the psychophysical performance of an ideal observer comparing the responses of neurons tuned to the direction of motion and to the opposite direction, have been shown to be fitted by the function

$$p = 1 - 0.5 \exp(-(c/\alpha)^{\beta}) \qquad (6.1)$$

where p is the probability of correctly detecting the motion direction (out of 2 oppositely directed possibilities) at coherence c, α is termed the threshold for detection, and β is a measure of the steepness of the function (Britten et al., 1992; Britten et al., 1993). Detection at threshold ($c=\alpha$) corresponds to correctly detecting the direction of motion on $1-0.5e^{-1}$ = 82% of trials (compared to the 50% obtained by chance for a zero coherence signal: Fig.

6.2b). Experimentally, this 82% success rate for detecting motion can be achieved by comparing the responses of neurons tuned to the direction of motion and of neurons tuned to the opposite direction when stimuli have a coherence of 14% (from the neuron data in Fig. 9A of Britten et al. (1992), weighted by the number of cells). Having derived this threshold coherence allowed me to calculate the mean firing rate of MT cells when detecting motion.

The action potential rate of MT neurons responding to motion in their preferred direction increases with coherence of the stimulus at a rate of 0.39 Hz/(% coherence), while the rate in cells whose preferred direction is opposite to the stimulus decreases at 0.11 Hz/(% coherence) (Britten et al., 1993). Thus, for 14% coherence, these cells will increase and decrease their rate by 5.47 Hz and 1.55 Hz respectively. Adding the 20 Hz firing occurring in the presence of a 0% coherence stimulus (see above), these cells will therefore fire at 25.47 and 18.45 Hz respectively. A column of MT cells analysing motion in a retinal area (Albright et al., 1984) contains cells responding to all possible directions of motion which, in general, will respond at a rate between these extremes (Fig. 6.2c). The firing rate can be expressed as

$$D \exp(-(x/\sigma)^2) + E \qquad (6.2)$$

where x is the angle relative to the preferred direction, σ is the bandwidth of the response and D and E are constants (Britten and Newsome, 1998) (Fig. 6.2c). Using $\sigma = 88^{\circ}$ for 14% coherence (from Fig. 3 of Britten and Newsome (1998)), and fitting this equation to firing rates of 25.47 and 18.45 Hz at 0^0 and 180^0, gives D=7.13 Hz and E=18.34 Hz. The mean firing rate averaged over all of the cells in the column is thus

$$\int_0^{180} \{ D \exp(-(x/\sigma)^2) + E \}\, dx/180 = (D/2).(\sigma/180).(\sqrt{\pi}).\mathrm{erf}(180/\sigma) + E = 21.4 \text{ Hz} \qquad (6.3)$$

when the motion is perceived at threshold. In contrast, when viewing a 0% coherence stimulus, the firing rate is 20 Hz (see above). Thus, the motion percept is associated with a 7% increase in mean firing rate {100% x (21.4 – 20)/20}.

To convert this increased firing rate to an increase of energy usage, I assume that the fractional change in total firing-related energy use is equal to the fractional change in the firing rate of the recorded postsynaptic cells (as discussed in the Methods and assessed in the

Appendix to this Chapter). However, in addition to these action potential driven processes, energy is also expended on the resting potentials of neurons and glia, and on non-signalling housekeeping tasks (Attwell and Laughlin, 2001). If action potential driven signalling energy is ~50-75% of the total energy consumption, with the remainder spent on the resting potential and housekeeping tasks (Attwell and Laughlin, 2001), then the 7% increase of firing rate occurring during motion detection implies an increase of energy consumption of 50-75% of 7% = 3.5-5.3% (Fig. 6.5).

Perception of motion by MT neurons evokes an increase in energy use only because of an asymmetry in the neural responses to motions in the preferred and non-preferred directions of the cells: stimuli in the preferred motion direction evoke a larger increase in firing than the decrease of firing evoked by stimuli in the opposite motion direction (Britten et al., 1993). In principle the system need not be constructed with this asymmetry, and it might be possible for perception to occur with no change of energy usage at all relative to viewing a 0% coherence stimulus (or even a decrease in energy usage if the relative strengths of the responses in the preferred and opposite directions were reversed).

6.3.2 Detection of skin vibration

For the somatosensory modality, I analysed the detection of "flutter", a sensation which is produced when 5-50 Hz vibrations are applied to the skin, which activate Meissner's mechanoreceptors (Mountcastle et al., 1967). In monkeys, information from these receptors is passed to somatosensory cortical area S1, where neurons are active during the period of vibration, and also to higher areas (Romo et al., 2004) (S2, prefrontal cortex, and ventral and medial premotor cortex: Fig. 6.1). In these higher areas the neural activity evoked outlasts the period of stimulation, providing a working memory trace that can be used to compare the frequency of a second stimulus (Fig. 6.3a) with that of an earlier stimulus (with both of the individual stimuli being well above the threshold for detection) (Romo et al., 2004). In humans, flutter vibration also activates areas S1 and S2 (Maldjian et al., 1999), and in

psychophysical experiments (Fig. 6.3b) monkeys and humans distinguish the frequency of sequentially applied vibrations with a similar performance (LaMotte and Mountcastle, 1975). Here I estimate the energy expended in area S2 to generate neural activity which can support the discrimination of the frequency of two stimuli (either in S2 itself or in higher areas that the information in S2 is passed to), i.e. the increase in energy expenditure associated with perception of the frequency difference, above that needed merely to represent two stimuli which are not perceived as different.

Neurons in monkey S2 change their firing when a flutter stimulus is applied, but only 40% of these cells show a response that depends on the vibration frequency (Romo et al., 2002). Of these, 57% show an increase in firing rate with increasing vibration frequency, and 43% show a decrease in rate with increasing frequency (Romo et al., 2003). When two stimuli of different frequency, f1 and f2, are applied for 0.5 sec, separated by a few seconds in time (Fig. 6.3a), the action potential firing rate response to the second stimulus can be represented as a function of f1 and f2 as follows (Romo et al., 2002):

$$\text{rate}(f1, f2) = a1.f1 + a2.f2 + \text{constant} \qquad (6.4)$$

where a1 and a2 are experimentally determined functions of time that evolve so that for much of the response $a1(t) = -a2(t)$ and the rate depends solely on the difference in frequency, f2-f1. For an initial frequency of f1= 20 Hz, I evaluated the difference in spike count ($\int$ rate(f1,f2) dt) when f2 was sufficiently above f1 to be distinguished perceptually from a second presentation of a stimulus with f2=f1=20 Hz. Using the definition of threshold in equation (6.1), i.e. 82% of behavioural choices correct (Fig. 6.3b), and taking correlations between neuronal responses into account (Romo et al., 2003), the threshold for perceiving that f2>f1 is reached when f2 is raised from 20 to 24.6 Hz (from Fig. 4 of Romo et al. (2003)), and the resulting increase of spike count from equation (6.4) is

$$\int \text{rate}(f1=20, f2=24.6)\, dt - \int \text{rate}(f1=20, f2=20)\, dt = 4.6\text{Hz} \cdot \int a2(t)\, dt \qquad (6.5)$$

The motor response defining the monkey's choice of whether f2>f1 starts, on average, 836 ms after the start of the f2 stimulus (Romo et al., 2002). Mean values of a2(t) were obtained

for times 25-90 ms, 90-295 ms, 295-500 ms and 500-836 ms after the start of the f2 stimulus by averaging over the experimental data for cells in Fig. 6a, 6b, 6c and 6d (respectively) of Romo et al. (2002), taking into account the fact that 95, 61, 17 and 60 cells (respectively) of the 208 cells studied are not plotted in those figures because a2 was not significantly different from zero (Romo et al., 2002). This procedure gave mean values for a2 of 0.119, 0.046, 0.421 and 0.106 (respectively) for the four time periods (Fig. 6.3c), and thus a mean increase in spike count of 0.64 action potentials per neuron. This mean increase is very low because similar numbers of cells show increases (for which a2 is positive) and decreases (for which a2 is negative) in firing rate in response to the flutter stimuli (Romo et al., 2002). Since only 40% of neurons show responses dependent on the stimulus frequency (Romo et al., 2002), averaged over all the cells in S2 the mean increase of action potentials/neuron is 0.26, for the 3 second period during which the two stimuli are applied. The baseline firing rate of these cells is ~ 15 Hz (Fig. 7b of Romo et al., (2002), data for $t<0$), so this corresponds to 0.57% increase of firing over the 3 second trial.

As estimated above for visual perception, if action potential driven energy use is ~50-75% of the total energy consumption, with the remainder spent on housekeeping tasks (Attwell and Laughlin, 2001), this implies that the 0.57% increase of firing occurring during flutter detection will lead to an increase of energy consumption of 50-75% of 0.57% = 0.29-0.43% (Fig. 6.5).

6.3.3 Detection of auditory tone difference

For the auditory modality, I studied tone stream segregation. A repeated sequence of (suprathreshold) tones alternating between two frequencies, A and B, such as ABA-ABA-ABA- (Fig. 6.4a), is heard by humans as two separate streams of constant pitch tones if A and B are sufficiently different (i.e. heard as A-A-A- and B-B-B-, with the stream separation building up over time, Fig. 6.4b), but as a single tone stream with a galloping rhythm if A and B are close (Bregman and Campbell, 1971). Tone stream segregation has also been

demonstrated in psychophysical experiments on monkeys (Izumi, 2002). A possible neural basis for this phenomenon is suggested by experiments on primary auditory cortical (A1) neurons in monkeys (Fishman et al., 2001; Micheyl et al., 2005). For the ABA-ABA-ABA- stimulus, if A and B are sufficiently different, neurons with a best frequency equal to that of the A tone show a different time course of adaptation to the repeated presentation of the A and B tones: although the responses to both tones decrease over the first few presentations of the tone triplet, the response to the off-best frequency B tone is not only smaller but shows more (percentage) adaptation with repeated presentation of the triplet tones (Fig. 6.4c). Similarly, for a neuron with a best frequency equal to that of the B tone, the response to the A tones would decrease more over time than the response to the B tone.

Thus, if the A and B tones are sufficiently separated, after some duration of exposure to the tone sequence, high signal to noise ratio responses will only be produced for the A tones in neurons tuned to the A frequency, and for the B tones in neurons tuned to the B frequency. In contrast, when A and B are close, the extra adaptation to the B tone is not seen in neurons tuned to the A frequency (Fig. 6.4c), and vice versa, so that information on both tones will be encoded with a high signal to noise ratio by both sets of neurons. This representation of the tone sequence in 2 discrete sets of cells when A and B are sufficiently different, but in the same cells when A and B are close, is postulated to underlie the different perceptions produced (Fishman et al., 2001; Micheyl et al., 2005) (Fig. 6.4a). Human magneto-encephalographic (Gutschalk et al., 2005) and fMRI (Cusack, 2005) studies suggest that auditory areas outside A1 (Fig. 6.1) may also contribute to the perceptions produced, perhaps by controlling attention to the information streams produced in cells at different locations in A1.

The change in energy expenditure associated with tone stream segregation in A1 can be estimated as follows. Psychophysical experiments (Micheyl et al., 2005) on the response of humans to ABA triplet tone sequences applied at 0.5 second intervals show that if B is 6 semitones ($\sqrt{2}$-fold) above A in frequency then stream segregation occurs over a period of seconds, and after 2 presentations of the triplet tone the probability of correctly perceiving the

segregated streams reaches 64% (which, since the probability rises from 0 to ~100%, is equivalent to the 82% criterion used in equation (6.1) for an experiment where the probability rises from 50 to 100%, as 82% = 50% + (100-50)%x64%). In contrast, if B is only 1 semitone (6%) above A in frequency, or the same as A, then stream segregation does not occur even after 10 seconds of the stimulus (Fig. 6.4b, from Fig. 1 of Micheyl et al. (2005)). In primary auditory cortical neurons of monkeys with a best frequency of A, Fig. 3 of Micheyl et al., (2005, reproduced as Fig 5.4c here), shows that, when B is 6 semitones above A, the first 2 presentations of the triplet tone sequence evoke 8.82 and 6.79 action potentials respectively in response to the two first A tones (a total of 15.61 spikes), 5.97 and 4.46 action potentials in response to the two B tones (a total of 10.43 spikes, much less than for the A tone because of the adaptation described above), and 7.48 and 6.77 action potentials in response to the last A tones (a total of 14.25 spikes), giving a grand total of 40.29 spikes in response to the 2 triplet sequences (this includes the baseline firing rate of ~25 Hz: C. Micheyl, personal communication). In contrast, when B is only 1 semitone above A, although the total spikes in response to the two first and two last A tones of the 4 triplets were little changed (15.28 and 14.81 respectively), the total spike number in response to the intervening B tones was increased from 10.43 to 13.69 (because of the absence of the adaptation described above: Fig. 6.4c), giving a grand total of 43.78 spikes in response to the 2 triplet sequences.

The difference in total spike count between the responses to the triplets with the B tone 6 and 1 semitones above A is therefore 3.49 spikes, out of a total response of 43.78 spikes when B is not detectably different from A in frequency. Thus, there is an 8.0% decrease (3.49/43.78) in total spikes occurring associated with the switch from a perception of one tone stream to two separate streams of different tones.

As estimated above for visual perception, if action potential driven energy use is ~50-75% of the total energy consumption, with the remainder spent on housekeeping tasks (Attwell and Laughlin, 2001), this implies that the 8% decrease of firing occurring during auditory stream detection will lead to a decrease of energy consumption of 50-75% of 8% = 4-6% (Fig. 6.5). This is an overestimation of the fractional energy change occurring in all of

A1, because although a change of this magnitude will occur at the locations in (the tonotopically arranged) A1 where cells have best frequencies of A and B (Fishman et al., 2001), at other locations the difference in firing rate and energy change will be smaller.

6.3.4 Stimuli that are well above the threshold for perception

The calculations above detail the change in cortical energy use associated with the threshold perception of a stimulus attribute. Larger energy changes are expected for stimuli above threshold, but repeating the calculations for this case shows that even well above threshold, where stimulus detection is highly reliable, the fractional change of energy use is still surprisingly small.

For the detection of visual motion calculation described above, if the coherence is twice the threshold value in equation (6.1), i.e. 28% (from the neuron data in Fig. 9A of Britten et al. (1992)) then, for a steepness parameter of α=1.4 (from the neuron data in Fig. 9B of Britten et al., (1992), weighted by number of cells), equation (6.1) predicts that stimulus motion will be correctly detected 96.4% of the time. Repeating the calculation above for 28% coherence predicts that this highly reliable detection of the motion percept is associated with a 14% increase in mean firing rate, and a 7-10.6% increase in energy consumption.

Similarly I repeated the calculation for flutter perception given above, but for comparison of a 30 Hz vibration with a 20 Hz vibration, for which the correct behavioural choice (Fig. 6.3b) is made 97% of the time (from Fig. 4F of Romo et al. (2003)). Averaged over all the cells in S2, the mean increase of action potentials/neuron is then 0.56, for the 3 second period during which the two stimuli are applied, i.e. a 1.2% increase over the basal firing rate, corresponding to an 0.6-0.9% increase in energy expenditure.

For the tone sequence experiment with tone B 6 semitones above A, psychophysical experiments on humans show that perception of the two tone streams reaches its maximum (94% correct) after 5 seconds of repeating the tone triplets (Fig. 6.4b, from Fig. 1 of Micheyl

et al. (2005)). Extending to 5 seconds the counting of the spikes of monkey A1 neurons (from Fig. 3 of Micheyl et al. (2005)) showed that (including the 25 Hz baseline firing rate) the total spike count with B 6 semitones above A was 16.7 spikes less than the 195.8 spikes occurring when B was just one semitone above A, i.e. an 8.5% difference, which would correspond to a 4.3-6.4% difference in energy consumption over the 5 seconds.

6.4 Discussion

6.4.1 Conscious perception is associated with only a small change in energy use

Until now, the relative size of the changes in neural firing rate and energy use devoted to simply processing incoming information, and representing conscious percepts, has been unknown. Because of the importance of conscious perception for determining behaviour, one might expect that the perception of a stimulus attribute would be associated with a set of neurons increasing their firing robustly. However my results show that, although the representation of information from which a percept is derived can involve a high neural firing rate and energy use, perception, i.e. the change from not being able to distinguish two stimuli to perceiving them as different, is associated with a surprisingly small change of mean neuronal firing rate and energy consumption.

I estimated how much brain energy is needed to produce information which can be used to generate a percept, over and above the energy needed to represent the incoming stimuli when the percept is absent, for example the energy needed for visual processing of dot stimuli which move sufficiently coherently to generate a percept of general movement, relative to that needed for the processing of the same number of dots which move randomly and so generate no general movement percept. At the threshold of perception all three cortical areas studied show only a small change of energy usage (<6%) associated with perception (Fig. 6.5), despite the difference in modalities that they serve (vision, touch, audition) and despite large differences in baseline firing rate, suggesting that this result is of general relevance. Even when the strengths of stimuli are increased to be well above the threshold of

perception, the predicted change of cortical energy consumption is small (<11% in all three areas), showing that the small change of neural firing and energy use associated with perception is not merely a consequence of evaluating the changes at the threshold of perception.

A major reason for the small size of this energy change, at least for the visual motion and somatosensory flutter stimuli considered, is that sensory attributes are not represented purely as an increase of cell firing, but as a combination of an increased firing in some neurons and a decreased firing in other neurons. Across the population of neurons considered, therefore, the change in mean firing rate and energy usage are much less than would occur if firing simply increased in all neurons with the strength of the sensory attribute. Thus, encoding stimuli across a population of neurons as a mixture of increased and decreased firing confers the advantage that the energy demand of the brain is kept more constant and requires smaller blood flow changes (rather than requiring that blood flow increases dramatically when a stimulus is given). Previous work has pointed out that this encoding strategy also aids the removal of noise that is common to all cells (Romo et al., 2003) and ensures high temporal resolution at all stimulus strengths (Attwell, 1986).

For these conclusions to hold for humans, I must assume that experimental measurements of the change of action potential frequency evoked by sensory stimuli in awake monkeys can be extrapolated to humans. While there is no easy way to verify this, the similar psychophysical results (Bregman and Campbell, 1971; LaMotte and Mountcastle, 1975; Britten et al., 1992; Izumi, 2002) obtained in monkey and human for all three sensory stimuli studied suggest that the cellular mechanisms underlying perception are similar in the two species.

6.4.2 Unconscious information processing is associated with a larger energy use

If the change in energy use is so small, why has evolution produced systems that increase blood flow when neurons are active? It is important to note that my predictions of a

small increase in firing rate and energy expenditure are only for the perception of a feature of the incoming sensory information. Thus, in the vision example given above, the presence of a zero coherence array of randomly moving dots increases the mean firing rate in area V5 from ~8 to ~20 Hz (Huk and Shadlen, 2005). Similarly, neurons representing tactile flutter stimuli can double their firing frequency when the stimulus is present (Fig. 7b of Romo et al. (2002)), and A1 neurons increase their firing 6-fold when a tone is applied (Fig. 2 of Fishman et al. (2001)). Converting these firing rate changes to energy use changes is complicated by the fact that, unlike for the changes associated with perception discussed above, these firing rates may not be exclusively in the range where the input-output relationship of the synapse is linear (see the Appendix to this Chapter). Nevertheless, the much larger firing rate changes associated with unconscious information processing than with perception suggest that the changes in energy expenditure associated with conscious perception are much smaller than those associated with the unconscious representation of incoming sensory information, for which the increase in blood flow associated with neuronal activity will be more important.

6.4.3 Implications for functional imaging experiments

Functional imaging experiments often subtract brain "activation" images for two situations designed to differ only in the perception of some stimulus attribute (Tootell et al., 1995; Phillips et al., 1997; McKeefry and Zeki, 1997; Epstein and Kanwisher, 1998). My calculations show that, in the tasks I consider, perception is associated with only a small change in energy usage (the exact size of which varies between cortical areas, being an order of magnitude smaller for the somatosensory flutter task than for the visual motion task, and even a decrease in the case of tone stream segregation). For such a small increase of neural firing and energy usage it is unclear whether an increase in blood supply is actually needed to power the neural activity, or whether an increased extraction of oxygen and glucose from the blood (driven by the lowered local concentration of these substrates) would suffice. It does, however, seem likely that any neurotransmitter-mediated (Drake and Iadecola, 2007) increase

of blood flow associated with perception need only be small. Interestingly, the blood flow increases generating functional imaging signals are rather small (Raichle and Mintun, 2006), typically less than 5-10%, and the BOLD signal increase associated with the perception of a stimulus property at threshold is less than 1% in the visual motion (Rees et al., 2000), flutter discrimination (Hegner et al., 2007) and tone stream segregation (Wilson et al., 2007) tasks that I have considered. It seems possible, therefore, that perception of a stimulus attribute in some brain areas, particularly those where a decrease in the firing of some neurons (and thus a decrease in downstream neurotransmitter release) outweighs an increase in the firing of (and transmitter release by) other neurons, may fail to be detected by BOLD fMRI.

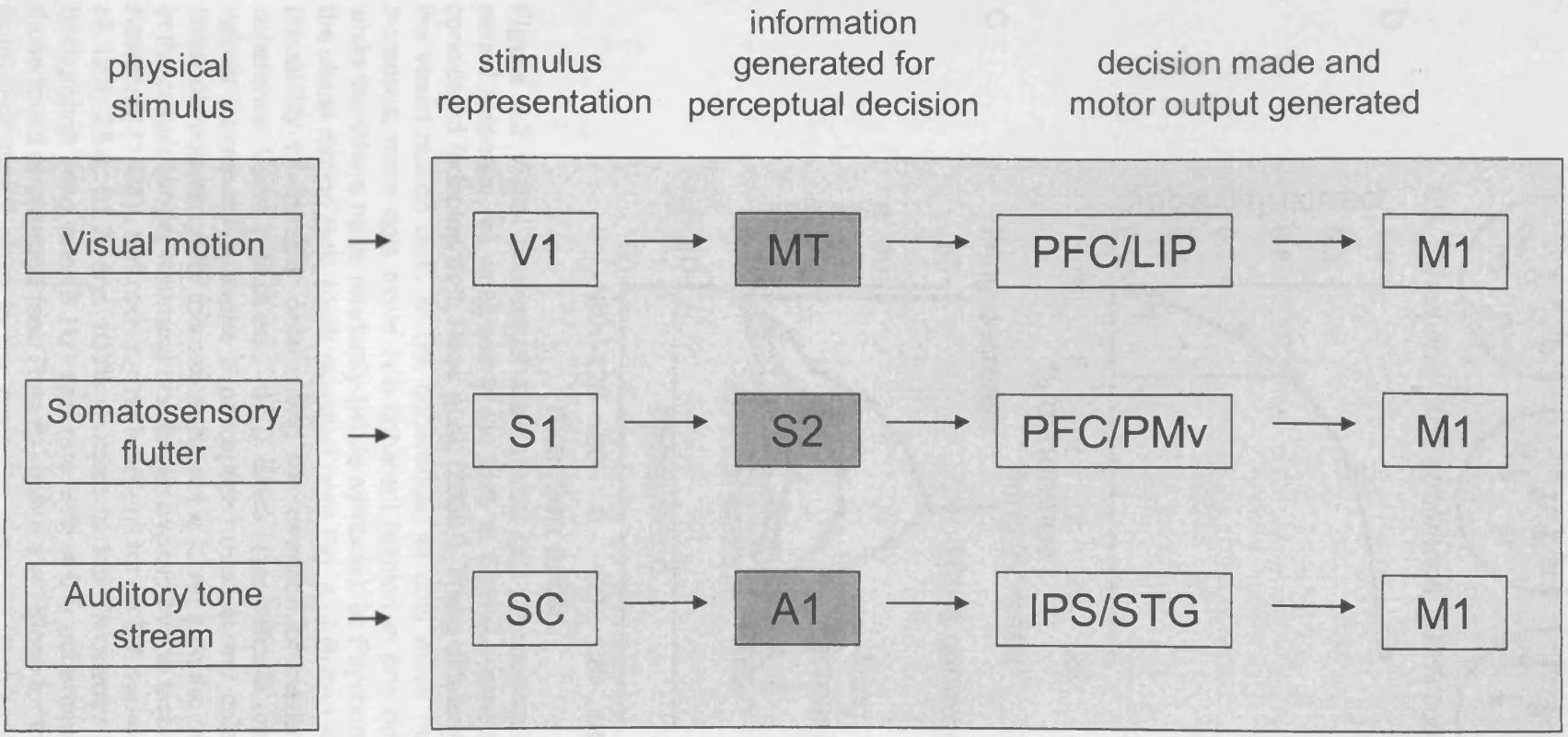

Fig. 6.1 Brain regions involved in the perceptual tasks considered. Incoming stimuli are represented as neural firing in areas such as V1, S1 and SC. Areas MT, S2 and A1, which I analyse here, are the first areas where firing rate provides information allowing a decision on the presence of a percept of visual movement, altered skin vibration ("flutter") frequency or the grouping of sounds ("tone stream segregation"). Subsequent areas may make the perceptual decision and generate motor output (note that although I show a pure feed-forward flow of information, in reality there are also reverse interactions between different areas which probably contribute to the perceptual decision). V1, primary visual cortex; S1, primary somatosensory cortex; SC, superior colliculus; MT, middle temporal area; S2, secondary somatosensory cortex; A1, primary auditory cortex; PFC, prefrontal cortex; LIP, lateral intraparietal area; PMv, ventral premotor area; IPS, intraparietal sulcus; STG, superior temporal gyrus; M1, primary motor cortex.

Figure 6.2 Visual perceptual task stimuli (**a**), psychophysical response (**b**), and neural response (**c**), analysed in the text. **a:** Stimulus schemata for the visual task considered (adapted from Rees et al. (2000)). Three different levels of coherence in the visual motion task. At 0% coherence, all dots move randomly. As coherence increases, more dots move in a coherent fashion in one direction (black symbols) while the others move randomly (white symbols). **b:** Psychometric curve obtained in the visual motion task, (data replotted from Fig. 4 of Britten et al. (1992). Data show probability of correctly determining the direction of motion, as a function of % coherence. Curve is fit of eqn. (6.1)). Black lines indicate examples of the threshold values (necessary to evoke a perception) used in my calculations (note that the threshold coherence for this exemplar cell is lower than the mean value of 14% used in the calculation) **c:** Neuronal responses evoked by the task (adapted from Britten & Newsome (1998)). Direction tuning functions for an MT neuron at motion coherences of 12.8, 25.6, 51.2, and 100% (bottom to top; frequency scale adjusted so that background firing rate (8 Hz) and rate with a 0% coherence stimulus (20 Hz) are those found on average (see Results) rather than those for the cell these data come from). For stimuli close to the preferred direction, increased coherence increases firing, but as the orientation approaches 180° to the preferred direction, the rate decreases below the rate with a 0% coherence signal (arrows).

Figure 6.3 Somatosensory perceptual task stimuli (**a**), psychophysical response (**b**), and neural response (**c**), analysed in the text. **a:** Stimulus schemata for the somatosensory task considered (adapted from Romo et al. (2002)), showing a frequency discrimination trial where the second stimulus (f2) has a higher frequency than the first stimulus (f1). **b:** Psychometric curve (probability of detecting a difference in frequency between f2 and f1, as a function of f2-f1) obtained in the somatosensory task (data replotted from Fig. 1e of Romo et al. (2002); curve is fit of eqn. (6.1)). Black lines indicate examples of the threshold values (necessary to evoke a perception) used in my calculations; the threshold value for f2-f1 in these exempler data is higher than the mean value of 4.6 Hz used in the text). **c:** Neuronal response evoked by the tasks (adapted from Romo et al. (2002)). The average firing rate parameter a2 for S2 neurons, derived by fitting the equation *firing rate* = *a1*f1 + a2*f2 + constant*, during f2 presentation (where a1 and a2 depend only on time, and not on f1 or f2). The dependence of the firing rate on f2 changes over time. For my calculation I only need to know a2(t): the difference in energy use between the situations when f2 ≠ f1 and when f2 = f1 does not depend on a1(t), as shown by equation (6.5).

Figure 6.4 Auditory perceptual task stimuli (**a**), psychophysical response (**b**), and neural response (**c**), analysed in the text. **a:** Stimulus schemata for the auditory task considered (adapted from Micheyl et al. (2005)). Auditory percepts evoked during stream segregation. The stimulus sequences consist of repeating tone triplets, ABA, where A and B represent tones of different frequencies. This can be perceived as a single stream of connected tones (solid lines) or as two monotonic streams with different tempi playing in parallel (dashed lines). **b:** Psychometric curve obtained in the auditory task (data replotted from Micheyl et al. (2005)), with A and B separated by 1 or 6 semitones. Black lines indicate examples of the threshold values (necessary to evoke a perception) used in my calculations. **c:** Neuronal responses evoked by the task (adapted from Micheyl et al. (2005)). Spike counts (per 125 ms) evoked in A1 neurons with best frequency A, by the A and B tones in repeating ABA triplets.

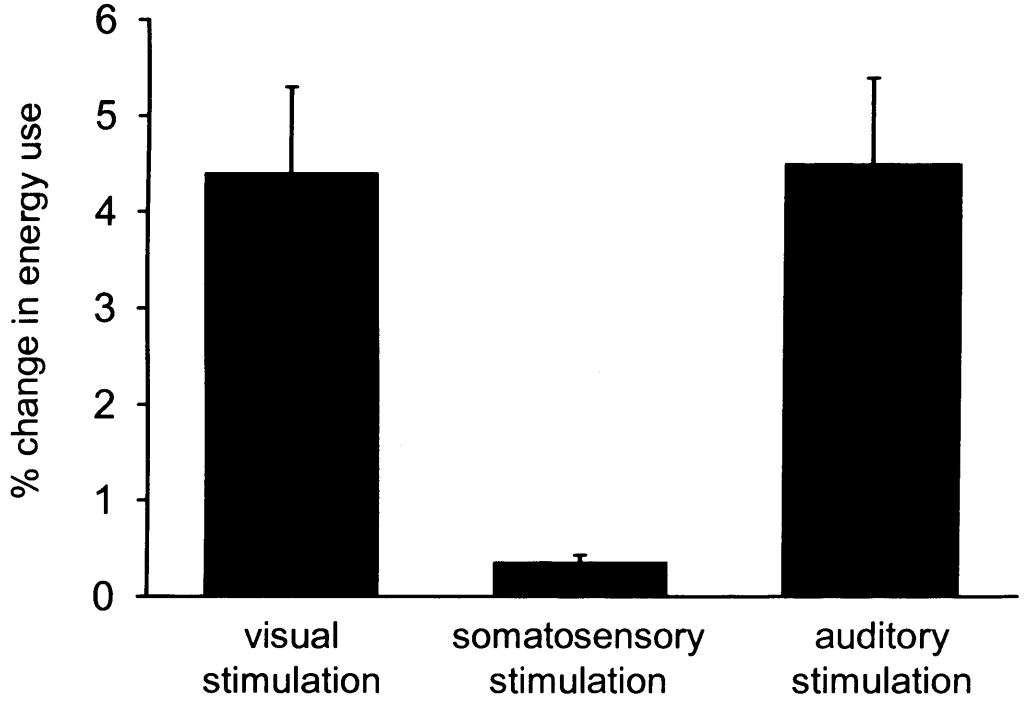

Figure 6.5 Estimated percentage changes in brain energy use associated with conscious perception of stimuli. Mean increase in energy use associated with perception of a moving stimulus, increase in energy use associated with detection of a difference in flutter frequency, or decrease in energy use associated with detection of tone streaming (s.e.m. was calculated from the 2 results obtained assuming that either 50 or 75% of total energy is action potential driven).

Appendix to Chapter 6

The relationship between cortical pyramidal cell firing rate and energy use

In chapter 6 I use the mean changes of firing of cortical pyramidal cells to estimate the change of energy use occurring in a cortical area as a result of altered activity in the recorded cells themselves, and in their input synapses and surrounding glia. Cortical energy use initiated by action potentials has components proportional to postsynaptic and presynaptic action potential frequency (Attwell and Laughlin, 2001) (the relative magnitudes of which differ for rodent and primate cortex (Attwell and Laughlin, 2001), owing to the different cell and synapse densities present). The energy used to reverse the ion movements generating postsynaptic action potentials is proportional to postsynaptic firing rate, while energy use on presynaptic action potentials and transmitter release, transmitter and vesicle recycling, and reversal of postsynaptic ion movements generated by transmitter release, is proportional to presynaptic firing rate (Attwell and Laughlin, 2001).

In chapter 6 I use the fact that the fractional change in the total (pre- and postsynaptic) action potential driven energy use is equal to the fractional change in postsynaptic firing frequency, provided that fractional changes in presynaptic frequency are equal to fractional changes in postsynaptic frequency, i.e. excitatory synapses onto the recorded pyramidal cells generate an output frequency proportional to input frequency. Simulations of cortical neurons (Salinas and Sejnowski, 2000) and dynamic clamp experiments on cortical neurons (Fig. A1(i)) (Desai and Walcott, 2006) and cerebellar neurons (Fig. A1(ii)) (Mitchell and Silver, 2003) suggest that over much of the middle of the firing range of neurons this is a reasonable approximation, but that near the threshold for firing the fractional increase in postsynaptic rate is larger than the fractional increase in presynaptic rate (which would lead to my energy use values being overestimates, because I would overestimate the energy use driven by presynaptic action potentials, as shown in Fig. A2(ii)), while the reverse is true at high firing rates where the synapses saturate (leading to my energy use values being underestimates, as in Fig. A2(iii)). In addition, a "push-pull"

organization of synaptic inputs (Andersen et al., 2000), where excitation increases while inhibition decreases, would result in postsynaptic firing increasing by a larger fraction than presynaptic firing, and so would also result in an overestimation of the fractional energy increase occurring (simplistically, by a factor of ~2 if the increase of firing is produced half by the decrease of inhibition and half by the increase of excitation, assuming that reversing synaptic Na^+ entry is the dominant energy consuming process in primate neurons (Attwell and Laughlin, 2001)). Detailed investigations have not been reported of the input-output relations for the synapses projecting to the pyramidal cells involved in the three perceptual tasks I have considered, however the following summary of the response properties of these cells establishes that during these tasks they are firing in the middle of their response range, far from the threshold for firing and far from saturation (which is more important for my conclusion that perception is associated with little energy use, since approaching saturation would, as outlined above, lead to an underestimation of energy use based solely on postsynaptic firing rate), implying that the linear synapse assumption is reasonable. Consequently, if the recorded cells fire simply as a result of increased excitation, my energy estimates should be fairly accurate, while if a push-pull input arrangement occurs then the change in energy use associated with perception will be even smaller than I estimate.

Visual motion task

For the 14% coherence stimuli considered, which produce firing between 18 and 25 Hz, MT neurons are in the middle of their firing range: their spontaneous rate in darkness is 8 Hz, a 0% coherence stimulus results in firing at 20 Hz (see main text of Chapter 6), while a 100% coherence stimulus will (given the measured dependence of firing rate on coherence (Britten et al., 1993)) result in cells responsive to motion in that direction increasing their firing to ~60 Hz. Consequently fractional changes in postsynaptic firing frequency are likely to be approximately proportional to fractional changes in presynaptic frequency.

Skin vibration task

In the main text of Chapter 6 I consider flutter frequency discrimination around a frequency of 20 Hz. This frequency of vibration evokes a firing rate in area S2 pyramidal

cells which is roughly in the middle of the firing rates evoked by low and high flutter frequencies, both for cells that increase their firing at higher vibration frequencies and for cells that decrease their firing at higher frequencies (a 10 Hz stimulus evokes responses of ~8 and 53 Hz respectively, while a 40 Hz stimulus evokes responses of ~40 and 17 Hz respectively. See Fig. 2B,E of Romo et al. (2003)). Since the input synapses are operating far from the threshold for evoking spikes and far from saturation, fractional changes in postsynaptic firing frequency are likely to be approximately proportional to fractional changes in presynaptic frequency.

Tone segregation task

The baseline firing rate of area A1 pyramidal neurons is about 25 Hz (Fig. 2 of Micheyl et al. (2005)). The difference in spike counts that generate the perceptual response to the B tone in A-B-A triplets occurs around a firing rate (averaged over the response to the B tone) of 60 Hz (Fig. 2 of Micheyl et al. (2005)), which is much lower than the cells' maximum firing rate of at least 150 Hz (the highest rate evoked by the A tone (Fig. 2 of Micheyl et al. (2005)). Thus, since the input synapses are operating far from the threshold for evoking spikes and far from saturation, fractional changes in postsynaptic firing frequency are likely to be approximately proportional to fractional changes in presynaptic frequency.

Electrophysiological sampling bias

The changes of firing rate that I use to estimate cortical energy consumption are probably dominated by recordings from neurons which are large (pyramidal cells) and which fire at a high rate. Omission of smaller cortical interneurons (smooth and spiny stellate cells) should not alter my conclusions significantly because they comprise only 25% of the neurons present (Abeles, 1991), and because their percentage change of firing rate may be similar to that of the principal neurons. The omission of cells that fire rarely or not at all will imply, provided that they increase their firing rate by less than the pyramidal cells, that the change of mean firing rate per neuron is lower than I assume, and lead to my deduced energy usage

being an overestimate, reinforcing further the point that perception is associated with only a small change of cortical energy use.

Figure A1 Dynamic clamp experiments on cortical (i) and cerebellar neurons (ii). (i) Firing rates of cortical neurons, averaged over all cells, in response to trains of different frequencies (taken from Fig. 7b, Desai and Walcott, 2006). (ii) Output firing frequency-input frequency relationships for synaptic excitation under normal conditions and during 1 nS inhibition, fit with linear functions (taken from Fig. 1b, Mitchell and Silver, 2003).

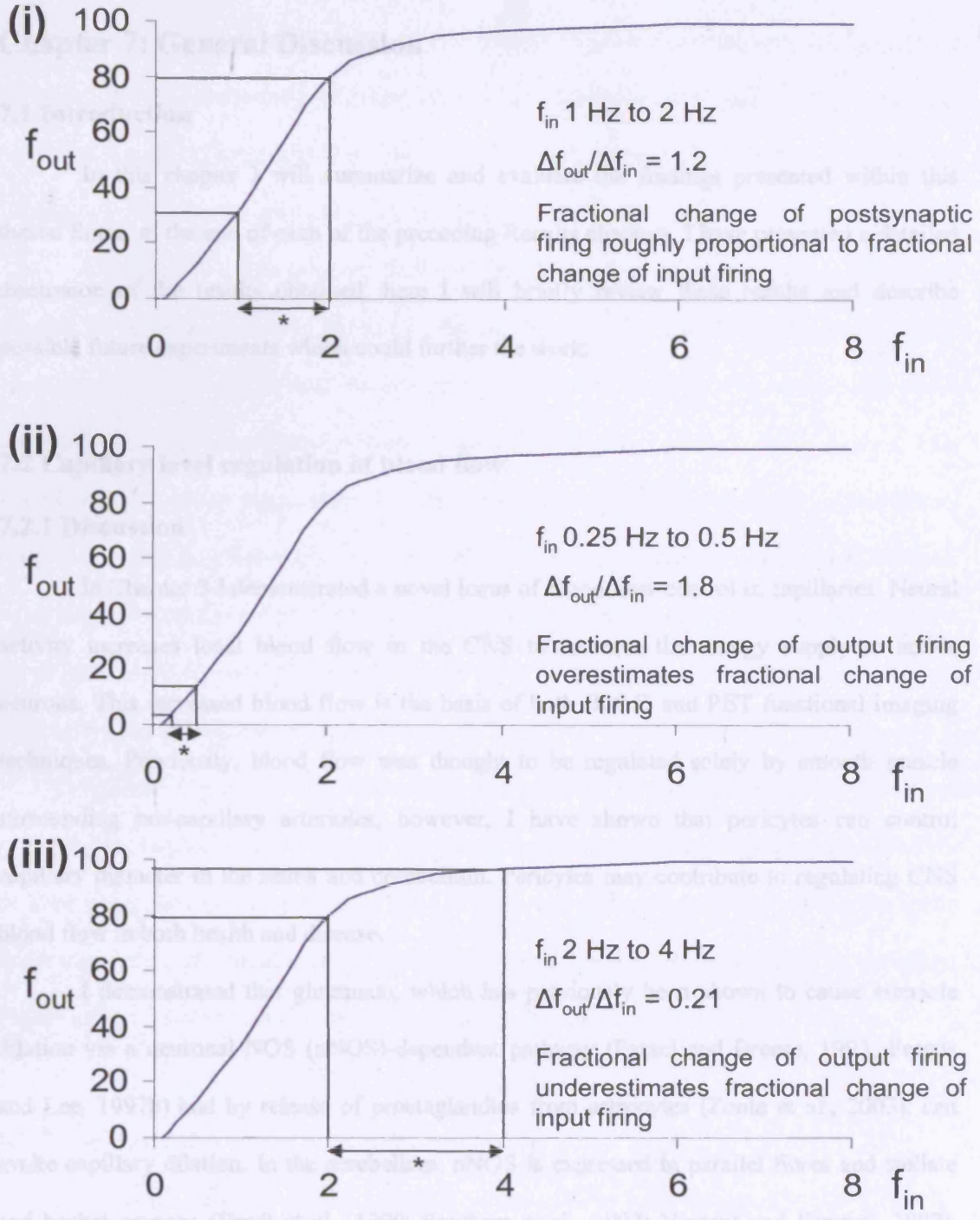

Figure A2 Effect of saturation and threshold in the firing rate input-output relation. Blue curve shows typical input-output relation with a threshold at low input strength, and saturation at high input strength. Over much of the middle of the cell's firing range, the fractional change in postsynaptic firing frequency is approximately equal to the fractional changes in presynaptic frequency (i). Near the threshold for firing, the fractional increase in postsynaptic rate is larger than the fractional increase in presynaptic rate (ii), while the reverse is true at high firing rates where the synapses saturate (iii).

* = doubling of f_{in}.

Chapter 7: General Discussion

7.1 Introduction

In this chapter I will summarize and evaluate the findings presented within this thesis. Since, at the end of each of the preceding Results chapters, I have presented a detailed discussion of the results obtained, here I will briefly review these results and describe possible future experiments which could further the work.

7.2 Capillary level regulation of blood flow

7.2.1 Discussion

In Chapter 3 I demonstrated a novel locus of blood flow control in capillaries. Neural activity increases local blood flow in the CNS to increase the energy supply to active neurons. This increased blood flow is the basis of both BOLD and PET functional imaging techniques. Previously, blood flow was thought to be regulated solely by smooth muscle surrounding pre-capillary arterioles, however, I have shown that pericytes can control capillary diameter in the retina and cerebellum. Pericytes may contribute to regulating CNS blood flow in both health and disease.

I demonstrated that glutamate, which has previously been shown to cause arteriole dilation via a neuronal NOS (nNOS)-dependent pathway (Faraci and Breese, 1993; Fergus and Lee, 1997b) and by release of prostaglandins from astrocytes (Zonta et al., 2003), can evoke capillary dilation. In the cerebellum, nNOS is expressed in parallel fibres and stellate and basket neurons (Bredt et al., 1990; Southam et al., 1992; Vincent and Kimura, 1992), suggesting that BOLD fMRI signals produced when glutamate acts via nNOS as described in Chapter 1, section 1.4.4, would reflect the information processing occurring within the cerebellum, rather than its output. This is in agreement with work by Mathiesen et al. (1998), who found that an increase in Purkinje cell spike rate was not required for regional CBF to increase, and Logothetis et al. (2001), who proposed that it may not be neuronal spiking activity but synaptic events which generate the blood flow increase leading to fMRI signals.

As nNOS will be expressed at different synapses in different brain regions, BOLD signals generated by NO release may reflect information processing in some regions while reflecting output in others. Similar arguments could be made for the BOLD signals generated by glutamate acting on glial mGluRs to dilate blood vessels.

The increase of blood flow produced by glutamate (Chapter 3, section 3.3.6) may depend on the aminergic tone present in the blood vessels. With too little aminergic tone, vessels may be so dilated that further glutamate-evoked dilations are small, while with excessive aminergic constriction, glutamate may not be able to evoke a large dilation. This would complicate the interpretation of fMRI experiments on subjects with amine disturbances (including depression, schizophrenia and attention deficit hyperactivity disorder (ADHD)) or when drugs are administered to alter amine pathways. In these cases, alterations of the fMRI signal, which are commonly assumed to reflect altered neural processing, may instead reflect an altered vascular readout of neural activity.

It remains unknown how the arteriole and capillary levels of vascular control interact to provide more global regulation. As shown in Chapter 3, pericytes may regulate blood flow by constricting or dilating capillaries, but it is unknown whether astrocytes (which play a role in the regulation of arteriole diameter, see Chapter 1, section 1.4) also signal to pericytes. Possible experiments to investigate these areas are discussed below.

7.2.2 Further work

To assess whether astrocytes signal to pericytes in order to regulate blood flow in capillaries, Ca^{2+} uncaging could be used in astrocyte endfeet in brain slices and the effect on pericytes observed. If nearby pericytes constrict or dilate, this would suggest that astrocytes do indeed signal to pericytes.

In arterioles, unlike capillaries, constriction usually occurs in a uniform manner (Chapter 3, Fig. 3.1c,d), but occasionally localised, sphincter-like constrictions have also been observed (Cauli et al., 2004; Metea and Newman, 2006), often at vessel branch points

(Eric Newman, personal communication). I have observed that occasionally there seem to be pericytes located on arterioles at branch points with capillaries (Fig. 3.2b in Chapter 3) and I propose that the sphincter-like constrictions reported occur as a result of local pericyte-evoked constrictions of the arterioles. In order to test this, neurons near arterioles could be stimulated in vitro and if sphincter-like constrictions are observed the cells responsible could be marked (by dye filling) and NG2 labelling used to identify whether they are pericytes (as in Chapter 3, Fig. 3.2b,c). A coordinating role for pericytes in arteriole contraction has not been reported previously and would be an important discovery.

Further work is needed to establish the mechanism of the propagation of vasoconstriction seen in capillaries (Chapter 3, section 3.3.4 and Fig. 3.5). Pericytes do not appear to be connected, yet constriction propagates between cells. A first step to study this further would involve investigating the spatial extent of the propagation observed, as it is unknown how far along the capillary this propagation can occur. A Ca^{2+} wave was observed in response to glial or pericyte stimulation (Chapter 3, Fig. 3.7), although the speed of constriction of this wave was five-fold faster than the propagation velocity observed for the pericyte constriction. However, this does not rule out the possibility of a calcium wave underlying the propagation of constriction, as the constriction evoked by ATP release from underlying glia at the remote pericyte may occur with a longer latency than the constriction evoked at the stimulated pericyte, leading to an apparent conduction delay for the contraction that is artefactually longer than that for the Ca^{2+} wave. Propagation may be therefore due to a calcium wave propagating through the underlying glia or due to gap junction coupling via endothelial cells. The effect of Mn^{2+} on the propagation of pericyte constriction should be investigated as it has been shown previously that Mn^{2+} inhibits the spread of ATP-dependent Ca^{2+} waves through the astrocyte network (Tjalkens et al., 2006).

The spread of vasodilation along blood vessels has been reported previously in muscle (Berg et al., 1997) and in brain (Iadecola et al., 1997). Such a signalling mechanism, if it also occurs for dilation of capillaries, would allow a larger change of blood flow in response to localised activity, particularly if capillary dilation spreads back to upstream

arterioles (e.g. it is possible that neural activity evokes a signal in capillary pericytes which then spreads to arterioles). Imaging techniques, combined with Ca^{2+} uncaging in astrocytes or neuronal stimulation in brain slices, could be used to investigate whether vasodilation evoked in capillaries by astrocyte Ca^{2+} rises or neuronal activity (as seen by Zonta et al. (2003) and Takano et al. (2006)) spreads along brain blood vessels as far as arterioles.

Additionally, in order to confirm that the cells seen (e.g. Chapter 3, Fig. 3.2) are pericytes and do not include astrocytes, brain slices or retinae could be labelled with antibodies against glial fibrillary acidic protein (GFAP), which is specifically expressed in astrocytes, and against NG2, which labels pericytes (Hughes and Chan-Ling, 2004).

These experiments would advance our understanding of how brain blood flow is regulated, both at the arteriole and capillary levels, in response to neural activity. This knowledge is essential to understand normal brain function, functional imaging techniques, and what occurs when the brain energy supply is cut off in disorders such as stroke.

7.3 Energy supply and energy demand in the cerebellum

7.3.1 Discussion

To understand how blood-delivered energy substrates are used for neural computation, I constructed a theoretical energy budget for the cerebellar cortex from the bottom up, using the measured cellular properties (the ion fluxes resulting from the known membrane conductances, the size and frequency of synaptic and action potentials, synaptic anatomy and physiology, etc.). This is the first time that such an energy budget has been produced based on the detailed properties of each individual cell type in the tissue (rather than assuming average properties taken from a number of different neuronal types as in Attwell & Laughlin (2001)). Comparing my predicted energy usage with the distribution of cerebellar blood vessels shows that evolution has matched the blood vessel distribution to the spatial distribution of energy consumption. The predicted laminar distribution of energy use reflects the fact that a large proportion of energy is used to propagate the action potential

along the granule cells' axons, the parallel fibres, and is also used on the postsynaptic currents they evoke in the Purkinje cells. The molecular layer accounts for 60% of the energy use of the cerebellum, with the granular layer accounting for the remaining 40% (Chapter 4, section 4.4.6). The measured blood vessel surface area, which showed a ratio of 58%:42% between molecular layer:granule layer (Chapter 4, section 4.4.6), appears to be closely matched to this energy use distribution.

It has commonly been assumed that the energy use of a brain area correlates with the firing of the principal neurons, however, in Chapter 4 I showed that this is not the case for the cerebellum. Different brain areas will have a different distribution of energy use between cell types and so when considering this issue each brain area may need to be considered on an individual basis.

7.3.2 Further work

The properties of the different cells in the cerebellum alter during development which may lead to the energy distribution within the cerebellum also altering during development. Future work could involve extending the cerebellar energy budget to consider different ages during development. The predicted laminar energy distribution could then be compared with the vessel surface area distribution observed in rat pups of different ages, which varies considerably over the first few weeks after birth.

To further investigate the relationship between energy use and supply in the cerebellar layers, the oxygen consumption in response to white matter stimulation (to mimic neural input) could be measured in the different cerebellar layers. These results could be compared with the density of blood vessels, to determine whether energy supply is matched to oxygen usage in reality.

7.4 Division of energy use between cellular processes

7.4.1 Discussion

In Chapter 4, I predicted that, in the cerebellum, 40% of signalling energy goes on action potentials, and only a small fraction (6%) goes on transmitter release and recycling, while resting potentials account for 35% of signalling energy and postsynaptic currents account for the remaining 19%. Furthermore, the subcellular distribution of energy use varies dramatically between different cerebellar neuron types.

In Chapter 5, I showed that a large proportion (39%) of oxygen consumption in response to neuronal stimulation was accounted for by AMPA receptor mediated effects of synaptic transmission, in agreement with previous work by Offenhauser et al. (2005). Downstream action potentials were found to account for 20% of the oxygen consumption in response to neuronal stimulation. The parallel fibre stimulation applied during these experiments (Chapter 5, section 5.3.9) may also result in activation of inhibitory interneurons which release GABA onto the Purkinje cell dendrites. The effect of such a GABA release on oxygen consumption remains a controversial issue in the fMRI literature (Waldvogel et al., 2000; Buzsaki et al., 2007): in my theoretical energy budget I calculated that little energy is needed to restore the Cl^- gradient after activation of $GABA_A$ receptors, but this has not been tested directly.

7.4.2 Further work

In Chapter 5 I showed that applying muscimol (a GABA agonist) decreases the oxygen use in cerebellar slices in response to parallel fibre stimulation. Following on from this work, GABA could be applied to slices in the presence of glutamate receptor and action potential blockers, allowing direct GABA receptor mediated effects on energy consumption to be isolated.

It would be interesting to distinguish the oxygen use by synaptic currents and action potentials. Caesar et al. (2003) have activated synaptic input and prevented action potential

production by applying muscimol and baclofen, $GABA_A$ and $GABA_B$ receptor agonists, to keep cells hyperpolarised. An alternative method of investigating this question would be to apply glutamate, or AMPA, and test the effect on the oxygen response of blocking action potentials with TTX. Using this method, it would not be possible to quantify the relative usage by synaptic currents and action potentials. However, in TTX, glutamate-evoked Na^+ entry could be measured in voltage clamp experiments and oxygen usage measured simultaneously. One could then correlate the oxygen use with the Na^+ entry. Similarly in current clamp mode, with glutamate blockers present, one could inject current and correlate the number of action potentials produced with the oxygen usage.

The work performed in slices in Chapter 5 could be expanded by using the simple system of a single (cultured or isolated) neuron. The fall of oxygen concentration around the single neuron when action potentials are evoked by application of glutamate or depolarisation of the cell could be measured with the oxygen electrode. It should be possible to determine how long it takes the resulting rise of $[Ca^{2+}]_i$ to increase mitochondrial oxygen consumption, which is one determinant of the brain's response to energy consumption. Intracellular calcium buffering could be modified to see whether this determines the response time of mitochondrial respiration. The effect of lactate on the mitochondrial response could also be investigated.

7.5 Neuronal energy supply is not necessarily co-ordinated by glia

7.5.1 Discussion

It has been proposed by Pellerin & Magistretti (1994) that the energy supply to neurons is matched to neuronal needs by glial glycolysis evoked in response to glutamate uptake. I tested this by monitoring mitochondrial oxygen consumption while partially blocking glutamate uptake by combining pharmacological block with genetic knock-out. The increased oxygen consumption in response to neuronal stimulation was not greatly reduced as would have been expected if the ANLS hypothesis were true (Chapter 5, section 5.3.8),

suggesting that the energetic demands of active neurons can be met without glial glycolysis occurring in response to glial glutamate uptake. However, further experiments are needed in order to confirm the extent of the block of glial uptake and whether neuronal lactate transporters are saturated (which would imply that astrocyte lactate release would not increase the lactate supply to neurons).

Experiments using NAD(P)H imaging have been used to investigate the spatial and temporal segregation of oxidative and glycolytic metabolism (Kasischke et al., 2004; Brennan et al., 2006) however, results obtained using these techniques remain controversial (Kasischke et al., 2004; Cerdan et al., 2006; Brennan et al., 2006). The NADH response observed following neuronal stimulation is the sum of early NADH oxidation by the neuronal respiratory chain (causing a decrease in NADH fluorescence that is not initially compensated for by glycolysis and the TCA cycle) followed by slower NADH production by the neuronal TCA cycle and by astrocytic glycolysis (resulting in an increase in NADH fluorescence) (Aubert et al., 1964; Williamson et al., 1967; Jobsis et al., 1971; Brandes and Bers, 1996). Although their data have been proposed by some to support the ANLS hypothesis (Pellerin et al., 2007), it is unclear how the increase in NADH observed by Kasischke et al. (2004) can be reliably attributed to one of either the Krebs cycle or glycolysis. Furthermore, as discusssed in Chapter 1, section 1.5.2, Brennan et al. (2006) have suggested that the NADH fluorescence increases seen in response to neuronal stimulation actually reflect NADH generation by the neuronal mitochondrial TCA cycle rather than by glial glycolysis as proposed by Kasischke et al. (2004). Further investigations into the origin of the NADH signal are necessary.

7.5.2 Further work

Experiments partially blocking glial glutamate uptake (Chapter 5, section 5.3.8) should be repeated while simultaneously patch clamping a Bergmann glia cell in order to assess whether the time-integrated glial glutamate current is approximately halved, as expected from the modelling in Chapter 5. Further experiments could also block lactate

release by glia and lactate uptake by neurons to assess whether extracellular lactate is essential for neuronal oxidative metabolism to occur in response to parallel fibre stimulation.

Further investigations based on NAD(P)H fluorescence imaging (as used by Kasischke et al., 2004) could be undertaken in cerebellar slices when glial glutamate uptake is blocked both pharmacologically and genetically. Any differences in either the early decrease or late overshooting rise of the response to neural activity would imply that glial glutamate uptake is necessary for that portion of the response. If it is possible to image NADH in neurons and glia separately, it would be possible to check whether the two phases correspond to activity in glia and neurons, as proposed by Kasischke et al. (2004). Pharmacological interventions could be used to block glutamate receptors and glutamate uptake in order to assess what affects the rapid neuronal metabolic response and the slower glial one.

7.6 Changes in neuronal firing rate and energy consumption in cortical areas mediating conscious perception

7.6.1 Discussion

Employing an approach similar to that for the cerebellar energy budget, I estimated how much brain cortical energy is expended on conscious perception of stimuli, as opposed to unconscious information processing. Surprisingly, conscious perception uses only a small percentage of brain energy (<10%). This may be partly due to the fact that the population of neurons involved responds with a combination of increased and decreased firing, rather than all neurons increasing their firing rates. It seems possible that perception of a stimulus attribute in some brain areas may lead to a decrease in firing which is greater than the increased firing evoked in other neurons, resulting in a decrease in the total release of glutamate (which is thought to trigger vasodilation and the BOLD signal, see Chapter 1, section 1.4.4) and so may fail to be detected as a positive BOLD fMRI signal.

7.7 Conclusion

In summary, the work presented in this thesis has investigated the regulation of energy supply to the brain and the cellular and subcellular distribution of brain energy use. The experiments undertaken provide information which will further our understanding of the regulation of brain blood supply in health and disease. They also provide insight into the cellular mechanisms which underlie functional brain imaging and, hence, will aid our understanding and interpretation of such signals. The theory presented within this thesis investigated the distribution of signalling energy use between the various stages of cerebellar computation, and how the energy use and supply are matched within the layers of the cerebellum. In addition, I calculated the change of neural firing rate and cortical energy use which underlies conscious perception.

I hope to perform some of the further work described above during my postdoctoral research.

References

Abeles, M. (1991) Corticonics: Neural Circuits of the Cerebral Cortex. Cambridge University Press.

Aiello, L.C. and Wheeler, P. (1995) The Expensive-Tissue Hypothesis: The Brain and the Digestive System in Human and Primate Evolution. *Current Anthropology* **36,** 199-221.

Akgoren, N., Fabricius, M., and Lauritzen, M. (1994) Importance of nitric oxide for local increases of blood flow in rat cerebellar cortex during electrical stimulation. *Proc. Natl. Acad. Sci U. S. A* **91,** 5903-5907.

Akgoren, N., Mathiesen, C., Rubin, I., and Lauritzen, M. (1997) Laminar analysis of activity-dependent increases of CBF in rat cerebellar cortex: dependence on synaptic strength. *Am. J Physiol* **273,** H1166-H1176.

Albright, T.D., Desimone, R., and Gross, C.G. (1984) Columnar organization of directionally selective cells in visual area MT of the macaque. *J Neurophysiol* **51,** 16-31.

Albus, J.S. (1971) A theory of cerebellar function. *Mathematical Biosciences* **10,** 25-61.

Alkayed, N.J., Birks, E.K., Narayanan, J., Petrie, K.A., Kohler-Cabot, A.E., and Harder, D.R. (1997) Role of P-450 arachidonic acid epoxygenase in the response of cerebral blood flow to glutamate in rats. *Stroke* **28,** 1066-1072.

Alkayed, N.J., Narayanan, J., Gebremedhin, D., Medhora, M., Roman, R.J., and Harder, D.R. (1996) Molecular characterization of an arachidonic acid epoxygenase in rat brain astrocytes. *Stroke* **27,** 971-979.

Alle, H. and Geiger, J.R. (2006) Combined analog and action potential coding in hippocampal mossy fibers. *Science* **311,** 1290-1293.

Allen, N.J., Karadottir, R., and Attwell, D. (2005) A preferential role for glycolysis in preventing the anoxic depolarization of rat hippocampal area CA1 pyramidal cells. *J Neurosci.* **25,** 848-859.

Ames, A., III and Li, Y.Y. (1992) Energy requirements of glutamatergic pathways in rabbit retina. *J Neurosci.* **12,** 4234-4242.

Ames, A., III, Li, Y.Y., Heher, E.C., and Kimble, C.R. (1992) Energy metabolism of rabbit retina as related to function: high cost of Na+ transport. *J Neurosci.* **12,** 840-853.

Andersen, J.S., Carandini, M., and Ferster, D. (2000) Orientation tuning of input conductance, excitation, and inhibition in cat primary visual cortex. *J. Neurophysiol.* **84,** 909-926.

Arieli, A., Sterkin, A., Grinvald, A., and Aertsen, A. (1996) Dynamics of ongoing activity: explanation of the large variability in evoked cortical responses. *Science* **273,** 1868-1871.

Arriza, J.L., Fairman, W.A., Wadiche, J.I., Murdoch, G.H., Kavanaugh, M.P., and Amara, S.G. (1994) Functional comparisons of three glutamate transporter subtypes cloned from human motor cortex. *J Neurosci.* **14,** 5559-5569.

Astrup, J., Heuser, D., Lassen, N.A., Nilsson, B., Norberg, K., and Siesjo, B.K. (1978) Evidence against H^+ and K^+ as main factors for the control of cerebral blood flow: a microelectrode study. *Ciba Found. Symp.* 313-337.

Astrup, J., Sorensen, P.M., and Sorensen, H.R. (1981) Oxygen and glucose consumption related to Na^+-K^+ transport in canine brain. *Stroke* **12,** 726-730.

Attwell, D. (1986) The Sharpey-Schafer lecture. Ion channels and signal processing in the outer retina. *Q. J Exp. Physiol* **71,** 497-536.

Attwell, D. and Gibb, A. (2005) Neuroenergetics and the kinetic design of excitatory synapses. *Nat. Rev. Neurosci.* **6,** 841-849.

Attwell, D. and Iadecola, C. (2002) The neural basis of functional brain imaging signals. *Trends Neurosci.* **25,** 621-625.

Attwell, D. and Laughlin, S.B. (2001) An energy budget for signaling in the grey matter of the brain. *J. Cereb. Blood Flow Metab* **21,** 1133-1145.

Aubert, X., Chance, B., and Keynes, D. (1964) Optical Studies of Biochemical Events in the Electric Organ of Electrophorus. *Proc. R. Soc. London. Ser. B* **160,** 211-245.

Auger, C., Kondo, S., and Marty, A. (1998) Multivesicular release at single functional synaptic sites in cerebellar stellate and basket cells. *J. Neurosci.* **18,** 4532-4547.

Bandopadhyay, R., Orte, C., Lawrenson, J.G., Reid, A.R., De Silva, S., and Allt, G. (2001) Contractile proteins in pericytes at the blood-brain and blood-retinal barriers. *J Neurocytol.* **30,** 35-44.

Barbour, B. (2001) An evaluation of synapse independence. *J Neurosci.* **21,** 7969-7984.

Barlow, H.B. (1957) Increment thresholds at low intensities considered as signal/noise discriminations. *J Physiol* **136,** 469-488.

Berends, M., Maex, R., and De Schutter, E. (2004) A detailed three-dimensional model of the cerebellar granular layer. *Neurocomputing* **58-60,** 587-592.

Berg, B.R., Cohen, K.D., and Sarelius, I.H. (1997) Direct coupling between blood flow and metabolism at the capillary level in striated muscle. *Am. J Physiol* **272,** H2693-H2700.

Bergersen, L., Rafiki, A., and Ottersen, O.P. (2002) Immunogold cytochemistry identifies specialized membrane domains for monocarboxylate transport in the central nervous system. *Neurochem. Res.* **27,** 89-96.

Bittar, P.G., Charnay, Y., Pellerin, L., Bouras, C., and Magistretti, P.J. (1996) Selective distribution of lactate dehydrogenase isoenzymes in neurons and astrocytes of human brain. *J Cereb. Blood Flow Metab* **16,** 1079-1089.

Bordey, A. and Sontheimer, H. (2003) Modulation of glutamatergic transmission by bergmann glial cells in rat cerebellum in situ. *J. Neurophysiol.* **89,** 979-988.

Borowsky, I.W. and Collins, R.C. (1989) Metabolic anatomy of brain: a comparison of regional capillary density, glucose metabolism, and enzyme activities. *J Comp Neurol.* **288,** 401-413.

Bouzier-Sore, A.K., Voisin, P., Canioni, P., Magistretti, P.J., and Pellerin, L. (2003) Lactate is a preferential oxidative energy substrate over glucose for neurons in culture. *J Cereb. Blood Flow Metab* **23,** 1298-1306.

Brandes, R. and Bers, D.M. (1996) Increased work in cardiac trabeculae causes decreased mitochondrial NADH fluorescence followed by slow recovery. *Biophys. J* **71,** 1024-1035.

Brasnjo, G. and Otis, T.S. (2004) Isolation of glutamate transport-coupled charge flux and estimation of glutamate uptake at the climbing fiber-Purkinje cell synapse. *Proc. Natl. Acad. Sci. U. S. A* **101,** 6273-6278.

Bredt, D.S., Hwang, P.M., and Snyder, S.H. (1990) Localization of nitric oxide synthase indicating a neural role for nitric oxide. *Nature* **347,** 768-770.

Bregman, A.S. and Campbell, J. (1971) Primary auditory stream segregation and perception of order in rapid sequences of tones. *J Exp. Psychol.* **89,** 244-249.

Brennan, A.M., Connor, J.A., and Shuttleworth, C.W. (2006) NAD(P)H fluorescence transients after synaptic activity in brain slices: predominant role of mitochondrial function. *J Cereb. Blood Flow Metab* **26,** 1389-1406.

Brew, H., Gray, P.T., Mobbs, P., and Attwell, D. (1986) Endfeet of retinal glial cells have higher densities of ion channels that mediate K^+ buffering. *Nature* **324,** 466-468.

Britten, K.H. and Newsome, W.T. (1998) Tuning bandwidths for near-threshold stimuli in area MT. *J Neurophysiol* **80,** 762-770.

Britten, K.H., Shadlen, M.N., Newsome, W.T., and Movshon, J.A. (1993) Responses of neurons in macaque MT to stochastic motion signals. *Vis. Neurosci.* **10,** 1157-1169.

Britten, K.H., Shadlen, M.N., Newsome, W.T., and Movshon, J.A. (1992) The analysis of visual motion: a comparison of neuronal and psychophysical performance. *J Neurosci.* **12,** 4745-4765.

Brunel, N., Hakim, V., Isope, P., Nadal, J.P., and Barbour, B. (2004) Optimal information storage and the distribution of synaptic weights: perceptron versus Purkinje cell. *Neuron* **43,** 745-757.

Busija, D.W. and Leffler, C.W. (1989) Dilator effects of amino acid neurotransmitters on piglet pial arterioles. *Am. J Physiol* **257,** H1200-H1203.

Butryn, R.K., Ruan, H., Hull, C.M., and Frank, R.N. (1995) Vasoactive agonists do not change the caliber of retinal capillaries of the rat. *Microvasc. Res.* **50,** 80-93.

Buzsaki, G., Kaila, K., and Raichle, M. (2007) Inhibition and brain work. *Neuron* **56,** 771-783.

Caesar, K., Thomsen, K., and Lauritzen, M. (2003) Dissociation of spikes, synaptic activity, and activity-dependent increments in rat cerebellar blood flow by tonic synaptic inhibition. *Proc. Natl. Acad. Sci U. S. A* **100,** 16000-16005.

Carter, A.G. and Regehr, W.G. (2002) Quantal events shape cerebellar interneuron firing. *Nat. Neurosci.* **5,** 1309-1318.

Cauli, B., Tong, X.K., Rancillac, A., Serluca, N., Lambolez, B., Rossier, J., and Hamel, E. (2004) Cortical GABA interneurons in neurovascular coupling: relays for subcortical vasoactive pathways. *J Neurosci.* **24,** 8940-8949.

Cerdan, S., Rodrigues, T.B., Sierra, A., Benito, M., Fonseca, L.L., Fonseca, C.P., and Garcia-Martin, M.L. (2006) The redox switch/redox coupling hypothesis. *Neurochem. Int.* **48,** 523-530.

Chadderton, P., Margrie, T.W., and Hausser, M. (2004) Integration of quanta in cerebellar granule cells during sensory processing. *Nature* **428,** 856-860.

Chaudhry, F.A., Lehre, K.P., Van Lookeren, C.M., Ottersen, O.P., Danbolt, N.C., and Storm-Mathisen, J. (1995) Glutamate transporters in glial plasma membranes: highly differentiated localizations revealed by quantitative ultrastructural immunocytochemistry. *Neuron* **15,** 711-720.

Chedotal, A., Umbriaco, D., Descarries, L., Hartman, B.K., and Hamel, E. (1994) Light and electron microscopic immunocytochemical analysis of the neurovascular relationships of choline acetyltransferase and vasoactive intestinal polypeptide nerve terminals in the rat cerebral cortex. *J Comp Neurol.* **343,** 57-71.

Chih, C.P., Lipton, P., and Roberts, E.L., Jr. (2001) Do active cerebral neurons really use lactate rather than glucose? *Trends Neurosci.* **24,** 573-578.

Chklovskii, D.B., Schikorski, T., and Stevens, C.F. (2002) Wiring optimization in cortical circuits. *Neuron* **34,** 341-347.

Clark, B.A. and Barbour, B. (1997) Currents evoked in Bergmann glial cells by parallel fibre stimulation in rat cerebellar slices. *J. Physiol* **502 (Pt 2),** 335-350.

Clark, B.A. and Cull-Candy, S.G. (2002) Activity-dependent recruitment of extrasynaptic NMDA receptor activation at an AMPA receptor-only synapse. *J Neurosci.* **22,** 4428-4436.

Clarke, D. D. and Sokoloff, L. (1999) Basic Neurochemistry: Molecular, Cellular and Medical Aspects. 6 ed. Siegel, G. J., Agranoff, B. W., Albers, R. W., Fisher, S. K., and Uhler, M. D. Philadelphia, Lippincott. 637-670.

Cohen, Z., Bonvento, G., Lacombe, P., and Hamel, E. (1996) Serotonin in the regulation of brain microcirculation. *Prog. Neurobiol.* **50,** 335-362.

Cohen, Z., Molinatti, G., and Hamel, E. (1997) Astroglial and vascular interactions of noradrenaline terminals in the rat cerebral cortex. *J Cereb. Blood Flow Metab* **17,** 894-904.

Crambert, G., Hasler, U., Beggah, A.T., Yu, C., Modyanov, N.N., Horisberger, J.D., Lelievre, L., and Geering, K. (2000) Transport and pharmacological properties of nine different human Na, K-ATPase isozymes. *J Biol. Chem.* **275,** 1976-1986.

Creutzfeldt, O. D. (1975) Brain Work: The Coupling of Function, Metabolism and Blood Flow in the Brain, Alfred Benzon Symposium VIII. ed. Ingvar, D. H. and Lassen, N. A. Copenhagen, Munksgaard. 21-46.

Cruz, F., Villalba, M., Garcia-Espinosa, M.A., Ballesteros, P., Bogonez, E., Satrustegui, J., and Cerdan, S. (2001) Intracellular compartmentation of pyruvate in primary cultures of

cortical neurons as detected by (13)C NMR spectroscopy with multiple (13)C labels. *J Neurosci. Res.* **66,** 771-781.

Cusack, R. (2005) The intraparietal sulcus and perceptual organization. *J Cogn Neurosci.* **17,** 641-651.

D'Angelo, E., De Filippi, G., Rossi, P., and Taglietti, V. (1997) Synaptic activation of Ca2+ action potentials in immature rat cerebellar granule cells in situ. *J Neurophysiol* **78,** 1631-1642.

Dalsgaard, M.K. (2006) Fuelling cerebral activity in exercising man. *J Cereb. Blood Flow Metab* **26,** 731-750.

Dalsgaard, M.K., Ide, K., Cai, Y., Quistorff, B., and Secher, N.H. (2002) The intent to exercise influences the cerebral O(2)/carbohydrate uptake ratio in humans. *J Physiol* **540,** 681-689.

Dalsgaard, M.K., Quistorff, B., Danielsen, E.R., Selmer, C., Vogelsang, T., and Secher, N.H. (2004) A reduced cerebral metabolic ratio in exercise reflects metabolism and not accumulation of lactate within the human brain. *J Physiol* **554,** 571-578.

Danbolt, N.C. (2001) Glutamate uptake. *Prog. Neurobiol.* **65,** 1-105.

Danbolt, N.C., Storm-Mathisen, J., and Kanner, B.I. (1992) An [Na^+ + K^+]coupled L-glutamate transporter purified from rat brain is located in glial cell processes. *Neuroscience* **51,** 295-310.

De Schutter, E. (1995) Cerebellar long-term depression might normalize excitation of Purkinje cells: a hypothesis. *Trends Neurosci.* **18,** 291-295.

Dehnes, Y., Chaudhry, F.A., Ullensvang, K., Lehre, K.P., Storm-Mathisen, J., and Danbolt, N.C. (1998) The glutamate transporter EAAT4 in rat cerebellar Purkinje cells: a glutamate-gated chloride channel concentrated near the synapse in parts of the dendritic membrane facing astroglia. *J Neurosci.* **18,** 3606-3619.

Delaney, C.L., Brenner, M., and Messing, A. (1996) Conditional ablation of cerebellar astrocytes in postnatal transgenic mice. *J. Neurosci.* **16,** 6908-6918.

Desai, N.S. and Walcott, E.C. (2006) Synaptic bombardment modulates muscarinic effects in forelimb motor cortex. *J Neurosci.* **26,** 2215-2226.

Dienel, G.A. and Hertz, L. (2001) Glucose and lactate metabolism during brain activation. *J Neurosci. Res.* **66,** 824-838.

Dieudonne, S. (1998) Submillisecond kinetics and low efficacy of parallel fibre-Golgi cell synaptic currents in the rat cerebellum. *J. Physiol* **510 (Pt 3),** 845-866.

Dirnagl, U., Niwa, K., Lindauer, U., and Villringer, A. (1994) Coupling of cerebral blood flow to neuronal activation: role of adenosine and nitric oxide. *Am. J Physiol* **267,** H296-H301.

Dowd, L.A., Coyle, A.J., Rothstein, J.D., Pritchett, D.B., and Robinson, M.B. (1996) Comparison of Na^+-dependent glutamate transport activity in synaptosomes, C6 glioma, and Xenopus oocytes expressing excitatory amino acid carrier 1 (EAAC1). *Mol. Pharmacol.* **49,** 465-473.

Drake, C.T. and Iadecola, C. (2007) The role of neuronal signaling in controlling cerebral blood flow. *Brain Lang* **102,** 141-152.

Dubner, R. and Zeki, S.M. (1971) Response properties and receptive fields of cells in an anatomically defined region of the superior temporal sulcus in the monkey. *Brain Res.* **35,** 528-532.

Duffy, S. and MacVicar, B.A. (1995) Adrenergic calcium signaling in astrocyte networks within the hippocampal slice. *J Neurosci.* **15,** 5535-5550.

Dzubay, J.A. and Jahr, C.E. (1999) The concentration of synaptically released glutamate outside of the climbing fiber-Purkinje cell synaptic cleft. *J Neurosci.* **19,** 5265-5274.

East, S.J. and Garthwaite, J. (1991) NMDA receptor activation in rat hippocampus induces cyclic GMP formation through the L-arginine-nitric oxide pathway. *Neurosci. Lett.* **123,** 17-19.

Eccles, J. C., Ito, M, and Szentagothai, J. (1967) The Cerebellum as a Neuronal Machine. Berlin; Heidelberg; New York, Springer-Verlag.

Epstein, R. and Kanwisher, N. (1998) A cortical representation of the local visual environment. *Nature* **392,** 598-601.

Faraci, F.M. and Breese, K.R. (1993) Nitric oxide mediates vasodilatation in response to activation of N-methyl-D-aspartate receptors in brain. *Circ. Res.* **72,** 476-480.

Farrant, M. and Brickley, S.G. (2003) Properties of GABA(A) receptor-mediated transmission at newly formed Golgi-granule cell synapses in the cerebellum. *Neuropharmacology* **44,** 181-189.

Fergus, A. and Lee, K.S. (1997b) Regulation of cerebral microvessels by glutamatergic mechanisms. *Brain Res.* **754,** 35-45.

Fergus, A. and Lee, K.S. (1997a) GABAergic regulation of cerebral microvascular tone in the rat. *J Cereb. Blood Flow Metab* **17,** 992-1003.

Fiala, J. C and Harris, K. M (1999) Dendrites. ed. Stuart, G., Spruston, N., and Hausser, M. Oxford, Oxford University Press.

Field, D.J. (1994) What is the goal of sensory coding? *Neural Comput.* **6,** 559-601.

Filosa, J.A., Bonev, A.D., and Nelson, M.T. (2004) Calcium dynamics in cortical astrocytes and arterioles during neurovascular coupling. *Circ. Res.* **95,** e73-e81.

Filosa, J.A., Bonev, A.D., Straub, S.V., Meredith, A.L., Wilkerson, M.K., Aldrich, R.W., and Nelson, M.T. (2006) Local potassium signaling couples neuronal activity to vasodilation in the brain. *Nat. Neurosci.* **9,** 1397-1403.

Fiser, J., Chiu, C., and Weliky, M. (2004) Small modulation of ongoing cortical dynamics by sensory input during natural vision. *Nature* **431,** 573-578.

Fishman, Y.I., Reser, D.H., Arezzo, J.C., and Steinschneider, M. (2001) Neural correlates of auditory stream segregation in primary auditory cortex of the awake monkey. *Hear. Res.* **151,** 167-187.

Forti, L., Cesana, E., Mapelli, J., and D'Angelo, E. (2006) Ionic mechanisms of autorhythmic firing in rat cerebellar Golgi cells. *J Physiol* **574,** 711-729.

Fox, P.T. and Raichle, M.E. (1986) Focal physiological uncoupling of cerebral blood flow and oxidative metabolism during somatosensory stimulation in human subjects. *Proc. Natl. Acad. Sci U. S. A* **83,** 1140-1144.

Fox, P.T., Raichle, M.E., Mintun, M.A., and Dence, C. (1988) Nonoxidative glucose consumption during focal physiologic neural activity. *Science* **241,** 462-464.

Funk, R.H. (1997) Blood supply of the retina. *Ophthalmic Res.* **29,** 320-325.

Furuta, A., Rothstein, J.D., and Martin, L.J. (1997) Glutamate transporter protein subtypes are expressed differentially during rat CNS development. *J Neurosci.* **17,** 8363-8375.

Galante, M. and Marty, A. (2003) Presynaptic ryanodine-sensitive calcium stores contribute to evoked neurotransmitter release at the basket cell-Purkinje cell synapse. *J. Neurosci.* **23,** 11229-11234.

Galeffi, F., Foster, K.A., Sadgrove, M.P., Beaver, C.J., and Turner, D.A. (2007) Lactate uptake contributes to the NAD(P)H biphasic response and tissue oxygen response during synaptic stimulation in area CA1 of rat hippocampal slices. *J Neurochem.* **103,** 2449-61.

Garcia-Espinosa, M.A., Rodrigues, T.B., Sierra, A., Benito, M., Fonseca, C., Gray, H.L., Bartnik, B.L., Garcia-Martin, M.L., Ballesteros, P., and Cerdan, S. (2004) Cerebral glucose metabolism and the glutamine cycle as detected by in vivo and in vitro 13C NMR spectroscopy. *Neurochem. Int.* **45,** 297-303.

Gebremedhin, D., Ma, Y.H., Falck, J.R., Roman, R.J., VanRollins, M., and Harder, D.R. (1992) Mechanism of action of cerebral epoxyeicosatrienoic acids on cerebral arterial smooth muscle. *Am. J Physiol* **263,** H519-H525.

Gjedde, A. (1993) Functional Organisation of the Human Visual Cortex, Wenner-Green International Symposium Series, Vol. 61. ed. Gulyas, B., Ottoson, D., and Roland, P. E. Oxford, Pergamon. 291-306.

Gjedde, A. and Marrett, S. (2001) Glycolysis in neurons, not astrocytes, delays oxidative metabolism of human visual cortex during sustained checkerboard stimulation in vivo. *J Cereb. Blood Flow Metab* **21,** 1384-1392.

Grewer, C., Watzke, N., Wiessner, M., and Rauen, T. (2000) Glutamate translocation of the neuronal glutamate transporter EAAC1 occurs within milliseconds. *Proc. Natl. Acad. Sci U. S. A* **97,** 9706-9711.

Gundappa-Sulur, G., De Schutter, E., and Bower, J.M. (1999) Ascending granule cell axon: an important component of cerebellar cortical circuitry. *J. Comp Neurol.* **408,** 580-596.

Guthrie, P.B., Knappenberger, J., Segal, M., Bennett, M.V., Charles, A.C., and Kater, S.B. (1999) ATP released from astrocytes mediates glial calcium waves. *J Neurosci.* **19,** 520-528.

Gutschalk, A., Micheyl, C., Melcher, J.R., Rupp, A., Scherg, M., and Oxenham, A.J. (2005) Neuromagnetic correlates of streaming in human auditory cortex. *J Neurosci.* **25,** 5382-5388.

Haefliger, I.O., Zschauer, A., and Anderson, D.R. (1994) Relaxation of retinal pericyte contractile tone through the nitric oxide-cyclic guanosine monophosphate pathway. *Invest Ophthalmol. Vis. Sci.* **35,** 991-997.

Halestrap, A.P. and Meredith, D. (2004) The SLC16 gene family-from monocarboxylate transporters (MCTs) to aromatic amino acid transporters and beyond. *Pflugers Arch.* **447,** 619-628.

Halestrap, A.P. and Price, N.T. (1999) The proton-linked monocarboxylate transporter (MCT) family: structure, function and regulation. *Biochem. J* **343 Pt 2,** 281-299.

Hansen, A.J. (1985) Effect of anoxia on ion distribution in the brain. *Physiol. Rev.* **65,** 101-148.

Harder, D.R., Alkayed, N.J., Lange, A.R., Gebremedhin, D., and Roman, R.J. (1998) Functional hyperemia in the brain: hypothesis for astrocyte-derived vasodilator metabolites. *Stroke* **28,** 229-234.

Harper, A.M., Deshmukh, V.D., Rowan, J.O., and Jennett, W.B. (1972) The influence of sympathetic nervous activity on cerebral blood flow. *Arch. Neurol.* **27,** 1-6.

Harvey, R.J. and Napper, R.M. (1988) Quantitative study of granule and Purkinje cells in the cerebellar cortex of the rat. *J. Comp Neurol.* **274,** 151-157.

Harvey, R.J. and Napper, R.M. (1991) Quantitative studies on the mammalian cerebellum. *Prog. Neurobiol.* **36,** 437-463.

Hasler, U., Wang, X., Crambert, G., Beguin, P., Jaisser, F., Horisberger, J.D., and Geering, K. (1998) Role of beta-subunit domains in the assembly, stable expression, intracellular routing, and functional properties of Na,K-ATPase. *J Biol. Chem.* **273,** 30826-30835.

Hauck, E.F., Apostel, S., Hoffmann, J.F., Heimann, A., and Kempski, O. (2004) Capillary flow and diameter changes during reperfusion after global cerebral ischemia studied by intravital video microscopy. *J Cereb. Blood Flow Metab* **24,** 383-391.

Hausser, M. and Clark, B.A. (1997) Tonic synaptic inhibition modulates neuronal output pattern and spatiotemporal synaptic integration. *Neuron* **19,** 665-678.

Heeger, D.J., Boynton, G.M., Demb, J.B., Seidemann, E., and Newsome, W.T. (1999) Motion opponency in visual cortex. *J Neurosci.* **19,** 7162-7174.

Hegner, Y.L., Saur, R., Veit, R., Butts, R., Leiberg, S., Grodd, W., and Braun, C. (2007) BOLD adaptation in vibrotactile stimulation: neuronal networks involved in frequency discrimination. *J. Neurophysiol* **97,** 264-271.

Herman, I.M. and D'Amore, P.A. (1985) Microvascular pericytes contain muscle and nonmuscle actins. *J Cell Biol.* **101,** 43-52.

Hertz, L. and Dienel, G.A. (2005) Lactate transport and transporters: general principles and functional roles in brain cells. *J Neurosci. Res.* **79,** 11-18.

Hertz, L., Swanson, R.A., Newman, G.C., Marrif, H., Juurlink, B.H., and Peng, L. (1998) Can experimental conditions explain the discrepancy over glutamate stimulation of aerobic glycolysis? *Dev. Neurosci.* **20,** 339-347.

Hirase, H., Creso, J., Singleton, M., Bartho, P., and Buzsaki, G. (2004a) Two-photon imaging of brain pericytes in vivo using dextran-conjugated dyes. *Glia* **46,** 95-100.

Hirase, H., Qian, L., Bartho, P., and Buzsaki, G. (2004b) Calcium dynamics of cortical astrocytic networks in vivo. *PLoS. Biol.* **2,** E96

Hodgkin, A. (1975) The optimum density of sodium channels in an unmyelinated nerve. *Philos. Trans. R. Soc. Lond B Biol. Sci* **270,** 297-300.

Hoge, R.D., Atkinson, J., Gill, B., Crelier, G.R., Marrett, S., and Pike, G.B. (1999) Linear coupling between cerebral blood flow and oxygen consumption in activated human cortex. *Proc. Natl. Acad. Sci. U. S. A* **96,** 9403-9408.

Hu, Y. and Wilson, G.S. (1997) A temporary local energy pool coupled to neuronal activity: fluctuations of extracellular lactate levels in rat brain monitored with rapid-response enzyme-based sensor. *J Neurochem.* **69,** 1484-1490.

Hubel, D.H. and Wiesel, T.N. (1998) Early exploration of the visual cortex. *Neuron* **20,** 401-412.

Hughes, S. and Chan-Ling, T. (2004) Characterization of smooth muscle cell and pericyte differentiation in the rat retina in vivo. *Invest Ophthalmol. Vis. Sci.* **45,** 2795-2806.

Huk, A.C. and Shadlen, M.N. (2005) Neural activity in macaque parietal cortex reflects temporal integration of visual motion signals during perceptual decision making. *J Neurosci.* **25,** 10420-10436.

Iadecola, C. (1992) Does nitric oxide mediate the increases in cerebral blood flow elicited by hypercapnia? *Proc. Natl. Acad. Sci U. S. A* **89,** 3913-3916.

Iadecola, C., Li, J., Xu, S., and Yang, G. (1996) Neural mechanisms of blood flow regulation during synaptic activity in cerebellar cortex. *J Neurophysiol* **75,** 940-950.

Iadecola, C., Yang, G., Ebner, T.J., and Chen, G. (1997) Local and propagated vascular responses evoked by focal synaptic activity in cerebellar cortex. *J Neurophysiol* **78,** 651-659.

Ide, K., Schmalbruch, I.K., Quistorff, B., Horn, A., and Secher, N.H. (2000) Lactate, glucose and O2 uptake in human brain during recovery from maximal exercise. *J Physiol* **522 Pt 1,** 159-164.

Isope, P. and Barbour, B. (2002) Properties of unitary granule cell-->Purkinje cell synapses in adult rat cerebellar slices. *J. Neurosci.* **22,** 9668-9678.

Ito, M (1984) The Cerebellum and Neuronal Control. New York, Raven Press.

Ito, M. (1972) Neural design of the cerebellar motor control system. *Brain Res.* **40,** 81-84.

Itoh, Y., Esaki, T., Shimoji, K., Cook, M., Law, M.J., Kaufman, E., and Sokoloff, L. (2003) Dichloroacetate effects on glucose and lactate oxidation by neurons and astroglia in vitro and on glucose utilization by brain in vivo. *Proc. Natl. Acad. Sci U. S. A* **100,** 4879-4884.

Izumi, A. (2002) Auditory stream segregation in Japanese monkeys. *Cognition* **82,** 113-122.

Jahr, C.E. and Stevens, C.F. (1990) Voltage dependence of NMDA-activated macroscopic conductances predicted by single-channel kinetics. *J Neurosci.* **10,** 3178-3182.

Jakab, R.L. and Hamori, J. (1988) Quantitative morphology and synaptology of cerebellar glomeruli in the rat. *Anat. Embryol. (Berl)* **179,** 81-88.

Jin, X., Huguenard, J.R., and Prince, D.A. (2005) Impaired Cl^- extrusion in layer V pyramidal neurons of chronically injured epileptogenic neocortex. *J Neurophysiol* **93,** 2117-2126.

Jobsis, F.F., O'Connor, M., Vitale, A., and Vreman, H. (1971) Intracellular redox changes in functioning cerebral cortex. I. Metabolic effects of epileptiform activity. *J Neurophysiol* **34,** 735-749.

Jorntell, H. and Ekerot, C.F. (2006) Properties of somatosensory synaptic integration in cerebellar granule cells in vivo. *J Neurosci.* **26,** 11786-11797.

Kadekaro, M., Crane, A.M., and Sokoloff, L. (1985) Differential effects of electrical stimulation of sciatic nerve on metabolic activity in spinal cord and dorsal root ganglion in the rat. *Proc. Natl. Acad. Sci U. S. A* **82,** 6010-6013.

Kamouchi, M., Kitazono, T., Ago, T., Wakisaka, M., Ooboshi, H., Ibayashi, S., and Iida, M. (2004) Calcium influx pathways in rat CNS pericytes. *Brain Res. Mol. Brain Res.* **126,** 114-120.

Kang, J., Jiang, L., Goldman, S.A., and Nedergaard, M. (1998) Astrocyte-mediated potentiation of inhibitory synaptic transmission. *Nat. Neurosci.* **1,** 683-692.

Kanichay, R.T. and Silver, R.A. (2007) Putative mossy fibre input resets spontaneous Golgi cell firing with high efficacy. *Submitted*

Karakossian, M.H. and Otis, T.S. (2004) Excitation of cerebellar interneurons by group I metabotropic glutamate receptors. *J Neurophysiol* **92,** 1558-1565.

Kasischke, K.A., Vishwasrao, H.D., Fisher, P.J., Zipfel, W.R., and Webb, W.W. (2004) Neural activity triggers neuronal oxidative metabolism followed by astrocytic glycolysis. *Science* **305,** 99-103.

Katsuki, S., Arnold, W., Mittal, C., and Murad, F. (1977) Stimulation of guanylate cyclase by sodium nitroprusside, nitroglycerin and nitric oxide in various tissue preparations and comparison to the effects of sodium azide and hydroxylamine. *J Cyclic. Nucleotide. Res.* **3,** 23-35.

Kawamura, H., Kobayashi, M., Li, Q., Yamanishi, S., Katsumura, K., Minami, M., Wu, D.M., and Puro, D.G. (2004) Effects of angiotensin II on the pericyte-containing microvasculature of the rat retina. *J Physiol* **561,** 671-683.

Kawamura, H., Sugiyama, T., Wu, D.M., Kobayashi, M., Yamanishi, S., Katsumura, K., and Puro, D.G. (2003) ATP: a vasoactive signal in the pericyte-containing microvasculature of the rat retina. *J Physiol* **551,** 787-799.

Kenet, T., Bibitchkov, D., Tsodyks, M., Grinvald, A., and Arieli, A. (2003) Spontaneously emerging cortical representations of visual attributes. *Nature* **425,** 954-956.

Kennedy, C., Sakurada, O., Shinohara, M., Jehle, J., and Sokoloff, L. (1978) Local cerebral glucose utilization in the normal conscious macaque monkey. *Ann. Neurol.* **4,** 293-301.

Kety, S. S (1957) Metabolism of the nervous system. ed. Richter, D. London, Pergamon. 221-237.

Kim, J.N. and Shadlen, M.N. (1999) Neural correlates of a decision in the dorsolateral prefrontal cortex of the macaque. *Nat. Neurosci.* **2,** 176-185.

Klyachko, V.A. and Stevens, C.F. (2003) Connectivity optimization and the positioning of cortical areas. *Proc. Natl. Acad. Sci U. S. A* **100,** 7937-7941.

Kole, M.H., Letzkus, J.J., and Stuart, G.J. (2007) Axon initial segment kv1 channels control axonal action potential waveform and synaptic efficacy. *Neuron* **55,** 633-647.

Kondo, S. and Marty, A. (1998) Synaptic currents at individual connections among stellate cells in rat cerebellar slices. *J Physiol* **509 (Pt 1),** 221-232.

Krimer, L.S., Muly, E.C., III, Williams, G.V., and Goldman-Rakic, P.S. (1998) Dopaminergic regulation of cerebral cortical microcirculation. *Nat. Neurosci.* **1,** 286-289.

Kukley, M., Capetillo-Zarate, E., and Dietrich, D. (2007) Vesicular glutamate release from axons in white matter. *Nat. Neurosci.* **10,** 311-320.

Kuschinsky, W. and Wahl, M. (1978) Local chemical and neurogenic regulation of cerebral vascular resistance. *Physiol Rev.* **58,** 656-689.

LaMotte, R.H. and Mountcastle, V.B. (1975) Capacities of humans and monkeys to discriminate vibratory stimuli of different frequency and amplitude: a correlation between neural events and psychological measurements. *J Neurophysiol* **38,** 539-559.

Lang, E.J., Sugihara, I., Welsh, J.P., and Llinas, R. (1999) Patterns of spontaneous purkinje cell complex spike activity in the awake rat. *J. Neurosci.* **19,** 2728-2739.

Lange, W. (1974) Regional differences in the distribution of golgi cells in the cerebellar cortex of man and some other mammals. *Cell Tissue Research* **153,** 219-226.

Laughlin, S.B. and Sejnowski, T.J. (2003) Communication in neuronal networks. *Science* **301,** 1870-1874.

LeDoux, M.S. and Lorden, J.F. (2002) Abnormal spontaneous and harmaline-stimulated Purkinje cell activity in the awake genetically dystonic rat. *Exp. Brain Res.* **145,** 457-467.

Leffler, C.W., Beasley, D.G., and Busija, D.W. (1989) Cerebral ischemia alters cerebral microvascular reactivity in newborn pigs. *Am. J Physiol* **257,** H266-H271.

Legrand, C., Ghandour, M.S., and Clos, J. (1983) Histochemical and biochemical studies of butyrylcholinesterase activity in adult and developing cerebellum. Effects of abnormal thyroid state and undernutrition. *Neuropathol. Appl. Neurobiol.* **9,** 433-453.

Lehre, K.P. and Danbolt, N.C. (1998) The number of glutamate transporter subtype molecules at glutamatergic synapses: chemical and stereological quantification in young adult rat brain. *J Neurosci.* **18,** 8751-8757.

Lehre, K.P., Levy, L.M., Ottersen, O.P., Storm-Mathisen, J., and Danbolt, N.C. (1995) Differential expression of two glial glutamate transporters in the rat brain: quantitative and immunocytochemical observations. *J Neurosci.* **15,** 1835-1853.

Lennie, P. (2003) The cost of cortical computation. *Curr. Biol.* **13,** 493-497.

Levy, L.M., Warr, O., and Attwell, D. (1998) Stoichiometry of the glial glutamate transporter GLT-1 expressed inducibly in a Chinese hamster ovary cell line selected for low endogenous Na^+-dependent glutamate uptake. *J Neurosci.* **18,** 9620-9628.

Levy, W.B. and Baxter, R.A. (1996) Energy efficient neural codes. *Neural Comput.* **8,** 531-543.

Li, J. and Iadecola, C. (1994) Nitric oxide and adenosine mediate vasodilation during functional activation in cerebellar cortex. *Neuropharmacology* **33,** 1453-1461.

Llano, I., Tan, Y.P., and Caputo, C. (1997) Spatial heterogeneity of intracellular Ca^{2+} signals in axons of basket cells from rat cerebellar slices. *J. Physiol* **502 (Pt 3),** 509-519.

Loewenstein, Y., Mahon, S., Chadderton, P., Kitamura, K., Sompolinsky, H., Yarom, Y., and Hausser, M. (2005) Bistability of cerebellar Purkinje cells modulated by sensory stimulation. *Nat. Neurosci.* **8,** 202-211.

Logothetis, N.K., Pauls, J., Augath, M., Trinath, T., and Oeltermann, A. (2001) Neurophysiological investigation of the basis of the fMRI signal. *Nature* **412,** 150-157.

Logothetis, N.K. and Wandell, B.A. (2004) Interpreting the BOLD signal. *Annu. Rev. Physiol* **66,** 735-769.

Lovick, T.A., Brown, L.A., and Key, B.J. (1999) Neurovascular relationships in hippocampal slices: physiological and anatomical studies of mechanisms underlying flow-metabolism coupling in intraparenchymal microvessels. *Neuroscience* **92,** 47-60.

Lu, K., Clark, J.W., Jr., Ghorbel, F.H., Robertson, C.S., Ware, D.L., Zwischenberger, J.B., and Bidani, A. (2004) Cerebral autoregulation and gas exchange studied using a human cardiopulmonary model. *Am. J Physiol Heart Circ. Physiol* **286,** H584-H601.

Lyer, P.N., Wilkinson, K.D., and Goldstein, L.J. (1976) An -N-acetyl-D-glycosamine binding lectin from Bandeiraea simplicifolia seeds. *Arch. Biochem. Biophys.* **177,** 330-333.

Maex, R. and De Schutter, E. (1998) Synchronization of Golgi and Granule Cell Firing in a Detailed Network Model of the Cerebellar Granule Cell Layer. *J Neurophysiol* **80,** 2521-2537.

Magistretti, P.J. and Pellerin, L. (1999a) Astrocytes couple synaptic activity to glucose utilization in the brain. *News Physiol Sci* **14,** 177-182.

Magistretti, P.J. and Pellerin, L. (1999b) Cellular mechanisms of brain energy metabolism and their relevance to functional brain imaging. *Philos. Trans. R. Soc. Lond B Biol. Sci.* **354,** 1155-1163.

Magistretti, P.J., Pellerin, L., Rothman, D.L., and Shulman, R.G. (1999) Energy on demand. *Science* **283,** 496-497.

Maher, F., Vannucci, S.J., and Simpson, I.A. (1994) Glucose transporter proteins in brain. *FASEB J* **8,** 1003-1011.

Maher, F., vies-Hill, T.M., and Simpson, I.A. (1996) Substrate specificity and kinetic parameters of GLUT3 in rat cerebellar granule neurons. *Biochem. J* **315 (Pt 3),** 827-831.

Maldjian, J.A., Gottschalk, A., Patel, R.S., Pincus, D., Detre, J.A., and Alsop, D.C. (1999) Mapping of secondary somatosensory cortex activation induced by vibrational stimulation: an fMRI study. *Brain Res.* **824,** 291-295.

Malonek, D., Dirnagl, U., Lindauer, U., Yamada, K., Kanno, I., and Grinvald, A. (1997) Vascular imprints of neuronal activity: relationships between the dynamics of cortical blood flow, oxygenation, and volume changes following sensory stimulation. *Proc. Natl. Acad. Sci. U. S. A* **94,** 14826-14831.

Malonek, D. and Grinvald, A. (1996) Interactions between electrical activity and cortical microcirculation revealed by imaging spectroscopy: implications for functional brain mapping. *Science* **272,** 551-554.

Marcaggi, P. and Attwell, D. (2004) Role of glial amino acid transporters in synaptic transmission and brain energetics. *Glia* **47,** 217-225.

Marcaggi, P. and Attwell, D. (2005) Endocannabinoid signaling depends on the spatial pattern of synapse activation. *Nat. Neurosci.* **8,** 776-781.

Marcaggi, P., Billups, D., and Attwell, D. (2003) The role of glial glutamate transporters in maintaining the independent operation of juvenile mouse cerebellar parallel fibre synapses. *J Physiol* **552,** 89-107.

Marr, D. (1969) A theory of cerebellar cortex. *J Physiol* **202,** 437-470.

Mathiesen, C., Caesar, K., Akgoren, N., and Lauritzen, M. (1998) Modification of activity-dependent increases of cerebral blood flow by excitatory synaptic activity and spikes in rat cerebellar cortex. *J Physiol* **512 (Pt 2),** 555-566.

McKeefry, D.J. and Zeki, S. (1997) The position and topography of the human colour centre as revealed by functional magnetic resonance imaging. *Brain* **120,** 2229-2242.

McKenna, M.C., Sonnewald, U., Huang, X., Stevenson, J., and Zielke, H.R. (1996) Exogenous glutamate concentration regulates the metabolic fate of glutamate in astrocytes. *J Neurochem.* **66,** 386-393.

McKenna, M.C., Tildon, J.T., Stevenson, J.H., Boatright, R., and Huang, S. (1993) Regulation of energy metabolism in synaptic terminals and cultured rat brain astrocytes: differences revealed using aminooxyacetate. *Dev. Neurosci.* **15,** 320-329.

Meng, W., Tobin, J.R., and Busija, D.W. (1995) Glutamate-induced cerebral vasodilation is mediated by nitric oxide through N-methyl-D-aspartate receptors. *Stroke* **26,** 857-862.

Metea, M.R., Kofuji, P., and Newman, E.A. (2007) Neurovascular coupling is not mediated by potassium siphoning from glial cells. *J Neurosci.* **27,** 2468-2471.

Metea, M.R. and Newman, E.A. (2006) Glial cells dilate and constrict blood vessels: a mechanism of neurovascular coupling. *J Neurosci.* **26,** 2862-2870.

Micheyl, C., Tian, B., Carlyon, R.P., and Rauschecker, J.P. (2005) Perceptual organization of tone sequences in the auditory cortex of awake macaques. *Neuron* **48,** 139-148.

Mintun, M.A., Lundstrom, B.N., Snyder, A.Z., Vlassenko, A.G., Shulman, G.L., and Raichle, M.E. (2001) Blood flow and oxygen delivery to human brain during functional activity: theoretical modeling and experimental data. *Proc. Natl. Acad. Sci U. S. A* **98,** 6859-6864.

Misra, C., Brickley, S.G., Farrant, M., and Cull-Candy, S.G. (2000) Identification of subunits contributing to synaptic and extrasynaptic NMDA receptors in Golgi cells of the rat cerebellum. *J Physiol* **524 Pt 1,** 147-162.

Mitchell, S.J. and Silver, R.A. (2003) Shunting inhibition modulates neuronal gain during synaptic excitation. *Neuron* **38,** 433-445.

Monsivais, P., Clark, B.A., Roth, A., and Hausser, M. (2005) Determinants of action potential propagation in cerebellar Purkinje cell axons. *J Neurosci.* **25,** 464-472.

Mountcastle, V.B., Talbot, W.H., Darian-Smith, I., and Kornhuber, H.H. (1967) Neural basis of the sense of flutter-vibration. *Science* **155,** 597-600.

Mulligan, S.J. and MacVicar, B.A. (2004) Calcium transients in astrocyte endfeet cause cerebrovascular constrictions. *Nature* **431,** 195-199.

Nagamatsu, S., Kornhauser, J.M., Burant, C.F., Seino, S., Mayo, K.E., and Bell, G.I. (1992) Glucose transporter expression in brain. cDNA sequence of mouse GLUT3, the brain facilitative glucose transporter isoform, and identification of sites of expression by in situ hybridization. *J Biol. Chem.* **267,** 467-472.

Nagao, S., Kwak, S., and Kanazawa, I. (1997) EAAT4, a glutamate transporter with properties of a chloride channel, is predominantly localized in Purkinje cell dendrites, and forms parasagittal compartments in rat cerebellum. *Neuroscience* **78,** 929-933.

Napper, R.M. and Harvey, R.J. (1988) Number of parallel fiber synapses on an individual Purkinje cell in the cerebellum of the rat. *J. Comp Neurol.* **274,** 168-177.

Nawroth, J.C., Greer, C.A., Chen, W.R., Laughlin, S.B., and Shepherd, G.M. (2007) An energy budget for the olfactory glomerulus. *J Neurosci.* **27,** 9790-9800.

Nelson, C.W., Wei, E.P., Povlishock, J.T., Kontos, H.A., and Moskowitz, M.A. (1992) Oxygen radicals in cerebral ischemia. *Am. J Physiol* **263,** H1356-H1362.

Newman, E.A. (2001) Propagation of intercellular calcium waves in retinal astrocytes and Muller cells. *J Neurosci.* **21,** 2215-2223.

Newman, E.A. (1986) High potassium conductance in astrocyte endfeet. *Science* **233,** 453-454.

Nilsson, L. and Siesjo, B.K. (1975) The effect of phenobarbitone anaesthesia on blood flow and oxygen consumption in the rat brain. *Acta Anaesthesiol. Scand. Suppl* **57,** 18-24.

Offenhauser, N., Thomsen, K., Caesar, K., and Lauritzen, M. (2005) Activity-induced tissue oxygenation changes in rat cerebellar cortex: interplay of postsynaptic activation and blood flow. *J Physiol* **565,** 279-294.

Ogawa, S., Lee, T.M., Kay, A.R., and Tank, D.W. (1990a) Brain magnetic resonance imaging with contrast dependent on blood oxygenation. *Proc. Natl. Acad. Sci. U. S. A* **87,** 9868-9872.

Ogawa, S., Lee, T.M., Nayak, A.S., and Glynn, P. (1990b) Oxygenation-sensitive contrast in magnetic resonance image of rodent brain at high magnetic fields. *Magn Reson. Med.* **14,** 68-78.

Otis, T.S. and Jahr, C.E. (1998) Anion currents and predicted glutamate flux through a neuronal glutamate transporter. *J Neurosci.* **18,** 7099-7110.

Ozerdem, U., Grako, K.A., hlin-Huppe, K., Monosov, E., and Stallcup, W.B. (2001) NG2 proteoglycan is expressed exclusively by mural cells during vascular morphogenesis. *Dev. Dyn.* **222,** 218-227.

Palay, S. L. and Chan-Palay, V. (1974) Cerebellar cortex : cytology and organization. Berlin; Heidelberg; New York, Springer.

Parri, H.R., Gould, T.M., and Crunelli, V. (2001) Spontaneous astrocytic Ca^{2+} oscillations in situ drive NMDAR-mediated neuronal excitation. *Nat. Neurosci.* **4,** 803-812.

Pasti, L., Volterra, A., Pozzan, T., and Carmignoto, G. (1997) Intracellular calcium oscillations in astrocytes: a highly plastic, bidirectional form of communication between neurons and astrocytes in situ. *J Neurosci.* **17,** 7817-7830.

Patel, A.B., De Graaf, R.A., Mason, G.F., Rothman, D.L., Shulman, R.G., and Behar, K.L. (2005) The contribution of GABA to glutamate/glutamine cycling and energy metabolism in the rat cortex in vivo. *Proc. Natl. Acad. Sci. U. S. A* **102,** 5588-5593.

Paulson, O.B. and Newman, E.A. (1987) Does the release of potassium from astrocyte endfeet regulate cerebral blood flow? *Science* **237,** 896-898.

Pellerin, L., Bergersen, L.H., Halestrap, A.P., and Pierre, K. (2005) Cellular and subcellular distribution of monocarboxylate transporters in cultured brain cells and in the adult brain. *J Neurosci. Res.* **79,** 55-64.

Pellerin, L., Bouzier-Sore, A.K., Aubert, A., Serres, S., Merle, M., Costalat, R., and Magistretti, P.J. (2007) Activity-dependent regulation of energy metabolism by astrocytes: an update. *Glia* **55,** 1251-1262.

Pellerin, L. and Magistretti, P.J. (1994) Glutamate uptake into astrocytes stimulates aerobic glycolysis: a mechanism coupling neuronal activity to glucose utilization. *Proc. Natl. Acad. Sci U. S. A* **91,** 10625-10629.

Pellionisz, A. and Szentagothai, J. (1973) Dynamic single unit simulation of a realistic cerebellar network model. *Brain Res.* **49,** 83-99.

Peng, L., Swanson, R.A., and Hertz, L. (2001) Effects of L-glutamate, D-aspartate, and monensin on glycolytic and oxidative glucose metabolism in mouse astrocyte cultures: further evidence that glutamate uptake is metabolically driven by oxidative metabolism. *Neurochem. Int.* **38,** 437-443.

Peppiatt, C. and Attwell, D. (2004) Neurobiology: feeding the brain. *Nature* **431,** 137-138.

Phillips, M.L., Young, A.W., Senior, C., Brammer, M., Andrew, C., Calder, A.J., Bullmore, E.T., Perrett, D.I., Rowland, D., Williams, S.C., Gray, J.A., and David, A.S. (1997) A specific neural substrate for perceiving facial expressions of disgust. *Nature* **389,** 495-498.

Phillipson, O.T., Kilpatrick, I.C., and Jones, M.W. (1987) Dopaminergic innervation of the primary visual cortex in the rat, and some correlations with human cortex. *Brain Res. Bull.* **18,** 621-633.

Pierre, K., Magistretti, P.J., and Pellerin, L. (2002) MCT2 is a major neuronal monocarboxylate transporter in the adult mouse brain. *J Cereb. Blood Flow Metab* **22,** 586-595.

Pinard, E., Tremblay, E., Ben-Ari, Y., and Seylaz, J. (1984) Blood flow compensates oxygen demand in the vulnerable CA3 region of the hippocampus during kainate-induced seizures. *Neuroscience* **13,** 1039-1049.

Poitry, S., Poitry-Yamate, C., Ueberfeld, J., MacLeish, P.R., and Tsacopoulos, M. (2000) Mechanisms of glutamate metabolic signaling in retinal glial (Muller) cells. *J Neurosci.* **20,** 1809-1821.

Poitry-Yamate, C.L., Poitry, S., and Tsacopoulos, M. (1995) Lactate released by Muller glial cells is metabolized by photoreceptors from mammalian retina. *J Neurosci.* **15,** 5179-5191.

Porras, O.H., Loaiza, A., and Barros, L.F. (2004) Glutamate mediates acute glucose transport inhibition in hippocampal neurons. *J Neurosci.* **24,** 9669-9673.

Pouzat, C. and Hestrin, S. (1997) Developmental regulation of basket/stellate cell-->Purkinje cell synapses in the cerebellum. *J. Neurosci.* **17,** 9104-9112.

Powers, W.J., Hirsch, I.B., and Cryer, P.E. (1996) Effect of stepped hypoglycemia on regional cerebral blood flow response to physiological brain activation. *Am. J Physiol* **270,** H554-H559.

Raichle, M.E. (1998) Behind the scenes of functional brain imaging: a historical and physiological perspective. *Proc. Natl. Acad. Sci. U. S. A* **95,** 765-772.

Raichle, M.E. and Gusnard, D.A. (2002) Appraising the brain's energy budget. *Proc. Natl. Acad. Sci. U. S. A* **99,** 10237-10239.

Raichle, M.E., Hartman, B.K., Eichling, J.O., and Sharpe, L.G. (1975) Central noradrenergic regulation of cerebral blood flow and vascular permeability. *Proc. Natl. Acad. Sci U. S. A* **72,** 3726-3730.

Raichle, M.E. and Mintun, M.A. (2006) Brain work and brain imaging. *Annu. Rev. Neurosci.* **29,** 449-476.

Raichle, M. E., Mintun, M. A., and Herscovitch, P. (1985) Brain imaging and brain function. ed. Sokoloff, L. New York, Raven Press.

Rancillac, A. and Barbara, J.G. (2005) Frequency-dependent recruitment of inhibition mediated by stellate cells in the rat cerebellar cortex. *J. Neurosci. Res.* **80,** 414-423.

Rancillac, A., Rossier, J., Guille, M., Tong, X.K., Geoffroy, H., Amatore, C., Arbault, S., Hamel, E., and Cauli, B. (2006) Glutamatergic Control of Microvascular Tone by Distinct GABA Neurons in the Cerebellum. *J Neurosci.* **26,** 6997-7006.

Rees, G., Friston, K., and Koch, C. (2000) A direct quantitative relationship between the functional properties of human and macaque V5. *Nat. Neurosci.* **3,** 716-723.

Reiner, P.B., Laycock, A.G., and Doll, C.J. (1990) A pharmacological model of ischemia in the hippocampal slice. *Neurosci. Lett.* **119,** 175-178.

Reis, D.J. and Golanov, E.V. (1997) Autonomic and vasomotor regulation. *Int. Rev. Neurobiol.* **41,** 121-149.

Rivera, C., Voipio, J., Payne, J.A., Ruusuvuori, E., Lahtinen, H., Lamsa, K., Pirvola, U., Saarma, M., and Kaila, K. (1999) The K^+/Cl^- co-transporter KCC2 renders GABA hyperpolarizing during neuronal maturation. *Nature* **397,** 251-255.

Robertson, B.E., Schubert, R., Hescheler, J., and Nelson, M.T. (1993) cGMP-dependent protein kinase activates Ca-activated K channels in cerebral artery smooth muscle cells. *Am. J Physiol* **265,** C299-C303.

Rolfe, D.F. and Brown, G.C. (1997) Cellular energy utilization and molecular origin of standard metabolic rate in mammals. *Physiol Rev.* **77,** 731-758.

Roman, R.J. (2002) P-450 metabolites of arachidonic acid in the control of cardiovascular function. *Physiol Rev.* **82,** 131-185.

Romo, R., Hernandez, A., and Zainos, A. (2004) Neuronal correlates of a perceptual decision in ventral premotor cortex. *Neuron* **41,** 165-173.

Romo, R., Hernandez, A., Zainos, A., Lemus, L., and Brody, C.D. (2002) Neuronal correlates of decision-making in secondary somatosensory cortex. *Nat. Neurosci.* **5,** 1217-1225.

Romo, R., Hernandez, A., Zainos, A., and Salinas, E. (2003) Correlated neuronal discharges that increase coding efficiency during perceptual discrimination. *Neuron* **38,** 649-657.

Roth, A. and Hausser, M. (2001) Compartmental models of rat cerebellar Purkinje cells based on simultaneous somatic and dendritic patch-clamp recordings. *J. Physiol* **535,** 445-472.

Rothstein, J.D., Martin, L., Levey, A.I., Dykes-Hoberg, M., Jin, L., Wu, D., Nash, N., and Kuncl, R.W. (1994) Localization of neuronal and glial glutamate transporters. *Neuron* **13,** 713-725.

Roy, C. and Sherrington, C. (1890) On the regulation of the blood supply of the brain. *Journal of Physiology* **11,** 85-100.

Rucker, H.K., Wynder, H.J., and Thomas, W.E. (2000) Cellular mechanisms of CNS pericytes. *Brain Res. Bull.* **51,** 363-369.

Sakagami, K., Kawamura, H., Wu, D.M., and Puro, D.G. (2001) Nitric oxide/cGMP-induced inhibition of calcium and chloride currents in retinal pericytes. *Microvasc. Res.* **62,** 196-203.

Sakagami, K., Wu, D.M., and Puro, D.G. (1999) Physiology of rat retinal pericytes: modulation of ion channel activity by serum-derived molecules. *J Physiol* **521 Pt 3,** 637-650.

Salinas, E. and Sejnowski, T.J. (2000) Impact of correlated synaptic input on output firing rate and variability in simple neuronal models. *J Neurosci.* **20,** 6193-6209.

Sargent, P.B., Saviane, C., Nielsen, T.A., DiGregorio, D.A., and Silver, R.A. (2005) Rapid vesicular release, quantal variability, and spillover contribute to the precision and reliability of transmission at a glomerular synapse. *J Neurosci.* **25,** 8173-8187.

Sarpeshkar, R. (1998) Analog versus digital: extrapolating from electronics to neurobiology. *Neural Comput.* **10,** 1601-1638.

Sato, A. and Sato, Y. (1992) Regulation of regional cerebral blood flow by cholinergic fibers originating in the basal forebrain. *Neurosci. Res.* **14,** 242-274.

Schonfelder, U., Hofer, A., Paul, M., and Funk, R.H. (1998) In situ observation of living pericytes in rat retinal capillaries. *Microvasc. Res.* **56,** 22-29.

Schurr, A., Miller, J.J., Payne, R.S., and Rigor, B.M. (1999) An increase in lactate output by brain tissue serves to meet the energy needs of glutamate-activated neurons. *The Journal of Neuroscience* **19,** 34-39.

Schurr, A., West, C.A., and Rigor, B.M. (1988) Lactate-supported synaptic function in the rat hippocampal slice preparation. *Science* **240,** 1326-1328.

Shen, J., Petersen, K.F., Behar, K.L., Brown, P., Nixon, T.W., Mason, G.F., Petroff, O.A., Shulman, G.I., Shulman, R.G., and Rothman, D.L. (1999) Determination of the rate of the glutamate/glutamine cycle in the human brain by in vivo 13C NMR. *Proc. Natl. Acad. Sci. U. S. A* **96,** 8235-8240.

Shepro, D. and Morel, N.M. (1993) Pericyte physiology. *FASEB J* **7,** 1031-1038.

Shigeri, Y., Shimamoto, K., Yasuda-Kamatani, Y., Seal, R.P., Yumoto, N., Nakajima, T., and Amara, S.G. (2001) Effects of threo-beta-hydroxyaspartate derivatives on excitatory amino acid transporters (EAAT4 and EAAT5). *J Neurochem.* **79,** 297-302.

Shimamoto, K., Lebrun, B., Yasuda-Kamatani, Y., Sakaitani, M., Shigeri, Y., Yumoto, N., and Nakajima, T. (1998) DL-threo-beta-benzyloxyaspartate, a potent blocker of excitatory amino acid transporters. *Mol. Pharmacol.* **53,** 195-201.

Shin, C. (2000) Neurophysiologic basis of functional neuroimaging: animal studies. *J Clin. Neurophysiol* **17,** 2-9.

Shinoda, Y., Sugiuchi, Y., Futami, T., and Izawa, R. (1992) Axon collaterals of mossy fibers from the pontine nucleus in the cerebellar dentate nucleus. *J Neurophysiol* **67,** 547-560.

Shulman, R.G., Rothman, D.L., Behar, K.L., and Hyder, F. (2004) Energetic basis of brain activity: implications for neuroimaging. *Trends Neurosci.* **27,** 489-495.

Sibson, N.R., Dhankhar, A., Mason, G.F., Rothman, D.L., Behar, K.L., and Shulman, R.G. (1998) Stoichiometric coupling of brain glucose metabolism and glutamatergic neuronal activity. *Proc. Natl. Acad. Sci. U. S. A* **95,** 316-321.

Siesjo, B (1978) Brain energy metabolism. New York, Wiley.

Silver, R.A., Colquhoun, D., Cull-Candy, S.G., and Edmonds, B. (1996a) Deactivation and desensitization of non-NMDA receptors in patches and the time course of EPSCs in rat cerebellar granule cells. *J. Physiol* **493 (Pt 1),** 167-173.

Silver, R.A., Cull-Candy, S.G., and Takahashi, T. (1996b) Non-NMDA glutamate receptor occupancy and open probability at a rat cerebellar synapse with single and multiple release sites. *J. Physiol* **494 (Pt 1),** 231-250.

Silver, R.A., Momiyama, A., and Cull-Candy, S.G. (1998) Locus of frequency-dependent depression identified with multiple-probability fluctuation analysis at rat climbing fibre-Purkinje cell synapses. *J. Physiol* **510 (Pt 3),** 881-902.

Simard, M., Arcuino, G., Takano, T., Liu, Q.S., and Nedergaard, M. (2003) Signaling at the gliovascular interface. *J Neurosci.* **23,** 9254-9262.

Sokoloff, L. (1960) Handbook of Physiology, Section I, Neurophysiology, vol. 3. ed. Field, J., Magoun, H. W., and Hall, V. E. Washington D.C., American Physiological Society. 1843-1864.

Sokoloff, L., Reivich, M., Kennedy, C., Des Rosiers, M.H., Patlak, C.S., Pettigrew, K.D., Sakurada, O., and Shinohara, M. (1977) The [14C]deoxyglucose method for the measurement of local cerebral glucose utilization: theory, procedure, and normal values in the conscious and anesthetized albino rat. *J Neurochem.* **28,** 897-916.

Sokoloff, L., Takahashi, S., Gotoh, J., Driscoll, B.F., and Law, M.J. (1996) Contribution of astroglia to functionally activated energy metabolism. *Dev. Neurosci.* **18,** 344-352.

Sonnewald, U., White, L.R., Odegard, E., Westergaard, N., Bakken, I.J., Aasly, J., Unsgard, G., and Schousboe, A. (1996) MRS study of glutamate metabolism in cultured neurons/glia. *Neurochem. Res.* **21,** 987-993.

Southam, E., East, S.J., and Garthwaite, J. (1991) Excitatory amino acid receptors coupled to the nitric oxide/cyclic GMP pathway in rat cerebellum during development. *J Neurochem.* **56,** 2072-2081.

Southam, E., Morris, R., and Garthwaite, J. (1992) Sources and targets of nitric oxide in rat cerebellum. *Neurosci. Lett.* **137,** 241-244.

Southan, A.P. and Robertson, B. (1998) Patch-clamp recordings from cerebellar basket cell bodies and their presynaptic terminals reveal an asymmetric distribution of voltage-gated potassium channels. *J. Neurosci.* **18,** 948-955.

Steuber, V., Mittmann, W., Hoebeek, F.E., Silver, R.A., De Zeeuw, C.I., Hausser, M., and De Schutter, E. (2007) Cerebellar LTD and pattern recognition by Purkinje cells. *Neuron* **54,** 121-136.

Storck, T., Schulte, S., Hofmann, K., and Stoffel, W. (1992) Structure, expression, and functional analysis of a Na(+)-dependent glutamate/aspartate transporter from rat brain. *Proc. Natl. Acad. Sci. U. S. A* **89,** 10955-10959.

Strata, P. and Rossi, F. (1998) Plasticity of the olivocerebellar pathway. *Trends Neurosci.* **21,** 407-413.

Stuart, G. and Hausser, M. (1994) Initiation and spread of sodium action potentials in cerebellar Purkinje cells. *Neuron* **13,** 703-712.

Sultan, F. and Bower, J.M. (1998) Quantitative Golgi study of the rat cerebellar molecular layer interneurons using principal component analysis. *J. Comp Neurol.* **393,** 353-373.

Sundstrom, R., Muntzing, K., Kalimo, H., and Sourander, P. (1985) Changes in the integrity of the blood-brain barrier in suckling rats with low dose lead encephalopathy. *Acta Neuropathol. (Berl)* **68,** 1-9.

Swanson, R.A. (1992) Astrocyte glutamate uptake during chemical hypoxia in vitro. *Neurosci. Lett.* **147,** 143-146.

Swanson, R.A., Yu, A.C., Chan, P.H., and Sharp, F.R. (1990) Glutamate increases glycogen content and reduces glucose utilization in primary astrocyte culture. *J Neurochem.* **54,** 490-496.

Tabernero, A., Vicario, C., and Medina, J.M. (1996) Lactate spares glucose as a metabolic fuel in neurons and astrocytes from primary culture. *Neurosci. Res.* **26,** 369-376.

Takano, T., Tian, G.F., Peng, W., Lou, N., Libionka, W., Han, X., and Nedergaard, M. (2006) Astrocyte-mediated control of cerebral blood flow. *Nat. Neurosci.* **9,** 260-267.

Tempia, F., Miniaci, M.C., Anchisi, D., and Strata, P. (1998) Postsynaptic current mediated by metabotropic glutamate receptors in cerebellar Purkinje cells. *J Neurophysiol* **80,** 520-528.

Thompson, J.K., Peterson, M.R., and Freeman, R.D. (2003) Single-neuron activity and tissue oxygenation in the cerebral cortex. *Science* **299,** 1070-1072.

Tildon, J.T., McKenna, M.C., Stevenson, J., and Couto, R. (1993) Transport of L-lactate by cultured rat brain astrocytes. *Neurochem. Res.* **18,** 177-184.

Tjalkens, R.B., Zoran, M.J., Mohl, B., and Barhoumi, R. (2006) Manganese suppresses ATP-dependent intercellular calcium waves in astrocyte networks through alteration of mitochondrial and endoplasmic reticulum calcium dynamics. *Brain Res.* **1113,** 210-219.

Tootell, R.B., Reppas, J.B., Dale, A.M., Look, R.B., Sereno, M.I., Malach, R., Brady, T.J., and Rosen, B.R. (1995) Visual motion aftereffect in human cortical area MT revealed by functional magnetic resonance imaging. *Nature* **375,** 139-141.

Tyrell, T. and Willshaw, D. (1992) Cerebellar cortex: its simulation and the relevance of Marr's theory. *Philos. Trans. R. Soc. Lond.* **336,** 239-257.

Ullensvang, K., Lehre, K.P., Storm-Mathisen, J., and Danbolt, N.C. (1997) Differential developmental expression of the two rat brain glutamate transporter proteins GLAST and GLT. *Eur. J Neurosci.* **9,** 1646-1655.

Ulrich, D. and Stricker, C. (2000) Dendrosomatic voltage and charge transfer in rat neocortical pyramidal cells in vitro. *J Neurophysiol* **84,** 1445-1452.

Van der Want, J.J., Vrensen, G.F., and Voogd, J. (1985) Differences in synaptic size in the superficial and deep layers of the molecular layer of the cerebellar cortex of the cat. An electronmicroscopic and autoradiographic study. *Anat. Embryol. (Berl)* **172,** 303-309.

Van Essen, D.C., Maunsell, J.H., and Bixby, J.L. (1981) The middle temporal visual area in the macaque: myeloarchitecture, connections, functional properties and topographic organization. *J Comp Neurol.* **199,** 293-326.

Vetter, P., Roth, A., and Hausser, M. (2001) Propagation of action potentials in dendrites depends on dendritic morphology. *J. Neurophysiol.* **85,** 926-937.

Vincent, S.R. and Kimura, H. (1992) Histochemical mapping of nitric oxide synthase in the rat brain. *Neuroscience* **46,** 755-784.

Viswanathan, A. and Freeman, R.D. (2007) Neurometabolic coupling in cerebral cortex reflects synaptic more than spiking activity. *Nat. Neurosci.* **10,** 1308-1312.

Vogel, J., Sperandio, M., Pries, A.R., Linderkamp, O., Gaehtgens, P., and Kuschinsky, W. (2000) Influence of the endothelial glycocalyx on cerebral blood flow in mice. *J Cereb. Blood Flow Metab* **20,** 1571-1578.

Volny-Luraghi, A., Maex, R., Vosdagger, B., and De Schutter, E. (2002) Peripheral stimuli excite coronal beams of Golgi cells in rat cerebellar cortex. *Neuroscience* **113,** 363-373.

Vos, B.P., Volny-Luraghi, A., and De Schutter, E. (1999) Cerebellar Golgi cells in the rat: receptive fields and timing of responses to facial stimulation. *Eur. J. Neurosci.* **11,** 2621-2634.

Voutsinos-Porche, B., Bonvento, G., Tanaka, K., Steiner, P., Welker, E., Chatton, J.Y., Magistretti, P.J., and Pellerin, L. (2003) Glial glutamate transporters mediate a functional metabolic crosstalk between neurons and astrocytes in the mouse developing cortex. *Neuron* **37,** 275-286.

Wadiche, J.I., Arriza, J.L., Amara, S.G., and Kavanaugh, M.P. (1995) Kinetics of a human glutamate transporter. *Neuron* **14,** 1019-1027.

Wadiche, J.I. and Jahr, C.E. (2001) Multivesicular release at climbing fiber-Purkinje cell synapses. *Neuron* **32,** 301-313.

Waldvogel, D., van Gelderen, P., Muellbacher, W., Ziemann, U., Immisch, I., and Hallett, M. (2000) The relative metabolic demand of inhibition and excitation. *Nature* **406,** 995-998.

Walz, W. and Mukerji, S. (1988) Lactate release from cultured astrocytes and neurons: a comparison. *Glia* **1,** 366-370.

Wang, G.J., Chung, H.J., Schnuer, J., Pratt, K., Zable, A.C., Kavanaugh, M.P., and Rosenberg, P.A. (1998) High affinity glutamate transport in rat cortical neurons in culture. *Mol. Pharmacol.* **53,** 88-96.

Wang, Q., Paulson, O.B., and Lassen, N.A. (1992) Effect of nitric oxide blockade by NG-nitro-L-arginine on cerebral blood flow response to changes in carbon dioxide tension. *J Cereb. Blood Flow Metab* **12,** 947-953.

Wen, Q. and Chklovskii, D.B. (2005) Segregation of the brain into gray and white matter: a design minimizing conduction delays. *PLoS. Comput. Biol.* **1,** e78

Williamson, J.R., Herczeg, B.E., Coles, H.S., and Cheung, W.Y. (1967) Glycolytic control mechanisms. V. Kinetics of high energy phosphate intermediate changes during electrical discharge and recovery in the main organ of Electrophorus electricus. *J Biol. Chem.* **242,** 5119-5124.

Wilson, E.C., Melcher, J., Micheyl, C., Gutschalk, A., and Oxenham, A.J. (2007) Cortical fMRI activation to sequences of tones alternating in frequency: Relationship to perceived rate and streaming. *J Neurophysiol* **97,** 2230-2238.

Winkler, B.S. (1981) Glycolytic and oxidative metabolism in relation to retinal function. *J Gen. Physiol* **77,** 667-692.

Wu, D.M., Kawamura, H., Sakagami, K., Kobayashi, M., and Puro, D.G. (2003) Cholinergic regulation of pericyte-containing retinal microvessels. *Am. J Physiol Heart Circ. Physiol* **284,** H2083-H2090.

Wyatt, K.D., Tanapat, P., and Wang, S.S. (2005) Speed limits in the cerebellum: constraints from myelinated and unmyelinated parallel fibers. *Eur. J. Neurosci.* **21,** 2285-2290.

Yamada, K., Watanabe, M., Shibata, T., Tanaka, K., Wada, K., and Inoue, Y. (1996) EAAT4 is a post-synaptic glutamate transporter at Purkinje cell synapses. *Neuroreport* **7,** 2013-2017.

Yu, A.C., Schousboe, A., and Hertz, L. (1982) Metabolic fate of 14C-labeled glutamate in astrocytes in primary cultures. *J Neurochem.* **39,** 954-960.

Zaksas, D. and Pasternak, T. (2006) Directional signals in the prefrontal cortex and in area MT during a working memory for visual motion task. *J Neurosci.* **26,** 11726-11742.

Zeki, S., Watson, J.D., Lueck, C.J., Friston, K.J., Kennard, C., and Frackowiak, R.S. (1991) A direct demonstration of functional specialization in human visual cortex. *J Neurosci.* **11,** 641-649.

Zeki, S.M. (1974) Functional organization of a visual area in the posterior bank of the superior temporal sulcus of the rhesus monkey. *J Physiol* **236,** 549-573.

Ziskin, J.L., Nishiyama, A., Rubio, M., Fukaya, M., and Bergles, D.E. (2007) Vesicular release of glutamate from unmyelinated axons in white matter. *Nat. Neurosci.* **10,** 321-330.

Zonta, M., Angulo, M.C., Gobbo, S., Rosengarten, B., Hossmann, K.A., Pozzan, T., and Carmignoto, G. (2003) Neuron-to-astrocyte signaling is central to the dynamic control of brain microcirculation. *Nat. Neurosci.* **6,** 43-50.